VOLUME 77 OCTOBER 11, 1973 / NUMBER 21

JPCHAx

THE JOURNAL OF PHYSICAL CHEMISTRY

PUBLISHED BIWEEKLY BY THE AMERICAN CHEMICAL SOCIETY

THE JOURNAL OF

PHYSICAL CHEMISTRY

AMERICAN CHEMICAL SOCIETY, *1155 Sixteenth St., N.W., Washington, D.C. 20036*

Books and Journals Division

JOHN K CRUM *Director*
RUTH REYNARD *Assistant to the Director*

CHARLES R. BERTSCH *Head, Editorial Processing Department*
D. H. MICHAEL BOWEN *Head, Journals Department*
BACIL GUILEY *Head, Graphics and Production Department*
SELDON W. TERRANT *Head, Research and Development Department*

 Published biweekly by the American Chemical Society at 20th and Northampton Sts., Easton, Pa. 18042. Second-class postage paid at Washington, D. C., and at additional mailing offices.

All manuscripts should be sent to *The Journal of Physical Chemistry*, Department of Chemistry, University of Minnesota, Minneapolis, Minn. 55455.

Additions and Corrections are published once yearly in the final issue. See Volume 76, Number 26 for the proper form.

Extensive or unusual alterations in an article after it has been set in type are made at the author's expense, and it is understood that by requesting such alterations the author agrees to defray the cost thereof.

The American Chemical Society and the Editor of *The Journal of Physical Chemistry* assume no responsibility for the statements and opinions advanced by contributors.

Correspondence regarding accepted copy, proofs, and reprints should be directed to Editorial Processing Department, American Chemical Society, 20th and Northampton Sts., Easton, Pa. 18042. Head: CHARLES R. BERTSCH. Assistant Editor: EDWARD A. BORGER. Editorial Assistant: JOSEPH E. YURVATI.

Advertising Office: Centcom, Ltd., 142 East Avenue, Norwalk, Conn. 06851.

Business and Subscription Information

Send all new and renewal subscriptions *with payment* to: Office of the Controller, 1155 16th Street, N.W., Washington, D. C. 20036. Subscriptions should be renewed promptly to avoid a break in your series. All correspondence and telephone calls regarding changes of address, claims for missing issues, subscription service, the status of records, and accounts should be directed to Manager, Membership and Subscription Services, American Chemical Society, P.O. Box 3337, Columbus, Ohio 43210. Telephone (614) 421-7230.

On changes of address, include both old and new addresses with ZIP code numbers, accompanied by mailing label from a recent issue. Allow four weeks for change to become effective.

Claims for missing numbers will not be allowed (1) if loss was due to failure of notice of change in address to be received before the date specified, (2) if received more than sixty days from date of issue plus time normally required for postal delivery of journal and claim, or (3) if the reason for the claim is "issue missing from files."

Subscription rates (1973): members of the American Chemical Society, $20.00 for 1 year; to nonmembers, $60.00 for 1 year. Those interested in becoming members should write to the Admissions Department, American Chemical Society, 1155 Sixteenth St., N.W., Washington, D. C. 20036. Postage to Canada and countries in the Pan-American Union, $5.00; all other countries, $6.00. Single copies for current year: $3.00. Rates for back issues from Volume 56 to date are available from the Special Issues Sales Department, 1155 Sixteenth St., N.W., Washington, D. C. 20036.

Subscriptions to this and the other ACS periodical publications are available on microfilm. Supplementary material not printed in this journal is now available in microfiche form on a current subscription basis. For information on microfilm or microfiche subscriptions, write Special Issues Sales Department at the address above.

Notice to Authors last printed in the issue of June 21, 1973

THE JOURNAL OF
PHYSICAL CHEMISTRY

Volume 77, Number 21 October 11, 1973

JPCHAx 77(21) 2493–2586 (1973)
ISSN 0022-3654

■ Supplementary material for this paper is available separately, in photocopy or microfiche form. Ordering information is given in the paper.

* In papers with more than one author, the asterisk indicates the name of the author to whom inquiries about the paper should be addressed.

AUTHOR INDEX

THE JOURNAL OF
PHYSICAL CHEMISTRY

VOLUME 77, NUMBER 21 OCTOBER 11, 1973

HF and DF Infrared Chemiluminescence and Energy Partitioning from the Reactions of Fluorine Atoms with C_6–C_{10} Cycloalkanes and Propane-d_6

K. C. Kim and D. W. Setser*

Department of Chemistry, Kansas State University, Manhattan, Kansas 66506 *(Received April 24, 1973)*

The infrared emission from the HF and DF products from the reactions of F atoms with cyclohexane, cyclohexane-d_{12}, cycloheptane, cyclooctane and cyclodecane has been studied. The initial product HF relative vibrational populations, $N_1{:}N_2{:}N_3{:}N_4$, are: C_6H_{12} = 0.28:0.56:0.18:trace, C_6D_{12} = 0.08:0.32:0.43:0.17, C_7H_{14} = 0.25:0.54:0.20:0.01, C_8H_{16} = 0.27:0.50:0.20:0.02, and $C_{10}H_{20}$ = 0.26:0.54:0.20:0.01. The mean fractional conversion of the available energy to vibrational energy of HF by these reactions (50%) is lower than for reactions with typical primary C–H bonds (60%). In order to provide reference data for reaction with a noncyclic secondary C–H bond, HF and DF overtone emission from F + $CD_3CH_2CD_3$ was studied. The relative vibrational populations are $N_2{:}N_3$ = 0.62:0.38 for HF and $N_2{:}N_3{:}N_4$ = 0.37:0.41:0.23 for DF. A very small HF, v' = 4 population was observed from the cyclic alkanes but not from $CD_3CH_2CD_3$, which is consistent with the difference in bond energies. Although the steady-state HF rotational populations are partially relaxed, an estimate of the initial rotational distributions suggests that ~7% of the available energy was partitioned as HF rotational energy for the reaction of fluorine atoms with cyclic alkanes.

Introduction

In preceding papers,[1,2] the results of the HF infrared chemiluminescence from the F atom abstraction reactions with polyatomic hydride molecules were reported. Relative rate constants for formation of HF in individual vibrational quantum states and information about the general nature of energy partitioning patterns were obtained. The importance of thermochemistry, differing mass combinations, variable bond types, substituent effects, and other factors have been discussed.

We report here the HF infrared chemiluminescence arising from the reaction of F atoms with secondary C–H bonds of C_6–C_{10} cyclic alkanes[3] and $CD_3CH_2CD_3$. The results from $CH_3CD_2CH_3$ and previously published[1] data from reactions with other primary C–H bonds are used for reference. The bond energy of the secondary C–H bonds is ~6 kcal mol^{-1} lower than the bond energies of primary C–H bonds, and this change could affect the energy partitioning. If the claim[1,2,4] that these F atom abstraction reactions populate vibrational–rotational levels up to the thermochemical limit is valid, then the lowered C–H bond energy should be evident from the highest observed HF level. Furthermore, a comparison between the secondary C–H bonds of cyclic and aliphatic alkanes should illustrate the consequences of the cyclic radical reorganization energy[3] and possibly other factors upon the HF vibrational and rotational populations.

Reactions of F atoms with polyatomic deuteride molecules have not previously been studied by the chemiluminescence technique. Although the DF fundamental spectrum falls in the region where the sensitivity of the lead sulfide detector is declining very rapidly, the enhanced sensitivity in the overtone region compensates somewhat for the smaller Einstein coefficients, relative to HF, and the slower reaction rates, relative to F + HR. Since the spacing of the vibration–rotational energy levels for DF are smaller than for HF, the DF results from F + c-C_6D_{12}, CD_4, and $CD_3CH_2CD_3$ provide a check for the relative rate constants and the energy partitioning patterns of the F + c-C_6H_{12}, CH_4, and $CH_3CD_2CH_3$ reactions.

The experiments were carried out in a fast flow apparatus[1,2] with the walls of the reaction vessel cooled to liquid nitrogen temperature.[5] The absence of vibrational relaxation was tested by varying reagent flow rate, background pressure, and F atom source. For some conditions, the degree of rotational relaxation could be altered and tentative estimates can be placed on the fractional conversion of the total energy into HF rotational energy.

Experimental Section

Apparatus and Techniques. All cyclic alkanes were purchased from Columbia Organic Chemicals Co. Cyclic C_6D_{12} was obtained from Stohler Isotope Chemicals with the specified isotopic purity of 99.5%. $CD_3CH_2CD_3$ was prepared from CD_3COCD_3 according to the standard $LiAlH_4$ reduction followed by chlorination of the resulting 2-propanol-d_6 and hydrolysis of the Grignard reagent. Mass spectral analysis showed greater than 98% isotopic and chemical purity. CD_4 and $CH_3CD_2CH_3$ were obtained from Merck Laboratory Chemicals.

The main features of the apparatus have been described previously.[1] The cold-walled (77°K) reactor was pumped through a liquid nitrogen trap by a 6-in. diffusion pump and a 500-l./min mechanical pump. The systems of gas inlets, pressure measuring devices, the optics, monochromator, and PbS detector were functionally the same as that used in the previous work.[1] The detector signal was amplified by a PAR Model HR-8 lock-in amplifier and PAR Model BZ-1 chopper, which was operated at 600 Hz.

Fluorine atoms were produced by microwave discharge of SF_6 or CF_4 in a quartz tube. The discharged CF_4 or SF_6 was mixed with reagent *via* a concentric mixing arrangement; the central quartz tube (0.8 mm i.d.) was 1 cm longer than the outer tube. A typical flow for SF_6 or CF_4 was ~4 μmol/sec. Typical flows of reagents were 2–6 μmol/sec. In addition to concentric mixing, a nozzle geometry in which the F atom flow was crossed with the flow of the substrate was tried. For the latter geometry, the tips of the two nozzles were ~4 cm apart.

The reagents were introduced to the vacuum line from a reagent flask after thorough degassing. The vapor pressure of the cyclic alkanes at room temperature was used as the back pressure and the flow was monitored with a Gilmont flowmeter. The operating pressure, measured at the bottom of the reactor under stabilized flow conditions, was $1\text{–}2 \times 10^{-4}$ Torr for typical experimental conditions. The actual density of the gas mixture in the mixing and emission zone undoubtedly is higher than indicated by the static pressure measurement.

The entire optical system was purged continuously before and during the experiment with dry nitrogen to minimize the absorption by atmospheric water. Emission from vibrationally excited $HF_{v,J}$ was recorded in the fundamental (0.4-mm slit) and overtone (2.0-mm slit) spectral region for most substrates. Typical sets of HF and DF spectra are shown in Figure 1 (F + c-C_8H_{16}) and Figure 2 (F + c-C_6D_{12}).

Data Treatment. Population analyses were made by computer simulation[2] of the observed spectra. The transition probabilities were calculated by the methods of Heaps and Herzberg[6a] and Herman–Wallis[6b] for the first term in the dipole moment expansion, with the spectroscopic constants of Mann, *et al.*[7] The detector response in the frequency range of interest was calibrated with a Barnes Engineering black body source. The line positions were calculated using the Herzberg expression. These positions were confirmed subsequently with the more accurate Dunham expression. It is necessary to use the latter for populations involving J levels higher than those observed in this work. An approximate set of initial populations ($N_{v',J'}$) and the detector response are entered into the program which calculates line positions and intensities which then are combined according to a triangular peak shape. The rotational populations of each vibrational level are normalized. Thus the relative vibrational populations and the shapes of the rotational distribution for each vibrational level are varied until the experimental spectrum is reproduced. The computer simulation was carried out for both the fundamental and the first overtone spectra.

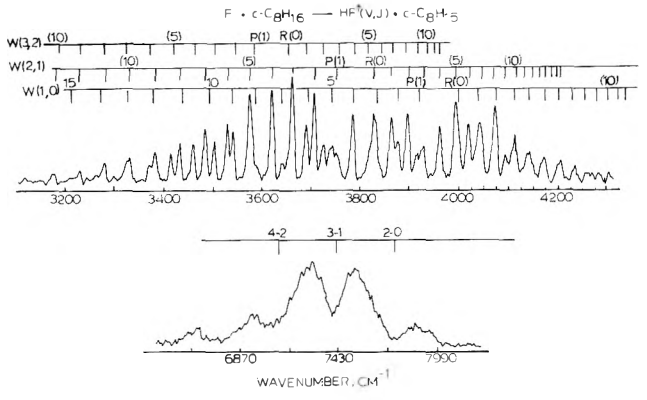

Figure 1. Fundamental and overtone spectra from F + cyclooctane at 10^{-4} Torr. The fundamental and overtone spectra were taken with slit widths of 0.4 and 2 mm, respectively. The feature at 6950 cm^{-1} is the R transitions from 4 to 2. The *apparent* feature at 6590 cm^{-1} was not assigned (see text).

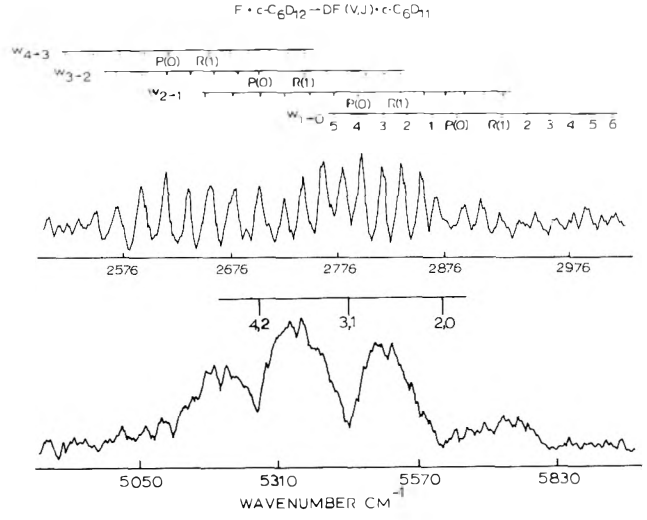

Figure 2. Fundamental and overtone spectra from F + cyclohexane-d_{12}.

The vibration–rotation populations for HF(v = 1, 2 and 3) were assigned by fitting the fundamental spectra. For the v = 2 and 3, the overtone data served as a check on the vibrational and rotational population assignments. For the higher vibrational states ($v \geq 4$) the fundamental emission falls in the region where the PbS detector sensitivity declines rapidly. However, the relative detector response in the overtone region for the higher levels is increasing and the small v' = 4 populations from the C_7–C_{10} compounds are based on comparison of the v' = 4 and 3 bands in the overtone spectra. The relative DF populations are based primarily upon analysis of the overtone spectra, except for DF(v = 1 and 2) from F + C_6D_{12}.

We experienced considerable difficulty in obtaining a good calibration for our spectrometer in the 7500–8100-cm^{-1} region because the response declines in this region and the black body intensity also is low. The lack of confidence in the calibration curve prevented us from using the HF overtone spectra to the fullest advantage. Although the v = 2 and 3 population ratios deduced from the fundamental spectrum frequently did not match that

TABLE I: Summary of Energy Partitioning

Compound	Initial vibrational[a] population $v = 1$	$v = 2$	$v = 3$	$v = 4$	$D°_0$ (C–H)	E_T, kcal mol^{-1} [b]	$\%E_V$[c]
c-C_6H_{12}	0.28	0.56	0.16	<0.005	94.0[d]	41.4	50
c-C_6D_{12}	0.08	0.32	0.43	0.17	96.8	40.2	54
c-C_7H_{14}	0.25	0.54	0.20	0.01	91.0[d]	44.4	49
c-C_8H_{16}	0.27	0.50	0.20	0.02	91.0[d]	44.4	48
c-$C_{10}H_{20}$	0.26	0.54	0.20	0.01	91.0[d]	44.4	49
$CD_3CH_2CD_3$(HF)		0.62	0.38		93.0[e]	42.4	—
$CD_3CH_2CD_3$(DF)		0.37	0.41	0.23	99.6[e]	37.8	—
$CH_3CD_2CH_3$(HF)	(≤0.24)[g]	0.50	0.26		96.8[e]	39.0	≥57[h]
CD_4	(0.05)[g]	0.29	0.56	0.10	104.9[f]	33.2	65[h]

[a] The steady-state populations obtained from the spectral analysis were corrected for radiative decay using a 0.2-msec residence time for HF. No corrections were made for DF because the radiative lifetime is sufficiently long that radiative decay is unimportant. The sums of the populations are normalized to unity. [b] $E_T = D°_0(H–F) - D°_0(H–R) + E°$; $E°$ is the threshold energy for reaction. The value[9] used for $D°_0(H–F)$ was 135.4 kcal mol^{-1}; $E°$ for the secondary C–H bonds was assumed to be zero; for CH_4[10] and $CH_3CD_2CH_3$[11] values of 1.1 and 0.4 kcal mol^{-1} were used. [c] $\%E_V = (\Sigma^4_{i=1} N_i E_i / E_T) \times 100$; the population of the $v = 0$ level is assumed to be negligible. The E_i's for $J = 0$ are 11.32 (8.31), 22.14 (16.35), 32.49 (24.14), 42.38 (31.65), and 52.10 (38.98) kcal for $v = 1$, 2, 3, 4, and 5 of HF(DF). [d] Reference 3c. [e] Reference 12. [f] Reference 13. [g] Estimated by extrapolation of Figure 5. [h] The $\%E_v$ previously found for CH_4 and C_2H_6 are 61 and 62%, respectively.

from the overtone spectra, the data are not of sufficient reliability to test the ratios of transition probabilities[8] for the $\Delta v = 1$ and $\Delta v = 2$ transitions. The disparity in the $v' = 2$ and 3 population ratios from the $\Delta v = 1$ and $\Delta v = 2$ spectra was similar to the variation from different experiments. As already stated the $v = 1$, 2, and 3 HF populations are based on the fundamental spectra, except for the experiments with $CD_3CH_2CD_3$ and $CH_3CD_2CH_3$.

The thermochemistry and relative vibrational populations (the sum of the relative populations are normalized to unity) are summarized in Table I. We previously[1,2] have argued that these populations are the original relative vibrational populations produced by the reactions. An additional and even more compelling argument is that the same vibrational populations were obtained for differing degrees of rotational relaxation for the F + c-C_8H_{16} reaction (see Figure 3). An estimate of the random experimental error in the relative populations was given in our earlier report.[1] The use of both the overtone and fundamental spectra, the improvement in our simulation techniques (primarily the addition of a Calcomp plotter to the Computer Center), and a more systematic approach to the assignment of rotational populations reduced our random error (see Table II of ref 1) by approximately a factor of 2. The most uncertain portion of our assignment is the population of the high J levels of $v = 1$. The emission is intrinsically weak because of low populations and low Einstein coefficients and this is compounded by overlapping of the P lines and low sensitivity[2] for the R lines.

F + c-C_6H_{12} and c-C_6D_{12}. The F + c-C_6H_{12} reaction was used in previous work[1] as a reference reaction. In the present study data from C_6H_{12} at somewhat lower pressure and with c-C_6D_{12} were obtained.[8] Since the vibrational–rotational spacings for DF are considerably smaller than those for HF, obviously a larger number of levels are populated and the spectrum contains more overlapped lines. The relative DF vibrational–rotational populations for $v' = 2$, 3, and 4 were based on analysis of the overtone spectrum and the relative population for $v = 1$ and 2 was obtained from the fundamental spectrum.

The exoergicity from F + c-C_6D_{12} (40.2 kcal mol^{-1}) is lower than that from F + c-C_6H_{12} (41.4 kcal mol^{-1}) because of zero point energy changes. These amounts of energy are sufficient to populate DF($J' = 6$ of $v' = 5$ and HF($J' = 12$ of $v' = 3$); however, DF emission from $v' = 5$ was not detected. The highest observed DF level was $J' = 12$ of $v' = 4$ (35.9 kcal mol^{-1}). The highest identified HF level in the fundamental spectrum was $J' = 8$ of $v' = 3$ (36.2 kcal mol^{-1}), but the overtone spectra suggested a trace of emission from HF($v' = 4$), which would require utilization of the thermal energy of the collision.

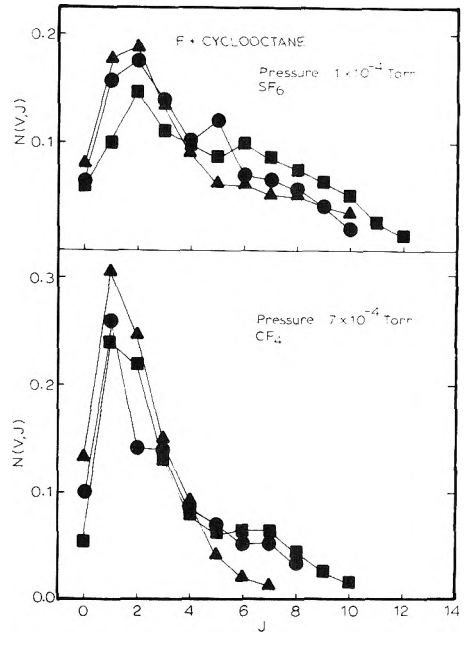

Figure 3. Relative rotational populations ($v = 1$, ●; $v = 2$, ■; $v = 3$, ▲) from F + c-C_8H_{16}. The distribution for each vibrational level is normalized to unity. The top set of distributions, which shows less rotational relaxation, was obtained at 1×10^{-4} Torr with SF_6 as the F atom source, and the lower one was recorded at 7×10^{-4} Torr using CF_4 as the F atom source. The steady-state distributions shown here at 10^{-4} Torr are preferred over the F + C_6H_{12} data of Figure 7, ref 1, as being representative of sec-C–H bonds under 1×10^{-4} Torr operating conditions.

Figure 4 shows the relative vibrational populations for F + c-C_6H_{12} and F + c-C_6D_{12} (scaled to fit the HF distribution at DF($v = 3$) plotted on a continuous energy scale. Within the experimental error the DF vibrational distribution fits that for HF. The low DF($v = 1$) relative population supports the assignment of a negligible population to the HF($v = 0$) level. The DF($v = 2$ and 3) levels pro-

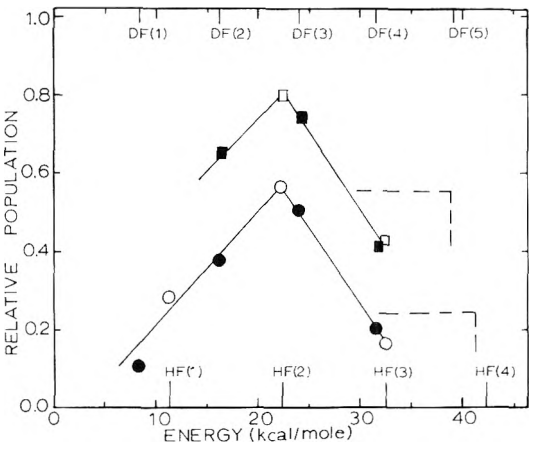

Figure 4. Relative vibrational populations from F + c-C_6H_{12} (O) and F + c-C_6D_{12} (●). The DF distribution was scaled to fit the HF distribution at v(DF) = 3. Also shown are the HF populations from F + $CH_3CD_2CH_3$ (□) combined with the DF populations from F + $CD_3CH_2CD_3$ (■). The dotted vertical lines indicate the potential energy released by the reactions.

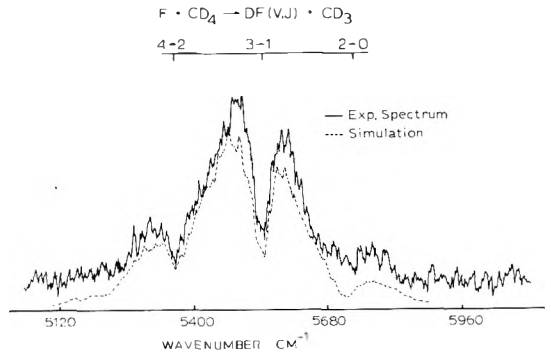

Figure 5. F + CD_4 overtone spectra at 5 × 10^{-4} Torr. The solid and dashed lines indicate experimental and simulated spectra, respectively. The simulated spectrum is displaced downward for clarity of presentation.

vide useful intermediate points between the widely spaced HF levels.

F + c-C_7H_{14}, c-C_8H_{16}, and c-$C_{10}H_{20}$. The fundamental spectra[13] from all of these reactions were nearly identical with that shown in Figure 1 for F + c-C_8H_{16}. The rotational distributions (1 × 10^{-4} Torr) shown in Figure 3 were derived from this fundamental spectrum, and they should be taken as representative steady-state populations for these three reactions (and C_6H_{12}). According to Figure 3, the steady-state rotational distributions of v = 1 and 3 are less extended than v = 2. This might have been expected for v = 3 but not for v = 1. Considerable study was put into simulating the 2–1 and 1–0 emission bands but we could find no evidence to support higher populations of the observed rotational states or any indication of emission from higher J levels. The low population for v = 1, J = 4 is an artifact of absorption by water and is probably exaggerated. The populations (10^{-4} Torr) of Figure 3 are used in the Discussion section to estimate *initial* rotational distributions.

The effect of increasing pressure from 6 × 10^{-5} to ~10^{-3} Torr on the rotational populations was tested using CF_4 as the F atom source. Extensive rotational relaxation was found at ~10^{-3} Torr, see Figure 3; however, the relative vibrational populations from the two sets of data shown in Figure 3 were the same. Two different types of nozzle geometry also were tested using c-C_8H_{16} as the reagent. Under our best experimental conditions (≤10^{-4} Torr static background pressure) no consistent differences in the total intensity or in the extent of the rotational relaxation were observed between the concentric and crossed nozzle arrangements for the same F atom source. However, rotational relaxation was more extensive with CF_4 than with SF_6. This is attributable to the higher background pressure corresponding to increased gas phase collisional deactivation by CF_4, since it is not fully condensable at 77°K.

Simulation of the overtone spectrum of Figure 1, using the rotational distribution of Figure 3, required the addition of a significant HF(v = 4) population. The feature of the spectrum responsible for this is apparent at ~6950 cm^{-1}. Careful examination of high-intensity fundamental spectra showed the presence of weak emission peaks in the 4–3 transition region (3200–3600 cm^{-1}) which confirm the presence of HF(v = 4). From the overtone data, J = 4 of v = 4 (43.4 kcal mol^{-1}) was estimated to be the highest level; the highest level from v = 3 was J = 10.

Experiments were done to vary the total emission intensity in order to test for the possibility that energy pooling, 2HF(v = 3) → HF(v = 4) + HF(v = 2), might contribute to the observed emission from high v levels. However, no correlation of the 4–2 emission with total emission intensity was found.

The feature at 6590 cm^{-1} in the overtone spectrum of Figure 1 remains unexplained. It was observed in some, but not all, of the F + c-C_8H_{16} experiments but was absent from the F + c-C_7H_{14} or c-$C_{10}H_{20}$ spectra. It is not assignable, in a reasonable way, to emission from HF.

F + $CD_3CH_2CD_3$, $CH_3CD_2CH_3$, and CD_4. For these compounds the available quantities of material permitted the scanning of only one or two overtone spectra. The results are thus less complete and less reliable. The main point of these experiments was to provide information to confirm trends expected from other results, and the data are of sufficient quality for this purpose. The spectrum and simulation from F + CD_4 are shown in Figure 5 for reference.

The F + $CD_3CH_2CD_3$ reaction was studied in order to compare results from cyclic and aliphatic *sec*-C–H bonds. The bond energy, $D°_0$(H–$CH(CD_3)_2$), is about 2 kcal higher than for cycloheptane and about 1 kcal less than for cyclohexane. Therefore, differences in HF populations arising from thermochemical effects should be minimal. The relative HF(v = 3) population from $CD_3CH_2CD_3$ (N_3/N_2 = 0.63) is considerably higher than that from cyclic alkanes, (N_3/N_2 = 0.37), but there was no evidence for a significant v = 4 population. Although information on the HF(v = 1) relative population is lacking, based upon the significantly higher v = 3 relative population, the fractional conversion into vibration energy is estimated to be higher than that for cyclic alkanes.

The HF results from F + $CH_3CD_2CH_3$ and the DF results from F + $CD_3CH_2CD_3$ provide another set of populations for a "typical" primary C–H bond. The combined results are plotted in Figure 4 with HF(v = 2) population set to 0.8 and DF(v = 3) scaled to fit the line connecting HF(v = 2) and HF(v = 3). If the HF(v = 1) population is estimated by extrapolation of Figure 4, $\%E_v$ can be assigned as ≥57%. The very similar HF(v = 2; v = 3) population ratio from the primary and secondary positions of $CD_3CH_2CD_3$ and $CH_3CD_2CH_3$ strongly suggests that $\%E_v$ is less for the secondary position because E_T is larger.

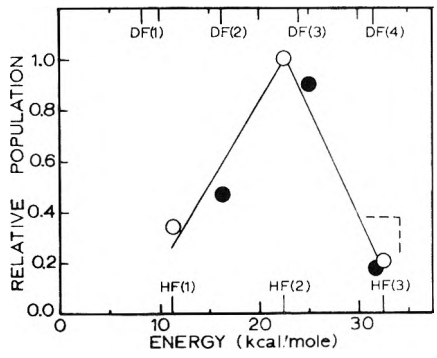

Figure 6. The relative vibrational populations from F + CD_4, ●, and F + CH_4,[1,13] ○. The DF distribution was scaled to obtain an approximate match to the HF distribution at the DF(v = 3) point. The vertical dotted line indicates the available potential energy.

The F + CH_4 data[14] shown in Figure 6 were obtained at 4 × 10^{-4} Torr and are in agreement with our previous study.[1] As with cyclohexane, the DF population distribution from CD_4 matches the HF distribution from CH_4. The highest DF rotational level from the spectral simulation of the F + CD_4 overtone spectrum was J = 5 of v = 4 (35.3 kcal/mol). The v = 1, 2, 3 relative vibrational populations from F + C_2H_6 have been reported as 0.14:0.50:0.36; this distribution was confirmed for both conditions of Figure 3 in the present study. The variation in $\%E_v$ and the N_2/N_3 ratio can be compared for CH_4 (61%, 5.0), C_2H_6 (62%, 1.4), $CH_3CD_2CH_3$ (≥57%, 1.9), and $C(CH_3)_4$ (56%, 4.1). The abrupt change in N_2/N_3 for CH_4 and C_2H_6 probably can be attributed to the difference in C–H bond energies.[15]

Discussion

Comparison of Results from Primary and Secondary C–H Bonds. The vibrational (HF) energy distributions from the F + c-C_6–C_{10} reactions are all similar and constitute a set of data for these secondary C–H bonds. One of the most prominent features is that the fractional conversion of the available energy to vibrational energy is ~50% as compared to 60% for most primary C–H bonds. The ring strain energies for C_7–C_{10} cyclic alkanes are sizeable, and the difference in strain energy between a molecule and its cyclic radical may be significant because a carbon atom undergoes a rearrangement from sp^3 to sp^2 configuration, which generally increases the strain. Since the duration of the abstraction reactions proceeding by the direct[15] mechanism is of the order of 10^{-14} sec, the radical fragments do not have sufficient time to rearrange to their equilibrium configurations and this radical distortion energy is not *freely* available to the HF† fragment († indicates an HF fragment as it initially is born, subsequent interactions[15] with the R group may modify this initial energy distribution before it becomes an HF product). Cyclohexane, in its most stable conformation, is nearly strain free while the ring strain energies for C_7–C_{10} cyclic alkanes are 4–10 kcal relative to cyclohexane. Therefore, the change in ring strain energy from the molecular configuration to the cyclic radical configuration should be larger for c-C_6H_{12} than for the rest of the cyclanes. This may explain the energy defect observed for c-C_6H_{12} (and C_6D_{12}).

The distribution from F + $CD_3CH_2CD_3$ provides results from a noncyclic secondary C–H bond for reference. Additional data would be desirable; however, the overtone spectrum indicated that N_3/N_2 was considerably higher than that from the cyclic alkanes, which suggests that the change in ring strain energy contributes to the distortion energy of the cyclic radicals, which affects the energy released to the HF product.

The HF vibrational distribution pattern from the primary and secondary bonds in propane were virtually identical, in spite of the availability of 4 kcal mol^{-1} more energy for abstraction from the secondary position. Thus, a smaller fraction of energy was partitioned to HF vibrational energy from secondary C–H bonds than from primary C–H bonds. This conclusion from an intramolecular comparison agrees with conclusions from intermolecular comparisons. This reduced $\%E_v$ is somewhat surprising since the saddle point might be expected to occur at somewhat greater H–F distances for secondary C–H bonds. According to a three-body simulation[15] of the F + HR reactions, moving the thermochemical limit from 2 kcal in excess of the v = 3 limit to 7 kcal mol^{-1} in excess greatly enhanced the relative HF(v = 3) yield. Further calculations are needed to check for the effect of advancing the thermochemical limit from 7 kcal mol^{-1} in excess up to the v = 4 limit (10 kcal mol^{-1} in excess). If the trend can be extrapolated, then an explanation of the reduction in $\%E_v$ is required. The simplest point of view is that the additional energy is not available to the HF on the time scale of the reaction. Stated in another way, the radical distortion energy (which we assume to be released late in the reaction) is larger for isopropyl than for *n*-propyl radicals. According to this view, the difference in secondary and primary C–H bond energies[16] is largely the difference in the radical distortion energies.

Except for cyclohexane, the highest observed HF vibrational–rotational level does closely correspond to that permitted by the available energy. This total energy release to HF for a small fraction of the events is not too surprising considering the complexity of some trajectories for transfer of H from R to F, even for the three-body approximation.[15] Although emission from HF(v = 3) corresponded closely with the thermochemical limit, no HF(v = 4) emission was observed from the F + $CD_3CH_2CD_3$ reaction even though there is just enough energy. In contrast, the excess potential energy for (v = 4) from F + CD_4 is ~0.5 kcal mol^{-1}; it is even less for HF(v = 3) from F + CH_4, but emission is observed from both of these levels. Evidently abstraction from primary C–H bonds tends to favor higher HF vibrational levels than does abstraction from secondary C–H bonds. Formation of v = 4 from C_7, C_8, and C_{10} but not from $CD_3CH_2CD_3$ may be a consequence of the slightly higher bond energy for the latter.

Estimation of Rotational Energy Partitioning. Rotational relaxation was not fully arrested in these experiments, but there are indications of a secondary maxima in the distribution around J = 5–8 in Figure 3. If one *assumes* that the original distributions peak at intermediate J and assigns the contour of high J levels as the remnant of the unrelaxed population, then an estimate of the original populations can be made with the aid of simulated steady-state populations according to a preassigned relaxation model.[2,17] The model that was used for the down transitions was of the form $P_{i \to j} = Ng_j \exp[-(E_i - E_j)/RT]$ with T = 200° and N = 0.3. The details of the model are not particularly important, as long as the basic forms of the transition probabilities are not changed; *i.e.*, if the total inelastic cross section is reduced, then a larger $\bar{Z}$ is required to fit the same degree of relaxation. For these

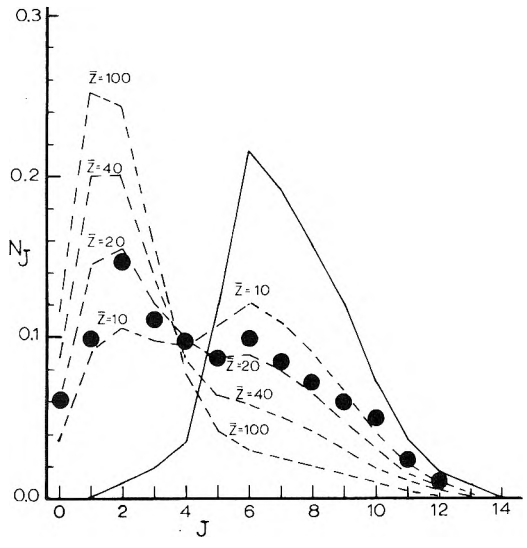

Figure 7. Comparison of experimental low pressure HF(v = 2) data of Figure 4 and computed (- - -) steady-state rotational distributions, which were obtained from the original (—) distribution and the mean number of collisions, $\bar{Z}$, for the rotational relaxation model specified in the text. The average energy of the initial distribution was 1256 cm^{-1}.

calculations an equilibrium distribution of collision times was used; hence, the designation of $\bar{Z}$ for the average number of collisions before observation.

The agreement between the simulated (for $\bar{Z} \sim 15$) and experimental population for $v = 2$ is reasonable as shown in Figure 7. The initial population is not, however, unique. For example, an initial distribution shifted upward by one J unit and broadened ($\langle E \rangle$ = 1540 cm^{-1} as contrasted to 1256 cm^{-1} in Figure 7) gave only a slightly less satisfactory fit for $\bar{Z}$ = 25. If the assumption regarding a "symmetric" form for the original population is valid, the estimated distribution of Figure 7 should be a reasonable one. Applying the same model and the same $\bar{Z}$ to the v = 1 and 3 levels, gives distributions of the same general form as that of Figure 7, but with average energies of 1032 and 920 cm^{-1}, respectively. For these distributions the fraction of energy released to rotation is 7% for the C_8H_{16} thermochemistry. Based upon other symmetric type distributions which are compatible with the data, the range for $\%E_R$ probably extends from 6 to 9%. According to this analysis there is no inverse correlation of E_R with v. This appears to be a general feature of F + hydrocarbon reactions and is quite different from the Cl + HI or F + HCl reactions,[5a,18] which have similar dynamical features. Although this is the most obvious interpretation of the data, some reservation should be maintained because, as already explained, the high J transitions of v = 1 are difficult to observe with our detection system. On the other hand, the steady-state rotational population, obtained in our apparatus from F + HCl, which is known[18] to favor high J levels, differs significantly from that of Figure 3. This strongly suggests that our estimates for the hydrocarbon reactions are, at least, qualitatively valid.

Conclusions

For the reactions of F atoms with C_6–C_{10} cyclic alkanes, 49% of the energy is partitioned as vibrational energy and ~7% as rotational energy of the HF product. From a less detailed study of $CD_3CH_2CD_3$, the fraction of HF vibrational energy appeared to be somewhat larger than for the cyclic alkanes, although still lower than for reaction with primary C–H bonds. The reduced fraction of energy released to HF from the secondary C–H bonds relative to primary bonds suggests that all of the energy is not accessible to the HF† on the time scale for separation of HF from the R fragment. One explanation is that the radical distortion energy (which is released late in the course of the reaction) may be larger for secondary radicals (isopropyl) than for primary radicals (*n*-propyl). Our data do not permit a distinction to be made between the normal view (α-alkylation leads to a stabilization of the free radical center) and a more recent suggestion[16] (greater strain in the molecule state with increasing alkylation) as to the origin of the difference of bond energies in primary and secondary CH bonds, because energy release from either effect would occur slower than the time for the initial[15] transfer of H to the attacking F atom. Better data, especially of the rotational distributions, and a greater understanding of how secondary and complex encounters[15] between the HF† and R fragment may influence the hydrogen fluoride vibrational and rotational distributions are needed before simple interpretations are accepted with any degree of confidence. Nevertheless, the HF energy partitioning patterns are not only of interest in themselves but may provide insight concerning the origin of energy differences in molecules and radicals.

Acknowledgments. We thank Dr. Denis Bogan for permission to show the F + C_8H_{16} data, which were obtained with CF_4 as the atom source, and to quote his results from the F + C_2H_6 reaction. This work was supported by the National Science Foundation (NSF-27536X).

References and Notes

(1) H. W. Chang and D. W. Setser, *J. Chem. Phys.*, **58**, 2298 (1973).
(2) W. H. Duewer and D. W. Setser, *J. Chem. Phys.*, **58**, 2310 (1973).
(3) (a) J. D. Cos, *Tetrahedron*, **19**, 1175 (1963); (b) K. B. Wiberg, *J. Amer. Chem. Soc.*, **87**, 1070 (1965); (c) K. C. Ferguson and E. Whittle, *Trans. Faraday Soc.*, **67**, 2620 (1971).
(4) (a) J. C. Polanyi and K. B. Woodall, *J. Chem. Phys.*, **57**, 1574 (1972); (b) J. C. Polanyi and D. C. Tardy, *ibid.*, **51**, 5717 (1969).
(5) (a) K. G. Anlauf, D. S. Horne, R. G. McDonald, J. C. Polanyi, and K. B. Woodall, *J. Chem. Phys.*, **57**, 1547 (1972); (b) D. H. Maylotte, J. C. Polanyi, and K. B. Woodall, *ibid.*, **57**, 1561 (1972).
(6) (a) H. S. Heaps and G. Herzberg, *Z. Phys.*, **133**, 48 (1952); (b) R. C. Herman and R. F. Wallis, *J. Chem. Phys.*, 23, 637 (1955).
(7) (a) D. E. Mann, B. A. Thrush, D. R. Lide, Jr., J. J. Ball, and N. Acquista, *J. Chem. Phys.*, **34**, 420 (1961); (b) R. N. Spanbauer and K. Narahari Rao, *J. Mol. Spectrosc.*, **16**, 100 (1965).
(8) The values of the HF transition probabilities used for analysis of the data are A_0^1 = 183, A_1^2 = 330, A_2^3 = 445, A_3^4 = 536 and A_0^2 = 22.8, A_1^3 = 62.9, A_2^4 = 116.1 sec^{-1}. For DF the values are A_0^1 = 72.6, A_1^2 = 134, A_2^3 = 187, A_3^4 = 232 and A_0^2 = 9.1, A_1^3 = 25.6, A_2^4 = 48.7, A_3^5 = 76.9 sec^{-1}. The data of R. L. Spellicy, R. E. Meredith and F. G. Smith, *J. Chem. Phys.*, **57**, 5119 (1972), were used to scale the relative values to absolute quantities.
(9) W. A. Chupka and J. Berkowitz, *J. Chem. Phys.*, **54**, 5126 (1971).
(10) J. Warnatz, H. G. Wagner, and C. Zetsch, *Ber. Bungenges. Phys. Chem.*, **74**, 585 (1970); **75**, 119 (1971).
(11) (a) R. Foon and G. P. Reid, *Trans. Faraday Soc.*, **67**, 3515 (1971); (b) R. F. Walker and M. A. A. Clyne, private communication, 1972.
(12) J. A. Kerr, *Chem. Rev.*, **66**, 465 (1966).
(13) B. deB. Darwent, "Bond Dissociation Energies in Simple Molecules," NSRDS-NBS-31, U. S. Government Printing Office, Washington, D. C., 1970.
(14) K. C. Kim, Ph.D. Thesis, Kansas State University, 1973.
(15) R. L. Johnson, K. C. Kim, and D. W. Setser, *J. Phys. Chem.*, **77**, 2499 (1973).
(16) C. Rüchart, *Angew. Chem., Int. Ed. Engl.*, **9**, 380 (1970).
(17) J. C. Polanyi and K. B. Woodall, *J. Chem. Phys.*, **56**, 1563 (1972).
(18) A. M. G. Ding, L. J. Kirsch, D. S. Perry, J. C. Polanyi, and J. L. Schreiber, *Discuss. Faraday Soc.*, in press.

Trajectory Studies of Abstraction Reactions. Fluorine Atoms with Substituted Methanes and Deuterium Atoms with Chloroiodide

R. L. Johnson, K. C. Kim, and D. W. Setser*

Department of Chemistry, Kansas State University, Manhattan, Kansas 66506 *(Received April 24, 1973)*

Classical three-body trajectory calculations with LEPS potential surfaces have been done for F + HR → FH + R type reactions. The mass and other properties of the R body were adjusted to closely simulate the reaction with CH_4 and CH_3Br (or CH_2Cl_2). The objective was to provide computed results, within the three-body approximation, which could be compared to experimental energy partitioning patterns for these two reactions and for reactions with CH_3F, CH_3OD, CH_3Cl, CH_3I, and CH_3HgCH_3. The general pattern, *i.e.*, release of ~60% of the energy as vibrational energy of HF, is reproduced by the LEPS surface. The computed results show only a small mass effect which appears as a slight broadening of the vibrational distribution. The calculations suggest that the HF(v = 3) population is quite sensitive to the thermochemistry, if the thermochemical limit is close to the HF(v = 3) energy. A significant fraction of the trajectories show complex (indirect) trajectories and also delayed secondary encounters. This feature is emphasized by the central light atom and suggests that care should be exercised in using the three-body approximation for hydrogen atom abstraction reactions. In the course of development of the trajectory computer program, calculations were done for the D + ClI reaction with an LEPS surface. Good agreement is found with experimental data for the DI channel, but the potential surface for the DCl channel needs improvement.

I. Introduction

Reactions of fluorine atoms with hydrogen-containing molecules are fast and exothermic; consequently, the HF and other products may be produced with nonequilibrium energy state distributions. These distributions, being a clue to the fundamental dynamics, are being studied by infrared emission spectroscopy,[1-5] laser techniques,[6,7] and molecular beam experiments.[8,9] The present classical trajectory computations are concerned with providing a reference point for F + HR → HF + R type reactions within a three-body approximation and a London-Eyring-Polanyi-Sato (LEPS) surface. The impetus was to correlate our experimental data[1-3] with the dominant features of the potential function. Classical trajectory calculations[10] for F + H_2 with a LEPS potential encompass most of the features of this reaction. The reactions of interest here, however, are not strictly of the A + BC type because six atoms are involved. Nevertheless, we have used the simple A + BC model, which emphasizes the F-H and H-R interactions, in an attempt to isolate the major features such as mass effects, changes of thermochemistry, and general energy partitioning pattern for the F + H-C → FH + C reaction in which the mass of the carbon atom is adjusted to fit the total mass of CH_3 and CH_2Br (or $CHCl_2$). Four LEPS surfaces were investigated with a total of 2609 trajectories. No consideration was given to the spin multiplet ($^2P_{1/2}$, $^2P_{3/2}$) problem[10d,e] of fluorine atoms.

The D + ClI reaction was simulated during the course of the development of the computer program because the execution time for the trajectory of the lighter atom was shorter than for the F atom reactions. In addition we were interested in more fundamental points such as (i) having a different type of mass combination as a reference point and (ii) checking whether the measured[11] translational and angular distributions could be reproduced by a LEPS surface with low directionality. These computed results are only briefly described since our main interest is with the F + H-R systems.

The HF infrared chemiluminescence experiments have been described[1-3] and only the results for F + CH_4, CH_3F, CH_3Cl, CH_3Br, CH_3I, and CH_3HgCH_3 will be given here. Our best efforts for $CH_4(CD_4)$ are reported in the preceding paper.[3a] The complete data for CH_3OD will be reported later.[3c] The vibrational-rotational populations reported here for CH_3Cl and CH_3Br are derived from new data[12] obtained at somewhat lower pressures than the previously reported results;[2a] however, the relative vibrational populations are the same as reported earlier.[2] We have argued that for most reagents vibrational relaxation has been arrested, but that rotational relaxation is only partially arrested.

The original HF product vibrational populations are summarized in Table I and an example of the steady state rotational distribution in shown in Figure 1. Although the $\%E_V$ is virtually constant, except for CH_3HgCH_3, the shapes of the distributions do change, especially the N_2/N_3 ratio. The steady-state rotational populations for all these reagents are similar to that of Figure 1, except for CH_3OD,[3c] which has larger populations in the higher levels for all three vibrational states. There is evidence for a residue of the original rotational distribution in Figure 1. If the original HF product distribution is assumed to be "symmetric," the data can be interpreted in the same way as the C_8H_{16} data were treated in the preceding paper[3a] and very similar "initial" rotational populations could be obtained. At the present time we cannot discount the possibility of a significant formation rate into low J levels; however, it appears that <10% of the energy is partitioning as rotational energy of HF. Another result, which is not quantitatively established but appears correct, is the lack of an inverse correlation of rotational excitation with diminishing vibrational level.

Although the F + CH_2Cl_2 and $CHCl_3$ reactions have been studied,[2a] the data appear to be affected by secon-

TABLE I: Relative HF Vibrational Populations

Reagent	$D°_0$ (H-R),[c] kcal mol^{-1}	Initial population[a] $v = 1$	$v = 2$	$v = 3$	$\langle E_V \rangle$, kcal mol^{-1}	$\%E_V$[b]
CH_4	102.5[d]	0.22	0.65	0.13	21.1	62
CH_3F	101.3[d]	0.17	0.61	0.21	22.2	64
CH_3Cl	99.4[d]	0.25	0.39	0.39	24.1	65
CH_3Br	100.5[d]	0.23	0.42	0.35	23.3	65
CH_3I	102.1[d]	0.26	0.46	0.29	22.5	66
CH_3OD	97.0[e]	0.27	0.43	0.31	22.6	58
$(CH_3)_2Hg$	100.5[f]	0.41	0.45	0.11	18.2	51

[a] Corrected for radiative decay using a 0.2-msec residence time; for our earlier work 0.3 msec was used. [b] Calculated from $\Sigma^3_{i=0} N_i E_i / E_a \times 100$ and assuming that the relative population of $v = 0$ is negligible. E_a was calculated from $D°_0$(F-H) $- D°_0$(H-R) $+ E_0$. The threshold energy was taken as 1.1 kcal mol^{-1} for CH_4 and 0.8 kcal mol^{-1} for the other reagents. [c] The highest observed rotational level from HF ($v = 3$) correlated closely with the available energy, E_a. In particular, emission was found from higher J levels for CH_3Br and CH_3Cl than for CH_3I and CH_3F, which supports the claim that the bond energies for CH_3I and CH_3F are higher than for CH_3Br or CH_3Cl. However, from the highest observed J levels, D(H-CH_2I) $\approx$ D(H-CH_2F) rather than being 2 kcal mol^{-1} higher. In order to make more firm distinctions about the bond energies from the highest observed level, more care would have to be made in regard to regulating the temperature of the reagents and discharged SF_6 and in identification of a cutoff, rather than a gradual decline, in the populations of the high rotational levels of HF($v = 3$). [d] S. Furuyama, D. M. Golden, and S. W. Benson, *J. Amer. Chem. Soc.*, **91** 7564 (1969). [e] (i) F. R. Cruickshank and S. W. Benson, *J. Phys. Chem.*, **73**, 733 (1969). (ii) Z. B. Afassi and D. M. Golden, *ibid.*, **76**, 3314 (1972). [f] Calculated from E_0 = 0.8 kcal mol^{-1}, $D°$(HF) = 135.4 kcal mol^{-1} and the highest observed rotational level of HF ($v = 3$).

dary reactions or other complications, and these results will not be included in the present discussion. Reactions which compete with H abstraction are not expected for CH_4, CH_3F, or CH_3Cl;[9a] however, Br, I,[9b] and D abstraction probably are important for CH_3Br, CH_3I, and CH_3OD. A displacement reaction with CH_3HgCH_3 probably can not be ruled out.

II. Computation Methods

A. Equation of Motion. Of the various three-dimensional models[13,14] used for three-particle systems, our model is most like the one described by Karplus, Porter, and Sharma.[13] Of the nine coordinates, only the six which describe relative motion are of interest. Three of these, Q_1, Q_2, and Q_3, were used to locate atom A from the center of mass (cm) of BC, and the remaining three, Q_4, Q_5, and Q_6, were used to locate atom B with respect to C. The resulting classical Hamiltonian (eq 1) is easily understood in terms of the kinetic energy of A and BC, the kinetic energy of B and C, and the potential energy of the system.

$$H = (2M_{A\text{-}BC})^{-1}(P_1^2 + P_2^2 + P_3^2) + (2M_{B\text{-}C})^{-1}(P_4^2 + P_5^2 + P_6^2) + V(Q_1, \ldots, Q_6) \quad (1)$$

$$M_{A\text{-}BC} = \frac{m_a(m_b + m_c)}{m_a + m_b + m_c}$$

$$M_{B\text{-}C} = \frac{m_b m_c}{m_b + m_c}$$

Integration of the equations of motion (eq 2 and 3) was done with a modified Hamming's fourth order predictor-corrector algorithm.[15] To debug the computer program and to ensure that the time interval for integration was small enough, the constancy of the Hamiltonian and the total cm angular momentum were checked in every trajectory. Also, for selected trajectories integration was done both in the forward and backward directions to make sure

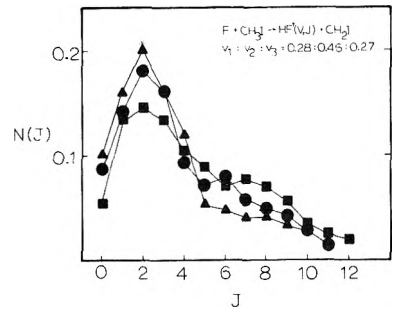

Figure 1. The experimental steady state rotational distributions from F + CH_3I for $v = 1$ (●), $v = 2$ (■), and $v = 3$ (▲).

that the initial conditions would be regenerated from the final values of the coordinates and momenta.

$$\frac{dP_i}{dt} = -\frac{\partial H}{\partial Q_i} = -\sum \frac{\partial V}{\partial r_j}\frac{\partial r_j}{\partial Q_i} \quad (2)$$

$$\frac{dQ_i}{dt} = \frac{\partial H}{\partial P_i} \quad (3)$$

B. Potential Functions. The basic LEPS potential form,[16] eq 4-6, was used with $c_1 = c_2 = c_3$

$$V = \frac{Q_1}{1 + c_1} + \frac{Q_2}{1 + c_2} + \frac{Q_3}{1 + c_3} - \left[\frac{a_1^2}{(1 + c_1)^2} + \frac{a_2^2}{(1 + c_2)^2} + \frac{a_3^2}{(1 + c_3)^2} - \frac{a_1 a_2}{(1 + c_1)(1 + c_2)} - \frac{a_2 a_3}{(1 + c_2)(1 + c_3)} - \frac{a_3 a_1}{(1 + c_3)(1 + c_1)}\right]^{1/2} \quad (4)$$

$$\frac{Q_i + a_i}{1 + c_i} = D_i\{\exp[-2\beta_i(r_i - r_i^0)] - 2\exp[-\beta_i(r_i - r_i^0)]\} \quad (5)$$

$$\frac{Q_i - a_i}{1 - c_i} = \frac{D_i}{2}\{\exp[-2\beta_i(r_i - r_i^0)] + 2\exp[-\beta_i(r_i - r_i^0)]\} \quad (6)$$

The spectroscopic data for the HF, ClI, DCl, and DI system are readily available.[17] Our selection for D(H-F) is in agreement with the most recent determination.[18] For the pseudodiatomic molecules, H-R_{15} and F-R_{15}, the data were estimated from the bond energies, bond distances, and frequencies of CH_4 and CH_3F. In the scheme for generating the spectroscopic parameters, first the value of D_e for H-R_{15} was set at 110 kcal/mol in accordance with the H-CH_3 bond energy at 0°K and the zero point energies of CH_4 and CH_3. The value of D_e for F-R_{15} was set at 90 kcal/mol. This value, which is several kcal/mol lower than D(F-C), was chosen to block the channel for the F-R_{15} product. If this was not done, the kinematics for the H + LH combination favor the *H-H* product rather than the desired *H-L* product.[16] The ω_e and $\omega_e\chi_e$ values were then adjusted to fit the υ(H-CH_3) = 3000 cm^{-1} and υ(F-CH_3) = 1100 cm^{-1} stretching frequencies.[19] The r^0 values of H-R and F-R were set equal to the H-CH_3 and F-CH_3 bond lengths of 1.09 and 1.39 Å. These values also were used to calculate the rotational constants for the $\upsilon = 0$ levels. The Morse parameter, β, for H-R_{15} and F-R_{15} was calculated using the standard expression.[19] Surfaces 1 and 2 differ only in the choice of c in eq 4. For 3 D(H-R) was lowered by 5 kcal mol^{-1} but the β values of 1 and 2 were

TABLE II: Spectroscopic and LEPS Parameters

Surface	Interaction	D_e, kcal/mol	β, Å^{-1}	R_e,[a] Å	c
	H–F	141	2.2123	0.9168	0.155
1	H–R	110	1.8801	1.09	0.155
	F–R	90	2.2259	1.39	0.155
	H–F	141	2.2123	0.9168	0.18
2	H–R	110	1.8801	1.09	0.18
	F–R	90	2.2259	1.39	0.18
	H–F	141	2.2123	0.9168	0.18
3	H–R	105	1.8801	1.09	0.18
	F–R	90	2.2259	1.39	0.18
	H–F	141	2.2123	0.9168	0.18
4	H–R	110	1.9302	1.09	0.18
	F–R	90	3.0231	1.39	0.18
	D–Cl	106.5	1.8617	1.27462	0.173
5	Cl–I	50.15	1.8513	2.3207	0.173
	D–I	73.89	1.7437	1.6091	0.173

Interaction	ω_e, cm^{-1}	$\omega_e\chi_e$, cm^{-1}	B_e, cm^{-1}	α_e, cm^{-1}
H–F	4138.33	89.652	20.9548	0.7939
H–R_{15}	3127.1	63.542	15.369	0.4683
H–R_{83}	3127.1	63.542	14.582	0.4437
F–R_{15}	1119.9	9.961	1.047[b]	0.0122[b]
F–R_{83}	1119.9	9.961	0.5671[b]	0.0055[b]
D–Cl	2144.77	26.92	5.44839	0.11226
Cl–I	384.293	1.501	0.114146	0.000536
D–I	1640.14	20.16	3.2840	0.06142

[a] The r^0 in eq 5 and 6 is the same as the R_e of this table. [b] These B_e and α_e values were obtained by solving simultaneously the relationship $B_0 = B_e - \alpha_e/2$ and the relationship among α_e, B_e, ω_e and $\omega_e\chi_e$ as given in ref 19. For the R_{83} case, the rotational constants were altered to account for the increase in mass over the R_{15} species.

retained. The β values for 4 were adjusted to fit R_{83}; everything else was the same as for surface 2.

The F + HR surfaces decrease in repulsive character in the order they are numbered. The general nature of these surfaces in the collinear configuration is shown in Figure 2 for surface 4 and the parameters describing the saddle points of the collinear geometry are summarized in Table II. As the surfaces become less "repulsive," the saddle point moves to larger R_1* values; the barrier energy, V_c*, decreases; and the directionality of surfaces decreases, as is evidenced by the decrease in the bending force constants f_{33} and f_{44}.[20] The calculated absolute rate theory activation energies, E_a, are in the proper range for this series of reactions.[21] (See Table III.)

Three methods (see Table IV) were used to classify the surfaces according to "attractive," "mixed," and "repulsive" categories.[10,15,20] Method a is the primitive rectlinear method. Method b, which utilizes the minimum energy path, provides a measure of the mixed energy release, which is very important for the F + HR mass combination. Although (a) and (b) are based upon collinear geometry, method c used the actual three-dimensional trajectories. The $\%(A + M)_{3t}$ was calculated by $100\Delta V/(D_{e1} - D_{e2})$ where ΔV is the change in the potential energy from ($R_1 \sim \infty$, $R_2 = R_2^0$) to the point at which R_1 first reaches R_1^0; $\%R_{3t}$ was taken as $100 - \%(A + M)_{3t}$. The values vary from one trajectory to another, and an average over 5–10 trajectories was taken for Table IV. Since the trajectories are begun with zero point energy, the R_2 coordinate and, hence, the potential energy is not

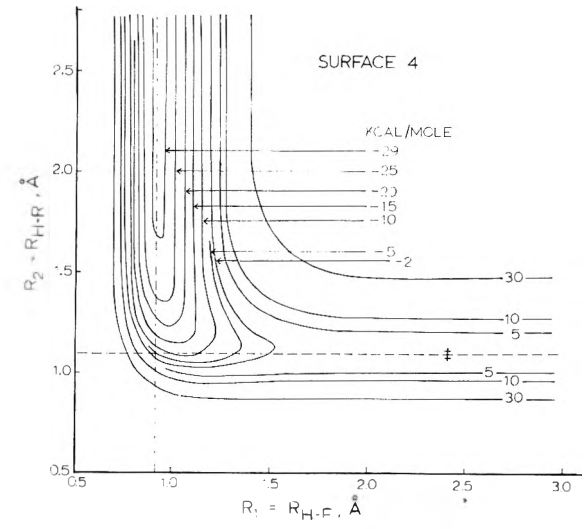

Figure 2. Contour plot of the potential energy for collinear geometry on surface 4. The dotted lines show the rectlinear method for assigning "attractive" and "repulsive" character. The location of the barrier (0.06 kcal mol^{-1}) is indicated by the ‡.

constant even at $R_1 = \infty$. For obtaining $\%(A + M)_{3t}$ the initial potential energy was taken as the minimum value associated with the zero point energy of oscillation. The values for $\%(A + M)_{3t}$ on surfaces 1–4 were consistently greater than the corresponding values from the minimum path method. This difference arises because (c) includes the mass effect on the mixed energy release. However, for both (b) and (c) the $\%(A + M)$ does *slowly* increase in the series 1–4.

C. Initial and Final Conditions. The manner in which initial values were assigned to Q_1, Q_2, Q_3, P_1, P_2, and P_3 parallels that of Karplus, Porter, and Sharma, except that ρ, the initial distance of A from the cm of BC, was constant, and averaging over the phase angles of BC was done in a different way. The impact parameter, b, was selected in two ways. In the calculations for the total cross section, it was selected randomly in even intervals up to the maximum value that gave reaction, b_{max}; but in the calculations for energy distributions the random selection was weighted by b which means that $b = b_{max}(RN)^{1/2}$. In all instances RN denotes a random number from 0 to 1. Limited resources required the use of a fixed relative velocity; see footnote 1 of Table V. The initial values of Q_4, Q_5, Q_6, P_4, P_5, and P_6 were first selected with BC aligned along the z axis. In this orientation the only nonzero coordinate is Q_6 which has the value of r_2. The value for r_2 can be obtained by assigning values to the vibrational and rotational quantum numbers, v and J, and the phase of the BC Morse oscillator. For these calculations v was set at zero, but J was selected by $(RN) = \exp[-J(J + 1)B_v/kT]$. The procedure that was used to incorporate the phase angle is given by $r_2 = r_m + r_a \sin\Delta$, where r_m is the midpoint between the maximum and minimum CTP's of the appropriate Morse oscillator, r_a is the amplitude from the midpoint, and Δ, the phase angle, is given by $2\pi(RN)$. Initial values for the momenta in this preliminary orientation can be generated by the selection of one more condition besides v, J, and Δ. This condition was taken as the angle between the x axis and the component of linear momentum perpendicular to the BC molecular axis (z axis). This angle was selected in a manner analogous to that for the phase angle. The remaining two initial conditions were used to randomize the orientation of BC by rotation

TABLE III: Surface Properties for Linear "Activated Complex" Configuration[a]

	Surface 1	Surface 2		Surface 3		Surface 4		Surface 5	
	F-H-R_{15}	F-H-R_{15}	F-H-R_{83}	F-H-R_{15}	F-H-R_{83}	F-H-R_{15}	F-H-R_{83}	D-Cl-I	D-I-Cl
$R_1{}^{b*}$	1.657	1.931		2.024		2.411		3.456	3.607
$R_2{}^{b*}$	1.102	1.093		1.092		1.090		2.321	2.321
$V_c{}^{b*}$	0.935	0.206		0.163		0.055		0.028	0.033
f_{11}*	−0.066	−0.014		−0.011		−0.0028		−0.00094	−0.00102
f_{22}*	4.83	5.16		4.96		5.56		2.34	2.34
f_{12}*	0.275	0.068		0.47		0.0058		0.0011	0.0016
f_{33}*, f_{44}	0.0168	0.0052		0.0037		0.00021		0.00007	0.00003
ν_1*	135i	55i	41i	48i	36i	23i	18i	28i	30i
ν_2*	2776	3016	2935	2968	2889	3168	3085	380	380
ν_3*, ν_4*	260	137	136	114	113	30	30	30	30
$E_0{}^c$	1.22	0.48	0.36	0.30	0.18	0.24	0.13	0.11	0.11
$E_a{}^d$	1.52	1.02	0.91	0.89	0.79	1.05	0.93	0.91	0.92

[a] Internuclear distances are in Å; energies in kcal/mol; force constants in mdyn/Å and mdyn·Å/rad²; and frequencies in cm^{-1}. [b] R_1 is the F-H coordinate, R_2 is the H-R coordinate, and the asterisk denotes the values of the coordinates and other properties at the saddle points. [c] The threshold energy, which is V_c* plus zero point energy difference. [d] The absolute rate theory activation energy.

TABLE IV: Classification of Surfaces

System	Surface	a: $\%A_\perp$	a: $\%R_\perp$	b: $\%A_m$	b: $\%M_m$	b: $\%R_m$	c: $\%(A+M)_{3l}$	c: $\%R_{3l}$
(1) F + HR_{15} → HF + R_{15}	1	5	95	31	21	48	74	26
	2	16	84	42	16	42	82	18
	3	21	79	45	14	41	86	14
	4	35	65	61	6	33	90	10
(2) F + HR_{83} → HF + R_{83}	2	16	84	42	16	42	84	16
	3	21	79	45	14	41	89	11
	4	35	65	61	6	33	91	9
(3) D + ClI → DCl + I	5	69	31	70	9	21	68	32
(4) D + ClI → DI + Cl	5	59	41	55	21	24	49	51

[a] Rectilinear method in which $\%A_\perp = 100E_m/\Delta D$ where E_m is the maximum decrease in potential energy along the entry line $R_2 = R_2{}^0$ and $\Delta D = D_1 - D_2$; $\%R_\perp = 100 - \%A_\perp$. [b] Minimum path method in which $\%A_{:n} = 100E_2/\Delta D$ where E_2 is the decrease in potential energy along the minimum path from $R_1 \sim \infty$ to the classical turning point (CTP) of R_2; $\%M_m = E_{21}/\Delta D$ where E_{21} is the energy decrease from the CTP of R_2 to the CTP of R_1; $\%R_m = 100 - A_m - \%M_m$; the CTP's for HR, HF, ClI, DCl, and DI were taken as 1.21, 1.01, 2.38, 1.36, and 1.70 Å, respectively. [c] Estimated from three dimension trajectories (explained in text). The variation in $\%(A + M)_{3l}$ was small ($<\pm 3\%$) for the F + HR trajectories for a given surface; however, for D + ClI the deviation from the mean was large and values as high as 63% and as low as 22% were found for the DI channel.

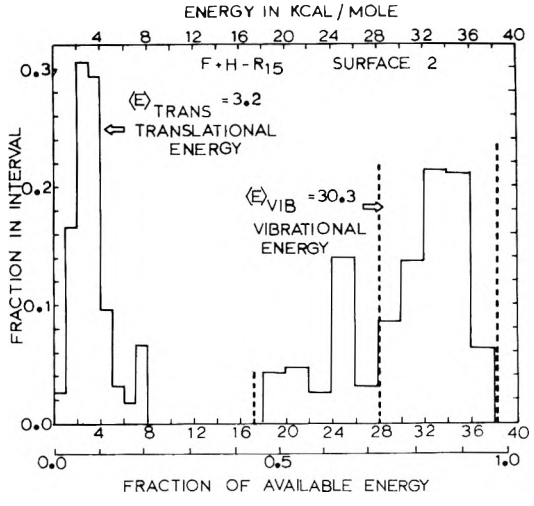

Figure 3. Energy partitioning pattern from F + HR_{15} on surface 2. Note that the size of the interval changes from 1 kcal/mol^{-1} for the translational distribution to 2 kcal/mol^{-1} for the vibrational distribution. The bar graph is for the total vibrational energy, including the zero point energy of HF. The heavy dotted lines result from reducing (see text) the vibrational distribution to the quantized vibrational levels (v = 0, 1, 2, 3). This graph summarizes the results of 32 reactive trajectories from 300 attempts.

of θ about the y axis and ϕ about the z axis.[22] The angles θ and ϕ were chosen by $\cos\theta = 2(RN) - 1$ and $\phi = 2\pi(RN)$.

Resolving the final results into the desired energy quantities was accomplished by first separating out the relative translational energy. The remaining energy was partitioned between the rotation and vibration of the diatomic molecule by first calculating the J which corresponds to the classical angular momentum of the diatomic molecule and then iterating on v until the quantum vibrational and rotational energy expression equaled the classical Hamiltonian.

III. Calculated Results

A. F + HR. Since our main objective was to obtain results which could be compared with the experimental energy partitioning data, only enough reactive trajectories were collected to represent the energy pattern. Except for surface 4, the statistics were not sufficient for correlation of one calculated result with another. The calculated results are summarized in Figures 3-6 and in Table V. The least amount of effort was done with surface 1 because the reaction probability was low. Even for an initial relative velocity corresponding to 5.0 kcal mol^{-1}, the small number of reactions (14 out of 270 attempts) on surface 1 may make the results of Table V subject to statistical uncertainty.

All surfaces released a very high fraction, ~90%, of the available energy to $E_V + E_R$, as a consequence of the low directionality and high degree of mixed energy release. A very noticeable aspect is the constancy of the fraction of available energy appearing as HF vibrational energy from F + HR_{15}. Figures 3-5 do show that the distributions change more than is suggested by the $\%E_V$ and, in fact, N_3/N_2 is fairly sensitive to the potential surface. In par-

TABLE V: Average Energies (kcal/mol) and Average CM Scattering Angles (degs)

System	Surface[a]	E_{avail}[b]	E_T (%E_T)	E_V (%E_V)	E_R (%E_R)	θ_{cm}[c]
F + HR_{15} →	1	41.3	4.9 (12)	29.7 (72)	6.7 (16)	125
HF + R_{15}	2	38.8	3.2 (8)	30.3 (78)	5.3 (14)	79
	3	43.7	3.9 (9)	33.3 (76)	6.5 (15)	81
	4	38.7	4.9 (13)	27.4 (71)	6.4 (16)	69
F + HR_{83} →	2	38.6	4.5 (12)	26.1 (68)	8.0 (20)	85
HF + R_{83}	3	43.9	3.8 (9)	34.4 (78)	5.7 (13)	72
	4	38.8	4.7 (12)	26.1 (67)	8.0 (21)	69
D + ClI →						
DCl + I	5	67.4	15.1 (23)	37.9 (56)	14.4 (21)	99
D + ClI →						
DI + Cl	5	34.8	12.2 (35)	10.1 (29)	12.5 (36)	98

[a] The number of reactive trajectories is specified in the Figures 3–6 and 10, except for surface 1 (14/270) and HR_{83} on surfaces 2(21/360) and 3(27/439). [b] The available energy (kcal/mol), is the initial energy ($E_T + E_V + E_R$) + $D_{e_1} - D_{e_2}$, E_T was fixed at 2.5 kcal for surfaces 2, 3, and 4, and E_T was fixed at 5.0 kcal for surface 1. E_R varied between 0.7 and 0.9 kcal and E_V was 4.4 kcal, which is in the H–R zero point energy, for calculations on surfaces 1, 2, 3 and 4. E_T was set at 9.9 kcal; E_R was 0.6 kcal, and E_V was 0.5 kcal for surface 5. [c] The CM scattering angle is defined relative to the extension of the relative velocity vector of the atom; *i.e.*, 0° is forward scattering of HF. These average angles are not weighted by a $(\sin\theta)^{-1}$ factor. [d] The reaction cross sections were 8.0 and 7.2 Å^2 for the DCl and DI channels, respectively.

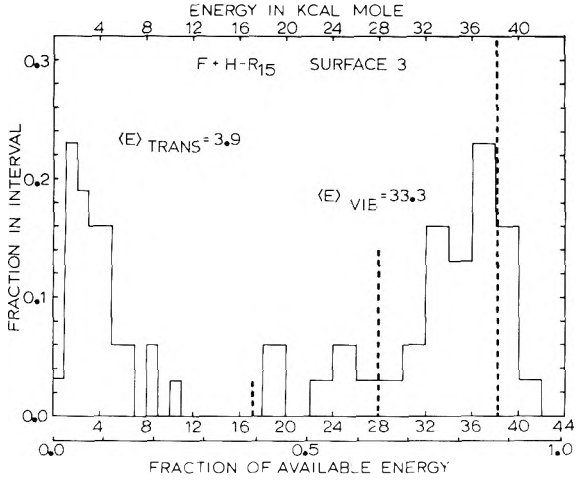

Figure 4. Energy partitioning pattern from F + HR_{15} on surface 3. This graph represents the results of 31 reactive trajectories from a total of 505 attempts. See Figure 3 for further description.

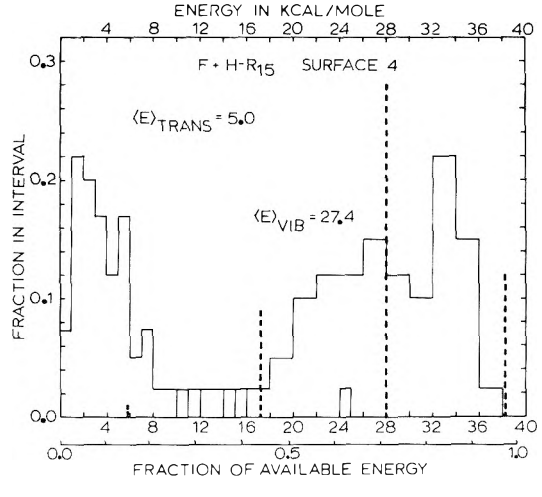

Figure 5. Energy partitioning pattern from F + HR_{15} on surface 4. This graph represents 51 reactive trajectories from a total of 330 attempts. See Figure 3 for further description.

ticular the greater available potential energy for surface (e) gave a dramatic increase in N_3/N_2, for *both* HR_{15} and HR_{83}. The $\%A_1$ or $\%(A + M)_{3t}$ classification of the surfaces would imply that the $\%E_V$ should increase more than what was found. This failue of $\%E_V$ to increase with increasing $\%(A + M)$ character of the surface has been attributed to multiple encounters in the trajectory.[16] As we shall see this is a plausible explanation for F + HR systems too. Although the statistics are not adequate to show good correlation between E_V, E_R and E_T, the results from surface 4 were sufficient to definitely establish that high E_V correlates with low E_R and vice versa. This also is apparent from the relatively small spread in the translational energy distributions shown in Figures 3–6.

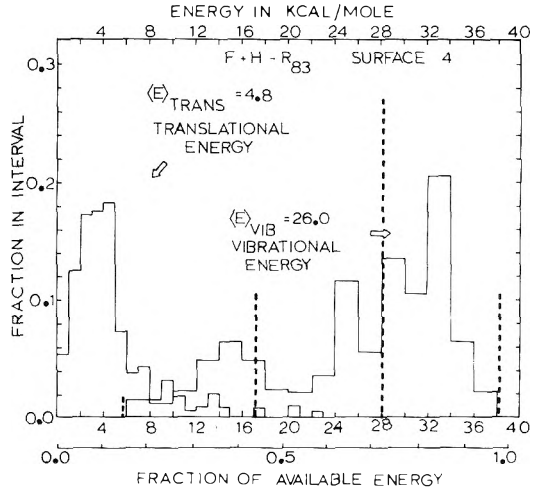

Figure 6. Energy partitioning pattern from F + HR_{83} on surface 4. This graph represents 93 reactive trajectories from a total of 405 attempts. See Figure 3 for further description.

A comparison of the effects of changing the mass from R_{15} to R_{83} on surface 4 (Figures 3 and 6) shows that the $\%E_V$ declined slightly and $\%E_R$ increased slightly. A similar result was found for surface 2. However, for surface 3 there was virtually no change in $\%E_V$ with mass. This may be a consequence of poor statistics or it may be real. In any event, the main conclusion is that the mass effect is quite minor for the energy partitioning. One might have anticipated that increasing the mass of R would lower the degree of mixed energy release (lower $\%E_V$) for a given potential surface because the greater mixed energy release occurs for $M_A \gg M_C$ and M_B large.[20] Apparently the variation in mixed energy release for changing of M_C from 15

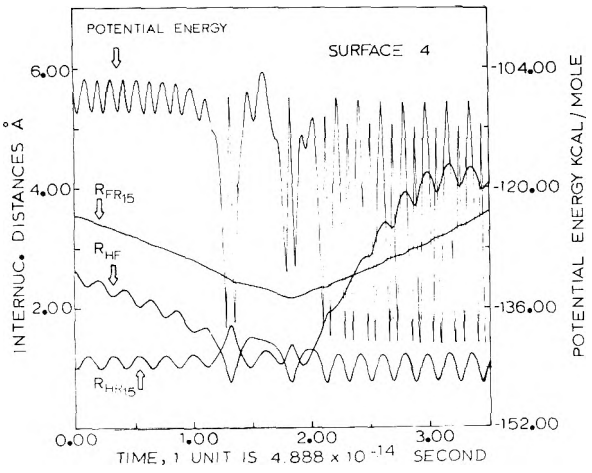

Figure 7. Plot of internuclear distances and total potential energy during the course of reaction. This is an example of a complex (indirect) trajectory.

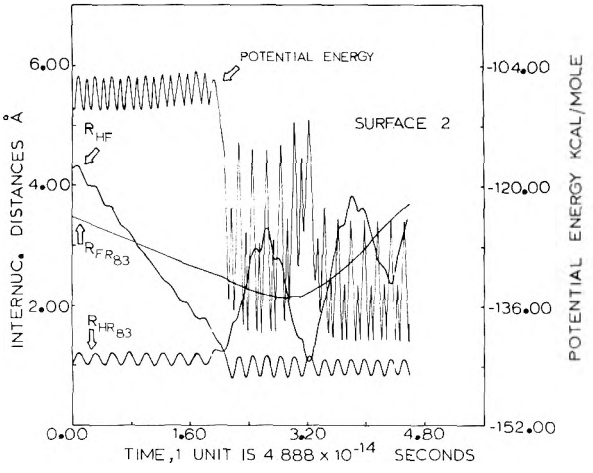

Figure 8. Plot of internuclear distances and total potential energy during the course of reaction. This is an example of a simple (direct) primary encounter followed by a delayed secondary encounter. This secondary encounter had the effect of removing vibrational energy from HF†.

to 83 is small, as also is indicated by the $\%(A + M)_{3t}$ values of Table IV. In a three-body simulation of the K + IR (R = CH_3, C_2H_5, C_3H_7, C_4H_9) reaction, the mass effect on $\% E_V$(KI) also was found to be negligible.[23]

Definitions of direct, complex (indirect), primary and secondary encounters have been reported[20,24,25] and descriptive terms, defined by the types of forces acting between the products, have been applied to the secondary encounters.[25,26] Inspection of our trajectory plots suggested three classifications for reactive encounters of F + HR. These are (i) simple (direct), (ii) complex (indirect), see Figure 7, and (iii) delayed secondary encounter, see Figure 8. The latter group are identified by a distinct time period after the transfer of H to F during which H begins to separate from R, but another encounter subsequently results as a consequence of the rotation of HF† (the dagger denotes an HF which has been formed but has not yet escaped from the influence of the R group) which brings the H back to the vicinity of R. In most cases the primary encounter for type iii was simple (direct); however, in a few instances a delayed secondary encounter occurred after a complex (indirect) interaction. For type iii interactions the usual result of the secondary encounter was a lowering of the amplitude of HF† oscillation, see Figure 8, although

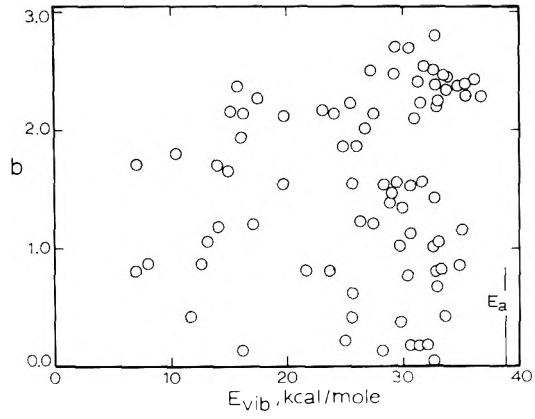

Figure 9. Plot of vibrational excitation of HF *vs.* the initial impact parameter for F + HR_{83} on surface 4. The available energy is marked in the lower right-hand corner. A plot of E_R *vs.* *b* also showed no correlation; this should be self-evident from the above and the statement of inverse correlation of E_V and E_R.

in a few instances, E_v was increased by the secondary encounter. The appearance of type ii trajectories varied a great deal. That shown in Figure 7 is a fairly extreme case; in many instances the R_{HR} distance goes through only one complete cycle of motion after R_{HF} first becomes $<R_{HR}$. Typical interaction times are 2–5 × 10^{-14} sec for complex type trajectories; the time for transfer of H from R to F in the primary encounter is 0.5–1 × 10^{-14} sec. From visual inspection of plots such as Figures 7 and 8 it appeared that complex trajectories often were associated with approach of F along the H–R molecular axis (but not necessarily with small impact parameters), whereas the direct trajectories tended to have a large component of motion perpendicular to the H–R axis. About one-half of the reactive trajectories appeared to be complex. Of the remaining one-half, 50% showed evidence for delayed secondary encounters. There also appears to be some enhancement of (ii) and (iii) with R_{83} relative to R_{15}. Since surfaces 2, 3, and 4 partition a high fraction of energy to rotational energy, the delayed secondary encounters may be over emphasized. Reference 25 should be consulted for additional discussion of complex encounters in the Cl + HI reaction.

The extent to which the vibrational distributions are dependent on impact parameter is indicated by Figure 9. Although the uppermost range of *b* contributed slightly more to the higher range of E_V, the vibrational distribution is not strongly dependent on the impact parameter. In contrast the cm scattering angle of HF, relative to the extension of the initial direction of F, definitely tended to decrease (more forward scattering) at large *b*. For example, with F + HR_{83} on surface 4, the average scattering angles for *b* in the ranges 0–0.2, 1.0–1.2, and 2.0–2.2 Å were 161°, 103°, and 45°, respectively. Throughout the whole range of *b* complex trajectories occurred; however, they did not disturb this correlation and the relative breadth of the angular distribution was more a consequence of relative values of *b* than an effect of complex trajectories. The average scattering angles are given in Table V.

B. D + Cl2 System. The calculated results, which were done with an initial translational energy of 9.9 kcal mol^{-1} for ease of comparison with experimental data, are summarized in Figures 10 and 11 and in Table V. The potential surface is relatively attractive and has low direction-

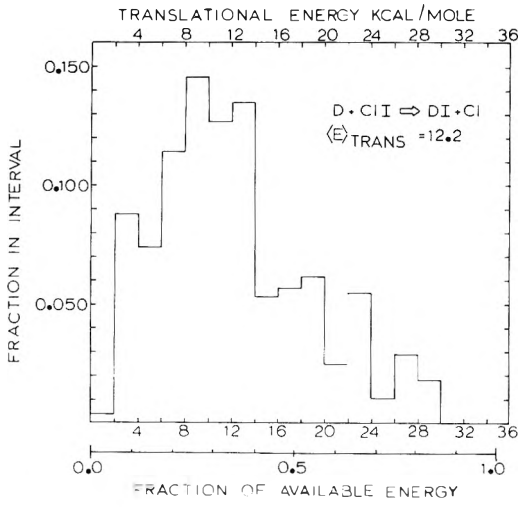

Figure 10. Translational energy distribution from D + CII → DI + CI, surface 5. This graph represents 121 reactive trajectories giving DI from a total of 1020 attempts.

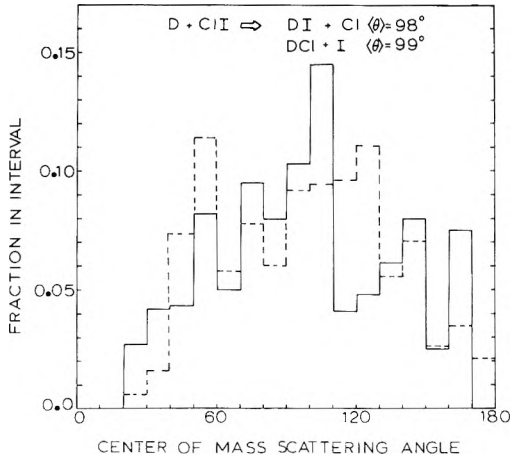

Figure 11. Distribution of scattering angles for D + CII → DI + CI (solid line) and DCI + I (dashed line); the average angles are 98 and 99°, respectively. If these distributions are weighted by $(\sin\theta)^{-1}$ for comparison of in-plane experimental scattering measurements the average angles are 107 and 115°, respectively.

ality; the characteristics of the potential surface at the barriers of both channels are virtually identical. The three methods of classifying the surface give similar results, as would be expected because the $L + H\text{-}H$ mass combination given rise to very little mixed energy-release. This absence of mixed energy release for $L + H\text{-}H$ (implying an approximate perpendicular path across the potential surface) is the essence of the phenomenon termed the light atom anomaly by Polanyi.[20] This has the result that a smaller portion of the energy is released as vibrational energy and more as relative translational energy (see also ref 25). The amount of energy released as rotational energy of DI and DCl is, however, quite high. In contrast to the F + HR trajectories, no complex encounters were observed, which is a consequence of the different relative masses and the higher initial translational energy. Some trajectories did show delayed secondary encounters, but this was a small fraction which correlated with those trajectories giving forward scattering. In spite of the higher initial relative translational energy, the duration of the primary encounter was much longer, $\sim 5 \times 10^{-13}$ sec, for release of the potential energy in the D + CII trajectories relative to F + HR. This, of course, is a consequence of the slow separation of the heavy masses of Cl and I. The average scattering angles for formation of DI from groups of trajectories with impact parameters centered at b value = 1.0, 1.4, 2.0, and 2.9 Å were 108, 114, 96, and 98°. Thus the scattering angle correlates only very weakly with impact parameter for D + CII.

V. Discussion

A. F + HR Reactions. Our primary objective was to obtain calculated three-body results which might provide insight for interpreting the experimental energy partitioning results for the polyatomic F + HR systems. The $\%E_T$ values will not be discussed because the experimental difference between the available energy $-(E_V$ plus $E_R)$ is the relative translational energy *plus* the internal energy of the R fragment. The most significant general aspects of the calculations are: (a) the mixed energy release aspect for this type of mass combination,[25] (b) the very short time period $1\text{–}0.5 \times 10^{-14}$ sec, for the transfer of H from R to F in the primary encounter, (c) increasing the mass of R from 15 to 83 had a minor effect upon the energy partitioning, (d) minor changes in the thermochemistry did not affect $\%E_V$, but, of course, the vibrational distribution was changed, (e) the high probability for multiple encounters in the trajectories. We now wish to use the calculated results, the experimental data, and other intuitive guidelines in examining the validity of the three-body model.

Since the $\%E_V$ was found not to be particularly sensitive to the three body surface and since reasonable agreement between the experimental ($\sim$62%) and the calculated results ($\sim$70%) were obtained for $\%E_V$, this suggests that a three-body approximation is not too bad for that aspect of the data. However, the large fraction of the reactive trajectories which showed complex behavior and delayed secondary encounters suggests (even for other less attractive surfaces) that representing groups like CH_3 or CH_2I by a single atom of equivalent mass must introduce serious approximations relative to the real potential surface and the dynamics on the real surface. Two problems immediately come to mind. The first, which we already have emphasized,[2] is the release of the energy of the R fragment when it relaxes from the geometry in the molecule to the equilibrium geometry of the free radical and the transfer of energy to and from the $HF^\dagger$ and the R during the complex (indirect) encounter. The second is the greater likelihood of delayed secondary encounters for the complete representation of the R fragment.

In the present computations treating R as an atom meant, for the most part, that in the secondary encounter incipient $HF^\dagger$ vibrational and rotational energy was converted into relative translational energy of HF and R. Treating R more exactly would mean that instead of swinging around and interacting with an atom, the $H\text{-}F^\dagger$ would be interacting with a group, *e.g.*, CH_3 or CH_2I. This would seem especially important for larger groups, such as $CH_2(CH_3)_3$, or groups which interact at long range, either attractively or repulsively, with $HF^\dagger$ (the † denotes the initially formed HF before it has escaped from the influence of the R group). An experimental observation[3a] which may illustrate the effects of delayed secondary encounters is the slight, but systematic, decline in $\%E_V$ (HF) in the series F + C_2H_6, $CH_3CD_2CH_3$, $(CH_3)_4C$.

If the period ($\sim 5 \times 10^{-14}$ sec) of the bending vibration of CH_3 is taken as a measure of the necessary time for CH_3 to change from tetrahedral to planar geometry, this

corresponds to the interaction times of the more involved of the complex trajectories but is much longer than the characteristic time for transfer of H from R to F in the primary encounter. The surprising fact that the highest observed HF level usually is very close to that permitted by the H-R bond energy (see footnote c of Table I) may be a consequence of the small fraction of complex-type encounters which permit the radical distortion energy to reach the $HF^{\dagger}$ product. For radicals with larger distortion energies, such as resonance stabilized radicals or even cyclohexyl radicals,[3a] the highest observed level may be less than that permitted by the bond energy because of the slow release of the radical distortion energy. (The radical distortion energies of CH_2X radicals has been estimated[2,27] as $\sim$5 kcal mol^{-1}.) For mass combinations which lead to a longer time for the transfer of B from C to A, the radical distortion energy of C may be more readily available to $AB^{\dagger}$ even for direct interactions. Mass combinations which lead to longer total interaction times presumably enhance this effect, as well as the transfer of energy from $AB^{\dagger}$ back to the C group. A four-body (A + BCD $\rightarrow$ AB + CD) simulation[28] of the K + IC_2H_5 reaction with an attractive surface, which showed both direct and complex-type collision trajectories, provided some support for the reasoning because a substantial increase in the energy of the CD fragment was found for complex-type trajectories. The duration of the complex-type interaction appears to be significantly longer ($\sim$10 from the published example) for K + IC_2 relative to F + HR_{15}.

An important result of the calculations was the increase in N_3/N_2 for lowering of D(H-R) by 5 kcal mol^{-1}, which is remarkably similar to what is found experimentally (see Table I). This sensitivity of the three-body calculation to the available energy further emphasizes the importance of the radical distortion energy and its mechanism for release during the course of the reaction; *i.e.*, in the extreme case the radical distortion energy would not be available to $HF^{\dagger}$.

The effects from changing the mass from 15 to 83 were minor (for a three-body surface), but the nature of the effect was to broaden the vibrational energy distribution with a slight drop in $\%E_V$. Such a tendency may be in the data but it easily could be overshadowed by other unknown effects. Since the mass ratio of $(CH_3)_2Hg$ to CH_3I is only 1.6, it is very unlikely that the difference between the two vibrational distributions arises from a mass effect since other reagents with larger mass differences show lesser changes in $\%E_V$ or in the distributions. The decline in the N_3/N_2 ratio with increasing complexity of hydrocarbon, but with the same bond energy, *i.e.*, C_2H_6, $CH_3CD_2CH_3$, and $C(CH_3)_4$ previously has been noted. However, for that series the N_1/N_2 ratio does not change significantly, which is in strong contrast to CH_3I and CH_3HgCH_3. The low $\%E_V$ and high population of N_1 for CH_3-$HgCH_3$ may be related to the linear geometry, heavy central mass and relatively low rotational moment of CH_2HgCH_3, which may give more delayed secondary encounters than CH_2I.

The most interesting (or troublesome) feature is the disparity between the calculated ($\sim$15%) and experimental (<10%) values of $\%E_R$. Furthermore the calculations show a fairly strong inverse correlation between E_V and E_R, which is not found experimentally. For the other well studied example[25] of mixed energy release (Cl + HI), both the calculated and experimental results show the inverse correlation but the calculations also tended to overestimate the correlation. We suspect that the interactions between $HF^{\dagger}$ and the polyatomic R fragment are an important aspect of the rotational energy distributions. Attempts to refine the three-body F-H-C potential do not seem worthwhile without insight into the nature of the many-body problem.[24] Additional theoretical and experimental work on the rotational energy partitioning by F + HCX_3 reactions is needed.

B. D + ICl. The results for the DI channel (see Table V and Figures 10 and 11) are in reasonable agreement with experimental data,[11] which show sidewise peaking with $E_T \simeq 10$ kcal mol^{-1}. For this type of mass combination the scattering angle is not so dependent upon b (as was the case for the F + HR systems) as the angle of the "activated" configuration. Such a dependence is, of course, due to the low mass of the deuterium atom. The average angle of the "activated" configuration for both channels was essentially the scattering angle, $\sim$100°; however, weighting the calculated scattering angle distributions by $\sin\theta^{-1}$ does increase the difference between the average values; *i.e.* $\langle\theta\mathrm{cm}\rangle_{DI} = 107°$ and $\langle\theta\mathrm{cm}\rangle_{DCl} = 115°$. This fits the DI results adequately, but for DCl the angle needs to be increased to $\sim$150°. Also, the calculated cross section for DCl (8.0 Å^2) was too large relative to DI (7.2 Å^2) because the experimental ratio favors DI by a factor of at least 3-4. To bring the DCl results into better agreement with experiment, this channel must be made more "repulsive." The changes must be made without significantly altering the DI channel since it needs only minor improvements. Making the DCl channel more repulsive would correct both the cross section and the scattering angle inadequacies. As the repulsive character is increased, the barrier would "move in" and become higher,[15] and secondly, this change in barrier position would increase the directionality. These effects can be seen in Table III by a comparison of R_1^*, V_c^*, and f_{33} and f_{44}. The most important conclusion is that relatively good agreement with the DI channel was obtained without a deliberate attempt to construct a surface which favored strongly bent configuration. However, the surface which would, in fact, give good agreement with the data has the properties that a greater degree of collinear geometry is required for D-Cl-I relative to D-I-Cl, which is in agreement with the analysis of ref 11.

Acknowledgments. We are grateful for the support provided by the National Science Foundation (G.P. 27536 X) and by the Kansas State University Computing Center.

References and Notes

(1) H. W. Chang, D. W. Setser, and M. J. Perona, *J. Phys. Chem.*, **75**, 2070 (1971).
(2) (a) H. W. Chang and D. W. Setser, *J. Chem. Phys.*, **58**, 2298 (1973); (b) W. H. Duewer and D. W. Setser, *ibid.*, **58**, 2310 (1973).
(3) (a) K. C. Kim and D. W. Setser, *J. Phys. Chem.*, **77**, 2493 (1973); (b) K. C. Kim and D. W. Setser, *J. Chem. Phys.*, submitted; (c) K. C. Kim and D. W. Setser, *J. Phys. Chem.*, to be submitted.
(4) J. C. Polanyi and K. B. Woodall, *J. Chem. Phys.*, **57**, 1587 (1972).
(5) N. Jonathan, C. M. Melliar-Smith, and D. H. Slater, *Mol. Phys.*, **20**, 93 (1971).
(6) J. H. Parker and G. C. Pimentel, *J. Chem. Phys.*, **48**, 5273 (1968).
(7) M. C. Lin and W. H. Green, *J. Chem. Phys.*, **53**, 3383 (1970).
(8) (a) T. P. Schafer, P. E. Siska, J. M. Parson, F. P. Tully, Y. C. Wong, and Y. T. Lee, *J. Chem. Phys.*, **53**, 3385 (1970); (b) J. M. Parsons and Y. T. Lee, *ibid.*, **56**, 4655 (1972).
(9) (a) C. E. Kolb and M. Kaufman, *J. Phys. Chem.*, **76**, 947 (1972); (b) J. W. Bozzelli and M. Kaufman, *ibid.*, **77**, 1748 (1973).
(10) (a) J. T. Muckerman, *J. Chem. Phys.*, **56**, 2997, 3191 (1972); (b) R. L. Jaffe and J. B. Anderson, *ibid.*, **54**, 2224 (1971); (c) R. L. Wilkens, *ibid.*, **57**, 912 (1972); (d) J. T. Muckerman and M. D. Newton, *ibid.*, **56**, 3191 (1972); (e) D. G. Truhlar, *ibid.*, **56**, 3189 (1972).

(11) J. D. McDonald, P. R. LeBreton, Y. T. Lee, and D. R. Hershbach, *J. Chem. Phys.*, **56**, 769 (1972).
(12) K. C. Kim, Ph.D. Thesis, Kansas State University, Manhattan, Kan. 1973.
(13) K. Karplus, R. N. Porter, and R. D. Sharma, *J. Chem. Phys.*, **43**, 3529 (1965).
(14) D. L. Bunker, *Methods Comput. Phys.*, **10**, 287 (1971).
(15) (a) A. Ralston and H. S. Wilf, "Mathematical Methods for Digital Computers," Wiley-Interscience, New York, N. Y. (1960); (b) A. Ralston, *MTAC*, **16**, 431 (1962).
(16) P. J. Kuntz, E. M. Nemeth, J. C. Polanyi, S. D. Rosner, and C. E. Young, *J. Chem. Phys.*, **44**, 1168 (1966).
(17) (a) The data for the various F + HR systems were taken from "JANAF Thermochemical Tables" (U. S. Government Printing Office). (b) The data for the diatomic pairs of the D + ICl system were taken from B. Rosen, "Selected Constants Spectroscopic Data Relative to Diatomic Molecules," Pergamon Press, New York, N. Y., 1970.
(18) W. A. Chupka and J. Berkowitz, *J. Chem. Phys.*, **54**, 5126 (1971).
(19) G. Herzberg, "Molecular Spectra and Molecular Structure. I. Spectra of Diatomic Molecules," Van Nostrand, Princeton, N. J., 1950, pp 108, 101.
(20) J. C. Polanyi, *Accounts Chem. Res.*, **5**, 161 (1972).
(21) (a) R. Foon and N. S. McAskil, *Trans. Faraday Soc.*, **65**, 3005 (1969); R. Foon and G. P. Reid, *ibid.*, **67**, 3515 (1971); (b) R. F. Walker and M. A. A. Clyne, University of London, Queen Mary College, private communication, 1972.
(22) L. M. Raff, private communication.
(23) L. M. Raff and M. Karplus, *J. Chem. Phys.*, **44**, 1212 (1966).
(24) D. L. Bunker and M. C. Pattengil, *J. Chem. Phys.*, **53**, 3041 (1970).
(25) C. A. Parr, J. C. Polanyi, and W. H. Wong, *J. Chem. Phys.*, **58**, 5 (1973).
(26) B. A. Hodgson and J. C. Polanyi, *J. Chem. Phys.*, **55**, 4745 (1971).
(27) D. L. McFadden, E. A. McCullough, Jr., F. Kalos, and J. Ross, *J. Chem. Phys.*, **59**, 121 (1973).
(28) L. M. Raff, *J. Chem. Phys.*, **44**, 1202 (1966); **50**, 2276 (1969).

The Reaction of Nitrogen Dioxide with Ozone

C. H. Wu, E. D. Morris, Jr.,* and H. Niki

Scientific Research Staff, Ford Motor Company, Dearborn, Michigan 48121 *(Received April 6, 1973)*

Publication costs assisted by the Ford Motor Company

The mechanism and rate constant of the reaction $NO_2 + O_3 \rightarrow NO_3 + O_2$ were investigated at the parts-per-million concentration level. A chemiluminescent detection method was used to monitor the decay of O_3 in excess NO_2. From these data a rate constant of 4.4×10^{-17} cm^3 molecule^{-1} sec^{-1} at 26° was determined with an uncertainty of ±15%. Long-path infrared was used to measure the overall stoichiometry ($\Delta NO_2/\Delta O_3$). Since the primary reaction is rapidly followed by $NO_2 + NO_3 \rightleftarrows N_2O_5$, the observed stoichiometry ranged from 1.65 to 2.00.

The reaction of NO_2 with O_3 plays an important role in photochemical smog and acts as a sink for both NO_2 and O_3.[1] The mechanism proposed[2] for this reaction is

$$NO_2 + O_3 \longrightarrow NO_3 + O_2 \quad (1)$$

$$NO_2 + NO_3 \rightleftarrows N_2O_5 \quad (2)$$

In the atmosphere, N_2O_5 is subsequently removed by reactions involving water and solid surfaces.[3]

In 1922, Wulf, Daniels, and Karrer[4] measured the stoichiometry ($\Delta NO_2/\Delta O_3$) of this reaction by titrating NO_2 with O_3 until the brown color of NO_2 disappeared. From the initial concentration of NO_2 (10–50 Torr) and the amount of O_3 added, they concluded that two molecules of NO_2 were consumed for every molecule of O_3. A few of their data points gave results significantly less than 2, but they were attributed to a faulty ozone analysis.

The most extensive kinetic data on this reaction are those of Johnston and Yost.[2] They followed the concentration of NO_2 by its absorption at 4400–4800 Å in a stopped flow reactor. The ozone concentration during the reaction was determined assuming a stoichiometry of 2. From the decay of O_3, they report a rate constant at 21° of 6.1×10^{-17} cm^3 molecule^{-1} sec^{-1} with a standard deviation of 10% over the range of 1 to 10 Torr initial concentrations. An activation energy of 7.0 ± 0.6 kcal/mol was obtained over the temperature range of 13 to 29°.

Ford, Doyle, and Endow[5] measured the rate of the $NO_2 + O_3$ reaction in a 50-l. stirred-flow reactor using concentrations in the ppm range. (Throughout this paper the unit ppm refers to 760 Torr at 25° so that 1 ppm = 2.45×10^{13} molecules/cm^3.) Ozone was determined *in situ* by an ultraviolet photometric method, while NO_2 was measured at the exit of the reactor by a continuous wet chemical method. The analysis of their data is based in the mechanism (1)-(2) which requires a stoichiometry of 2. However, the stoichiometry calculated from the NO_2 and O_3 concentrations given in this paper range from 0.9 to 4.8. Although the individual determinations scatter over a factor of 4, these authors derived an average rate constant of 3.3×10^{-17} cm^3 molecule^{-1} sec^{-1}. This is in reasonable agreement with the value of Johnston and Yost obtained at much higher concentrations.

Scott, Preston, Andersen, and Quick[6] monitored the decay of NO_2 produced by the flash photolysis of O_3 in N_2O. From their high-pressure data (>400 Torr), they estimated k_1 as 1.3×10^{-17} cm^3 molecule^{-1} sec^{-1}. Experiments performed at 100 Torr yield a value for k_1 some 5–6 times smaller. This suggests the mechanism for the formation of NO_2 even at higher pressures is not entirely correct.

In a recent paper from this laboratory, Stedman and Niki[7] used a chemiluminescent detector to follow the

first-order decay of small amounts of O_3 (0.1–0.01 ppm) in the presence of 1–8 ppm of NO_2. Under these conditions a rate constant can be determined on the assumption that O_3 is consumed only in the primary step. They reported a rate constant for k_1 of 6.5×10^{-17} cm^3 molecule^{-1} sec^{-1}. This was based on rather preliminary data and the uncertainties in their rate constant judged to be ±50%.

Thus there is considerable uncertainty in the reported rate constant for the reaction of NO_2 with O_3. In addition, no mechanistic studies have been done under the conditions which were used for kinetic measurements. In the present work, more extensive kinetic data have been gathered using chemiluminescent detection of ozone to obtain a more precise rate constant. Experiments were also performed to investigate the reaction mechanism using long-path infrared spectroscopy.

Experimental Section

The kinetics and mechanism of the NO_2–O_3 reaction were studied in the ppm range using two experimental methods. The kinetics was studied at atmospheric pressure in N_2 in a 45-l. Pyrex bell jar. The jar was sealed to a Teflon-coated stainless steel base plate which was connected to a mechanical pump through a 1-in. line and a liquid nitrogen cooled trap. The reactor was evacuated below 10^{-3} Torr for a minimum of 30 min between runs. The leak rate under vacuum was less than 10^{-3} Torr/min.

Nitrogen dioxide was prepared by adding excess oxygen to prepurified NO. The NO_2 was then frozen out and excess O_2 was pumped off. The NO content was less than 0.1%. Ozone was prepared by passing high-purity oxygen through a silent discharge ozonizer. As a precaution, the O_2 was first passed through heated CuO to remove hydrocarbon impurities. The O_3 produced was trapped in silica gel at −78° and excess O_2 was pumped off. The purity of the ozone was found to be 98 ± 2% by decomposing a small portion and measuring the pressure rise. Ozone could be stored in the cold trap for up to a week without significant decomposition. Ultrahigh-purity nitrogen (<1 ppm CH_4) was used as a diluent gas without further purification.

Reactant mixtures of NO_2 and O_3 at ppm levels were prepared by first filling calibrated volumes (10–60 cm^3) with a few Torr of reactant. This pressure was measured with a Pace Wiancko transducer which had been calibrated against an oil manometer. The reactants were then flushed with diluent nitrogen through a multiperforated Pyrex inlet tube into the reactor. A thermistor with a 1-sec time response indicated that the temperature during the kinetic measurements was 26 ± 1°.

Analyses of NO, NO_2, and O_3 were made with chemiluminescent detectors which have been described in detail previously.[8,9] The noise level of these detectors was equivalent to 3 ppb with a 1-sec time constant. The NO detector was calibrated using a standard mixture of NO in nitrogen. The NO_2 was analyzed using an NO instrument equipped with a molybdenum impregnated carbon tube which quantitatively (>99%) reduces NO_2 to NO. This detector thus responds to the sum of NO + NO_2. In a mixture of NO and NO_2, NO_2 can be obtained by subtracting NO. The NO_2 and O_3 detectors were calibrated relative to the NO detector using an NO titration method based on the reaction

$$O_3 + NO \longrightarrow NO_2 + O_2$$

All of these calibrations were cross checked against known concentrations prepared in the bell jar by the standard volume method described earlier. The results agreed within ±2%.

It was noted that the molybdenum carbon convertor was also sensitive to other oxides of nitrogen such as N_2O_5 and HNO_3. Since these are known products of the reaction under investigation, the decay of NO_2 could not be measured during the course of the reaction. Therefore, all experiments were performed in NO_2 excess with continuous monitoring of O_3.

Long-path (40 m) infrared spectrometry was used to monitor the reactants and product of the NO_2–O_3 reaction. The reaction cell was constructed of glass except for the mirror supports which were coated with Teflon. This cell was routinely conditioned with ozone. Under these conditions either O_3 or NO_2 alone in the cell was stable for several hours. Ozone was prepared by passing dried oxygen through a silent discharge ozonizer directly into the 70-l. Pyrex reaction vessel. NO_2 was prepared by adding 760 Torr of oxygen to 10–20 Torr of purified NO in a standard volume.

The infrared absorption coefficient of NO_2 was calibrated at 1600 and 1620 cm^{-1} by introducing known concentrations of NO_2 into the reaction cell. The ozone absorption at 1060 cm^{-1} was calibrated relative to NO_2 by introducing ozone into the cell and taking its spectrum. Excess NO (NO_2 free) was then added to convert all the O_3 into NO_2 *via* reaction 5. Measurement of the resulting NO_2 then gave the concentration of ozone initially present. The O_2 and NO concentrations were low enough so that the termolecular reaction NO + NO + O_2 → $2NO_2$ was too slow to interfere with the calibration. Since the infrared peaks of NO_2 and O_3 were pressure sensitive, care was taken to make calibrations and measurements at the same pressure.

Measurements of the stoichiometry ($\Delta NO_2/\Delta O_3$) were performed by adding ozonized oxygen to the evacuated cell until the desired concentration (as indicated by ir) was reached. A known quantity of NO_2 was then added together with argon to bring the total pressure in the reactor to 400 Torr. The infrared spectrometer was set at either 1620 or 1060 cm^{-1} to monitor whichever species was present in excess. When the reaction was complete, as indicated by a stable ir signal, a measurement was made of the concentration remaining. The stoichiometry was determined by combining this with the initial concentrations. The analytical sensitivity was adequate to detect 1 ppm of NO_2 or O_3. However, concentrations of 5–25 ppm were used to obtain good accuracy for the stoichiometric measurements.

Results

Mechanism. The overall stoichiometry of reactions 1 and 2 was measured under conditions of both NO_2 excess and O_3 excess. Initial concentrations were chosen so that either NO_2 or O_3 was completely consumed within several minutes. The results of these measurements are shown in Table I for a variety of initial conditions. In the case of ozone excess, $\Delta NO_2/\Delta O_3 = 1.88$; for the NO_2 excess condition $\Delta NO_2/\Delta O_3 = 1.68$. The maximum error in these measurements is estimated to be ±0.15. The stoichiometry observed under O_3 excess conditions was consistently greater than in the NO_2 excess case. This remained true for three independent sets of calibrations and experiments. Since the error limits overlap, it could not be de-

TABLE I: Stoichiometry Measured in O_3 Excess and in NO_2 Excess[a]

$[O_3]_{initial}$	$[O_3]_{final}$	$[NO_2]_{initial}$	$[NO_2]_{final}$	$\Delta NO_2/\Delta O_3$
17.7	11.7	12	0	2.00
18.4	5.5	24	0	2.03
10.5	7.1	6	0	1.77
11.4	5.6	10	0	1.73
18.1	11.5	12	0	1.82
11.6	8.2	6	0	1.77
16.7	10.8	12	0	2.03
15.8	5.3	20	0	1.91
17.3	11.7	10	0	1.79
21.2	9.1	24	0	1.98
16.8	4.0	24	0	1.88
17.4	6.9	20	0	1.91
13.9	5.3	16	0	1.85
				Av 1.88 ± 0.15
7.4	0	20	7.7	1.67
7.8	0	20	7.1	1.65
9.5	0	24	7.5	1.73
9.6	0	24	7.6	1.71
6.8	0	20	9.0	1.62
5.1	0	18	9.3	1.68
4.9	0	15	6.9	1.63
3.8	0	15	8.8	1.63
8.2	0	24	10.0	1.71
6.5	0	24	12.7	1.74
				Av 1.68 ± 0.15

[a] Concentrations in ppm units (= 2.45×10^{13} molecules/cm^3).

termined whether this is due to a real effect or a systematic error. Additional experiments were performed to determine the effect of total pressure of argon diluent. Data taken at 100, 400, or 750 Torr under NO_2 excess conditions gave the same stoichiometry.

Dinitrogen pentoxide was observed as a product in the infrared at 1240 cm^{-1} but is not stable in this system and decayed to HNO_3 with a 20–30-min half-life.[3] If the absorption cross section for N_2O_5 determined by Cramerossa and Johnston[10] is used here, 10 ppm of NO_2 + excess O_3 initially produces 4.9 ppm of N_2O_5. This absorption cross section is dependent on total pressure and optical resolution. Since an effort was made to use similar experimental conditions here, the quantitative measurement of N_2O_5 should not be greatly in error. Therefore, N_2O_5 is the major nitrogen-containing product.

Kinetics. Prior to investigating the reaction of NO_2 with O_3, the decay of O_3 alone in pure nitrogen was measured in the bell jar system. Depending on the wall conditions, decay rates of 0.002–0.025 min^{-1} were observed for initial O_3 of 0.05 to 1.0 ppm. The lower rates were obtained after the vessel had been exposed to higher concentrations of ozone for an extended period. Therefore a standard procedure was adopted of treating the vessel overnight with 10 ppm of O_3 in N_2. This procedure gave a decay rate between 0.003 and 0.005 min^{-1} and was used for all experiments except where stated otherwise. This rate is insignificant compared to that observed when 1–10 ppm NO_2 has been added.

When enough NO_2 is present so that $[NO_2]/[O_3] > 30$, a pseudo-first-order decay of O_3 was observed. Figure 1 shows typical plots of ln $[O_3]$ *vs.* time for several different NO_2 concentrations between 1 and 10 ppm. The dependence of the O_3 decay slope, $d \ln [O_3]/dt$, is shown as a function of $[NO_2]$ in Figure 2, curve A. This plot is linear with a zero intercept. From the slope a bimolecular rate constant of 4.3×10^{-17} cm^3 molecule^{-1} sec^{-1} was determined. The experimental precision of the slope measurements in these experiments was better than ±0.2 in the same units. To check the effect of wall treatment on the rate constant, a second set of experiments were carried out by replacing the O_3 pretreatment of the vessel with

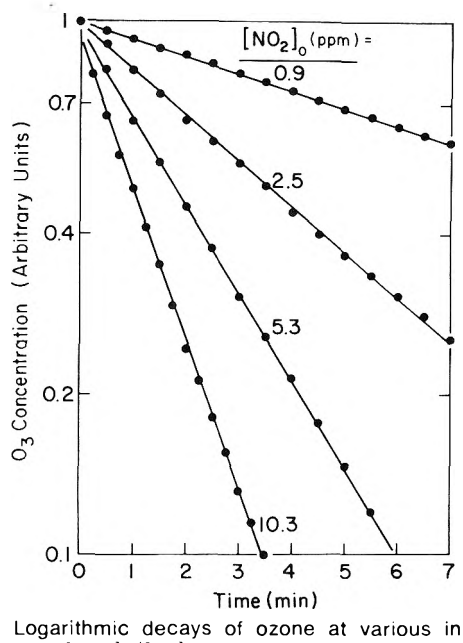

Figure 1. Logarithmic decays of ozone at various initial NO_2 concentrations. $[NO_2]_0/[O_3]_0 > 30$.

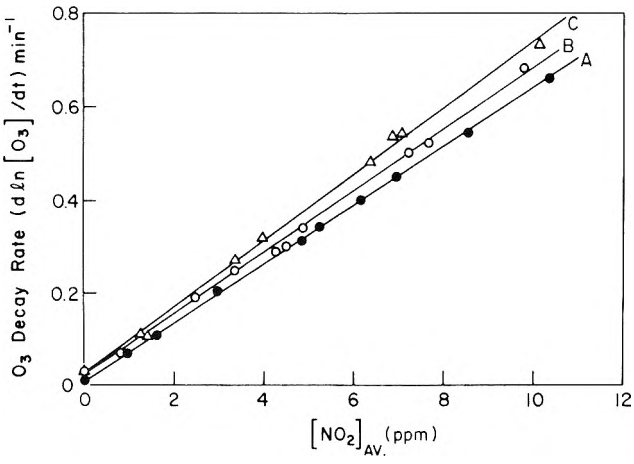

Figure 2. Decay of ozone as a function of $[NO_2]_0$ for the wall conditions: A, = O_3 treatment; B, = NO_2 treatment; C, = evacuation only.

NO_2 pretreatment. Ozone again exhibited first-order decay at various NO_2 concentrations. A plot of d ln $[O_3]/dt$ *vs.* $[NO_2]$ for data taken under these conditions is given in Figure 2, curve B. This line has a slope corresponding to a rate constant of 4.5×10^{-17} cm^3 molecule^{-1} sec^{-1} and a small positive intercept. This slope is slightly greater than that found with O_3-treated walls but is within experimental uncertainty. To study the wall effect further, kinetic data were obtained after subjecting the vessel to overnight pumping. When these data are plotted in the form d ln $[O_3]/dt$ *vs.* $[NO_2]$ (Figure 2, curve C), the slope gives a rate constant of 4.9×10^{-17} cm^3 molecule^{-1} sec^{-1}. This value is greater than that observed with either O_3 or NO_2 pretreatment.

The dependence of the O_3 decay rate on the initial ozone concentration was investigated at a fixed $[NO_2]_0$ = 4.9 ppm. In this experiment $[O_3]_0$ was varied from 0.1 to 1.0 ppm. When $[NO_2] \gg [O_3]$, d ln $[O_3]/]dt$ *vs.* time is linear with a constant slope as shown in Figure 3. At higher O_3 concentrations, these plots become curved as shown in this figure. The points are experimental data taken from the continuous recording of the ozone detector. The lines are from a computer analysis using reactions 1 and 2 (stoichiometry = 2) and a rate constant for $k_1 = 4.4 \times 10^{-17}$ cm^3 molecule^{-1} sec^{-1}. The experimental data do not start at time zero since it requires 1–2 min to fill the cell. Accordingly, the time scale of the experimental points has been shifted to take this into account. The calculation gives an excellent fit to all the data including those at the higher O_3 concentrations where NO_2 is no longer in large excess. A number of calculations were performed assuming various stoichiometries between 1.0 and 2.0. The data show a good fit to calculations with a stoichiometry between 1.7 and 2.0. Below 1.7 the calculation exhibits significant deviation from the experimental data. These results are in agreement with the stoichiometric determinations made in the long-path infrared cell.

Discussion

In all previous studies of this reaction the mechanism (1)–(2) and the corresponding stoichiometric value of 2 were assumed in the data analysis. Before proceeding to kinetic measurements, we wished to confirm the validity of this mechanism at the ppm concentration level. The stoichiometry measured in the long-path infrared cell was

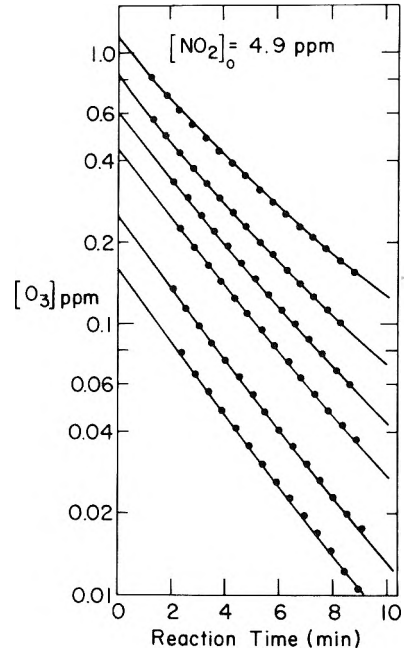

Figure 3. Concentration *vs.* time profiles of ozone at various initial concentrations with fixed $[NO_2]_0$ = 4.9 ppm. The points are experimental data while the lines are computed results using reactions 1 and 2 and $k_1 = 4.4 \times 10^{-17}$ cm^3 molecules^{-1} sec^{-1}.

1.88 ± 0.15 with ozone excess and 1.68 ± 0.15 for NO_2 excess. It was not possible to determine whether this difference was caused by a change in mechanism or by a systematic error in the experiments. A similar stoichiometric value could be inferred from O_3 decay in nonpseudo-first-order conditions. These measurements thus indicate the reaction is proceeding largely *via* the proposed mechanism. However, the measured stoichiometries tend to indicate other reactions may be occurring to reduce the ratio of $\Delta NO_2/\Delta O_3$ below 2.0 as predicted by the simple mechanism.

The following reactions can be incorporated into the mechanism

$$NO_3 + NO_2 \longrightarrow NO + NO_2 + O_2 \quad (3)$$

$$NO + NO_3 \longrightarrow 2NO_2 \quad (4)$$

$$NO + O_3 \longrightarrow NO_2 + O_2 \quad (5)$$

The overall stoichiometry is reduced by competition of reaction 3 with reaction 2. The NO formed in reaction 3 can react either *via* reaction 4 or 5. A computer integration of the mechanism (1)–(5) was carried out using rate constants suggested by Johnston.[11] The predicted stoichiometry is 1.95.

In addition, an alternative path for reaction 1

$$NO_2 + O_3 \longrightarrow 2O_2 + NO \quad (6)$$

cannot be ruled out entirely. If this reaction is occurring, it would have a strong effect on the stoichiometry. For example, if $k_1/k_6 = 20$ the overall stoichiometry is calculated to be 1.76.

The present stoichiometric data indicate the reaction proceeds greater than 90% *via* mechanism (1)–(2) at ppm concentrations. This is supported by the observation of an N_2O_5 yield approximately one-half the initial NO_2. A stoichiometry of 2.0 is an upper limit. Several possible minor reactions tend to reduce this value under the present experimental conditions.

The equation for O_3 decay has been demonstrated in this study to be $d[O_3]/dt = -k[NO_2][O_3]$ from the decay of O_3 and the dependence on NO_2 where $k = 4.4 \times 10^{-17}$ cm^3 molecule^{-1} sec^{-1}. The scatter in the individual determinations is less than 5%. Possible systematic errors in the rate constant could result from the absolute calibration of reactant concentrations. The NO and NO_2 calibrations were based on a standard mixture of NO which was analyzed independently by two laboratories reporting results within ±4%. The absolute calibration of ozone is not necessary for the rate constant determination. However, the calibration was done for purposes of cross checking and investigation of the second-order region. The temperature of the reaction mixture was monitored and found to be 26 ± 1°, which results in a maximum error of 3% assuming 7 kcal/mol for the activation energy. The stoichiometric value does not affect the rate constant derived from O_3 decay unless reactions such as (6) which consume extra ozone are occurring. In that case the rate constant measured here would be too large by the fraction k_6/k_1. However, this ratio is not likely to be greater than 0.05. The rate constant obtained from results in the "untreated" reactor is larger than that obtained with either O_3 or NO_2 treatment. This is likely a major cause of the larger value reported by Stedman and Niki. Based on these considerations, the overall uncertainty in the rate constant is estimated to be ±15%.

The present value of $k_1 = 4.4 \pm 0.6 \times 10^{-17}$ cm^3 molecule^{-1} sec^{-1} is larger than that determined by Ford, *et al.*,[5] and that estimated by Scott, *et al.*[6] However, both of these studies exhibited large uncertainty. Johnston and Yost report a rate constant of $6.1 \pm 0.6 \times 10^{-17}$ cm^3 molecule^{-1} sec^{-1} at 21°.[2] Using the reported activation energy of 7.0 ± 0.6 kcal/mole, their value at 25° is $7.2 \pm 1 \times 10^{-17}$. The rate constant derived in the present work is somewhat smaller than this. However in view of the vastly different experimental conditions used in their work, this should be considered in good agreement with the present value.

After the completion of this work another report of k_1 appeared. Ghormley, Ellsworth, and Hochandel[12] observed the decay of NO_2 produced in the flash photolysis of O_3 in N_2O. Due to an error in their rate equation, the rate constant as printed is incorrect. With the proper kinetic equation, their data yield a value of 3.2×10^{-17} cm^3 molecule^{-1} sec^{-1} for k_1.[13]

References and Notes

(1) H. Niki, E. E. Daby, and B. Weinstock, *Advan. Chem. Ser.* **No. 113**, 16 (1972).
(2) H. S. Johnston and D. M. Yost, *J. Chem. Phys.*, **17**, 386 (1949).
(3) E. D. Morris, Jr., and H. Niki, *J. Phys. Chem.*, **77**, 1929 (1973).
(4) O. R. Wulf, F. Daniels, and S. Karrer, *J. Amer. Chem. Soc.*, **44**, 2398 (1922).
(5) H. W. Ford, G. J. Doyle, and N. Endow, *J. Chem. Phys.*, **26**, 1336 (1957).
(6) P. M. Scott, K. F. Preston, R. J. Andersen, and L. M. Quick, *Can. J. Chem.*, **49**, 1808 (1971).
(7) D. H. Stedman and H. Niki, "Kinetics and Mechanism for the Photolysis of NO_2 in Air," Ford Motor Co., Scientific Research Staff Report Jan 17, 1973.
(8) D. H. Stedman, E. E. Daby, F. Stuhl, and H. Niki, *J. Air Pollut. Contr. Ass.*, **22**, 260 (1972).
(9) L. P. Breitenbach and M. Shelef, *J. Air Pollut. Contr. Ass.*, **23**, 128 (1973).
(10) F. Cramarossa and H. S. Johnston, *J. Chem. Phys.*, **43**, 727 (1965).
(11) H. S. Johnston, "Project Clean Air," University of California, 1970.
(12) J. A. Ghormley, R. L. Ellsworth, and C. J. Hochandel, *J. Phys. Chem.*, **77**, 1341 (1973).
(13) Private communication.

Kinetics of Gas-Phase Reactions of Ozone with Some Olefins

D. H. Stedman, C. H. Wu,* and H. Niki

Scientific Research Staff, Ford Motor Company, Dearborn, Michigan 48121

(Received February 22, 1973)

Publication costs assisted by the Ford Motor Company

Gas-phase reactions of ozone with ethylene, propylene, *trans*-2-butene, and 1-hexene were studied at 299 ± 2°K using a 45-l. static reactor and low reactant concentrations (~mTorr) at 760 Torr total pressure. Ozone was analyzed by the NO/O_3 chemiluminescence method, while hydrocarbons were monitored by gas chromatography. The kinetics was studied in both hydrocarbon and ozone excess conditions in the presence and absence of O_2. Absolute values of the second-order rate constant were determined to be 1.55 ± 0.15, 12.5 ± 1, 275 ± 23, and 11 ± 1.5 × 10^{-18} cm^3 molecule^{-1} sec^{-1} for ethylene, propylene, *trans*-2-butene, and 1-hexene, respectively. For propylene and *trans*-2-butene, a stoichiometry of unity was observed in both nitrogen and air diluents.

Introduction

Ozonolysis of simple olefins plays a key role in the formation of photochemical smog.[1,2] As a result, the kinetics of the gas-phase reactions of ozone with olefins has been the subject of numerous studies.[3-9] The available kinetic data on ethylene, propylene, *trans*-2-butene, and 1-hexene are summarized in Table I. Most of the studies listed here were carried out at low reactant concentrations (~mTorr) in air near atmospheric pressure. While the rate constants for 1-hexene show a general agreement, there is considerable discrepancy in rate constants and stoichiometries for the other olefins. In particular, an order of magnitude variation exists among the reported values for *trans*-2-bu-

TABLE I: Summary of Previous Kinetic Studies on Gas-Phase Ozonolysis of Ethylene, Propylene, *trans*-2-Butene, and 1-Hexene

Initial concn, mTorr		Diluent pressure, Torr		Stoichiometry, $\Delta[HC]/\Delta[O_3]$	Rate constant (ambient temp), $10^{18} \times$ cm^3 molecule^{-1} sec^{-1}	Ref
$[HC]_0$	$[O_3]_0$					
		Ethylene				
$\sim(2-3) \times 10^3$	$\sim(3-5) \times 10^2$	$\sim$150–650	(Air)	1.9–3.2	3.0 ± 1.3[a]	3
$\sim$15	$\sim$15	$\sim$760	(Air)	0.9	1.3[b]	4
$\sim$6	$\sim$2	$\sim$760	(Air)	1.6	2.6 ± 0.4[c]	7
$\sim(2-4) \times 10^4$	$\sim(0.3-2) \times 10^4$	$\sim$50–500	(O_2)	...	4.0[d]	8
$\sim 2.4 \times 10^4$	$\sim 4 \times 10^3$	$\sim$100	(O_2)	1.4–2.0	2.6[d]	9
$\sim 2.4 \times 10^4$	$\sim 4 \times 10^3$	$\sim$100	(N_2)	1	2[d]	9
		Propylene				
$\sim$8–16	$\sim$0.8	$\sim$760	(Air)	...	6.2[e]	3
$\sim$30	$\sim$8	$\sim$760	(Air)	1.06	8.0[b]	4
$\sim(2-4) \times 10^4$	$\sim(0.3-2) \times 10^4$	$\sim$50–500	(O_2)	...	11.2[d]	8
$\sim 2.4 \times 10^4$	$\sim 4 \times 10^3$	$\sim$100	(O_2)	1.4–2.0	10.6[d]	9
$\sim 2.4 \times 10^4$	$\sim 4 \times 10^3$	$\sim$100	(N_2)	1	9.2[d]	9
		trans-2-Butene				
...	...	$\sim$760	(Air)	...	166[b]	1, 6
$\sim$0.2	$\sim$0.3	$\sim$760	(Air)	1.5	430[c]	7
$\sim(2-4) \times 10^4$	$\sim(0.3-2) \times 10^4$	$\sim$50–500	(O_2)	...	38[d]	8
$\sim 2.4 \times 10^4$	$\sim 4 \times 10^3$	$\sim$100	(O_2)	1.4–2.0	35[d]	9
$\sim 2.4 \times 10^4$	$\sim 4 \times 10^3$	$\sim$100	(N_2)	1	21[d]	9
		1-Hexene				
$\sim$0.8–8	$\sim$0.8–8	$\sim$760	(Air)	1.6–2.5	9.0 ± 0.2[e]	3
...	...	$\sim$760	(Air)	...	10.0[b]	4
$\sim$0.8–30	$\sim$0.2–60	$\sim$760	(Air)	...	9.2[f]	5
...	...	$\sim$760	(Air)	1	11.0[b]	1, 6
$\sim$0.65	$\sim$0.5	$\sim$760	(Air)	1.8	11.0 ± 0.2[e]	7
$\sim(2-4) \times 10^4$	$\sim(0.3-2) \times 10^4$	$\sim$50–500	(O_2)	...	...[d]	8
$\sim 2.4 \times 10^4$	$\sim 4 \times 10^3$	$\sim$100	(O_2)	1.4–2	...[d]	9
$\sim 2.4 \times 10^4$	$\sim 4 \times 10^3$	$\sim$100	(N_2)	1	...[d]	9

[a] O_3 and olefins analyses by ir. [b] O_3 and olefins analyses by long-path ir. [c] O_3 analysis by iodometric method and olefins by gas–liquid chromatography. [d] Relative rate method, products analyses by gas–liquid chromatography, rate constants normalized to 1-hexene = 10.2×10^{-18} cm^3 molecule^{-1} sec^{-1}. [e] O_3 analysis by iodometric method. [f] O_3 analysis by iodometric and by converting O_3 to NO_2 and measuring NO_2 equivalent.

tene. Although the observed stoichiometry, $\Delta[HC]/\Delta[O_3]$, is unity with nitrogen diluent,[9] it varies between 1 and 3 in the presence of oxygen.[3,4,7,9] The present study was undertaken in an effort to resolve these uncertainties. Ozone was analyzed by the NO/O_3 chemiluminescence method and olefins by gas chromatography. The rate constants and stoichiometries were examined at several oxygen concentrations and various initial reactant ratios.

Experimental Section

Ozonolysis was carried out in a 45-l. Pyrex bell jar with a Teflon-coated stainless steel base. The reactor could be evacuated to below 1 mTorr with a mechanical pump and a liquid nitrogen trap. The leak rate was less than 1 mTorr min^{-1} upon isolation from the pumping system.

Pure ozone was prepared by condensing ozonized oxygen in a silica gel trap at 195°K and pumping off oxygen. The purity of ozone was checked by decomposing a sample in a Pyrex bulb ($\sim$100 cm^3) with a tesla coil and measuring the pressure change. The observed purity was 98 ± 3%. The research grade olefins (Phillips) were vacuum distilled prior to use. Nitrogen (American Cryogenics, ultrahigh purity, stated O_2 impurity $\leq$10 ppm) and oxygen (Matheson, ultrahigh purity) were used as received.

Reactant mixtures of ozone and olefin in the ppm concentration range (1 ppm = 2.45×10^{13} molecules cm^{-3} at 760 Torr 298°K) were prepared by first filling calibrated volumes to the desired pressures. The contents of these were then flushed into the evacuated bell jar with diluent gases to a total pressure of 760 Torr. The individual reactant pressures up to 20 Torr in the calibrated volumes were measured by a pressure transducer (Pace Wiancko, CD25) which had been calibrated against an oil manometer. The reactant concentrations in the gas mixtures thus prepared can be reproduced better than ±3%. The temperature of the gas mixture was 26 ± 2° during kinetic measurements.

Ozone was continuously sampled from the reactor using a capillary probe (flow rate $\sim$35 cm^3 min^{-1}) and was analyzed by an NO/O_3 chemiluminescence detector.[10] The overall response time of the instrument is less than 1 sec. The ozone concentration was calibrated by titration with NO of known concentration.[10] Linearity of the signal *vs.* concentration was checked from 10^{-3} to 10^2 ppm using an exponential dilution method.[11] Olefins were analyzed gas chromatographically using a flame ionization detector and a stainless steel column (⅛ in. × 12 ft) packed with DC 200 on chromosorb W. The reaction mixture was sampled into a 0.2-cm^3 loop and introduced to the column using a Carle minivolume valve. Olefin concentrations were calibrated by preparing known concentrations in the bell jar by the standard pressure–volume technique mentioned above. The lower limit of the detection sensitivity was about 10^{-3} ppm.

Results

In this study, the second-order rate constants for ozone–olefin reactions were determined mainly from the measurements of ozone decay rate in excess olefins using

$$\frac{d \ln [O_3]}{dt} = - k[HC]_0 \quad (1)$$

According to this equation, the exponential decay of ozone, d ln $[O_3]/dt$, is proportional to the initial hydrocarbon concentration, $[HC]_0$, and is independent of the ozone concentration, $[O_3]$. These kinetic relationships were examined extensively in the presence and absence of the molecular oxygen. For propylene and *trans*-2-butene, the rate constants were also checked by measurements of olefin decay rate in excess ozone concentration.

The comparison of the rate constants obtained by the two methods, *i.e.*, hydrocarbon and ozone excess conditions, gives measurements of stoichiometry. In addition, the stoichiometric data, $\Delta[HC]/\Delta[O_3]$, were obtained from the decays of both reactants in near equimolar mixtures.

1-Hexene and Ethylene. The rate constant for 1-hexene was measured to determine if the chemiluminescence method gives a result consistent with previous studies. Figure 1 shows the exponential decay of ozone at several 1-hexene concentrations. The slopes of these lines are plotted against 1-hexene concentration in Figure 2. The filled circles designate values obtained in air ($[O_2] = 2 \times 10^5$ ppm), and the open circles designate values obtained in N_2. These kinetic data obtained over the range of [HC] from 1 to 16 ppm are well represented by eq 1 and are not affected by the presence of molecular oxygen. From the slope of the line in Figure 2, a rate constant for 1-hexene was determined to be $1.10 \pm 0.15 \times 10^{-17}$ cm^3 molecule^{-1} sec^{-1}. This value is in good agreement with those of the previous studies listed in Table I. The overall uncertainties assigned to the rate constants in this work were estimated from the precision of the first-order decay slopes and from the accuracy of the olefin concentrations prepared. Figure 2 also shows the kinetic data for ethylene over the range from 5 to 55 ppm. The derived rate constant is $1.55 \pm 0.15 \times 10^{-18}$ cm^3 molecule^{-1} sec^{-1}. Although only one run was made in N_2 the result appears to be independent of the presence of O_2. Stoichiometric data were not obtained for these two olefins.

Propylene. The first-order decay rate of ozone was measured as a function of propylene concentration (1–16 ppm) at three oxygen levels, *i.e.*, $[O_2] \leq 10$, 2×10^5, and 8.5×10^5 ppm. The results are shown in Figure 3. These data were obtained over a period of several months to check for possible random errors associated with the measurements. The O_2 effect is not discernible in this figure. Thus a rate constant of $1.25 \pm 0.1 \times 10^{-17}$ cm^3 molecule^{-1} sec^{-1} was derived from the combined data. Another set of runs was made to determine the rate constant from the decay of propylene in excess ozone (1–12 ppm). The first-order decay was observed both in the presence and absence of O_2. The slopes are plotted against O_3 concentration in Figure 4. The line drawn in this figure was taken from Figure 3 for comparison. The consistency in rate constants derived from both sets of data suggests that the stoichiometry, $\Delta[HC]/\Delta[O_3]$, is unity under these conditions. In addition, the stoichiometry was measured directly from the decays of both propylene and ozone in near stoichiometric mixtures, the results of which are given in Table IIA. The data indicate that the stoichiometry is unity and is independent of the O_2 concentration.

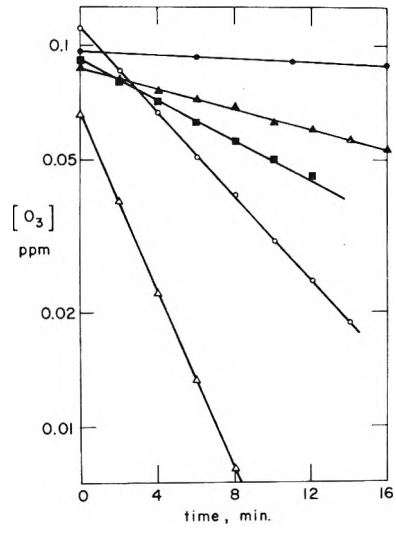

Figure 1. First-order decays of ozone in various 1-hexene concentrations at 299°K, 760 Torr of air ($[O_2] = 2 \times 10^5$ ppm), [1-hexene] (ppm) = ●, 0; ▲, 1.6; ■, 3.3; ○, 7.8; △ 15.7.

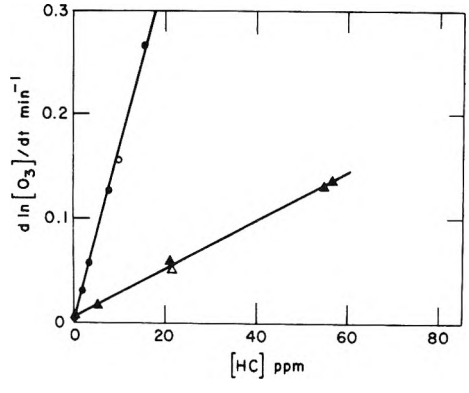

Figure 2. First-order decay rate of ozone as a function of excess concentration of 1-hexene (circles) and ethylene (triangle) at 299°K and 760 Torr total pressure, $[O_2]$ (ppm): ○, △, ≤10; ●, ▲, 2×10^5.

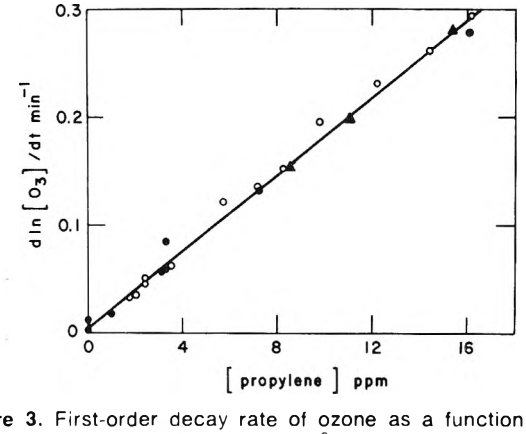

Figure 3. First-order decay rate of ozone as a function of excess propylene concentration at 299°K and 760 Torr total pressure, $[O_2]$ (ppm): ○, ≤10; ●, 2×10^5; ▲, 8.5×10^5.

trans-2-Butene. The rate of ozone removal in excess *trans*-2-butene was studied at relatively low concentrations since *trans*-2-butene reacts with ozone at a much faster rate than do the terminal olefins. The first-order decay rates of ozone both in N_2 and in air are plotted in Figure 5 as a function of *trans*-2-butene concentrations from 0.2 to 3 ppm. The data show a linear relationship and the rate constant derived from the slope is 2.75 ± 0.23

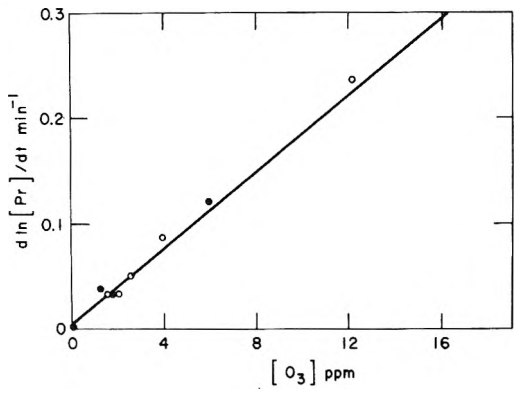

Figure 4. First-order decay rate of propylene as a function of excess ozone concentration at 299°K and 760 Torr total pressure, $[O_2]$ (ppm): O, ≤10; ●, 2×10^5.

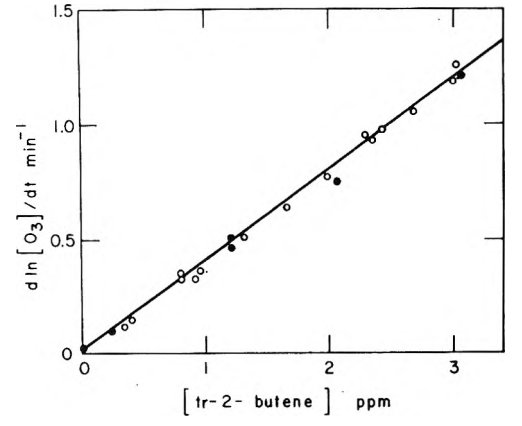

Figure 5. First-order decay rate of ozone as a function of excess *trans*-2-butene concentration at 299°K and 760 Torr total pressure, $[O_2]$ (ppm): O, ≤10; ●, 2×10^5.

TABLE II: Stoichiometric Data of the Ozonolysis of Propylene and *trans*-2-Butene

Diluent at 760 Torr	$[O_3]_0$, ppm	[HC], ppm	$\Delta[O_3]$, ppm	Δ[HC], ppm	Δ[HC]/$\Delta[O_3]$
		A. Propylene			
Air	1.45	2.5	0.29	0.31	1.07
Air	5.7	0.77	0.35	0.33	0.94
N_2	12.2	0.48	0.5	0.45	0.9
N_2	1.62	2.72	0.52	0.62	1.19
Air	1.63	0.33	0.07	0.07	1.0
N_2	2.0	0.84	0.12	0.13	1.08
				Av	1.03 ± 0.1 (σ)[a]
		B. *trans*-2-Butene			
Air	1.05	0.49	0.36	0.39	1.08
Air	0.23	0.74	0.13	0.12	0.92
N_2	1.0	0.43	0.33	0.38	1.15
N_2	0.80	0.40	0.35	0.39	1.11
N_2	0.96	0.2	0.18	0.19	1.05
				Av	1.06 ± 0.06 (σ)[a]

[a] σ is standard deviation.

$\times 10^{-16}$ cm^3 molecule^{-1} sec^{-1}. The first-order decay of *trans*-2-butene in excess ozone was also measured in order to compare the rate constants obtained by the two methods and to check the stoichiometry. With $[O_3]_0 = 0.6$ and 0.74 ppm in N_2, the decay rates of *trans*-2-butene were 0.26 and 0.32 min^{-1}, respectively. With $[O_3]_0 = 0.82$ ppm in air, the decay rate was 0.32 min^{-1}. These results give the same rate constant within experimental error as shown in Figure 5 for O_3 decay in excess *trans*-2-butene. Therefore, a stoichiometry is unity for this reaction. The Δ[HC]/$\Delta[O_3]$ ratio was further studied in near equimolar mixtures of ozone and *trans*-2-butene in N_2 and in air. These results are shown in Table IIB. Again the stoichiometry for this reaction is unity and independent of oxygen concentration.

Discussion

Linear plots shown in Figures 1-5 demonstrate that the reactions of ozone with simple olefins are first order with respect to both reactants under the present experimental conditions. For propylene and *trans*-2-butene, the stoichiometry was shown to be unity both by equal decrements of the reactants (Table II) and by identical rate constants for O_3 decay in excess [HC] and olefin decay in excess $[O_3]$ (Figures 3, 4, and 5). In addition, all the kinetic data were independent of $[O_2]$. Therefore, the results strongly suggest that the rate constants obtained thereby can be assigned to the primary ozonolysis steps of these olefins.

The present results are in general agreement with those obtained by previous workers using long-path ir analysis.[4,6] It was pointed out[5] that the iodometric method for ozone analysis may be susceptible to the interference from oxidant products. Therefore, part of the results[3,7] indicating stoichiometrics greater than 1 may be due to such effect.

Vrbaski and Cvetanović,[8] and Wei and Cvetanović worked at much higher concentrations using competitive product analysis. Their results showed first-order reaction with respect to hydrocarbon and unit stoichiometry in the presence of N_2. However, their stoichiometry of 1.4–2.0 in the presence of O_2, the effect of O_2 on the relative rate constants, and the low rate constant for *trans*-2-butene do not agree with the low-concentration studies. The source of these differences is not clear, although it has been suggested[4] that zwitterions formed by the initial reaction $O_3 + RCH = CHR \rightarrow$ adduct $\rightarrow RHC^+OO^- + RCHO$ may react further with olefins at high concentrations but undergo unimolecular decomposition at lower concentrations. In order to resolve these differences, it is desirable to carry out time-resolved analysis of both reactants and products at both high and low reactant concentrations. Such an attempt is currently underway in this laboratory using a flow system coupled to a quadrupole mass detector.

References and Notes

(1) P. A. Leighton, "Photochemistry of Air Pollution," Academic Press, New York, N. Y., 1961.
(2) H. Niki, E. E. Daby, and B. Weinstock, *Advan. Chem. Ser.*, **No. 113**, 16 (1972).
(3) R. D. Cadle and C. Schadt, *J. Amer. Chem. Soc.*, **74**, 6002 (1952).
(4) P. L. Hanst, E. R. Stephens, W. E. Scott, and R. C. Doerr, "Atmospheric Ozone-Olefin Reactions," The Franklin Institute, Philadelphia, Pa., 1958.
(5) B. E. Saltzmann and N. Gilbert, *Ind. Eng. Chem.*, **51**, 1415 (1959).
(6) E. A. Schuck, G. J. Doyle, and N. Endow, Report No. 31, Air Pollution Foundation, San Marino, Calif., 1960.
(7) J. J. Bufalini and A. P. Altshuller, *Can. J. Chem.*, **43**, 2243 (1965).
(8) T. Vrbaski and R. J. Cvetanović, *Can. J. Chem.*, **38**, 1053, 1063 (1960).
(9) Y. K. Wei and R. J. Cvetanović, *Can. J. Chem.*, **41**, 913 (1963).
(10) D. H. Stedman, E. E. Daby, F. Stuhl, and H. Niki, *J. Air Pollut. Contr. Ass.*, **22**, 260 (1972).
(11) A. Fontijn, A. J. Sabadell, and R. J. Ronco, *Anal. Chem.*, **42**, 575 (1970).

An Investigation of Photochemically Induced Reactions in a Chlorine–Ozone System at −10.5 and 0.0°[1]

Richard W. Davidson and Dale G. Williams*

The Institute of Paper Chemistry, Appleton, Wisconsin 54911 *(Received February 21, 1973)*

The reactions of the system were induced by light of wavelength 365–366.5 mμ. The products of the system were removed from the reactor and dissolved in water. The water solution was tested for the ionic chlorine species chloride, hypochlorite, chlorite, chlorate, and perchlorate. Dichlorine heptoxide was found to be the only stable chlorine oxide product of the reaction. The formation of dichlorine heptoxide was studied with respect to the light intensity, reactant concentration, presence of diluents, temperature, and total pressure. The observed data and information already in the literature were used to develop a reaction mechanism which was based on the formation of a proposed chlorine atom–ozone complex. Analysis of the mechanism showed that it adhered to the observed data and the use of certain known rate constants allowed the attainment of several rate constants concerning the formation of the chlorine atom–ozone complex.

Introduction

Systems containing chlorine oxides are very complex, as indicated in reviews by Mellor,[2] Farrar,[3] Schmeisser and Brandle,[4] and Eachus.[5] The photochemically induced reactions in a chlorine–ozone system can involve most of the known chlorine oxides: chlorine monoxide (ClO), chlorine dioxide (ClO_2), chlorine peroxide (ClOO), chlorine trioxide (ClO_3), dichlorine dioxide (Cl_2O_2), dichlorine hexoxide (Cl_2O_6), and dichlorine heptoxide (Cl_2O_7). The last published work describing the system appeared in 1934 and was authored by Norrish and Neville.[6] Others who directly studied the photochemical system were Weigert,[7] Bonhoeffer,[8] Bodenstein, *et al.*,[9] Bodenstein and Schumacher,[10] Allmand and Spinks,[11-13] Heidt, *et al.*,[14] and Byrns and Rollefson.[15-17] All of this early work used pressure measurement to study the breakdown of ozone to oxygen. The pressure increase was used to establish rates of ozone decomposition and quantum yields despite the evidence for the formation of the higher chlorine oxides, dichlorine hexoxide, and dichlorine heptoxide, which would cause a net decrease in pressure.

The reaction mechanisms proposed by these earlier workers appear somewhat in doubt in light of more recent studies of the photolysis of chlorine in the presence of oxygen[18] and knowledge gained in the past 40 years. In order to improve our understanding of the reaction mechanism, the present study focused on the system in light of the chlorine oxide products formed. Wet analytical techniques were used to measure the amounts of ionic chlorine species formed when the chlorine oxide products of the reaction were dissolved in water.

Experimental Section

Apparatus. The reactor was made from a Pyrex "Double-Tough" Drainline Straight Tee (Mooney Brothers Corp., Minneapolis, Minn.) with an inside diameter of 2 in. Pyrex plates were fused to the ends of the straight-through portion. The other opening was fitted with a Teflon manifold which had appropriate taps for entrance and exit of gases and liquids and insertion of a thermocouple. The volume of the reactor was 611.6 ± 0.1 ml. The overall inside length was 8.0 in. Chromatronix tubing (Chromatronix, Inc., Berkeley, Calif.) and Hamilton, Kel-F lined valves (Hamilton Co., Inc., Whittier, Calif.) were used in all tubing configurations. The oxygen and chlorine used in the study were Matheson Research grade gases, 99.99% and 99.965%, respectively. Helium (Matheson High Purity grade), when used as a diluent, was first passed through a liquid nitrogen gas trap. The ozone was prepared before each use in an apparatus similar to that described by Griggs and Kaye.[19] The reactor was evacuated using a vacuum pump with appropriate traps to prevent contamination of the oil. Initially, the temperature inside the reactor was monitored using a Kel-F coated copper–constantan thermocouple. This was eliminated when no heating effect due to the light beam was observed.

The reactor was immersed in a 2.5-gal temperature control bath fitted with double windows to allow passage of the activating light beam without frost buildup. The bath fluid was a 40% by volume solution of ethylene glycol in water which was kept at a constant specific gravity and was cleaned after each experimental run by passing it through activated charcoal and then through a 0.45-mμ Millipore filter (Millipore Filter Corp., Bedford, Mass.). Circulation of the fluid was achieved with a Teel submersible pump (Dayton Electric Mfg., Chicago, Ill.). Cooling of the bath was achieved through a compressor, appropriate cooling coil, and expansion valve. Temperature control was maintained by the addition of heat through knife heaters using a Precision electronic relay control box in conjunction with a Precision Micro-set differential range thermoregulator ±0.005°F, −35 to +500°F. All metal parts except the stainless steel knife heaters were coated with epoxy to prevent corrosion. Pressure was measured through the use of a calibrated Pace Model P7D differential-type pressure transducer (Whittaker Corp., North Hollywood, Calif.).

The light source was a Hanovia (Engelhard Hanovia, Inc., Newark, N. J.) 673A-10 500-W medium pressure mercury arc lamp used in conjunction with a Hanovia 20651-1 550-W ballast system. The lamp was mounted in an appropriate light housing and cooled by forced air circulation. The optical train consisted of the standard elements with a Corning (Corning Glass Works, Corning, N.

Y.) combination filter designed to pass light of wavelength 365 mμ (C.S. number 7-83). A light intensity in the order of 3.0×10^{15} quanta/sec was achieved with the optical train; however, the light beam entering the reactor was divergent. The concentration of chlorine in the system was maintained at a concentration of 8.82×10^{-3} mol/l., which ensured complete absorption of the incident light before the divergent beam reached the walls of the reactor.

Light intensity measurements were made using the potassium ferrioxalate system originally studied by Parker[20] and Hatchard and Parker[21] and recommended by Calvert and Pitts.[22] The procedures for the preparation and use of the actinometer system were taken from Calvert and Pitts.[22]

Procedures. The experimental procedures included three parts: (1) the initial procedures which consisted of starting up the equipment, preparing the ozone, calibrating the pressure transducer, and measuring the light intensity; (2) the reaction procedures which consisted of introducing the reactant gases to the reactor, initiating the reaction, monitoring the reaction, and terminating the reaction; and (3) recovery of products procedures which consisted of removing the chlorine oxides from the reactor by either dissolving them in carbon tetrachloride or purging with helium, dissolving the products in water, rinsing the reactor with water, and drying the reactor.[23]

The water solutions of chlorine and reaction products were analyzed using colorimetric techniques for hypochlorite (ClO^-), chlorite (ClO_2^-), chlorate (ClO_3^-), perchlorate (ClO_4^-), and chloride (Cl^-). Ozone was stripped from the solutions by purging with He during removal from the reactor. The chlorine was trapped in 0.1 *N* NaOH solution. The procedures used for the determination of hypochlorite, chlorite, and chloride were taken from the work of Chen.[24] The procedure used for determination of total chlorite and chlorate was a modified form of that given by Chen.[24] The modification was used to destroy hypochlorite in the sample as described in ref 23. The procedure used for determination of perchlorate was a modified form of that given by Trautwein and Guyon.[25] The modification was used to destroy hypochlorite, chlorite, and chlorate in the sample as described in ref 23.

Results and Discussion

Four of the five ionic chlorine species tested for in the analysis of the solutions were found. Chlorite was not found in any measurable quantities. The chloride, hypochlorite, and traces of chlorate found were products of the unreacted chlorine. The only ionic chlorine species found in abundance which could be attributed to a chlorine oxide product of the reaction was perchlorate. The perchlorate found was attributed to the hydrolysis of dichlorine heptoxide (Cl_2O_7). The presence of dichlorine hexoxide (Cl_2O_6) was considered negligible since it would hydrolyze to equal quantities of chlorate and perchlorate. Therefore, the following results will be based on the formation of dichlorine heptoxide as the only measurable product of the reaction system.

The apparent absence of detectable amounts of dichlorine hexoxide, which is a red liquid in the temperature range used, is a contradiction of the existing literature[6,13,15-17] on systems with comparable reactant concentrations and light intensities; however, the temperatures were 20–30°. A possible explanation for this is that the earlier workers may in fact have had abundant formation of dichlorine heptoxide but it was colored red by a small amount of dichlorine hexoxide. The literature indicates that no quantitative methods were used to determine the amounts of dichlorine hexoxide and dichlorine heptoxide present.

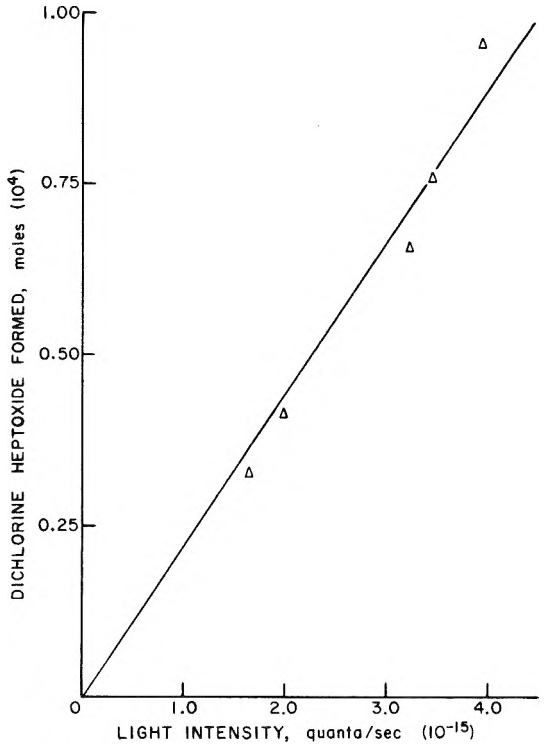

Figure 1. Relationship between light intensity absorbed and product formed at 0° and 10-hr reaction time with helium as the diluent.

In the system under study, approximately 90% of the light was absorbed in the first 2 in. of the reactor. Therefore, a reaction zone was considered that included the first 3 in. of the reactor with a diameter of 2 in., giving a volume of 155 ml. The rate of formation of the product dichlorine heptoxide is based on this volume. The concentration of chlorine atoms produced is also based on this volume, as is the concentration of short-lived intermediates. The concentrations of the reactants, chlorine and ozone, the diluents, helium and oxygen, and long-lived intermediates and products are based on the volume of the entire reactor. Diffusion calculations indicate that the concentration of the reactants would not be depleted in the reaction zone.

Results of Experimental Runs. All experimental runs, except where noted, were done with equimolar concentrations of ozone, chlorine, and helium, $9.15 \pm 0.05 \times 10^{-3}$ *M* at −10.5° and $8.82 \pm 0.05 \times 10^{-3}$ *M* at 0°.

A number of experimental runs were made using varying light intensities at the same initial reactant concentration and temperature. The results showed a direct proportionality between amount of light absorbed in the system and the amount of product formed as shown in Figure 1. Because of this direct proportionality, all of the data could be corrected to the same light intensity base of 3.05×10^{15} quanta/sec.

The data presented in Figure 2 show the results of experimental runs made at two different temperatures. It is seen from these data that there is no temperature dependence over the temperature range examined. The data also show that there is a very long constant rate period

TABLE I: Effect of He and O_2 as Diluent and of No Diluent at 0.0° for 10-Hr Runs

No. of runs	Moles of reactant added (10^3)				Cl_2O_7 formed, mol × 10^4	Rate of formation of Cl_2O_7, mol/l. sec	Quantum yield of formation of Cl_2O_7
	O_3	Cl_2	He	O_2			
2	5.39	5.38	—	—	0.73 ± 0.07	1.31 ± 0.13	0.40
5	5.41	5.38	5.36	—	0.65 ± 0.07	1.16 ± 0.13	0.36
2	5.40	5.38	—	5.45	0.61 ± 0.07	1.09 ± 0.13	0.33

TABLE II: Pressure and Concentration Changes in the Reactor during Different Reaction Times at 0.0° and the Same Initial Reactant Concentrations

	Time of reaction, hr					
	4	7	10	15	20	26
Change in pressure, mm	−0.67	0.40	1.76	1.90	6.75	5.20
Change in total mol × 10^4	−0.24	0.14	0.63	0.68	2.42	1.87
Cl_2O_7 formed, mol × 10^4	0.35	0.48	0.65	1.14	1.60	1.86

despite qualitative evidence that the concentration of ozone was reduced significantly at 20 hr of reaction time. These data, however, cannot show the presence or absence of an induction period under about 1 hr.

The previous data were taken using helium as a diluent. The data presented in Table I show the effect of the removal of helium and also the replacement of helium with oxygen for 10-hr runs at 0.0°. The quantities of product formed are significantly different at the 80% confidence level. Both helium and oxygen retard the formation of dichlorine heptoxide with the latter being more effective.

Norrish and Neville[6] found no effect on the decomposition of ozone due to introduction of nitrogen and carbon dioxide. It is apparent that the effect of introduction of helium in this study is small so that the pressure measurements used by them to follow the reaction may not have been sensitive enough to show a small effect due to nitrogen and carbon dioxide.

The effect of the variation of ozone on the production of dichlorine heptoxide at a constant amount of chlorine, 8.83×10^{-3} M, and different amounts of helium to give a constant total pressure of 450 mm is shown in the data given in Figure 3. At low concentrations of ozone (less than 3.0×10^{-3} M) there is a greater than zero order relationship with respect to ozone, but as the amount of ozone increases the relationship approaches one of zero order.

During the course of the reaction, a small pressure rise was encountered. This was attributed to the decomposition of ozone to oxygen. However, since preliminary experiments showed that there was negligible thermal and photochemical decomposition of ozone in the absence of chlorine, the decomposition of ozone to oxygen in the reaction system must involve chlorine or some of the chlorine oxides formed. The data given in Table II indicate that the increase in total moles in the system, under most conditions, was less than the moles of dichlorine heptoxide formed. These observations have been interpreted to mean that the formation of the final product, dichlorine heptoxide, is accomplished through reactions which give no net change in total moles. The increase in pressure has then been assumed to be due to side reactions which cause breakdown of chlorine oxides to chlorine and oxygen or to direct decomposition of ozone catalyzed by chlorine atoms or reactive chlorine oxides. To further confuse the pressure measurement data, a net decrease in total moles was encountered during early stages of the reaction (first 4 hr). This was believed to be due to reaction of dichlorine heptoxide with water absorbed on the surface of the reactor, accounting for the observed formation of a white film.

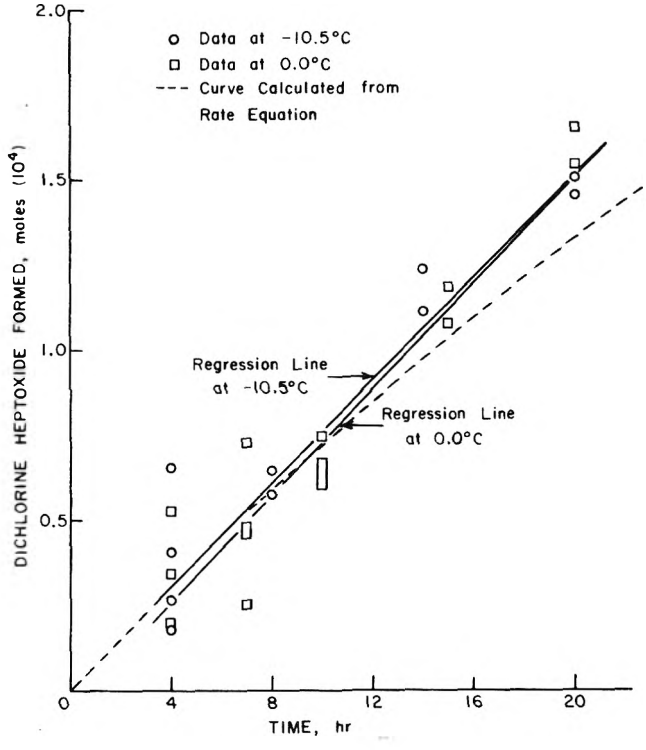

Figure 2. Moles of dichlorine heptoxide formed vs. time at −10.5 and 0.0° with helium as the diluent.

The quantum yield of Cl_2O_7 production has been shown to be fairly constant over a period of a run and unaffected by the temperature as shown by the data listed in Table III. The effect of diluent on the quantum yield is shown by the data in Table I. The direct proportionality between dichlorine heptoxide formation and light intensity also points out that the quantum yield of Cl_2O_7 production is independent of light intensity.

Because the concentration of ozone at the end of a reaction was not measured, the rate and quantum yield of ozone decomposition was estimated based on the amount of dichlorine heptoxide formed and the pressure rise in the system. These estimates showed that the quantum yield of ozone decomposition for the O_3–Cl_3, O_3–Cl_2–He, and

TABLE III: Quantum Yield of Cl_2O_7 Formation at −10.5 and 0.0°

Temp, °C	Time of reaction, hr	Moles of Cl_2O_7 formed × 10^4		Quantum yield of Cl_2O_7 formation
−10.5	4.0	0.31		0.42
	8.0	0.61		0.42
	14.0	1.18		0.46
	20.0	1.48		0.41
	26.0	1.77		0.37
			Av	0.42
0.0	4.0	0.36		0.49
	7.0	0.48		0.38
	10.0	0.65		0.36
	15.0	1.14		0.42
	20.0	1.60		0.44
	26.0	1.86		0.40
			Av	0.42

O_3–Cl_2–O_2 systems were 3.82, 2.72, and 3.06, respectively. These quantum yields are within the magnitude expected for the system based on the data of earlier workers.[6,13]

The preceding results on the formation of dichlorine heptoxide have been interpreted as follows.

1. The lack of temperature dependence, the magnitude of the quantum yield, and the direct proportionality between product formation and light intensity indicates that dichlorine heptoxide is formed in a nonchain stepwise manner. Since no high-energy atoms are produced in the photodissociation of chlorine,[18] the reactions leading to dichlorine heptoxide formation must have low activation energies.

2. The slight decrease of dichlorine heptoxide formation due to introduction of diluent is due to increased recombination of chlorine atoms because of the additional third bodies. Although decomposition of simple radicals, deactivation of "hot" radicals, and lower diffusion rates may be factors they are considered to be of minor importance.

3. The quantum yield of dichlorine heptoxide formation of 0.3 to 0.4 indicates certain reactions in the system that lead to inefficient use of the chlorine atoms formed. This again has been attributed to chlorine atom recombination.

4. The rather low pressure increase in the system indicates the net mole change in the reaction is essentially zero. Thus, every mole of ozone used in forming Cl_2O_7 produces one mole of O_2.

5. The relationship of dichlorine heptoxide formation with ozone concentration indicates an approach to a zero-order relationship. This interpretation is supported further by the observation of a rather long constant rate portion of the product *vs.* time curve in spite of decreasing ozone concentration.

6. With no, or relatively short, induction period, there is little time delay in building up the equilibrium concentrations of necessary intermediates for stepwise formation of product indicating that these intermediates are short-lived.

Development of a Reaction Mechanism. The reaction mechanism has been developed based on the observations of the earlier workers and those of the present study. The major points that must be adhered to are the following: (1) the mechanism must account for a change in the light intensity relationship for ozone decomposition from one proportional to light intensity at relatively high concentrations of ozone, chlorine, and oxygen to one approaching an $I^{0.5}$ relationship when the concentrations of chlorine and oxygen are low;[12,13] (2) the mechanism must account for the chain breakdown of ozone when the chlorine and oxygen concentrations are low and a zero-order relationship with respect to ozone when the concentrations of chlorine and ozygen are high;[12,13] (3) dichlorine heptoxide must be formed in a stepwise nonchain process; (4) reactions must be occurring that lead to recombination of chlorine atoms; and (5) formation of dichlorine heptoxide is accomplished with no net change in moles in the system.

The first step in the proposed mechanism is the formation of chlorine atoms due to absorption of a quantum of light

$$Cl_2(^1\Sigma_{g^+}) + h\nu \longrightarrow Cl_2(^3\pi_{o+u}) \longrightarrow Cl(^2P_{3/2}) + Cl(^2P_{1/2}) \quad (1)$$

For the interest of simplicity, the chlorine atoms formed will be considered to be identical despite the small energy difference between the singlet and triplet states, 2.52 kcal/mol, and will be represented by the symbol Cl.

The second step in the mechanism is the proposed formation of a chlorine atom–ozone complex which is stabilized by a third-body collision

$$Cl + O_3 + M \longrightarrow ClOOO + M \quad (2)$$

This is similar in nature to the formation of chlorine peroxide (ClOO) when a chlorine atom and oxygen come together.[18] The third body would be those species in reasonably high concentrations, such as chlorine, ozone, helium, and oxygen. Under conditions where the total pressure is so low that the chlorine atom–ozone complex would not experience a stabilizing third body collision, it could decompose as

$$Cl + O_3 \longrightarrow ClOOO^* \longrightarrow ClO + O_2 \quad (3)$$

leading to a chain decomposition of ozone with ClO as the chain carrier[6]

$$ClO + O_3 \longrightarrow Cl + 2O_2 \quad (4)$$

The third step in the mechanism is the formation of chlorine dioxide

$$ClOOO + O_3 \longrightarrow ClO_2 + 2O_2 \quad (5)$$

The chlorine dioxide quickly reacts to form chlorine trioxide

$$ClO_2 + O_3 \longrightarrow ClO_3 + O_2 \quad (6)$$

which is a common preparative method for chlorine trioxide. The reaction of chlorine monoxide and ozone is not a major source of chlorine dioxide formation since the reaction of eq 4 is favored thermodynamically[26] and since increased oxygen concentrations inhibit dichlorine heptoxide formation (see Table I) even though the ClO concentration would be increased.[18]

The final step in the mechanism is the reaction of chlorine trioxide with ozone to form a complex, which is stabilized by the distribution of the collision energy over many bonds, followed by reaction with another chlorine trioxide molecule with the net reaction[27]

$$2ClO_3 + O_3 \longrightarrow Cl_2O_7 + O_2 \quad (7)$$

A very similar sequence of reactions, involving the production of chlorine tetroxide[15] rather than the complex,

TABLE IV: Estimated Rate Constants for the Indicated Reaction of Eq 2

Reaction[a]	Rate constant
$Cl + O_3 + O_2 \rightarrow ClOOO + O_2$	5.0×10^4 l.^{2}/mol^2 sec
$Cl + O_3 + He \rightarrow ClOOO + He$	$<1.0 \times 10^2$ l.^{2}/mol^2 sec
$Cl + O_3 + M' \rightarrow ClOOO + M'$	2.2×10^4 l.^{2}/mol^2 sec

[a] M′ is the sum of the chlorine and ozone concentrations when their ratio is one.

was discounted because of the evidence for the very short life of the former. Several other routes for the formation of dichlorine heptoxide have been suggested[28-31] and were discarded as explained in ref 23.

Of the many side reactions possible, only the following were considered as reasonable:[23] (1) the recombination of chlorine atoms

$$2Cl + M \longrightarrow Cl_2 + M \quad (8)$$

and

$$Cl \xrightarrow{\text{wall}} \tfrac{1}{2}Cl_2 \quad (9)$$

where M are the high concentration species oxygen,[18] chlorine, and helium, and (2) the breakdown of chlorine monoxide to chlorine and oxygen[18]

$$ClO + ClO \longrightarrow Cl + ClOO \quad (10)$$

$$Cl + ClOO \longrightarrow ClO + ClO \quad (11)$$

and

$$Cl + ClOO \longrightarrow Cl_2 + O_2 \quad (12)$$

To summarize: product formation is through reactions 1, 2, and 5–7; ozone decomposition is by reactions 3–7; and side reactions are reactions 8–12.

Using the steady-state assumption for Cl, ClO, ClOO, ClO_2, ClOOO, and ClO_3 the following rate expressions result

$$\frac{d[Cl_2O_7]}{dt} = Ak_2[O_3][M]/2B \quad (13)$$

and

$$-\frac{d[O_3]}{dt} = [A/B]\{(7/2)k_2[O_3][M] + k_3[O_3]\} + k_4[ClO][O_3] \quad (14)$$

where $A = 2I_{abs} + k_4[ClO][O_3]$ and $B = k_2[O_3][M] + 2 \cdot k_8[Cl][M] + k_9$. When the third bodies oxygen and helium are absent and the chlorine concentration is low, there is very little dichlorine heptoxide formation so that the rate of ozone loss reduces to an $I_{abs}^{0.5}$ relationship through the chlorine monoxide concentration which is consistent with the literature. When the third bodies oxygen and helium are present and the chlorine concentration is high, as in the present study, reactions 3 and 4 are negligible. Both rate expressions become directly proportional to I_{abs}. This is consistent with the observed direct proportionality of product concentration and independence of quantum yield with light intensity. The rate of dichlorine heptoxide formation would also go from first order with respect to ozone at very low ozone concentrations to that approaching zero order at high concentrations, which is consistent with the observed data.

Using the data obtained in the present study and the rate expression for product formation, eq 13, estimates of the rate constants for the reactions represented by eq 2 were made by a trial and error procedure.[23] The results

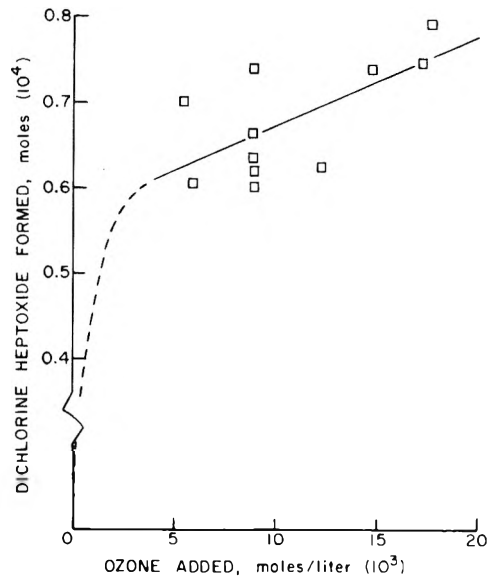

Figure 3. Moles of dichlorine heptoxide formed *vs.* moles per liter of ozone added for 10-hr runs at 0.0° for 8.83 mol/l. of chlorine at a total pressure of 450 mm established by the addition of helium.

are presented in Table IV. The rate constant for He is negligible compared to O_2 or M′. The rate constants for k_8 and k_9 required to make these calculations were estimated from the literature and are as follows: when M is chlorine, helium, and oxygen, the contributions to k_8 are 2.0×10^{10}, 4.25×10^9, and 2.05×10^{11} l.^{2}/mol^2 sec, respectively;[18,32] k_9 is 0.93 sec^{-1} using the surface recombination coefficient equation given by Herron[34] and reasonable values of the necessary parameters.[23,33] It is of interest to note that although oxygen is a good third body for the chlorine atom–ozone complex it is also a very good third body for chlorine atom recombination.

The integrated form of the dichlorine heptoxide rate of formation equation under the conditions represented in Figure 2 is given in the figure. A reasonable agreement with the observed data is evident. In addition, the quantum yields calculated from the integrated equation were in reasonable agreement with the observed data.

Conclusions

The only chlorine oxide product of the reaction system was found to be dichlorine heptoxide, in contradiction to that reported in the literature. It is proposed that this product is formed through a stepwise nonchain series of reactions involving ozone and a number of intermediate chlorine oxides. The key to the mechanism is the formation of a chlorine atom–ozone complex, ClOOO, which can be stabilized by a third body allowing further stepwise formation of dichlorine heptoxide.

The development of rate expressions from the mechanism shows that the mechanism accounts for essentially all of the experimental evidence that has been established about the system. The mechanism also indicates that third bodies can both speed up and slow down the formation of dichlorine heptoxide, increasing it by increasing the chlorine atom–ozone complex concentration and decreasing it by lowering the chlorine atom concentration through chlorine atom recombination reactions. In either case, chlorine and ozone, and oxygen were shown to be very effective third bodies while helium was shown to be much less effective.

Acknowledgments. The authors wish to express their appreciation to other members of the Ph.D. Advisory Committee, Drs. R. H. Atalla and G. A. Nicholls, for their many helpful discussions during the course of this research. R. W. D. acknowledges with thanks the fellowship support from The Institute of Paper Chemistry.

References and Notes

(1) A portion of a thesis submitted by R. W. Davidson in partial fulfillment of the requirements of The Institute of Paper Chemistry for the degree of Doctor of Philosophy from Lawrence University, Appleton, Wisc., June 1972. Present address is S. D. Warren Co., Westbrook, Me.
(2) Mellor's "Comprehensive Treatise on Inorganic and Theoretical Chemistry," Suppl. II, Part I, Longmans, Green and Co., New York, N. Y., 1956, p 1153.
(3) R. L. Farrar, Jr., "Safe Handling of Chlorine Trifluoride and the Chemistry of the Chlorine Oxides and Oxyfluorides," AEC Research and Development Report, K-1416, 1960, p 33.
(4) M. Schmeisser and K. Brandle, *Advan. Inorg. Chem. Radiochem.*, **5**, 41 (1963).
(5) R. S. Eachus, *Leicester Chem. Rev.*, **10**, 29 (1969).
(6) R. G. W. Norrish and G. H. J. Neville, *J. Chem. Soc.*, 1864 (1934).
(7) F. Weigert, *Ann. Phys.*, **24**, 243 (1907).
(8) K. F. Bonhoeffer, *Z. Phys.*, **13**, 94 (1923).
(9) M. Bodenstein, P. Harteck, and E. Padelt, *Z. Anorg. Allg. Chem.*, **147**, 233 (1925).
(10) M. Bodenstein and H. J. Schumacher, *Z. Phys. Chem.*, **B5**, 233 (1929).
(11) A. J. Allmand and J. W. T. Spinks, *Nature (London)*, **124**, 651 (1929).
(12) A. J. Allmand and J. W. T. Spinks, *J. Chem. Soc.*, 1652 (1931).
(13) A. J. Allmand and J. W. T. Spinks, *J. Chem. Soc.*, 599 (1932).
(14) L. J. Heidt, G. B. Kistiakowsky, and G. S. Forbes, *J. Amer. Chem. Soc.*, **55**, 223 (1933).
(15) G. K. Rollefson and A. C. Byrns, *J. Amer. Chem. Soc.*, **56**, 364 (1934).
(16) A. C. Byrns and G. K. Rollefson, *J. Amer. Chem. Soc.*, **56**, 1250 (1934).
(17) A. C. Byrns and G. K. Rollefson, *J. Amer. Chem. Soc.*, **56**, 2245 (1934).
(18) H. S. Johnston, E. D. Morris, Jr., and J. Van den Bogaerde, *J. Amer. Chem. Soc.*, **91**, 7712 (1969).
(19) M. Griggs and S. Kaye, *Rev. Sci. Instrum.*, **39**, 1685 (1968).
(20) C. A. Parker, *Proc. Roy. Soc., Ser. A*, **220**, 104 (1953).
(21) C. G. Hatchard and C. A. Parker, *Proc. Roy. Soc., Ser. A*, **235**, 518 (1956).
(22) J. G. Calvert and J. N. Pitts, "Photochemistry," Wiley, New York, N. Y., 1966, p 899.
(23) R. W. Davidson, Doctor's Dissertation, The Institute of Paper Chemistry, Appleton, Wis., 1972, p 208.
(24) T.-h. Chen, *Anal. Chem.*, **39**, 804 (1967).
(25) N. L. Trautwein and J. C. Guyon, *Anal. Chem.*, **40**, 639 (1968).
(26) "JANAF Thermochemical Tables," U. S. Government Printing Office, U. S. National Bureau of Standards, Washington, D. C., 1965.
(27) C. F. Goodeve and A. E. L. Marsh, *J. Chem. Soc.*, 1332 (1939).
(28) H. J. Schumacher, *Z. Phys. Chem. (Frankfurt am Main)*, **13**, 353 (1957).
(29) A. J. Arvia, W. H. Basualdo, and H. J. Schumacher, *Z. Anorg. Allg. Chem.*, **286**, 58 (1956).
(30) J. W. T. Spinks and H. Taube, *J. Amer. Chem. Soc.*, **59**, 1155 (1937).
(31) J. W. T. Spinks and H. Taube, *Can. J. Res.*, **15B**, 499 (1937).
(32) E. Hutton and M. Wright, *Trans. Faraday Soc.*, **61**, 78 (1965).
(33) P. G. Ashmore, A. J. Parker, and D. E. Sterne, *Trans. Faraday Soc.*, **67**, 3081 (1971).
(34) J. T. Herron, *J. Phys. Chem.*, **67**, 2864 (1963).

Ionic Photodissociation of Weak Charge-Transfer Complexes. Donor Acetonitrile and Acceptor Tetracyanoethylene and Iodine

Katsumi Kimura,* Yohji Achiba, and Shunji Katsumata

Physical Chemistry Laboratory, Institute of Applied Electricity, Hokkaido University, Sapporo 060, Japan *(Received April 24, 1973)*

Publication costs assisted by the Institute of Applied Electricity, Hokkaido University

Ionic photodissociations of weak charge-transfer complexes of acetonitrile with tetracyanoethylene (TCNE) and iodine have been studied spectroscopically. From quantitative measurements of spectral intensity, it was found that acetonitrile and TCNE form a 1:1 charge-transfer complex in which acetonitrile works as an electron donor toward TCNE. Flash-irradiation in the charge-transfer band gave rise to a transient species assigned to the TCNE anion. It is concluded therefore that ionic photodissociation takes place *via* the excited state of the charge-transfer complex. This experimental evidence has revealed the mechanism of the photoinduced anion formation of TCNE in acetonitrile reported by Sofue and Nagakura. The known charge-transfer complex of the donor acetonitrile and the acceptor iodine was also flash-irradiated in solution, and as a result the ionic photodissociation was found to occur forming a transient species attributed to the I_2 anion.

Introduction

It has been reported by Sofue and Nagakura[1] that the photoirradiation of solutions of tetracyanoethylene (TCNE) and tetracyanobenzene (TCNB) in acetonitrile gives rise to the corresponding anion radicals even in the absence of a definite electron donor. No explanation has so far been given for the mechanism of this photoinduced anion formation.

The photoinduced $TCNE^-$ formation in ethereal solvents such as tetrahydrofuran (THF) has been studied by several workers.[2-7] In our preliminary flash-photolysis work[8] of TCNE in dichloromethane solution containing a small amount of acetonitrile, a transient absorption spectrum attributable to $TCNE^-$ was obtained. This suggests that the photoinduced anion formation results either from an exciplex which was first proposed by Weller and his

collaborators[9] or from the excited state of a charge-transfer (CT) complex of TCNE with acetonitrile. In order to clarify the mechanism of the photoinduced $TCNE^-$ formation in acetonitrile, it should first be investigated if TCNE certainly forms a CT complex with acetonitrile in its ground state. According to a spectroscopic study by Popov and Deskin,[10] an acetonitrile molecule forms CT complexes with iodine and iodine halides (ICl and IBr). These complexes seem to be only a few examples in which acetonitrile works as an electron donor.

The present paper is concerned first with evidence of a complex formation between acetonitrile and TCNE and secondly with evidence of the ionic photodissociation of acetonitrile CT complexes with TCNE as well as with iodine. The present work provides typical examples of ionic photodissociation of weak CT complexes of acetonitrile.

Experimental Section

Commercial material of TCNE was purified by vacuum sublimation. Iodine was sublimed once. Acetonitrile was refluxed over P_2O_5 for several hours and finally distilled. Dichloromethane and 1,2-dichloroethane were purified by shaking with dilute sulfuric acid (10%), with aqueous alkaline solution (10%), and finally with water and distilled after drying over $CaCl_2$. In order to study electronic absorption of the acetonitrile–TCNE system, a series of solutions were prepared in dichloromethane with the concentration of acetonitrile ranging from 0.15 to 1.00 M and TCNE of about 4.6×10^{-4} M. Electronic absorption measurements were carried out on a Cary 15 spectrophotometer.

Flash photolysis experiments were performed with an apparatus equipped in our laboratory,[11] a quartz cell 12 cm long being used. The duration times of the photolysis-flash and spectro-flash argon lamps were 5.0 and 3.5 μsec, respectively. Transient absorption spectra were recorded photographically using a Shimazu grating spectrograph, Model GE-100. Solutions used in the present flash experiments were degassed with a freeze–pump–thaw technique except for those used in the study of oxygen effect.

Low-temperature photoirradiations were carried out in acetonitrile rigid matrices at 77°K with a 250-W high-pressure mercury lamp, using a 0.1-cm quartz cell capable of measuring absorption spectra of somewhat opaque matrices, with a neutral filter. The present low-temperature irradiation technique is essentially the same as that used previously.[12]

Results and Discussion

Acetonitrile–TCNE Complex. Electronic absorption spectra of dichloromethane solutions containing about 4.6×10^{-4} M TCNE and acetonitrile up to 1.0 M are shown in Figure 1a, from which it is seen that a new broad band appears in the range 320–450 nm by increasing acetonitrile concentration. This band was distinctly observed only in the degassed solutions. Such an absoprtion band has not been reported so far. The change in the intensity of the 320–450-nm band was found to be interpreted in terms of a 1:1 complex between acetonitrile and TCNE by applying the Benesi–Hildebrand method[13] and by using the following approximate equation

$$l[\mathrm{TCNE}]/D_{\mathrm{CT}} = 1/\epsilon_{\mathrm{CT}}k_{\mathrm{CT}}[\mathrm{CH_3CN}] + 1/\epsilon_{\mathrm{CT}} \qquad (1)$$

where D_{CT} and ϵ_{CT} denote the optical density and the molar extinction coefficient, respectively, [TCNE] and [CH_3CN] are the concentrations of TCNE and acetonitrile, respectively, k_{CT} is the charge-transfer equilibrium constant, and l is the path length. As shown in Figure 1b, a plot of l[TCNE]/D_{CT} vs. 1/[CH_3CN] indicates a satisfactory straight line, yielding k_{CT} = 1.86 l./mol at 25° from the slope ($1/\epsilon_{\mathrm{CT}}k_{\mathrm{CT}}$) as well as ϵ_{CT} = 55 l./mol cm from the intercept ($1/\epsilon_{\mathrm{CT}}$). This k_{CT} value considerably resembles that for the ether–TCNE complex reported by Merrifield and Phillips[14] and those for the tetrahydrofuran–TCNE and dioxane–TCNE complexes by Vars, *et al.*,[15] as shown in Table I, whereas the ϵ_{CT} value of the acetonitrile–TCNE complex is much less than those of the others. The acetonitrile–TCNE complex may be one of rare cases in which the acetonitrile molecule functions as an electron donor. This CT complex belongs to the same category as those found by Popov and Deskin[10] between acetonitrile and the halides (I_2, ICl, and IBr), their k_{CT} values being shown for comparison in Table II. According to Klaboe,[16] these halogen compounds also form stable 1:1 complexes with propionitrile which works as an electron donor toward the halides.

Flash Photolysis of Acetonitrile–TCNE Complex. Sofue and Nagakura[1] have reported that flash irradiation of rather concentrated solution of TCNE in acetonitrile gives rise to the long-lived $TCNE^-$ species detectable by an ordinary absorption measurement. We carried out the fol-

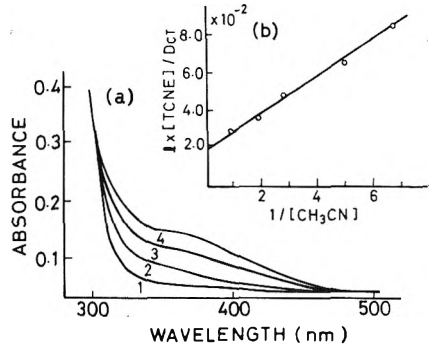

Figure 1. a, Dependence of the absorption spectra of dichloromethane solutions containing acetonitrile and TCNE upon the acetonitrile concentration (air-free): 1, 4.69×10^{-4} M TCNE; 2, 4.64×10^{-4} M TCNE and 0.20 M CH_3CN; 3, 4.60×10^{-4} M TCNE and 0.49 M CH_3CN; 4, 4.49×10^{-4} M TCNE and 0.95 M CH_3CN. b, Benesi–Hildebrand plot for the acetonitrile–TCNE complex.

TABLE I: Comparison of Absorption Maxima, Molar Extinction Coefficients, and Equilibrium Constants for Charge-Transfer Complexes of TCNE

	$\lambda_{\mathrm{CT\ max}}$, nm	ϵ_{CT}, l./mol cm	k_{CT}, l./mol
Acetonitrile–TCNE	360	55	1.86
Ether–TCNE[14]	335	—	1.54
Tetrahydrofuran–TCNE[15]	318	3125	1.15 ± 0.09
Dioxane–TCNE[15]	350	1859	2.13 ± 0.13

TABLE II: Comparison of Equilibrium Constants for Charge-Transfer Complexes of Acetonitrile

	k_{CT}, l./mol
Acetonitrile–TCNE	1.86
Acetontrile–ICl[10]	6.9 ± 0.3
Acetonitrile–IBr[10]	1.40 ± 0.03
Acetonitrile–I_2[10]	0.57 ± 0.02

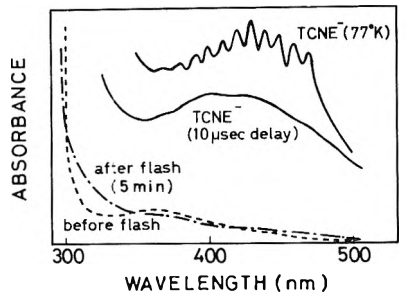

Figure 2. Absorption spectra before and after the flash photolysis of a solution of TCNE and acetonitrile in dichloromethane (air-free, 1×10^{-4} *M* TCNE + 0.1 *M* acetonitrile), and the $TCNE^-$ spectrum obtained at 77°K by irradiating TCNE in an acetonitrile rigid matrix, using a 0.1-cm quartz cell.

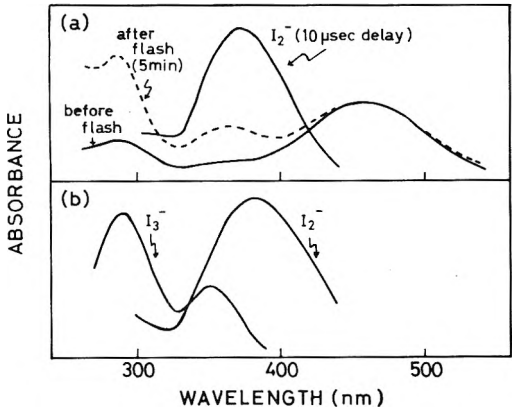

Figure 3. a, Absorption spectra before and after flash photolysis of iodine in acetonitrile (air-free, 2×10^{-4} *M*). b, Absorption spectra available for I_2^- (ref 19) and I_3^- (ref 18).

lowing experiments with acetonitrile solutions containing 10^{-4} *M* TCNE at room temperature as well as at 77°K by exciting the CT band. Irradiating TCNE in a rigid acetonitrile matrix at 77°K with a mercury lamp, the vibrational structure characteristic of the $TCNE^-$ band was observed as shown in Figure 2, in good agreement with that reported[17] for the TCNE anion formed by alkali metal reduction. The present room temperature flash photolysis gave rise to a transient species attributable to $TCNE^-$ and confirmed the previous report by Sofue and Nagakura.[1] The present results obtained by the CT band excitation strongly support that the formation of $TCNE^-$ takes place *via* the excited CT state of the TCNE–acetonitrile system. We also examined the effect of oxygen on the ionic photodissociation. It was found that the initial amount of $TCNE^-$ immediately after the flash is almost independent of oxygen. Since oxygen is known to work as a quencher for the triplet-state ionic dissociation in the case of the TCNE–tetrahydrofuran system,[7b] it may be inferred from the present result that the $TCNE^-$ formation in acetonitrile occurs in the excited singlet state of the CT complex rather than the excited triplet state. Flash excitation in the CT band of a degassed solution containing 1×10^{-4} *M* TCNE and 0.1 *M* acetonitrile in dichloromethane at room temperature gave rise to a transient band which is observable photographically within about 50 μsec in the range 350–500 nm as shown in Figure 2. This transient band again resembles the visible absorption band of $TCNE^-$ in spectral shape, although the vibrational structure was unresolved. Therefore, we may assign the transient species to $TCNE^-$ which is considered to form by an electron transfer from the donor CH_3CN to the acceptor TCNE.

Flash Photolysis of Acetonitrile–Iodine Complex. Since iodine has been reported to form a 1:1 CT complex with acetonitrile,[10] in the present work we carried out flash experiments for the acetonitrile–iodine system. The absorption spectrum of a fresh degassed solution of 2×10^{-4} *M* iodine in acetonitrile is shown in Figure 3a. As mentioned before, in such a solute–solvent complex most of the solute molecules (I_2) should exist as the CT complex. It may be considered from Figure 3a that the 460-nm band before flash corresponds to the iodine longest wavelength band and the 350- and 272-nm bands are attributable to I_3^- which was slightly produced by a slow change after the preparation of the solution. According to Popov and Deskin,[10] even in the absence of the ultraviolet radiation there is a slow transition of the outer complex to the inner complex. Absorption spectra available for the I_3 anion[18] as well as the I_2^- anion[19] are shown for comparison in Figure 3b.

Since no definite CT band has been reported for the acetonitrile–iodine complex, the present flash experiment was carried out without a cut-off filter. As shown in Figure 3a, the flash photolysis of the fresh degassed solution of iodine in acetonitrile gave a transient band peaking at 380 nm which is very close to the I_2^- band. Thus, the present result for the acetonitrile–iodine system suggests that the ionic photodissociation occurs to produce I_2^- *via* the CT excited state. The difference between the spectra before and after flash (5 min) may suggest that the stable photoproduct is I_3^- by reaction 1, $I_2^- + I_2 \rightarrow I_3^- + I$. Other reactions (2) $2I_2^- \rightarrow I_3^- + I^-$ and (3) $I_2^- + I \rightarrow I_3^-$ should also be considered, which have been mentioned by Grossweiner and Matheson[19] in the flash-photolysis study of aqueous alkali iodide solutions. Atomic iodine in (3) is considered to be produced by photodissociation of I_2. In the present experiment, the concentrations of I_2^- and I_3^- were roughly estimated to be 7×10^{-4} and 4×10^{-4} *M*, respectively, using known ϵ values (15,600[19] at 395 nm for I_2^- and 26,400[18] at 352 nm for I_3^-). Since the concentration (2×10^{-4} *M*) of I_2 in acetonitrile is much higher than the instantaneous concentration (7×10^{-7} *M*) of I_2^- produced immediately (10 μsec) after the flash, it may be considered that the reaction $I_2^- + I_2 \rightarrow I_3^- + I$ seems to be important. A more detailed kinetic study should be required to determine the mechanism of the formation of I_3^- from I_2^-. The observation of the stable I_3^- species in the photoirradiation of I_2 in acetonitrile strongly supports the formation of the transient I_2 anion rather than neutral transient species. According to the flash photolysis results by Gover and Porter,[20] no transient species due to I_2^- and no stable ionic photoproducts have been observed in a variety of solvents other than acetonitrile.

The absorption spectrum of a 1,2-dichloroethane solution containing 5×10^{-4} *M* iodine and 1 *M* acetonitrile before flash is shown in Figure 4a. A transient spectrum consisting of two bands at 300 and 380 nm was obtained immediately after flash. The 380-nm band may be assigned to I_2^- which has been known by many spectroscopic studies.[19] On the other hand, the 300-nm band seems to be attributed to a transient CT complex formed between a photoproduced iodine atom and 1,2-dichloroethane, since Strong, *et al.*,[21] have indicated from a gas-phase flash-photolysis study that transient CT complexes between an iodine atom and alkyl chlorides show CT band maxima in the 270–280-nm range, and Gover and Porter[20]

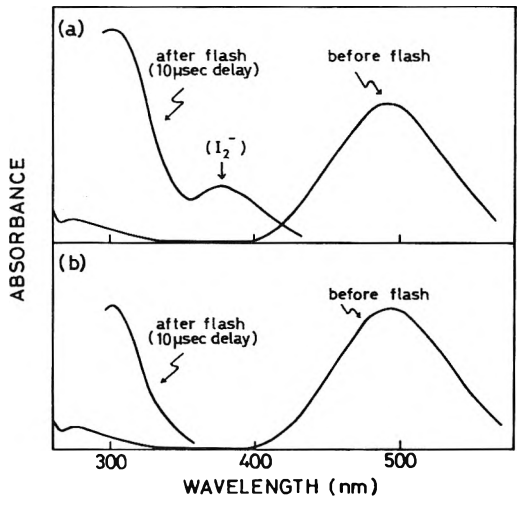

Figure 4. Absorption spectra before and after flash photolysis of degassed 1,2-dichloroethane solutions containing (a) 5×10^{-4} *M* iodine and 1 *M* acetonitrile and (b) 5×10^{-4} *M* iodine.

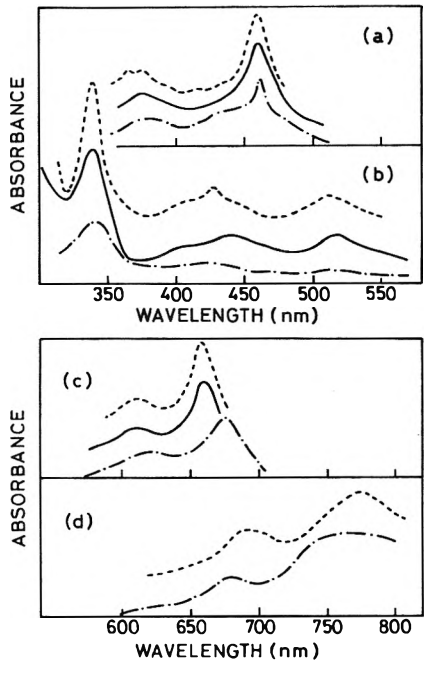

Figure 5. Transient absorption spectra (——) obtained immediately after the flash photolysis of (a) TCNB, (b) DCNB, (c) PMDA, and (d) TCNQ in acetonitrile (air-free, about 10^{-4} *M*) at room temperature, and ordinary absorption spectra (—·—·—) obtained from these compounds by uv irradiation in an acetonitrile matrix a 77°K. For comparison, the absorption spectra (·····) available for the anion radicals are shown: (a) $TCNB^-$ (ref 23), (b) $DCNB^-$ (ref 23), (c) $PMDA^-$ (ref 24), and (d) $TCNQ^-$ (ref 25).

have also observed CT complexes of iodine atom with a variety of solvents in the flash photolysis of I_2.

When a 1,2-dichloroethane solution containing 5×10^{-4} *M* iodine (without mixing acetonitrile) was flash-irradiated under the same condition, a transient band peaking at 300 nm was observed within 100 μsec, but no band due to I_2^-, as shown in Figure 4b. Thus, it may be reasonably considered that the 300-nm bands in Figure 4a and b are probably due to the iodine atom–1,2-dichloroethane complex.

Very recently, Fornier, *et al.*,[22] have carried out a laser flash photolysis of I_2 in hydroxylic solvents and have indicated that the transient absorptions in the range 250 to 400 nm are attributed to iodine atom–solvent CT complexes and the 385-nm transient absorption is reassigned to the I_2^- radical anion. These results seem to support the present interpretation for the I_2^- formation in acetonitrile.

Photoinduced Anion Formation of Other Acceptors. Further uv irradiation experiments were carried out with acetonitrile solutions of 1,2,4,5-tetracyanobenzene (TCNB), *p*-dicyanobenzene (DCNB), pyromellitic dianhydride (PMDA), and tetracyano-*p*-quinodimethane (TCNQ) at room temperature as well as at 77°K. Transient spectra obtained in the room-temperature flash photolysis of these compounds immediately after the flash are shown by solid curves in Figure 5, in good accord with the absorption spectra of the anions (broken curves) obtained by other workers.[23-25] Therefore, the transient species may be attributed to the corresponding anions. (The transient spectrum obtained for TCNQ is not shown in Figure 5 because of somewhat uncertainty in spectral shape. However, its absorption region was very similar to that of the anion.) The low-temperature uv irradiation gave rise to the anion species stable in rigid acetonitrile matrices at 77°K. The absorption spectra of the anions thus obtained are shown by ····· in Figure 5. All the experimental results obtained here for TCNB, DCNB, PMDA, and TCNQ indicate that photoinduced anion formations take place in acetonitrile at room temperature as well as at 77°K. We consider that these anion formations in acetonitrile proceed *via* the CT excited states rather than the exciplexes.

References and Notes

(1) M. Sofue and S. Nagakura, *Bull. Chem. Soc. Jap.*, **38**, 1048 (1965).
(2) C. Lagercrantz and M. Yhland, *Acta Chem. Scand.*, **16**, 1043, 1799, 1807 (1962).
(3) R. L. Ward, *J. Chem. Phys.*, **39**, 852 (1963).
(4) D. F. Ilten and M. Calvin, *J. Chem. Phys.*, **42**, 3760 (1965).
(5) F. E. Stewart and E. Eisner, *Mol. Phys.*, **12**, 173 (1967).
(6) R. T. Keys and W. R. Carper, *J. Chem. Phys.*, **47**, 3682 (1967).
(7) (a) Y. Achiba, S. Katsumata, and K. Kimura, *Bull. Chem. Soc. Jap.*, **45**, 1272 (1972); (b) Y. Achiba, S. Katsumata, and K. Kimura, *Chem. Phys. Lett.*, **13**, 213 (1972); (c) Y. Achiba and K. Kimura, *ibid.*, **19**, 45 (1973).
(8) Presented by Y. Achiba, S. Katsumata, and K. Kimura, at the 24th Annual Meeting of Chemical Society of Japan, Osaka, 1971.
(9) H. Leonhardt and A. Weller, *Z. Phys. Chem. (Frankfurt am Main)*, **29**, 277 (1961); *Ber. Bunsenges. Phys. Chem.*, **67**, 791 (1963).
(10) A. I. Popov and W. A. Deskin, *J. Amer. Chem. Soc.*, **80**, 2976 (1958).
(11) N. Kanamaru and K. Kimura, *Mol. Photochem.*, in press.
(12) K. Kimura, K. Yoshinaga, and H. Tsubomura, *J. Phys. Chem.*, **71**, 4485 (1967).
(13) H. A. Benesi and J. H. Hildebrand, *J. Amer. Chem. Soc.*, **71**, 2703 (1949).
(14) R. E. Merrifield and W. D. Phillips, *J. Amer. Chem. Soc.*, **80**, 2778 (1958).
(15) R. Vars, L. A. Tripp, and L. W. Pickett, *J. Phys. Chem.*, **66**, 1754 (1962).
(16) P. Klaboe, *J. Amer. Chem. Soc.*, **85**, 871 (1963).
(17) W. D. Phillips, J. C. Rowell, and S. I. Weissman, *J. Chem. Phys.*, **33**, 626 (1960).
(18) D. Meyerstein and A. Treinin, *Trans. Faraday Soc.*, **59**, 1114 (1963).
(19) For instance, see L. I. Grossweiner and M. S. Matheson, *J. Phys. Chem.*, **61**, 1089 (1957); A. Zalious-Gitter and A. Treinin, *J. Chem. Phys.*, **42**, 2019 (1965).
(20) T. A. Gover and G. Porter, *Proc. Roy. Soc., Ser. A*, **262**, 476 (1961).
(21) V. A. Brosseau, J. R. Basila, J. F. Smalley, and R. L. Strong, *J. Amer. Chem. Soc.*, **94**, 716 (1972), and consecutive papers.
(22) P. Fornier de Violet, R. Bonneau, and J. Joussot-Dubien, *Chem. Phys. Lett.*, **19**, 251 (1973).
(23) A. Ishitani and S. Nagakura, *Theor. Chim. Acta*, **4**, 236 (1966).
(24) Y. P. Pilette and K. Weiss, *J. Phys. Chem.*, **75**, 3805 (1971).
(25) L. R. Melby, R. J. Harder, W. R. Hertler, W. Mahler, R. E. Benson, and W. E. Mochel, *J. Amer. Chem. Soc.*, **84**, 3376 (1962).

Electron Scavenging by Bromobenzene in the Radiolysis of Hydrocarbon Solutions

Masayuki Tanaka and Kenji Fueki*

Department of Synthetic Chemistry, Faculty of Engineering, Nagoya University, Chikusa-ku, Nagoya, Japan
(Received June 14, 1973)

Publication costs assisted by Nagoya University

A quantitative study has been made of electron scavenging processes in γ-irradiated liquid hydrocarbons: *n*-pentane, cyclopentane, *n*-hexane, cyclohexane, 3-methylpentane, 2,3-dimethylbutane, 2,2-dimethylbutane, 2,2,4-trimethylpentane, and *n*-octane. The benzene yield observed upon electron scavenging by bromobenzene in the hydrocarbon solutions can be quantitatively described by an empirical model developed by Schuler and coworkers. The ion-pair yields and the reactivity parameters for electron scavenging were obtained by the analysis of data. The results indicate that the total ion-pair yields in liquid alkanes are about 4 and do not differ very much from the gas-phase values. The ranges of electrons in the hydrocarbons studied were also calculated based on a model in which a simple exponential distribution was assumed for initial electron–positive ion separation distances.

Introduction

In recent years there has been considerable interest in the ion-pair yields, the dynamics of electrons, and the reactivity of electrons toward scavengers in the radiolysis of hydrocarbon solutions. A large number of studies on these subjects have been carried out by various experimental methods. These methods may be classified into two categories: physical and chemical methods. Physical methods were applied to measurements of the free-ion yield[1-4] and, to a much lesser extent, the total ion-pair yield,[5,6] and the mobility of electrons.[4,7-11] The physical methods are undoubtedly the useful ones for studies of the free-ion yield and the electron mobility in liquid hydrocarbons. Chemical methods are more common approaches to studies of the total ion-pair yield and the reactivity of electrons in the radiolysis of hydrocarbon solutions. The current status of knowledge on electron scavenging processes in hydrocarbon solutions has been summarized in a recent article.[12] Various electron scavengers have been used for the studies of electron scavenging processes in a variety of hydrocarbon solutions. Nitrous oxide is known as one of the most common electron scavengers, which gives nitrogen as a result of electron scavenging processes.[13] It has been noted, however, that the nitrogen yields observed at high solute concentrations are too high to give the yields of scavenged electrons and indicate that some additional effects which involve secondary reactions are also present.[14-16] A quantitative treatment[13] of this subject has recently been made in terms of an empirical model developed by Schuler and coworkers.[17] The ion-pair yields in γ-irradiated cyclohexane,[18,19] *n*-hexane,[19] and 2,2,4-trimethylpentane[20] were determined by the quantitative studies of electron scavenging processes in the hydrocarbon solutions of alkyl halides. These studies made it possible to determine with considerable accuracy the yields of free and geminate ions. Perfluorocyclohexane was also used for determination of the ion-pair yields in the radiolysis of cyclohexane solutions.[21]

In a previous study[22] we have shown that bromobenzene can be used as an efficient electron scavenger in the radiolysis of hydrocarbons. In subsequent work[23] we have determined the ion-pair yields in liquid methylcyclohexane (MCH) and in glassy MCH and MCH–cyclopentane mixtures. In the present work we have extended such studies with bromobenzene as an electron scavenger to nine liquid alkanes and have determined the ion-pair yields and the reactivity parameters for electron scavenging in these alkanes. The ion-pair yields obtained are compared with the previously reported values for some of the same alkanes in the gaseous and liquid states. The ranges of electrons in the alkanes studied in this work are also calculated based on a model in which a simple exponential distribution is assumed for initial electron–positive ion separation distances.

Experimental Section

Bromobenzene (Nakarai Kagaku research grade) was distilled and passed through a column of activated alumina. Cyclohexane, *n*-hexane, cyclopentane, *n*-pentane, *n*-octane, 2,2-dimethylbutane, 2,3-dimethylbutane, and 2,2,4-trimethylpentane were obtained from Tokyo Kagaku Seiki Co. and 3-methylpentane from Nakarai Kagaku Co. They were the purest commercially available reagents and were purified by passage through a column of activated silica gel.

The samples containing the desired amount of bromobenzene were degassed by freeze–pump–thaw cycles. The samples were sealed off the vacuum line and irradiated at 23° with ^{60}Co γ rays at a nominal dose rate of 5.1×10^{19} eV g^{-1} hr^{-1} as determined by Fricke dosimeter. The dose absorbed in the samples, 9.6×10^{18} eV g^{-1}, was determined by correction for the appropriate electron density differences. Consumption of bromobenzene during γ irradiation was less than 5% of its initial amount in the samples. The benzene produced from bromobenzene was measured by a Hitachi K53 gas chromatograph with a flame ionization detector.

Results and Discussion

A fraction of the electrons produced by γ irradiation in liquid hydrocarbons containing bromobenzene are captured by bromobenzene to yield bromide anions and phenyl radicals. The phenyl radical thus produced immediately abstracts a hydrogen atom from a solvent molecule (RH) to form a benzene molecule and a solvent radical (R).

$$RH \longrightarrow RH^+ + e^- \quad (1)$$

$$C_6H_5Br + e^- \longrightarrow C_6H_5 + Br^- \quad (2)$$

$$C_6H_5 + RH \longrightarrow C_6H_6 + R \quad (3)$$

If the benzene is produced from the bromobenzene with unit efficiency in the electron scavenging process, it is anticipated that the concentration dependence of the yield of benzene is well described by[17]

$$\frac{1}{G(C_6H_6) - G_{fi}} = \frac{1}{G_{gi}} + \frac{1}{G_{gi}\alpha^{1/2}} \frac{1}{[C_6H_5Br]^{1/2}} \quad (I)$$

where G_{fi} and G_{gi} represent the yields of free and geminate ions, respectively, $[C_6H_5Br]$ is the concentration of bromobenzene, and α is a parameter which represents the reactivity of the electron toward the solute relative to the recombination processes.

Figure 1 illustrates a plot of $[G(C_6H_6) - G_{fi}]^{-1}$ *vs.* $[C_6H_5Br]^{-1/2}$ for 2,3-dimethylbutane, which shows that the data correspond well to the predicted dependence. To avoid complications which might arise from the possible positive charge transfer from the solvent to the solute, the concentration of bromobenzene was limited to about 0.1 *M*, below which the positive charge transfer is expected to be ineffective compared with electron scavenging as is the case with methylcyclohexane.[22] Since it was difficult to reliably measure the free-ion yield by our conventional analytical technique, the values of G_{fi} from Schmidt and Allen[1] were used in making the above plots. The geminate-ion yields and the total ion-pair obtained in this way are given in Table I. The estimated standard deviations in G_{gi} or G_t are about ±0.2 except for cyclopentane, 3-methylpentane, and 2,2,4-trimethylpentane where the standard deviations amount to ±0.3. The values of the parameter α are also given in Table I. The values of α are about the same for most of the alkanes studied, but those for the pentanes are significantly higher.

Ion-Pair Yield. Table II summarizes the total ion-pair yields in the alkanes in the gas and liquid phases. The values of G_t, which are given in Table II as determined by physical methods, were calculated from the corresponding *W* values.[24-26] In gases, the *W* value can be determined accurately by measurement of the saturation current induced by ionizing radiation. Recently an attempt has been made to determine the *W* value in liquid alkanes by measurement of the ionization current induced by ^{60}Co γ rays.[6] The data were analyzed by the use of Jaffe's theory to obtain the *W* value. The values of G_t obtained in this way are in general agreement with the gas-phase values. It is questionable, however, to interpret the sequence of events in liquids following ionization by γ rays in terms of Jaffe's theory which is based on the columnar model of ion recombination, although it may be applicable to such high LET radiation as α rays.

At the present time, chemical methods are more practical and probably more reliable for measurement of the total ion-pair yield in liquids. Various electron scavenging techniques have been used by a number of investigators with a variety of electron scavengers.[12] The values of G_t for cyclohexane and *n*-hexane obtained in the present work are in agreement with the previously reported values[18,19] within experimental error. However, our value of G_t for 2,2,4-trimethylpentane is somewhat lower than that in ref 20. This difference in G_t is due to that in G_{gi} between the two studies. The present results indicate that the total ion-pair yields in liquid alkanes at 23° do not differ very much from a value of 4 and the gas-phase values.

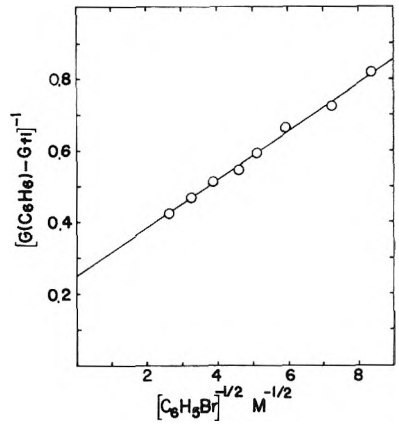

Figure 1. Plot of eq I: bromobenzene solutions in 2,3-dimethylbutane.

TABLE I: Ion-Pair Yields and the Reactivity Parameter for Electron Scavenging in γ-Irradiated Alkane Solutions of Bromobenzene at 23°

Compound	G_{fi}[a]	G_{gi}	G_t	α, M^{-1}
n-Pentane	0.145	3.7	3.8	23.6
Cyclopentane	0.155	3.8	4.0	23.0
n-Hexane	0.131	4.0	4.1	12.1
Cyclohexane	0.148	4.0	4.1	10.6
3-Methylpentane	0.146	4.0	4.1	13.5
2,3-Dimethylbutane	0.192	4.0	4.2	13.7
2,2-Dimethylbutane	0.304	4.0	4.3	13.4
2,2,4-Trimethylpentane	0.332	4.1	4.4	13.3
n-Octane	0.124	4.1	4.2	12.7

[a] Reference 1.

TABLE II: Comparison of the Total Ion-Pair Yields in Gaseous and Liquid Alkanes Irradiated with Different Types of Ionizing Radiation and as Determined by Physical and Chemical Methods

	Chemical method			Physical method	
	Liquid phase			Gas phase	
	γ Rays			β Rays	α Rays
Compound	I[a]	II[b]	III[d]	IV[e]	V[g]
n-Pentane	3.8			4.38, 4.26[f]	
Cyclopentane	4.0				3.94
n-Hexane	4.1	3.9	4.0	4.42, 4.27[f]	3.95
Cyclohexane	4.1	3.9, 4.3[c]	4.5	4.41[f]	3.99
3-Methylpentane	4.1			4.38	
2,3-Dimethylbutane	4.2			4.38	
2,2-Dimethylbutane	4.3			4.37	
2,2,4-Trimethylpentane	4.4	4.8	4.5		
n-Octane	4.2			4.37[f]	

[a] This work. [b] References 18, 19, and 20. [c] Reference 21. [d] Reference 6. [e] Reference 24. [f] Reference 25. [g] Reference 26.

Ranges of Electrons. Knowledge of the ranges of electrons is important to an understanding of radiation effects on liquids. Schmidt and Allen[1] have calculated the mean thermalization distances of electrons produced by X irradiation in a number of dielectric liquids. In this calcula-

TABLE III: Ranges of Electrons in Liquid Alkanes

Compound	b, Å		
	I[a]	II[b]	III[c]
n-Pentane	65.3	71.5	36
Cyclopentane	62.2	68.9	77
n-Hexane	58.1	67.4	42
Cyclohexane	57.5	66.1	
3-Methylpentane	61.3	69.6	50
2,3-Dimethylbutane	68.5	74.9	
2,2-Dimethylbutane	92.8	92.0	
2,2,4-Trimethylpentane	96.1	95.0	102
n-Octane	54.0	64.2	

[a] Calculated from eq II. [b] References 1. [c] Reference 27.

tion they have used the free-ion yields determined by the clearing field method and a total ion-pair yield of 4.3, and assumed a Gaussian distribution for electron thermalization distances. Holroyd, Dietrich, and Schwarz[27] have determined the ranges of photoinjected electrons in liquid hydrocarbons by measurements of the current efficiency of liquid-filled phototubes and analysis of the data in terms of a diffusion model. Since Holroyd's work concerns low-energy electrons, their values of electron ranges can not be compared directly to those of Schmidt and Allen. Nevertheless, a correlation is seen between the two sets of values, showing that most of the range of hot electrons is attained while the electron is in the epithermal energy region.[28] Recently, Abell and Funabashi[29] have shown that a simple exponential distribution of electron thermalization distances can satisfactorily account for recent experiments on electron scavenging and the effect of electric field strength on free-ion yields in some of alkanes. So we have attempted to calculate the electron ranges in the alkanes studied in the present work by the application of Abell and Funabashi's treatment.

The values of the parameter b, which is a measure of the mean range of electrons, were found numerically from eq II.[29]

$$4\pi \int_a^\infty \exp(-r_c/r) f(r,b) r^2 \, dr = G_{fi}/G_i \qquad \text{(II)}$$

$$f(r,b) = (C/r^2) \exp(-r/b)$$

where r_c is the Onsager length, $r_c = e^2/\epsilon kT$, in which the symbols have their usual meanings, and where C is a normalization constant. The reaction radius a was taken to be 5 Å.[29] The values of b obtained in this manner are shown in Table III along with those of Schmidt and Allen[1] and of Holroyd, *et al.*[27] It can be seen in Table III that most of the b values obtained with a simple exponential distribution for electron thermalization distances are somewhat smaller than those obtained with a Gaussian distribution. However, the b values for 2,2-dimethylbutane and 2,2,4-trimethylpentane are very close to each other. The b values determined by Holroyd, *et al.*, appear to be more dispersed from compound to compound than the values of b mentioned above.

At this point, it is interesting to compare the relative b values derived from the Nernst-Einstein relationship with those from Table III. It has been shown that the parameter α is given by

$$\alpha = k_s/\lambda \qquad \text{(III)}$$

where k_s is the rate constant for electron scavenging and λ is a constant for a given solvent and represents the rate of

TABLE IV: Relative Ranges of Electrons in Liquid Alkanes

Compound	b/b_{Hx}				
	I[a]	II[b]	III[c]	IV[d]	V[e]
n-Pentane	1.12	1.06	0.86	1.26	1.39
Cyclopentane	1.07	1.02	1.83	1.22	1.86
n-Hexane	1.00	1.00	1.00	1.00	1.00
Cyclohexane	0.99	0.98		0.94	1.17
3-Methylpentane	1.06	1.03	1.19	1.03	
2,3-Dimethylbutane	1.18	1.11		1.04	
2,2-Dimethylbutane	1.60	1.37		1.03	2.25
2,2,4-Trimethylpentane	1.65	1.41	2.43	1.02	2.11
n-Octane	0.93	0.95		1.01	

[a] Calculated from b(I) in Table III. [b] Calculated from b(II) in Table III. [c] Calculated from b(III) in Table III. [d] Calculated from eq VI. [e] Calculated from eq VII. The values of the electron mobility were taken from ref 7.

recombination of geminate electron–positive ion pairs.[30] If the Nernst-Einstein relationship applies to the recombination of the geminate ion pairs, λ can be expressed as[20]

$$\lambda = 3(D_e + D_+) r_c/b^3 \qquad \text{(IV)}$$

where D_e and D_+ are the diffusion coefficients of the electron and the positive ion, respectively. If the reaction of the electron with a solute is diffusion-controlled and D_e is much greater than D_+, α can be expressed as

$$\alpha = 4\pi R b^3/3r_c \qquad \text{(V)}$$

where R is the reaction radius. Taking a constant value of R for different solvents x and y, one obtains

$$\frac{b_x}{b_y} = \left[\frac{(\alpha r_c)_x}{(\alpha r_c)_y}\right]^{1/3} \qquad \text{(VI)}$$

Recently, Beck and Thomas[31] have found that the rate constant for reaction of the electron with biphenyl is proportional to the square root of the electron mobility in several alkanes. If one uses this relationship between the rate constant k_s and the mobility μ_e of the electron, one gets

$$\frac{b_x}{b_y} = \left[\frac{(\alpha r_c \sqrt{\mu_e})_x}{(\alpha r_c \sqrt{\mu_e})_y}\right]^{1/3} \qquad \text{(VII)}$$

Thus, one can calculate the relative values of b from eq VI or VII with known values of α, r_c and μ_e. The relative b values of electrons in alkanes are given in Table IV as b/b_{Hx}, where b_{Hx} is the b value for *n*-hexane.

It is seen in Table IV that there is a fairly good correlation between the relative b values calculated from eq VI and those calculated from b(I) or b(II) in Table III for *n*-pentane, cyclopentane, *n*-hexane, cyclohexane, and 3-methylpentane. However, there is no such correlation for branched alkanes such as 2,3-dimethylbutane, 2,2-dimethylbutane, and 2,2,4-trimethylpentane. For these branched alkanes the relative b values calculated from eq VI are much smaller than those calculated from b(I) or b(II) in Table III. The use of eq VII gives much larger values of b/b_{Hx} for the branched alkanes and yields a qualitative correlation between the two sets of values, although it also makes the correlation found with eq VI for some of the alkanes worse. It is interesting to note that the relative b values calculated from eq VII are in reasonable agreement with those calculated from b(III) in Table III.

References and Notes

(1) W. F. Schmidt and A. O. Allen, *J. Phys. Chem.*, **72**, 3720 (1968).
(2) P. H. Tewari and G. R. Freeman, *J. Chem. Phys.*, **49**, 4394 (1968).
(3) M. G. Robinson, P. G. Fuochi, and G. R. Freeman, *Can. J. Chem.*, **49**, 3657 (1971).
(4) P. G. Fuochi and G. R. Freeman, *J. Chem. Phys.*, **56**, 2333 (1972).
(5) W. F. Schmidt, *Radiat. Res.*, **42**, 73 (1970).
(6) T. Nakayama and M. Kawano, *Appl. Phys.*, **40**, 358 (1971).
(7) W. F. Schmidt and A. O. Allen, *J. Chem. Phys.*, **52**, 4788 (1970).
(8) J.-P. Dodelet and G. R. Freeman, *Can. J. Chem.*, **50**, 2667 (1972).
(9) R. M. Minday, L. D. Schmidt, and H. T. Davis, *J. Chem. Phys.*, **54**, 3112 (1971).
(10) R. M. Minday, L. D. Schmidt, and H. T. Davis, *J. Phys. Chem.*, **76**, 442 (1972).
(11) W. F. Schmidt and G. Bakale, *Chem. Phys. Lett.*, **17**, 617 (1972).
(12) R. H. Schuler and P. P. Infelta, *J. Phys. Chem.*, **76**, 3812 (1972).
(13) P. P. Infelta and R. H. Schuler, *Int. J. Radiat. Phys. Chem.*, **5**, 41 (1973), and the references cited therein.
(14) S. Sato, R. Yugeta, K. Shinsaka, and T. Terao, *Bull. Chem. Soc. Jap.*, **39**, 156 (1966).
(15) J. M. Warman, K.-D. Asmus, and R. H. Schuler, *Advan. Chem. Ser.*, **No. 82**, 25 (1968).
(16) Y. Hatano, K. Takeuchi, and S. Takao, *J. Phys. Chem.*, **77**, 586 (1973).
(17) See ref 12 and the references cited therein.
(18) J. M. Warman, K.-D. Asmus, and R. H. Schuler, *J. Phys. Chem.*, **73**, 931 (1969).
(19) J. M. Warman and S. J. Rzad, *J. Chem. Phys.*, **52**, 485 (1970).
(20) S. J. Rzad and K. M. Bansal, *J. Phys. Chem.*, **76**, 2374 (1972).
(21) N. H. Sagert, J. A. Reid, and R. W. Robinson, *Can. J. Chem.*, **47**, 2655 (1969).
(22) T. Kimura, K. Fueki, and Z. Kuri, *Bull. Chem. Soc. Jap.*, **43**, 3090 (1970).
(23) T. Kimura, K. Fueki, and Z. Kuri, *Bull. Chem. Soc. Jap.*, **44**, 2650 (1971).
(24) T. A. Stoneham, D. R. Ethridge, and G. G. Meisels, *J. Chem. Phys.*, **54**, 4054 (1971).
(25) P. Adler and H. K. Bothe, *Z. Naturforsch.*, **20a**, 1700 (1965).
(26) L. M. Hunter and R. H. Johnsen, *J. Phys. Chem.*, **71**, 3228 (1967).
(27) R. A. Holroyd, B. K. Dietrich, and H. A. Schwarz, *J. Phys. Chem.*, **76**, 3794 (1972).
(28) A. Mozumder and J. L. Magee, *J. Chem. Phys.*, **47**, 939 (1967).
(29) G. C. Abell and K. Funabashi, *J. Chem. Phys.*, **58**, 1079 (1973).
(30) S. J. Rzad, P. P. Infelta, J. M. Warman, and R. H. Schuler, *J. Chem. Phys.*, **52**, 3971 (1970).
(31) G. Beck and J. K. Thomas, *J. Chem. Phys.*, **57**, 3649 (1972).

Electron Reactions in Aqueous Concentrated Acid Solutions

O. I. Micić,* V. Marković, and D. Nikolić

Boris Kidrič Institute of Nuclear Science, Vinča, Yugoslavia

(Received December 12, 1972)

Competition between some organic compounds (glycine, acetic acid, propionic acid, and acetone) and hydronium ion for hydrated electrons in γ-irradiated aqueous concentrated acid solution has been studied. These compounds show an ability to reduce the initial yield of the hydrated electron without any direct correlation with the corresponding hydrated electron rate constants. The results are discussed taking into account the protonation effects, the time dependence of the rate constants, and the possibility of reaction with a hydrated electron precursor. They support the idea that radiation-produced electrons react before hydration.

Introduction

Hunt, *et al.*,[1-3] have discovered by pulse radiolysis technique at the picósecond time scale a significant decrease in the hydrated electron yield in the presence of high concentrations of some solutes (acetone, nitrate ion, hydrogen peroxide, glycine, etc.). Known rate constants of these solutes for reactions with e_{aq}^- could not fit the observations. Therefore, they concluded that (i) these solutes react with the precursor of e_{aq}^-, so called dry electron (e_{dry}^-), according to the model suggested by Hamill[4,5] and (ii) that the reaction rates of these solutes with e_{dry}^- are significantly faster than the corresponding rates of the reactions with e_{aq}^-.

Schwarz[6] argued against these conclusions pointing out that the time dependence of rate constants for diffusion-controlled reactions and reactions between charged species may be responsible for the observed e_{aq}^- yield decrease.

The experiments of Hunt, *et al.*, were usually performed in the presence of high concentrations of $HClO_4$. Taking into account protonation of organic compounds at high acidities and expected increase in reactivity toward e_{aq}^- due to protonation, Hayon[7] also cast some doubts on these conclusions. He claims that some of the observed decrease in e_{aq}^- yield at the end of a 20-psec electron pulse may be due to higher reactivity of protonated organic compounds toward e_{aq}^-.

We used the method of steady-state kinetics to investigate this problem from another approach. Solutes with different protonation constants were chosen (glycine, acetone, acetic acid, and propionic acid) and the effect of concentration of the solute and the hydronium ion on the molecular hydrogen yield was studied. These experiments were expected to give more information about the role of protonation and hydration on the possibility of scavenging electrons in aqueous concentrated acid solutions.

Experimental Section

The organic compounds were AR Merck and were used without purification. Double distilled $HClO_4$ was used as supplied by F. Smith Co. Water was triply distilled. The pH of the solutions and the ionic strength were adjusted with $HClO_4$ and $NaClO_4$, respectively.

Irradiations were carried out in a ^{60}Co gamma source at an absorbed dose rate of the order of 5 krads min^{-1}. Total absorbed doses were between 1.6 and 8 krads. They were

determined by a Fricke dosimeter. Solutions were deaerated on a vacuum line or by bubbling with argon stated to contain about 2 ppm of oxygen, obtained from Tehnogas. Acetone concentration in the solution was determined after this procedure by the volumetric method with iodine.[8] All absorbed doses were corrected for variation in solution composition on the basis of corresponding electron densities.

Molecular hydrogen was quantitatively measured by a Perkin-Elmer Model 154L gas chromatograph using a 4-m silica gel column at 50° and argon as the gas carrier.

Results and Discussion

Molecular hydrogen yield, $G(H_2)$, was measured as a function of $HClO_4$ concentration at varying concentrations of glycine, acetic acid, propionic acid, and acetone. The results are summarized in Figure 1. In the same figure the results obtained in pure $HClO_4$ solution are presented. All solutions contained 0.1 M ethanol as an H and OH scavenger.

The initial increase of $G(H_2)$ can be explained by competition between reactions 1 and 2 where $(SH^+)_{aq}$ repre-

$$e_{aq}^- + H_{aq}^+ \longrightarrow H \qquad (1)$$

$$e_{aq}^- + S \longrightarrow S_{aq}^- \qquad (2.1)$$

$$e_{aq}^- + (SH^+)_{aq} \longrightarrow SH \qquad (2.2)$$

sents the protonated form of the solute S. In the presence of ethanol

$$H + C_2H_5OH \longrightarrow H_2 + C_2H_4OH \qquad (3)$$

The yield of hydrogen in this systems is given by

$$G(H_2) = G_{H_2} + G_H + G(1) \qquad (4)$$

where

$$G(1) = G_{e_{aq}^-} \Big/ \left[1 + \frac{k_2}{k_1}\frac{(S_0)}{(H_{aq}^+)}\right] \qquad (5)$$

and

$$(S_0) = (S) + (SH_{aq}^+)$$

$$\alpha(1-\alpha) = (SH_{aq}^+)/(S) = K_P(H_{aq}^+)$$

$$k_2 = \alpha k_{2.2} + (1-\alpha)k_{2.1} \qquad (6)$$

where K_P and α are the constant and degree of protonation, respectively.

In Table I, $G(1)$ and k_2/k_1 values calculated from experimental results are given. $G_{H_2} + G_H = 0.7$ and $G_{e_{aq}^-} = 3.2$ were used for calculation, except for acetone where published values for $G_{H_2} + G_H$[5] were taken. In doing that, only results showing the main trend of the curves in Figure 1 are used for the calculations and are presented in Table I.

The product of the reaction 2.1 can to some extent form H_2

$$S_{aq}^- \longrightarrow H_2 \qquad (7)$$

$$S_{aq}^- \longrightarrow P \neq H_2 \qquad (8)$$

The ratio of rate constants k_7/k_8 is 0.56, 0.88, and 0.60 for glycine, acetic acid, and propionic acid, respectively.[9,10] However, in all cases $k_{2.1} \ll k_{2.2}$ as well as $k_{2.1} \ll k_1$.

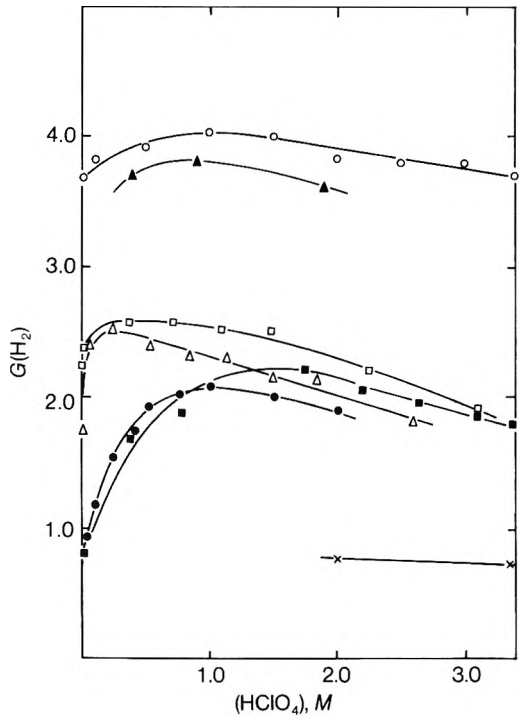

Figure 1. Molecular hydrogen yield as the function of $HClO_4$ concentration at varying solute concentrations: (○) $HClO_4$; (▲) 0.1 M glycine; (□) 3 M acetic acid; (■) 0.6 M acetone; (△) 3 M propionic acid; (●) 2 M glycine; (×) 4 M glycine.

TABLE I: Values of $G(1)$ and k_2/k_1

Solute	[S], M	$[HClO_4]$, $[H_{aq}^+]$, M	α	$G(H_2)^a$	$G(1)$	k_2/k_1
Glycine	0.1	0.5 0.40	0.99	3.70	3.00	0.28
	0.1	2.00 1.90	1.00	3.60	2.90	1.90
	2	2.40 0.42	0.99	1.73	1.03	0.44
	2	4.00 2.00	1.00	1.70	1.20	1.70
	4.0	6.00 2.01	0.99	0.76		26.15
	3.6	7.3 3.63	0.99	0.72		159
Acetone	0.57	2.0 1.74	0.45	2.19	1.84	2.28
	0.69	4.0 3.56	0.63	1.75	1.34	7.22
	1.03	0.92 0.68	0.23	1.40	1.09	1.27
	1.03	3.23 2.66	0.55	1.70	1.45	3.10
Acetic acid	3	0.50 0.36	0.05	2.56	1.86	0.09
	3	4.00 3.09	0.30	1.90	1.20	1.71
Propionic acid	3	0.50 0.26	0.08	2.52	1.82	0.07
	3	4.00 2.61	0.46	1.80	1.10	1.66

[a] Experimental values.

Therefore in the H_{aq}^+ concentration range from 0.1 to 3 M, reaction 7 did not contribute significantly to measured $G(H_2)$. H (or H_2) is not formed in reaction 2.2. For example, $G(H_2) = 0.7$ in 2 M glycine at pH 1 (Figure 1).

Another reaction had to be accounted for in these experiments, *i.e.*, the competition of the solute S with ethanol for H atoms

$$S + H \longrightarrow H_2 \qquad (9)$$

$$S + H \longrightarrow P \neq H_2 \qquad (10)$$

Glycine, acetic acid, and propionic acid react only through reaction 9[11] not influencing eq 4 and 5. Acetone, however, reacts in both ways at comparable rates.[12] There-

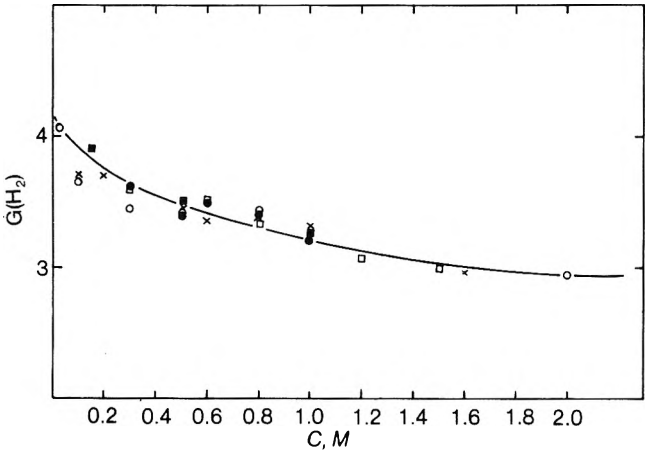

Figure 2. Molecular hydrogen yield as the function of acetic acid [(●) α = 0.06; (■) α = 0.005] anc propicnic acid [(×) α = 0.04; (□) α = 0.09; (○) α = 0.13] concentrations: 0.1–0.5 *M* $HClO_4$.

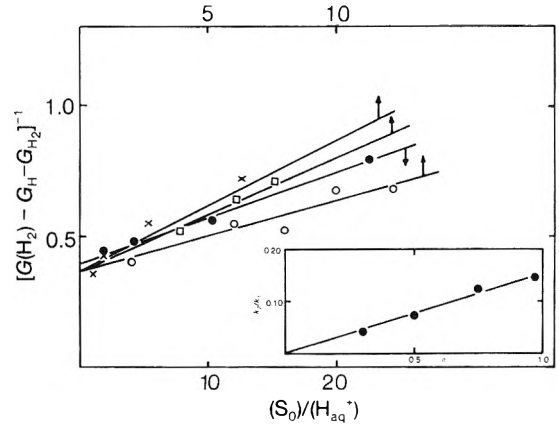

Figure 3. Competition between glycine and hydronium ions for hydrated electrons: (●) α = 0.30; (○) α = 0.50; (□) α = 0.75; (×) α = 0.96.

fore, corresponding corrections in the calculation of $G(1)$ and k_2/k_1 were made by using $k_9/k_3 = 0.068$ and $k_{10}/k_3 = 0.035$.

Figure 1 and Table I provide unambiguous evidence for incomplete scavenging of e_{aq}^- by H_{aq}^+ in the presence of high concentrations of glycine, acetic acid, propionic acid, and acetone. Furthermore, the "deficit" in e_{aq}^- yield increases with increasing solute concentration. These results obtained by steady-state radiolysis are similar to observations made by pulse radiolysis at the picosecond time scale.[2,3] The results should be analyzed taking into account protonation effects, time dependence of the rate constants, structural changes of solutions, direct action of radiation on the solute, and the possibility of the reactions with hydrated electron precursor ("dry" electron).

Time Dependence of the Rate Constants. Schwarz[6] has recently drawn attention to the effect of time needed for the formation of concentration gradients for diffusion-controlled reactions if one of the reactants, as it is the case in radiation chemistry, is formed instantaneously in the solution which contains the other reactant homogeneously distributed. As a consequence the apparent rate constants in some time interval after the start of an experiment can be different in comparison with the rate constant measured at some time later. He calculated the k_2/k_1 values for 0.6–2 *M* acetone in 0.2–2 *M* $HClO_4$, taking into account this time dependence of rate constants. These values were in agreement with the experimental results obtained by Peled and Czapski.[13] In this calculation, however, the protonation of acetone[14] has not been taken into account. This has two effects: the concentration of H_{aq}^+ is lower than assumed and consequently k_2/k_1 should be smaller than calculated, then, reaction 2.2 similar to reaction 1 occurs between oppositely charged species and $k_{2.2}$ should increase with time.

Under our experimental conditions the rate constants of reactions 1 and 2.2 are time dependent. The $k_{2.1}$ for acetone is also time dependent. Quantitative analysis of the k_2/k_1 values given in Table I has not been attempted here. However, all the results obtained indicate that the change of k_2/k_1 could not be explained by the time dependence of rate constants only. The values of k_2/k_1 increase with increasing concentration of glycine at constant H_{aq}^+ concentration which is opposite to the effect expected, since $k_{2.2}$ should decrease with increasing concentration. k_2/k_1 for other solutes changes much more drastically than might be explained by time dependence as both reactions are between species of opposite charge.

This effect is even less applicable to the results given in Figure 2. Here, neither $k_{2.1}$ nor $k_{2.2}$ are time dependent. However, significant decrease in $G(H_2)$ was observed again.

Protonation. Protonation constants of glycine, acetic acid, propionic acid, and acetone are 223, 0.14, 0.33, and 0.47, respectively.[14,15] In 0.1–2 *M* $HClO_4$ glycine is protonated completely and acetic acid only to about 30%.

The rate constant $k_{2.2} = 3.8 \times 10^9\ M^{-1}\ sec^{-1}$ was obtained from competition data at low glycine concentration at the ionic strength $\mu = 0.5$ (Figure 3) and $k_1 = 2.2 \times 10^{10}\ M^{-1}\ sec^{-1}$ ($\mu = 0$) assuming that the ionic strength effect is the same for both reactions 2.2 and 1. This value is in good agreement with $k_{2.2} = 4 \times 10^9\ M^{-1}\ sec^{-1}$ recently published.[16]

It is obvious that further increase of k_2/k_1 at higher glycine concentrations (Table I) cannot be explained by the rate of reaction 2 2.

$G(H_2)$ for acetic and propionic acids does not depend on $HClO_4$ concentrations. This is well illustrated in Figure 2. $G(H_2)$ is constant within experimental error from 0.05–0.5 *M* $HClO_4$, although in 0.5 *M* $HClO_4$ 6% of acetic acid and 14% of propionic acid are protonated. $k_{2.2} \leq 3 \times 10^9\ M^{-1}\ sec^{-1}$ is estimated from these results.

It was not possible to distinguish between reactions 2.1 and 2.2 in the case of acetone. Reaction 2.1 is considered to be diffusion controlled ($k_{2.1} = 7.6 \times 10^9\ M^{-1}\ sec^{-1}$)[3] since acetone is not a spherically symmetrical molecule. Further increase of the rate constant should not be expected, except for the electrostatic interaction factor between ions of opposite charge according to the Debye equation.[17] The value of $k_{2.2} = 1.4 \times 10^{10}\ M^{-1}\ sec^{-1}$ should be taken as the upper limit because of the opposite effect of ionic strength on the rate constant $k_{2.2}$.

Structural Changes. The rate constants can also be influenced by structural changes of the solution. Here, most important are the changes of dielectric properties, ionic strength, and viscosity. We supposed that the effect of these parameters on the $k_{2.2}/k_1$ rate constants ratio is not very significant since both reactions are of the same type.

Direct Radiation Effect. $G(1)$ should be expected to decrease at higher solute concentrations due to direct action

of radiation on the solute. This was observed in pure $HClO_4$ solution. This decrease, however, being less than 30% (4 *M* glycine, for example) could not account for the total decrease of $G(1)$.

Reactions of the Hydrated Electron Precursor. The analysis of different possible explanations for the increase of k_2/k_1 in concentrated solutions have shown that time dependence and protonation could only partially explain the observed increase. Besides, these two effects are obviously deficient in explaining the results of Figure 2. The effect observed with all solutes shows distinct regularities: the incomplete competition between reactions 1 and 2, the plateau of H_2 yield above certain $HClO_4$ concentration (Figure 1), and lowering of this plateau with the increase of solute concentrations. This can be taken as an evidence for the existence of fast reactions, faster than known reactions with hydrated electron, and reactions which could not be affected by $HClO_4$ concentration.

In similar experiments using pulse radiolysis the transient produced in the reaction of acetic acid with electron has been detected.[18] The concentration of this transient at high solute concentration could only be due to the certain limit suppressed by increasing the $HClO_4$ concentration. This limit was dependent on $HClO_4$ and acetic acid concentrations in the same way as hydrogen yield here.

These experiments, therefore, support the idea that some solutes react with the precursor of e_{aq}^- (called the "dry electron") at sufficiently high concentrations. As a consequence, the observed e_{aq}^- yields measured either directly, by pulse radiolysis, or indirectly, as in the present work, decrease significantly and more than can be explained without taking into account dry electron reactions. The results reported here support the possibility of chemical reactions of nonequilibrium electrons.

Acknowledgment. We are indebted to Dr. I. Draganić for some valuable discussions in preparing this manuscript and for continuous interest in this work. Our thanks are due to Mrs. M. Marović for technical assistance.

References and Notes

(1) M. J. Bronskill, R. K. Wolff, and J. W. Hunt, *J. Chem. Phys.*, **53**, 4201 (1970).
(2) R. K. Wolff, M. J. Bronskill, and J. W. Hunt, *J. Chem. Phys.*, **53**, 4211 (1970).
(3) J. E. Aldrich, M. J. Bronskill, R. K. Wolff, and J. W. Hunt, *J. Chem. Phys.*, **55**, 530 (1971).
(4) W. H. Hamill, *J. Phys. Chem.*, **73**, 1341 (1969).
(5) T. Sawai and W. H. Hamill, *J. Phys. Chem.*, **74**, 3914 (1970).
(6) H. A. Schwarz, *J. Chem. Phys.*, **55**, 3647 (1971).
(7) E. Hayon, *Nature (London), Phys. Sci.*, **238**, 76 (1972).
(8) I. M. Kolthoff and P. J. Elving, "Treatise on Analytical Chemistry," Interscience, New York, N. Y., 1966, p 189.
(9) R. L. Willix and W. M. Garrison, *Radiat. Res.*, **32**, 452 (1967).
(10) O. I. Mičić and V. Marković, *Int. J. Radiat. Phys. Chem.*, **4**, 43 (1972).
(11) P. Neta, R. W. Fessenden, and R. H. Schuler, *J. Phys. Chem.*, **75**, 1655 (1971).
(12) P. Neta, G. R. Holdren, and R. H. Schuler, *J. Phys. Chem.*, **75**, 449 (1971).
(13) E. Peled and G. Czapski, *J. Phys. Chem.*, **75**, 3626 (1971).
(14) C. F. Wells, *Trans. Faraday Soc.*, **63**, 147 (1967).
(15) R. M. Keefer and M. G. Reiber, *J. Amer. Chem. Soc.*, **63**, 689 (1941).
(16) F. A. Peter and P. Neta, *J. Phys. Chem.*, **76**, 630 (1972).
(17) P. Debye, *Trans. Electrochem. Soc.*, **82**, 265 (1942).
(18) B. Cerček and O. I. Mičić, *Nature (London), Phys. Sci.*, **238**, 76 (1972).

The Interaction between Halide Ions and Amphiphilic Organic Cations in Aqueous Solutions Studied by Nuclear Quadrupole Relaxation

Göran Lindblom* and Björn Lindman

Division of Physical Chemistry 2, The Lund Institute of Technology, Chemical Center, S-220 07 Lund 7, Sweden
(Received April 9, 1973)

Publication costs assisted by The Lund Institute of Technology

The nuclear quadrupole relaxation rates of $^{81}Br^-$ and $^{35}Cl^-$ counterions in aqueous solutions of cationic surfactants have been determined as a function of surfactant concentration, temperature, surfactant end group, and the length of the surfactant ion. A moderate increase in the relaxation rates at low concentrations is attributed to an enhanced anion–solvent interaction in the vicinity of the nonpolar groups of the cations. As micellar aggregates form, the counterion relaxation rates increase rapidly. By use of a simple model for micelle formation, critical micelle concentrations are determined from the concentration dependences of the relaxation rates. On the assumption that it is sufficient to consider one type of counterions bound to the micelles, intrinsic relaxation rates of the micellarly bound counterions are calculated. These intrinsic relaxation rates show that halide ions interact more strongly with micelles composed of alkylammonium ions than with those formed by alkyltrimethylammonium ions. The observed relaxation behavior is compared with that expected for various motional processes and it appears that the quadrupole relaxation is affected by the motion of water molecules. Upper limits of the time constants of the motion have been estimated. A smaller relative change in relaxation rate on micelle formation for $^{35}Cl^-$ than for $^{81}Br^-$ is ascribed to differences in ionic radii. In addition to the changes in counterion binding at the critical micelle concentrations a second change occurs at higher concentrations for some of the surfactants. This change in counterion binding to the micelles occurs at considerably lower concentrations for alkylammonium bromides than for alkyltrimethylammonium bromides.

Introduction

The interaction between anions and positively charged nitrogens is of importance in many biological systems and also in connection with some other phenomena in aqueous colloid solutions such as counterion binding to polycations and micellar catalysis. An important biological situation where this interaction is significant concerns the surfaces of biological membranes. Using proton nmr, Jendrasiak[1] was recently able to establish a strong interaction between certain small anions and the choline group for aqueous vesicular solutions of egg yolk lecithin. The binding of anions to nonmetallic proteins occurs *via* positively charged side chains in the amino acid sequence and it is interesting to note that there may be a close neighborhood of positively charged groups and hydrophobic side chains in the anion binding site of proteins. Thus recent work has shown that for serum albumin the binding sites for hydrophobic anions contain lysine and arginine as well as apolar amino acids.[2-5] It may, furthermore, be concluded from nmr studies[6,7] on aqueous serum albumin solutions that bromide and chloride ions have binding sites in common with hydrophobic anions such as anionic surfactants.

These and other examples motivate studies aimed at obtaining a better understanding of the mode of interaction between anions and positively charged nitrogens and in particular it would be desirable to establish how this interaction depends on the proximity of other charged, dipolar, or nonpolar groups. A very sensitive way of studying how certain small ions interact with other species in a solution is to study the nuclear quadrupole relaxation rate. We have previously applied this method to studies of the interaction between halide ions and substituted ammonium ions which can serve as simple models for anion binding sites in proteins.[8-10] These investigations were concerned with the interactions between halide ions and organic cations having alkyl chains so short that the solutions are mainly molecule-disperse. In the present study we have examined aqueous solutions containing substituted ammonium ions with long alkyl chains by ^{81}Br nmr and to some extent by ^{35}Cl nmr. First, the halide quadrupole relaxation data will provide information on how the anion–cation interactions are modified on cation self-association. Secondly, by investigating how the counterion quadrupole relaxation rate varies with the end group of the surfactant, some information on the mode of attachment of counterions to micellar aggregates is obtained. Due to the rather low sensitivity of ^{81}Br and ^{35}Cl nmr, the alkyl chain lengths were in most cases chosen so as to give critical micelle concentrations of the order of 0.1 *M*. Previously, we have investigated the interaction between bromide ions and a long chain surfactant incorporated in different types of aggregates[11-13] (normal and reversed micelles and hexagonal and lamellar mesophases).

Experimental Section

The ^{81}Br measurements were performed with a Varian V-4200 nmr spectrometer as described elsewhere.[9,10] The modulation frequency and the modulation amplitude settings were chosen[9,10] so that the instrumental broadening was less than 1%. For the bromine signals, the line widths were taken as the distance between maximum and minimum slopes of the nmr absorption curve. In order to improve the stability of the magnetic field a flux stabilizer was used when recording the rather narrow ^{35}Cl nmr sig-

nals. Here the line width was taken as the width at half-height of the absorption peak. The ^{35}Cl nmr signals were studied using a field modulation frequency of 400 Hz and the first side band of the absorption signal was recorded. Due to the inhomogeneity of the magnetic field the measured ^{35}Cl line widths are slightly too large. For the data given in Figure 4 no correction for this inhomogeneity, which was determined to be about 2 μT, has been applied, whereas the effect of the inhomogeneity broadening was eliminated when the quantities given in Table II were calculated. The sample temperature was 28 ± 2° if not otherwise specified. In the variable temperature studies sample temperature was controlled by means of a Varian V-4540 instrument. The actual temperature was measured with a copper–constantan thermocouple before and after the recording of each series of spectra at a given temperature and was found to be accurate within ±0.3°. In the determinations of the frequency dependence of the line widths, the sample temperature was stabilized at 32°.

Decyltrimethylammonium bromide, tetradecyltrimethylammonium bromide, cetyltrimethylammonium bromide, and octyltrimethylammonium chloride were purchased from The British Drug Houses, Ltd., Poole, England. Nonyltrimethylammonium bromide was obtained from Eastman Kodak, Rochester, N. Y. Nonylammonium bromide, decylammonium bromide, and octylammonium chloride were prepared by reaction of the appropriate amine with the hydrogen halide. All the ammonium salts were recrystallized twice from acetone. The amines were obtained from Fluka AG, Buchs, Switzerland. Decylpyridinium bromide was prepared by refluxing 1-bromodecane and dry pyridine and recrystallizing from acetone (*cf.* ref 14). For some of the surfactants the purity was determined by titration with $AgNO_3$. The purity was found to be better than 99%.

Experimental Results

For a number of amphiphilic ammonium halides the dependence of counterion quadrupole relaxation rate on surfactant concentration was investigated in a wide concentration region at 28°. The salts investigated were: nonylammonium bromide (NAB), decylammonium bromide (DAB), nonyltrimethylammonium bromide (NTAB), decyltrimethylammonium bromide (DTAB), tetradecyltrimethylammonium bromide (TTAB), hexadecyltrimethylammonium bromide (CTAB), decylpyridinium bromide (DPB), octylammonium chloride (OAC), and octyltrimethylammonium chloride (OTAC).

For the compounds having up to ten carbon atoms in the long alkyl chain, measurements could be made well below the critical micelle concentration (cmc). A general observation is that below the cmc the counterion nmr line width increases moderately with surfactant concentration whereas in the high concentration region the line widths increase much more rapidly with increasing concentration. This behavior is exemplified in Figure 1 for NAB and NTAB. An interesting observation is that below the cmc greater line widths are obtained with NTAB than with NAB, whereas above the cmc the reverse behavior is found. A corresponding dependence of counterion nmr line width on surfactant end group is found when the results for DTAB are compared with those obtained for DAB or when the results for OTAC are compared with those for OAC. DPB gives line widths intermediate between those of DTAB and DAB at low concentrations whereas at high concentrations it gives line widths about the same as those for DTAB.

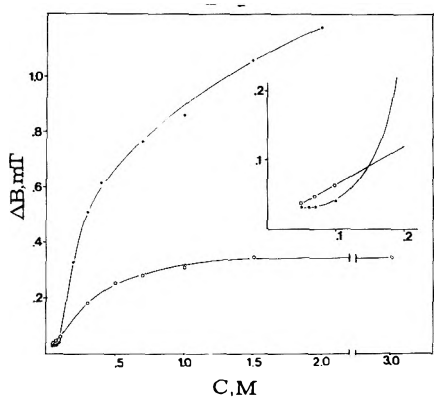

Figure 1. The ^{81}Br nmr line width, ΔB (in mT), as a function of the surfactant concentration for aqueous nonyltrimethylammonium bromide (O) and nonylammonium bromide (●) solutions. Inserted is shown the low-concentration region. Temperature 28°.

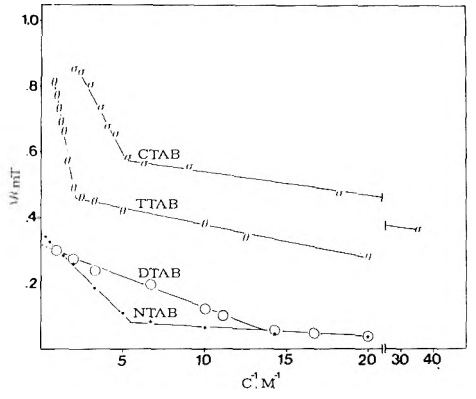

Figure 2. The ^{81}Br nmr line width, ΔB (in mT), as a function of the inverse surfactant concentration for four alkyltrimethylammonium bromides. The different lengths of the carbon chains of the surfactant salts are nonyl (●), decyl (O), tetradecyl (θ), and cetyl (σ). Temperature 28°.

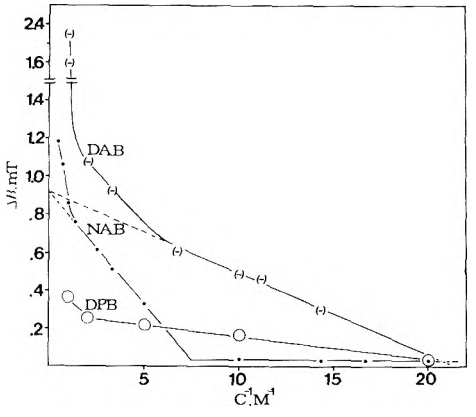

Figure 3. The ^{81}Br nmr line width, ΔB (in mT), as a function of the inverse concentration of nonylammonium bromide (●), decylammonium bromide (θ), and decylpyridinium bromide (O). Temperature 28°.

In Figures 2–4 we give the concentration dependences of the observed counterion nmr line widths for the different compounds investigated. In order to faciliate a comparison with a simple model of micelle formation (see below) the line widths are given as a function of the inverse surfactant concentration. The temperature dependence of the

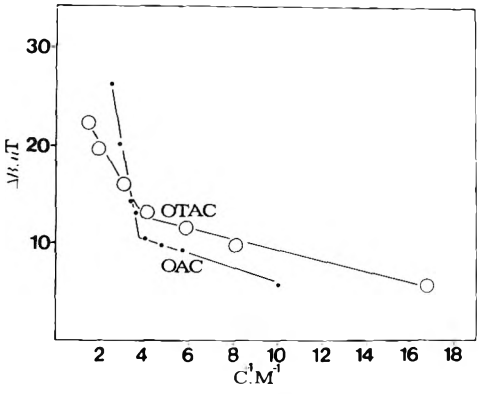

Figure 4. The ^{35}Cl nmr line width, ΔB (in μT), as a function of the inverse concentration of octyltrimethylammonium chloride (O) and octylammonium chloride (●). Temperature 28°.

line width was investigated for a 0.5 *M* NAB solution and a 1.0 *M* NTAB solution. The temperature range studied was 33–72°. In both cases the line width was found to decrease rapidly with increasing temperature. Apparent energies of activation of the relaxation process obtained from an Arrhenius plot (Figure 4) were calculated to be 26 ± 2 kJ mol^{-1} and 17 ± 2 kJ mol^{-1} for the NAB and NTAB solutions, respectively. (The accuracy of the activation energies was estimated from the accuracy of the measurements.) An investigation of the frequency dependence of the line width for a 1.5 *M* NTAB solution showed that the line width within the experimental error is independent of the resonance frequency between 8 and 16 MHz.

Discussion

For ^{81}Br and ^{35}Cl with spin quantum numbers $I = 3/2$ the dominant nuclear magnetic relaxation mechanism in solution is due to the interaction between the nuclear electric quadrupole moment and fluctuating electric field gradients at the nucleus. Under conditions of extreme narrowing the quadrupole relaxation rates for a nucleus with $I = 3/2$ are given by[15]

$$\frac{1}{T_1} = \frac{1}{T_2} = \frac{1}{10}\left(\frac{e^2qQ}{\hbar}\right)^2 \tau_c \qquad (1)$$

Here T_1 and T_2 are the longitudinal and transverse relaxation times, respectively, eq is the largest component of the electric field gradient tensor (the gradient is assumed to have cylindrical symmetry) taken in its principal axes system, eQ is the nuclear electric quadrupole moment, and τ_c is the correlation time which characterizes the time dependence of the interaction. The line width for Lorentzian-type signals is given by (in magnetic units)

$$\Delta B = \frac{2}{\sqrt{3}\gamma T_2} \qquad (2)$$

or

$$\Delta B = \frac{2}{\gamma T_2} \qquad (3)$$

Equation 2 refers to the case where the line width is measured between inflection points of the absorption curve (^{81}Br) and eq 3 to the case where the line width is measured at half-height of the absorption curve (^{35}Cl).

In solutions containing large aggregates, such as micelles, slow motional processes may be expected and, therefore, the validity of the extreme narrowing condition, *i.e.*, $\omega\tau_c \ll 1$, ω being the Larmor precession frequency, must be carefully examined. In the nonextreme narrowing case for spin 3/2 nuclei relaxation is nonexponential and the nmr spectrum consists of two component signals with different line widths. (The relaxation of spin 3/2 nuclei in the nonextreme narrowing case is treated in ref 16–18.) The narrow peak corresponds to 40% of the total intensity and is determined by motion for which $\omega\tau_c < 1$ whereas the broad component is determined by slower motion. If $\omega\tau_c \simeq 1$, $T_1 \neq T_2$ and the line width varies with the magnetic field strength. To investigate which situation is appropriate in the present case some investigations of the signal intensity and the frequency dependence of the line width were performed. As was described above, no frequency dependence of the line width for a fairly concentrated NTAB or CTAB solution[13] could be detected. We also measured the signal intensity of the ^{81}Br nmr signal for a 0.5 *M* CTAB solution.[13] It was found that this signal has the same integrated intensity as the ^{81}Br signal from a 0.5 *M* NaBr aqueous solution. From these experimental results it appears that there is no motion with $\omega\tau_c \simeq 1$, which contributes to the relaxation rate and that the ^{81}Br nmr signal contains only one component.

The observations accounted for above imply that the relaxation is adequately described by eq 1 and that all the transitions between the different nuclear spin states contribute to the observed nmr signal. With several types of halide binding sites in the solutions eq 1 gives the line width characteristic of a particular site whereas the observable relaxation rate will be a composite of the relaxation behavior in the different sites. If the halide ions are exchanging between the various sites much more rapidly than the relaxation the observable line width is given by

$$\Delta B_{obs} = \sum_i p_i \Delta B_i \qquad (4)$$

Here p_i is the fraction of halide ions occupying sites of type i and ΔB_i is the corresponding intrinsic line width. The applicability of eq 4 was, as in our previous studies, investigated by studying the temperature dependence of the line width and by a comparison of the ^{79}Br and ^{81}Br quadrupole relaxation rates. The rapid decrease in line width with increasing temperature (see Figure 5) implies that eq 4 is valid. The ratio $\Delta B(^{79}Br)/\Delta B(^{81}Br)$ was observed to be about 1.6 for a 1.5 *M* NTAB and a 1.0 *M* DTAB solution. This value is close to that expected for rapid exchange (*cf.* ref 19).

If we start by considering the experimental counterion relaxation data obtained at submicellar concentrations a striking observation is that the counterion nmr line widths also at low concentrations are markedly dependent on surfactant concentration. Thus the halide ions interact with the cations even in the absence of micelle formation. It can be inferred from the experimental data (for example, Figure 1) that the quadrupole relaxation of $^{81}Br^-$ at low concentrations is more effective for NTAB and DTAB than for NAB and DAB. From our previous studies[8-10] it can be inferred that this interaction is not an ion-pair formation with the normal meaning of this concept nor is it necessary to invoke a formation of so-called pre-micellar aggregates to explain these findings. Thus the same effect is obtained for considerably smaller organic cations where cation–cation association is unlikely to occur.[8,9] Instead, it appears that the explanation is that the nonpolar groups exert a structure-making effect on the water lattice and that part of the anions are incorporated into the mod-

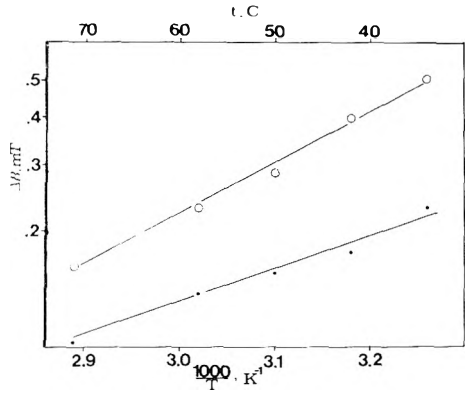

Figure 5. The ^{81}Br nmr line width, ΔB (in mT), on a logarithmic scale plotted against the inverse absolute temperature for 0.5 *M* nonylammonium bromide (O) and 1.0 *M* nonyltrimethylammonium bromide (●).

ified water structure in the vicinity of the cations.[8-10] The structure-making effect increases with increasing substitution on the nitrogen[20,21] and this explains why NTAB and DTAB solutions give greater line widths in the molecule-disperse concentration region than do NAB and DAB solutions.

The rapid increase in counterion quadrupole relaxation rate above the cmc can be referred to an attachment of part of the counterions to the micellar aggregates. (An effect of micelle formation on counterion quadrupole relaxation has been observed previously for some other surfactants.[22-24]) It is apparent from Figures 1-4 that the line-broadening obtained on micelle formation depends to a great extent on the cationic group of the surfactant. If the distribution of counterions among the different binding sites in the solutions were known we could by means of eq 4 calculate the intrinsic relaxation rate of the micellarly bound counterions. This intrinsic relaxation rate could be a useful quantity for obtaining a deeper insight into the mode of attachment of counterions to micellar aggregates.

For the description of micellization two theories are in current use, *i.e.*, the pseudo-phase separation model and the application of the law of mass action to the surfactant aggregation.[25,26] For large aggregation numbers the two models give the same results, except that in the presence of counterion dissociation a small deviation results. The aggregation numbers given by Shinoda[26] would imply that the phase separation approach could serve as a useful first approximation for the surfactants studied in the present work. We have, therefore, in order to obtain the quadrupole relaxation rates of the micellarly bound counterions employed this theory. As will be shown below, the observed concentration dependences of the counterion nmr line widths agree closely with that predicted by the theory.

Let us assume that in the micellar solutions only two types of halide ions need to be considered. One corresponds to a free ion, that is a halide ion not interacting with the micelles but only with the monomeric cations. We will refer to this by the subscript f. (The "free" ions in the sense given here correspond in fact to at least two types of halide ions, *i.e.*, halide ions not interacting at all with the surfactant and halide ions interacting with the nonassociated cations as described above for premicellar concentrations. ΔB_f is, therefore, a weighted average of the line widths of these two types of sites which, as described below, was taken into account on calculating ΔB_m from ΔB_{obs}.) The other type of halide ions would be those attached to the micelles, which are denoted by the subscript m. Equation 4 now reads if we introduce molar concentrations

$$\Delta B_{obs} = \frac{C_m}{C_t}\Delta B_m + \frac{C_t - C_m}{C_t}\Delta B_f \qquad (5)$$

Here C_m is the concentration of micellarly bound halide ions and C_t the total surfactant concentration. ΔB_f and ΔB_m are the intrinsic line widths of the two sites. Assuming now that the pseudo-phase separation model applies and that the ratio, β, of halide ions to surfactant ions in the micellar aggregates is independent of concentration we have

$$C_m = \beta(C_t - C_c) \qquad (6)$$

where C_c is the critical micelle concentration. Insertion of eq 6 into eq 5 yields

$$\Delta B_{obs} = \Delta B_f + \beta(\Delta B_m - \Delta B_f) - \frac{\beta C_c}{C_t}(\Delta B_m - \Delta B_f) \qquad (7)$$

Equation 7 holds for solutions where $C_t > C_c$ whereas below the cmc $\Delta B_{obs} = \Delta B_f$. Since the concentration dependence of ΔB_f is weak compared to the difference $\Delta B_m - \Delta B_f$ and ΔB_f varies nearly linearly with the inverse surfactant concentration our simple model should give two straight lines intersecting at the cmc if the observed line width is plotted as a function of the inverse total surfactant concentration.

It may be inferred from Figures 2-4 that eq 7 gives a good rationalization of the line width data in a wide concentration region around the cmc. (Due to sensitivity limitations TTAB and CTAB could not be studied in the vicinity of the cmc.) From the low concentration intersection points of the straight line segments in Figures 2-4 the critical micelle concentrations were obtained. These are listed in Table I together with cmc data for alkylammonium halides taken from the literature. In some cases where cmc values could not be found we made use of the experimental and theoretical observation that the logarithm of the cmc varies nearly linearly with the number of carbons in the hydrocarbon chain.[26] As can be seen from Table I, there is generally a good agreement between the cmc values obtained from the counterion quadrupole relaxation rates and those obtained by other methods.

As has been pointed out earlier,[27] it is necessary when discussing the variation of the cmc with the nature of the counterion to take into account not only how the counterions interact with the associated surfactant ions but also the interaction between the counterions and the monomeric surfactant which has been demonstrated in the present work. Also, the stronger interaction between bromide ions and alkyltrimethylammonium ions below the cmc should tend to increase the cmc values of alkyltrimethylammonium bromides relative to those of alkylammonium bromides. We find for the alkyltrimethylammonium bromides higher cmc values than for alkylammonium bromides but, of course, other factors may also give rise to the difference between the two types of surfactants.

As may be inferred from Figures 2-4, besides the change in counterion binding in the vicinity of the cmc a pronounced second slope alteration is observed at higher concentrations for some of the surfactants. Thus deviations from the behavior predicted by eq 7 become visible at

TABLE I: Critical Micelle Concentrations (cmc) Determined from Plots of Counterion Quadrupole Relaxation Rates against the Inverse Surfactant Concentrations. (See Figures 2-4.) Temperature 28°

Surfactant	Cmc, *M*	Lit. values
NAB	0.13	...
NTAB	0.18	0.14[a] (30°)
DAB	0.047	0.040–0.054[a] (DAC, 25°)
DTAB	0.074	0.065[b] (30°), 0.075[c] (25°)
DPB	0.047	0.047[d]
OAC	0.27	0.27,[d] 0.18[a] (25°), 0.27[e] (27°)
OTAC	0.25	0.22[a] (OTAB, 30°)

[a] P. Mukerjee and K. J. Mysels, "Critical Micelle Concentrations of Aqueous Surfactant Systems," *Nat. Stand. Ref. Data Ser., Nat. Bur. Stand.*, **36**, (1971). [b] R. F. Tuddenham and A. E. Alexander, *J. Phys. Chem.*, **66**, 1839 (1962). [c] H. B. Klevens, *J. Phys. Colloid Chem.*, **52**, 130 (1948). [d] Calculated assuming a linear relation between the logarithm of the cmc and the number of carbons in the alkyl chain. For DPB the values given in the book by Mukerjee and Mysels (see footnote a) were used whereas for OAC the expression given by Shinoda (ref 26, p 43) was employed. [e] H. Gustavsson and B. Lindman, *J. Chem. Soc., Chem. Commun.*, 93 (1973).

TABLE II: Quadrupole Relaxation Parameters for Micellarly Bound $^{81}Br^-$ and $^{35}Cl^-$ Ions[a]

Surfactant	$\beta(\Delta B_m - \Delta B_f)$, mT	ΔB_m, mT	$\Delta B_m/\Delta B_0$[b]	$\tau_{cm}^{max} \times 10^{10}$, sec[c]
NTAB	0.28	0.43	17	0.27[e]
DTAB	0.27	0.39	16	0.25
TTAB[d]	0.46	0.60	24	0.38
CTAB[d]	0.59	0.77	31	0.50
NAB	0.88	1.1	44	0.70
DAB	0.88	1.1	44	0.70
DPB	0.27	0.38	15	0.24
OTAC	0.016	0.031	12	0.27
OAC	0.047	0.068	26	0.59

[a] β is the ratio between counterions and surfactant ions in the micelles. β was assumed to be 0.8 in the calculation of ΔB_m. ΔB_m is the ^{81}Br or ^{35}Cl line width characterizing the counterions bound to the micelles. ΔB_f is the counterion nmr line width corresponding to the ions not attached to the micelles. ΔB_f was taken as the line width observed at low concentrations extrapolated to the critical micelle concentration. ΔB_0 stands for the ^{35}Cl or ^{81}Br line width for the free ions. τ_{cm}^{max} is the upper limit of the correlation time for the micellarly bound counterions. The calculations of the different parameters (as well as the assumptions made) are described in the text. [b] ΔB_0 was for ^{81}Br determined to 25 μT and was for ^{35}Cl taken to be 2.6 μT (R. L. Ward, *Biochemistry*, **9**, 2447 (1970)). [c] In the calculation of τ_{cm}^{max} we used the correlation times for free ions given by Hertz.[37] [d] For TTAB and CTAB all the quantities correspond to upper limits since measurements could not be performed in the vicinity of the critical micelle concentrations. [e] Concerning the absolute value of τ_{cm}^{max} only the first figure is significant.

about 0.91 *M* for NAB, 0.18 *M* for DAB, 0.48 *M* for TTAB, and at about 0.19 *M* for CTAB. The second change in counterion binding suggests that at the concentrations quoted an alteration of the charge densities of the micellar surfaces is commencing to take place. A charge density change at the interface between the micelles and the intermicellar solution should be connected with an altered arrangement of the amphiphilic ions in the micelles, which may lead to a change in the shape of the micelles, for example from spherical or nearly spherical micelles to long ellipsoidal aggregates. For CTAB it has been observed by means of other experimental techniques that a drastic elongation of the micelles takes place at the same concentration as where we observe that the counterion binding to the micelles changes (*cf.* ref 13). In analogy with the CTAB solutions it seems reasonable to postulate a change in micellar form also for NAB, DAB, and TTAB at the concentrations given above. It appears that for the same length of the surfactant ion the change in counterion binding to the micelles takes place at a considerably lower concentration for the alkylammonium bromides than for the alkyltrimethylammonium bromides.

From the slopes of the straight line segments in Figures 2-4 just above the cmc or from their intercepts with the ordinate axis the quantity $\beta(\Delta B_m - \Delta B_f)$ may be calculated for the first-formed micelles (*cf.* eq 7). These values are given in Table II for the different surfactants. In order to obtain ΔB_m from these quantities it is necessary to have information on β and ΔB_f. Since the line-broadening on micelle formation is substantial, the error introduced by neglecting ΔB_f is not serious in most cases. In our calculations we took, following the pseudo-phase separation approach, for ΔB_f the values obtained when the line widths observed for the submicellar concentrations are extrapolated to the cmc. It is a more delicate matter to estmate β. Of course, degrees of counterion association to micelles have been obtained by other methods,[28] and one possibility would be to use these values directly. However, it is not necessarily true that the association degree obtained by one method is the same which determines the magnitude of an entirely different experimental parameter. Therefore, in order to get at least a rough estimate of the β value relevant in the present situation some quadrupole relaxation experiments were undertaken. An obvious way to obtain β would be to study how ΔB_{obs} for the counterions is affected by the addition of, for example, an alkali bromide (or alkali chloride) (*cf.* eq 5). The crucial problem is that an unambiguous determination of β from such an experiment requires that the shapes of the micelles stay constant. On the other hand, it is often observed that electrolyte addition may induce a transformation from globular to rod-shaped micelles.[28] This would increase the line width according to our results. In order to circumvent this problem the experiments were performed with 0.5 *M* CTAB solutions where only rod-shaped micelles are expected. Simple considerations using eq 5 show that if $\beta \ll 1$ only small line width changes are expected on addition of alkali bromide, whereas if β is close to unity the line width should decrease rapidly and in such a way that the ratio between the residual line width and the initial line width is close to the ratio between the CTAB concentration and the total bromide concentration. Our experimental data conform closely to the latter situation. By assuming β to be 0.8 the calculated ΔB_m value is within our experimental error independent of the amount of NaBr added (up to 1.0 *M*). The same value has been obtained by studies using other techniques.[29,30] It must be noted, however, that due to the limited precision or our line width measurements our β value can only be taken as a rough estimate. There is on addition of NaBr to a CTAB solution a marked increase in viscosity but according to our studies on lyotropic mesophases[31] this is not expected to affect ΔB_m or ΔB_f significantly.

Using for β the value 0.8 we have obtained the ΔB_m values given in Table II. (Of course, β may vary slightly between the different surfactants but this is not serious for the present discussion.) To permit a comparison between the two different counterions we have included in Table II also the ratio $\Delta B_m/\Delta B_0$, ΔB_0 being the line width corresponding to a free halide ion. (ΔB_0 was ob-

tained from measurements on dilute alkali halide solutions.) According to eq 1-3 we can write

$$\frac{\Delta B_m}{\Delta B_o} = \frac{q_m^2 \tau_{cm}}{q_o^2 \tau_{co}} \quad (8)$$

where q_m and q_o are the field gradients experienced by the halogen nuclei in the two environments and τ_{cm} and τ_{co} are the time constants for the change in the field gradients. One can see from Table II that $q_m^2\tau_{cm}$ for a given length of the long alkyl chain is considerably larger for alkylammonium halides than for alkyltrimethylammonium halides or the alkylpyridinium salt. The difference between NAB and DAB on one side and NTAB and DTAB on the other can be understood if the enhanced relaxation is due, directly or indirectly, to the micellar surface charges since for NTAB and DTAB the methyl groups will cause the counterions and the charged nitrogens to be farther apart. Evidently, the interaction causing relaxation must be different from that found for free organic cations (*cf.* above and ref 8-10). If an incorporation of the counterions in a water lattice stabilized by nonpolar groups were the cause of the enhanced quadrupole relaxation we would expect, due to the methyl groups, ΔB_m to be larger for NTAB and DTAB than for NAB and DAB, which is contrary to observation. For DPB except for a shielding effect also a delocalization of the positive charge over the pyridinium ring may be an important factor in determining ΔB_m.

In order to characterize the counterion binding in more detail from quadrupole relaxation data it is necessary to establish which motion is causing relaxation and to attempt a separation of the two factors determining ΔB_m, *i.e.*, q_m and τ_{cm}. We will consider the former problem first. In a theoretical study,[32] counterion quadrupole relaxation rates for different types of motional processes are given as well as predictions of how the quadrupole relaxation rates depend on various factors, such as micellar radius, solvent isotopic effect, micellar shape and surfactant concentration. An application of these results to the surfactants studied in the present work strongly indicates that water motion is causing relaxation. Important points for this conclusion are the following.

(a) Were intermicellar counterion exchange the cause of the time variation of the field gradients, the relaxation rate should decrease with increasing micellar concentration. In no case has such a decrease been observed.

(b) For micellar rotation, amphiphile lateral diffusion and counterion translational motion along the amphiphile-water interface τ_{cm} should be strongly dependent on aggregate curvature, but we observe[31] no or very small relaxation rate changes at phase transitions (for example, micellar solutions → lamellar mesophase) in surfactant systems.

(c) For micellar rotation τ_{cm} should be proportional to the third power of the micellar radius if we assume a constant resistance toward reorientation. According to observation (Table II), for a given end group, ΔB_m varies to a much smaller extent with the length of long alkyl chain.

(d) The relative change in relaxation rate on substitution of heavy water for ordinary water[13] is the same as that obtained for nonassociated hydrated ions[10,33] and also close to the isotopic effect in water viscosity[34] and water translational diffusion.[34]

(e) The energy of activation of the relaxation process is nearly independent of aggregate shape.[13]

(f) Relaxation rate and macroscopic viscosity (which should be predominantly determined by the motion of the large aggregates) vary in a quite dissimilar way with the surfactant concentration.[13]

Our conclusion that the motion of water molecules effects the counterion quadrupole relaxation indicates that the counterions are hydrated also when they are attached to the micelles. In agreement with this it can be noted that for CTAB dissolved in molecule-disperse form in an organic solvent the ^{81}Br line width is considerably greater than for micellar solutions[11] and that contact ion-pairing is not of great importance for aqueous solutions.

Unfortunately, a separation of the field gradient and the correlation time is, except for the case where $\omega\tau_c$ is of the order of unity (see ref 35 and 36), difficult to achieve when, as for monoatomic ions, the relaxation is due to intermolecular interactions. One can envisage that the attachment of a counterion to a micellar aggregate would be accompanied by an increase in both q and τ_c. Thus for a hydrated ion the charged micellar surface will distort the hydration sphere so as to increase q at the same time as the water molecular motion is retarded. It is probable that both q_m and τ_{cm} are greater than the corresponding quantities for a nonassociated ion but we are at present unable to decide whether either the field gradient or the correlation time is making a major contribution to the enhanced counterion quadrupole relaxation observed on micelle formation. It was hoped that the temperature dependence of the line widths could be informative in this respect but the fact that the activation energies of ΔB_m are in the order CTAB (ref 13) ≃ NAB > NTAB is difficult to explain. By attributing the whole change in line width to a change in the correlation time an upper limit for τ_{cm} may be obtained. These upper limits of τ_{cm} are included in Table II. In the calculations we used for τ_{co} the figures given by Hertz.[37]

The fact that $\Delta B_m/\Delta B_0$ is larger for Br^- than for Cl^- and that for Rb^+ and Na^+ counterions this quantity is an order of magnitude smaller[23,24] can certainly be referred to differences in counterion charge densities which are in the sequence $Na^+ > Rb^+ > Cl^- > Br^-$. For an ion with a high charge density, hydration water molecular motion will be less susceptible to effects by the electric field from the micellar surface and, furthermore, on attachment of a strongly hydrated ion to a micelle the deformation of the hydration sphere will be smaller than for a weakly hydrated ion.

Acknowledgments. We are indebted to Mr. Håkan Wennerström for helpful theoretical discussions and to Mr. Sven Andersson and Mrs. Annika Raihle for technical assistance.

References and Notes

(1) G. L. Jendrasiak, *Chem. Phys. Lipids*, **9**, 133 (1972).
(2) J. B. Swaney and I. M. Klotz, *Biochemistry*, **9**, 2570 (1970).
(3) L.-O. Andersson, Dissertation, Uppsala, 1971.
(4) A. Jonas and G. Weber, *Biochemistry*, **10**, 1335 (1971).
(5) A. Jonas and G. Weber, *Biochemistry*, **10**, 4492 (1971).
(6) G. Gillberg-La Force and S. Forsén, *Biochem. Biophys. Res. Commun.*, **38**, 137 (1970).
(7) J. A. Magnusson and N. S. Magnusson, *J. Amer. Chem. Soc.*, **94**, 5461 (1972).
(8) B. Lindman, S. Forsén, and E. Forslind, *J. Phys. Chem.*, **72**, 2805 (1968).
(9) B. Lindman, H. Wennerström, and S. Forsén, *J. Phys. Chem.*, **74**, 754 (1970).
(10) H. Wennerström, B. Lindman, and S. Forsén, *J. Phys. Chem.*, **75**, 2936 (1971).

(11) G. Lindblom, B. Lindman, and L. Mandell, *J. Colloid Interface Sci.*, **34**, 262 (1970).
(12) G. Lindblom and B. Lindman, *Mol. Cryst. Liq. Cryst.*, **14**, 49 (1971).
(13) G. Lindblom, B. Lindman, and L. Mandell, *J. Colloid Interface Sci.*, **42**, 400 (1973).
(14) W. P. J. Ford, R. H. Ottewill, and H. C. Parreira, *J. Colloid Interface Sci.*, **24**, 522 (1966).
(15) A. Abragam, "The Principles of Nuclear Magnetism," Clarendon Press, Oxford, 1961, p 314.
(16) H. J. C. Berendsen and H. T. Edzes, presented at the International Conference on Physicochemical State of Ions and Water in Living Tissues and Model Systems, The New York Academy of Sciences, Jan 1972.
(17) P. S. Hubbard, *J. Chem. Phys.*, **51**, 1647 (1969).
(18) T. E. Bull, *J. Magn. Resonance*, **8**, 344 (1972).
(19) H. G. Hertz, *Ber. Bunsenges. Phys. Chem.*, **65**, 36 (1961).
(20) M. D. Zeidler in "Water, a Comprehensive Treatise," F. Franks, Ed., Vol. 2, "Aqueous Solutions of Simple Molecules and Ions," Plenum Press, New York, N. Y., in press.
(21) W.-Y. Wen in "Water and Aqueous Solutions. Structure, Thermodynamics, and Transport Processes," R. A. Horne, Ed., Wiley, New York, N. Y., 1972, p 613.
(22) J. C. Eriksson, A. Johansson, and L.-O. Andersson, *Acta Chem. Scand.*, **20**, 2301 (1966).
(23) B. Lindman and I. Danielsson, *J. Colloid Interface Sci.*, **39**, 349 (1972).
(24) I. D. Robb, *J. Colloid Interface Sci.*, **37**, 521 (1971).
(25) P. H. Elworthy, A. T. Florence, and C. B. Macfarlane, "Solubilization by Surface-active Agents," Chapman and Hall, London, 1968, p 48.
(26) K. Shinoda, T. Nakagawa, B.-I. Tamamushi, and T. Isemura, "Colloidal Surfactants," Academic Press, New York, N. Y., 1963.
(27) B. Lindman, *Proc. Intern. Congr. Surface Active Agents, 5th, Barcelona*, 1088 (1968).
(28) E. W. Anacker in "Surfactant Science Series," E. Jungermann, Ed., Vol. 4, Marcel Dekker, Inc., New York, N. Y., 1970, p 203.
(29) E. Keh, C. Gavach, and J. Guastalla, *C. R. Acad. Sci., Ser. C*, **263**, 1488 (1966).
(30) W. K. Mathews, J. W. Larsen, and M. J. Pikal, *Tetrahedron Lett.*, 6, 513 (1972).
(31) G. Lindblom and B. Lindman, *Proc. Intern. Congr. Surface Active Agents, 6th, Zürich, 1972*, in press.
(32) H. Wennerström, G. Lindblom, and B. Lindman, to be submitted for publication.
(33) M. Eisenstadt and H. L. Friedman, *J. Chem. Phys.*, **44**, 1407 (1966).
(34) G. S. Kelly in "Water, a Comprehensive Treatise," F. Franks, Ed., Vol. 1, Plenum Press, New York, N. Y., 1972, p 363.
(35) T. E. Bull, J. Andrasko, E. Chiancone, and S. Forsén, *J. Mol. Biol.*, **73**, 251 (1973).
(36) J. Andrasko, I. Lindqvist, and T. E. Bull, *Chem. Scripta*, **2**, 93 (1972).
(37) H. G. Hertz, *Progr. Nucl. Magn. Resonance Spectrosc.*, 3, 159 (1967).

Matrix Isolation Studies on the Gallium–Indium–Oxygen System. Infrared Spectra and Structures of Molecular Ga_2O, In_2O, and InOGa

A. J. Hinchcliffe and J. S. Ogden*

Inorganic Chemistry Laboratory, University of Oxford, Oxford, England *(Received June 14, 1973)*

When the vapor above heated gallium oxide is condensed in low-temperature matrices, two oxide species are frequently produced and these are identified by infrared spectroscopy as Ga_2O and a dimer species Ga_4O_2. The same molecules are also observed when oxygen gas is passed over heated gallium and the products are similarly isolated. The corresponding indium–oxygen system yields analogous species In_2O and In_4O_2, and when oxygen is passed over an alloy of gallium and indium, several new mixed species of the general formula $Ga_xIn_{4-x}O_2$ are identified in addition to the mixed metal suboxide InOGa. Infrared band assignments are supported by diffusion studies and the use of ^{18}O enrichment, and normal coordinate analyses for Ga_2O and In_2O yield principal force constants $F_{Ga-O} = 3.65 \pm 0.2$ mdyn/Å and $F_{In-O} = 3.15 \pm 0.25$ mdyn/Å and apex angles $\geq 142°$ and $\geq 135°$, respectively. The interpretation of these results is discussed in the context of previous work on these systems.

Introduction

The vapor phase oxides of gallium and indium have been studied fairly extensively by mass spectrometry,[1-4] and it is well established that Ga_2O and In_2O are the important species produced on heating the solid oxides Ga_2O_3 or In_2O_3. The molecule InOGa has also been recently detected in the vapor above heated In–Ga_2O_3 mixtures.[5]

However, despite several attempts to characterize these species more completely, considerable uncertainty still remains concerning their vibration frequencies and equilibrium geometries. The initial high-temperature electron diffraction results indicated[6] that both Ga_2O and In_2O had C_{2v} structures with apex angles of 140 and 150°, respectively, and that the Ga–O and In–O bond lengths were 1.84 ± 0.01 and 2.02 ± 0.01 Å. However, a reassessment[7] of the electron diffraction data, taking into account the effect of possible low-frequency bending vibrations, suggested that both the molecules were linear. This conclusion conflicts with a vapor phase infrared study[8] on Ga_2O and In_2O in which the symmetric and antisymmetric stretching modes appear to be ir active in both species. In an attempt to resolve some of these difficulties, we have been studying the ir spectra of these species trapped at low temperatures in inert matrices, and a preliminary report[9] based upon ^{18}O isotope frequency shifts favors a C_{2v} model for both Ga_2O and In_2O. These systems have also been studied independently by Carlson, *et al.*,[10] but a number of difficulties still remain concerning the inter-

pretation of the matrix isolation results.[11] This paper describes in detail our ir studies on matrix-isolated Ga_2O, In_2O, and InOGa, and presents additional data on the polymerization of these species.

Experimental Section

The Knudsen furnace and low-temperature cryotip used for these matrix isolation studies have been described previously.[12] In this work, the vapor phase oxides of gallium and indium were produced in two distinct ways. In the first type of experiment, solid samples of Ga_2O_3 or In_2O_3 were heated to ~1050 or ~950°K, respectively, in alumina or tantalum sample holders, and the vapor was deposited on a cooled CsI window with an excess of nitrogen or argon. The alternative procedure was to pass a regulated flow of oxygen gas (~0.1 mmol/hr) over elemental gallium or indium heated to ~1100°K in a quartz tube. At this temperature, the vapor pressures of gallium and indium are still low ($<10^{-3}$ Torr)[13] but any oxide produced is immediately vaporized, and is condensed with the inert matrix gas. This method proved to be a most convenient route to ^{18}O-labelled compounds.

A number of experiments were also carried out in an attempt to prepare mixed metal oxides (*e.g.*, InOGa) and these involved passing O_2 gas over heated Ga–In alloys or alternatively heating a mixture of the solid sesquioxides. Both these methods were successful but had the minor disadvantage that the composition of the vapor slowly changed with time. A number of additional experiments were also carried out in which O_2 gas was passed over indium and gallium heated *separately* to ~1100°K in parallel sample tubes and the vapors cocondensed simultaneously with the matrix.

The samples of Ga_2O_3 and elemental gallium and indium all had a stated purity ≥99.99%. Research grade $^{16}O_2$, Ar, and N_2 gases were obtained from the British Oxygen Company, and ^{18}O-enriched oxygen gas (93 atom %) was supplied by Miles Laboratories. The nitrogen or argon matrices were deposited at rates of 5–10 mmol/hr and matrix ratios were varied from an estimated 1:300 to 1:3000. During sample deposition, the cooled CsI window could be maintained at any fixed temperature between 15 and 27°K, and controlled diffusion experiments were carried out in the temperature range 20–35°K. Ir spectra were recorded at 20°K using a Perkin-Elmer 225 spectrophotometer, and the full range of this instrument (5000–200 cm^{-1}) was available through efficient dry air purging. The calibration of this instrument was carried out using standard gases, and frequency reproducibility was routinely within 0.1 cm^{-1}.

Results and Discussion

A large number of experiments were carried out using both argon and nitrogen matrices, and in common with most other matrix isolation studies, all ir absorptions were found to be dependent to a small extent upon the matrix environment. However, spectral resolution was generally superior in nitrogen, and the frequencies quoted in the text below refer to nitrogen matrices unless otherwise stated. For the same degree of isolation, no significant differences were observed between the spectra obtained from the M_2O_3 vaporizations and those obtained from the corresponding $M-O_2$ systems. However, varying the matrix ratio or altering the temperature of the cooled CsI window during deposition did produce significant changes in relative band intensities. The simplest spectra were always

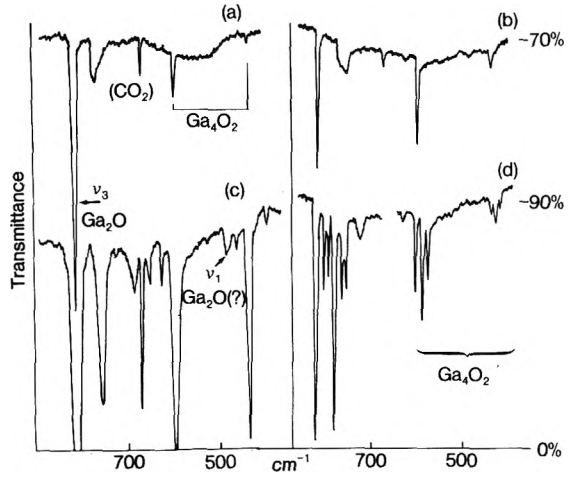

Figure 1. Ir spectra of gallium oxides isolated in nitrogen matrices: (a) from heated $Ga_2{}^{16}O_3$; matrix ratio ~1000:1; (b) after diffusing sample (a) to 32°K; (c) after prolonged deposition from heated Ga metal/$^{16}O_2$; (d) after passing $^{16}O_2$ + $^{18}O_2$ gas over heated gallium; products condensed at 25°K.

produced under conditions of optimum isolation at ~15°K, and in general spectra became more complicated as the matrix ratio was decreased or as the temperature of the CsI window was raised.

Gallium Oxides. When the vapor above heated Ga_2O_3 was cocondensed with a large excess (~3000:1) of nitrogen at 15°K, the ir spectrum showed only one prominent band at 809.4 cm^{-1}, together with traces of CO, H_2O, and CO_2. When the matrix ratio was reduced to ~1000:1, this band was still the most prominent feature in the spectrum, but it was accompanied by additional weaker features at 590.9, 423.9, and 749 cm^{-1}, and a typical spectrum obtained under these conditions is shown in Figure 1a. In argon matrices under the same conditions of isolation, the most prominent band appeared as a partially resolved doublet at 821.7/817.8 cm^{-1}, and the weaker features were observed at 594.7, 416.0, and 763 cm^{-1}. Figure 1b shows the spectral changes which take place as a result of warming the deposit shown in Figure 1a to a temperature of ~32°K, and it is evident that the bands at 590.9 and 423.9 cm^{-1} have increased in intensity at the expense of the 809.4-cm^{-1} band. A similar enhancement of these two bands was observed when lower matrix ratios (500:1) were used, and the results of several studies of this kind show that these two bands at 590.9 and 423.9 cm^{-1} were always present in approximately the same relative intensity (~5:1) which suggests that they belong to the same molecular species. As an alternative to lowering the matrix ratio, the intensity of these two bands could also be increased by depositing at a window temperature of >24°K, but under these conditions, two weak satellites were observed on the low-frequency side of the 809.4-cm^{-1} band at 793.7 and 783.5 cm^{-1}.

Even under high resolution, no fine structure due to gallium isotopes could be observed, but the effect of ^{18}O enrichment on this system is shown in Figure 1d. In this experiment, an approximately equimolar mixture of $^{16}O_2$ and $^{18}O_2$ was passed over heated gallium, and the products condensed at ~25°K in a nitrogen matrix (~1500:1). The high-frequency region shows two prominent bands at 809.4 and 768.5 cm^{-1}, each of which is accompanied by two weaker satellites at 793.7 and 783.5 and 753.6 and 744.2 cm^{-1}, respectively. In the 400–600-cm^{-1} region, the spectrum consists basically of two triplets with compo-

nents at 590.9, 575.0, and 563.1 cm^{-1}, and 423.9, 415.0, and 405.3 cm^{-1}.

These results therefore indicate that there are at least two different gallium oxide species trapped in these matrices, and these have been identified[11] as Ga_2O and Ga_4O_2. In contrast, the mass spectrometric results[1,3,4] show that the vapor is predominantly Ga_2O and that there is no evidence for any polymeric species. Our band assignments must therefore be discussed in detail.

Ga_2O. The intense band at 809.4 cm^{-1} (Figure 1a) is assigned to the antisymmetric stretching mode (ν_3) of $Ga_2{}^{16}O$. Only one accompanying band is observed at 768.5 cm^{-1} in ^{18}O enrichment experiments, and in our earlier communication,[9] it was shown that this frequency shift indicates a bent (C_{2v}) structure with an apex angle ~143°. The two remaining fundamentals of this molecule (both symmetry A_1) should therefore be observed in the ir spectrum and although the bending mode ν_2, might lie below the limit of our spectrometer, one should expect to see ν_1 the symmetric Ga–O stretch. A number of weaker features are present in Figure 1a, but these either remain unchanged or increase in intensity during diffusion (Figure 1b) whereas the band at 809.4 cm^{-1} decreases in intensity, and it is only when very large deposits are studied that a second absorption with similar diffusion characteristics is observed.

Figure 1c shows part of the ir spectrum of a large deposit of gallium oxides isolated in a nitrogen matrix (~1000:1). In addition to the intense bands present in Figure 1a, a number of weaker features are observed at 618, 548, 518, 472, 449, and 380 cm^{-1}. During diffusion, the 449-cm^{-1} band increased in intensity, and the 618 and 380-cm^{-1} bands decreased extremely rapidly. The others were unaffected apart from the 472-cm^{-1} band, which decreased in intensity at approximately the same rate as the 809.4-cm^{-1} band, and this band is therefore assigned as ν_1 Ga_2O. This 472-cm^{-1} absorption was always present when the 809.4-cm^{-1} band was very intense, but its assignment remains somewhat tentative as it was not possible to confirm *quantitatively* that the intensity ratio of these two fundamentals remained constant, and neither was it possible to carry out ^{18}O enrichment studies on such a weak feature. No evidence could be found for the bending frequency in these spectra, and this vibration is therefore assumed to lie below 200 cm^{-1}.

These results and band assignments for Ga_2O may be compared with the matrix isolation studies of Carlson, *et al.*,[10] and with the gas phase data of Mal'tsev, *et al.*[8] Carlson, *et al.*, obtain essentially the same value for ν_3 (Table I) but their assignment of features at 595.6 and 416.5 cm^{-1} as ν_1 and ν_2 has been shown[11] to be incorrect. The gas-phase ir spectrum of Ga_2O has been recorded[8] under low resolution at a temperature of 1450°K and shows two absorptions (band widths ~30 cm^{-1}) at 770 cm^{-1} and 420 cm^{-1}. These have been assigned as ν_3 and ν_1, respectively, and although the band centers are not precisely located, these frequencies differ significantly from the fundamentals observed here in a nitrogen matrix.

This difference may partly be accounted for by the occurrence of "hot bands" in the gas-phase spectrum, which would broaden the absorptions on the low-frequency side and thus shift apparent band centers. Another contributory factor could be that the vibrations of the Ga_2O molecule are rather sensitive to the matrix environment and might show a significant matrix shift compared with the gas phase, and this explanation might also account for the rather large frequency shift (~10 cm^{-1}) observed for ν_3 on passing from a nitrogen to an argon matrix.

TABLE I: Ir Frequencies (cm^{-1}) and Band Assignments for Matrix Isolated Gallium and Indium Oxides

Argon		Nitrogen			
(a)[a]	(b)[b]	(a)[a]	(b)[b]	(c)[c]	Assignment
822.6	821.7	808.1	809.4	809.4	$\nu_3 Ga_2{}^{16}O$ and
817.9	817.8		793.7	793.7	satellites
			783.5	783.5	
				768.5	$\nu_3 Ga_2{}^{18}O$ and
				753.6	satellites
				744.2	
			472		$\nu_1 Ga_2{}^{16}O$
595.6*	594.7	590.4*	590.9	590.9	$Ga_4{}^{16}O_2$
				575.0	$Ga_4{}^{16}O^{18}O$
				563.1	$Ga_4{}^{18}O_2$
416.5*	416.0	425.8*	423.9	423.9	$Ga_4{}^{16}O_2$
				415.0	$Ga_4{}^{16}O^{18}O$
				405.3	$Ga_4{}^{18}O_2$
	763		749	749	Polymeric Ga–O
				715	species
			449		Ga–O bands
			548		not assigned
			518		
			618		
			380		
734.9		721.8	722.4	722.4	$\nu_3 In_2{}^{16}O$ and
741.3			708.0	708.0	satellites
			697.0	697.0	
				684.3	$\nu_3 In_2{}^{18}O$
			442		$\nu_1 In_2{}^{16}O$
555.1*		550.5*	550.2	550.2	$In_4{}^{16}O_2$
				532.0	$In_4{}^{16}O^{18}O$
				522.1	$In_4{}^{18}O_2$
404.3*		412.6*	412.2	412.2	$In_4{}^{16}O_2$
				402.8	$In_4{}^{16}O^{18}O$
				393.0	$In_4{}^{18}O_2$
			579		
			524		In–O bands
			512		not assigned
			491		
			436		

[a] Reference 10. Bands labeled with an asterisk originally assigned as fundamentals of Ga_2O or In_2O. [b] This work, ^{16}O species only. [c] This work, ^{16}O + ^{18}O species. Frequency accuracy in (b) and (c) is ±0.1 cm^{-1} for ν_3, ±0.2 cm^{-1} for M_4O_2 species, and ±1 cm^{-1} for the remaining absorptions.

If our assignment of the 472-cm^{-1} band is correct, its observation provides additional confirmation that Ga_2O has C_{2v} symmetry when isolated in a nitrogen matrix. However, this band is very much weaker than ν_3, and it is important to examine more closely the assumptions which originally led to the estimate of ~143° for the GaOGa angle.

If one assumes that the vibrations of a C_{2v} XY_2 molecule are completely harmonic, the zero-order antisymmetric stretching frequency ω_3 is given by

$$4\pi^2\omega_3^2 = (F_r - F_{rr})(\mu_Y + 2\mu_X \sin^2\theta) \qquad (1)$$

where μ refers to a reciprocal mass and 2θ is the YXY apex angle. F_r and F_{rr} are the principal and interaction stretching constants, respectively. This equation indicates that if ω_3 is known for the two isotopic molecules $Ga_2{}^{16}O$ and $Ga_2{}^{18}O$, then the apex angle may be calculated *via*

$$\omega_3(^{16}O)/\omega_3(^{18}O) = \left[\frac{\mu_{Ga} + 2\mu(^{16}O)\sin^2\theta}{\mu_{Ga} + 2\mu(^{18}O)\sin^2\theta}\right]^{1/2} \quad (2)$$

These experiments, however, yield absorption frequencies which are uncorrected for anharmonicity, and it has been shown that if the observed frequency ratio $\nu_3(^{16}O)/\nu_3(^{18}O)$ is used in the above expression, the value of θ obtained is *lower* than the true value.[14] Substitution of ν_3, $Ga_2{}^{16}O$ and ν_3 $Ga_2{}^{18}O$ (Table I) into this equation, using the atomic weights Ga = 69.8 and O = 16.0 or 18.0 yields GaOGa = 142° 20′ with attendant error limits of +6° and −4° resulting from the experimental uncertainty (±0.1 cm^{-1}) in measuring band centers. If one assumes that the observed Ga_2O frequency ν_3 is related to the corresponding zero-order frequency by

$$\nu_3 = \omega_3(1 - \alpha)$$

and estimating the anharmonicity correction ($\omega_3{}^{16}\alpha^{16}$) to be 10.0 cm^{-1}, then ω_3 $Ga_2{}^{16}O$ lies at 819.4 cm^{-1}, and, assuming the Darling–Dennison rule,[15] the corresponding zero-order frequency for $Ga_2{}^{18}O$ lies at 777.5 cm^{-1}. The value of θ obtained from this "corrected" zero-order frequency ratio is now 86° 50′ and this value is significantly larger than the estimate obtained directly from the observed frequencies. This indicates that if the anharmonicity correction is 10.0 cm^{-1}, Ga_2O may in fact have an apex angle in the region of 174°. Diatomic GaO, which absorbs at 755.0 cm^{-1} in the gas phase,[16] has a zero-order frequency of 767.7 cm^{-1} and the estimated 10.0 cm^{-1} correction assumed here for Ga_2O is therefore not unreasonable.

The value of $F_r - F_{rr}$ obtained from eq 1 is 3.06 mdyn/Å using the experimentally observed frequencies, and although a complete solution to the general valence force field is not possible, some attempt may be made to estimate F_r and F_{rr} independently by combining this data with ν_1 at 472 cm^{-1}. The results of this exercise for the species Ga_2O, In_2O and InOGa are set out below.

Ga_4O_2. The intensity ratio of the two bands at 590.9 and 423.9 cm^{-1} remained constant throughout these experiments, and both bands were observed to increase in intensity during controlled diffusion at the expense of Ga_2O (Figures 1a and 1b). Each band gives rise to a triplet structure in ^{18}O enrichment experiments, (Figure 1d) suggesting that two equivalent atoms of oxygen are involved in these vibrations. Both bands are therefore assigned to a simple dimer species Ga_4O_2. It is significant that both these bands had negligible intensity under conditions of optimum isolation, and that their intensity could be enhanced either by decreasing the proportion of matrix gas or by depositing at window temperatures above 20°K. This species is therefore almost certainly formed by diffusion during the finite quenching time when the matrix is still soft, and its identification as Ga_4O_2 does not therefore conflict with the gas phase mass spectrometric data. One additional band was observed to increase in intensity on diffusion, and this was the weak feature at 449 cm^{-1}. However, the assignment of this band to Ga_4O_2 remains tentative, as it could only be observed in heavy deposits (*e.g.*, Figure 1c) and an intensity correlation with the two prominent dimer bands was not attempted.

In argon matrices, two prominent bands were observed at 594.7 and 416.0 cm^{-1} and although no ^{18}O enrichment experiments were carried out, these almost certainly correspond to the nitrogen matrix absorptions discussed above. Both the nitrogen and argon matrix frequencies are in good agreement with Carlson's observations[10] and the only significant difference between the two sets of ^{16}O results is that in his diffusion experiments these bands *decreased* in intensity in diffusion in the same way as ν_3 Ga_2O, and were consequently assigned as the ν_1 and ν_2 fundamentals of this molecule.

This anomalous diffusion behavior can perhaps be accounted for if Ga_2O is able to react rapidly with Ga_4O_2 to form higher polymers in addition to undergoing dimerization. The net effect on the Ga_4O_2 band intensities during diffusion will then be determined by the proportions of Ga_2O and Ga_4O_2 present in the initial deposit. Carlson's spectra show dimer bands which are considerably more intense than those observed in this work, and it is possible that under these conditions, the predominant diffusion reaction is $Ga_2O + Ga_4O_2 \rightarrow Ga_6O_3$ etc., rather than $2Ga_2O \rightarrow Ga_4O_2$.

The ^{18}O enrichment experiments indicate from simple statistics that two equivalent oxygen atoms are present, and a possible structure for this dimer molecule is discussed below.

Remaining Features. Three other bands were frequently observed in these experiments, and these are the two satellites to the main Ga_2O peak and the rather broad feature at ~750 cm^{-1}. The two satellites occur at 793.7 and 783.5 cm^{-1} and these bands were always produced when deposition was carried out at window temperatures in excess of ~23°K. On diffusion the 793.7-cm^{-1} band decreased in intensity while the 783.5-cm^{-1} band increased, but both these changes took place very much more rapidly than either the growth of the Ga_4O_2 bands or the decrease of the principal Ga_2O band at 809.4 cm^{-1}. Each of these satellites gave rise to only one additional feature in ^{18}O enrichment experiments (Figure 1d) and these bands are assigned to the antisymmetric stretching mode of Ga_2O molecules trapped in different matrix environments. This assignment is supported by the observation that the frequency ratios of the ^{16}O and ^{18}O satellites correspond very closely with the 809.4/768.5 ratio found for the principal $Ga_2{}^{16}O$–$Ga_2{}^{18}O$ bands, and the diffusion behavior may be qualitatively understood if one accepts that slight annealing of a matrix is likely to reduce the number of different trapping sites available. Argon matrices appear to show this multiple site effect to a much larger degree, and in common with Carlson, *et al.*, we were never able to obtain just one single absorption for ν_3 Ga_2O in argon (Table I).

The remaining feature in Figure 1a is a rather broad band centered at 749 cm^{-1}, and this has an ^{18}O counterpart at 715 cm^{-1} (Figure 1d). This species was relatively more intense in concentrated matrices, and although it could be assigned to diatomic GaO on the basis of frequency, we believe it arises from a higher polymer of Ga_2O. The proportion of GaO in the vapor phase is very low, and if this were isolated in the matrix as a diatomic molecule, one would expect to see a rather sharp absorption with a band width comparable to that observed for monomeric Ga_2O.

Indium Oxides. When the vapor above heated In_2O_3 was condensed in a nitrogen matrix (~2000:1) at ~20°K, an intense band was observed at 722.4 cm^{-1} together with two weaker features at 550.2 and 412.2 cm^{-1}, and the same bands were observed in analogous In–O_2 experiments (Figure 2a). During diffusion, the two weaker features increased in intensity at the expense of the 722.4-cm^{-1} band. The frequencies of these three bands are very

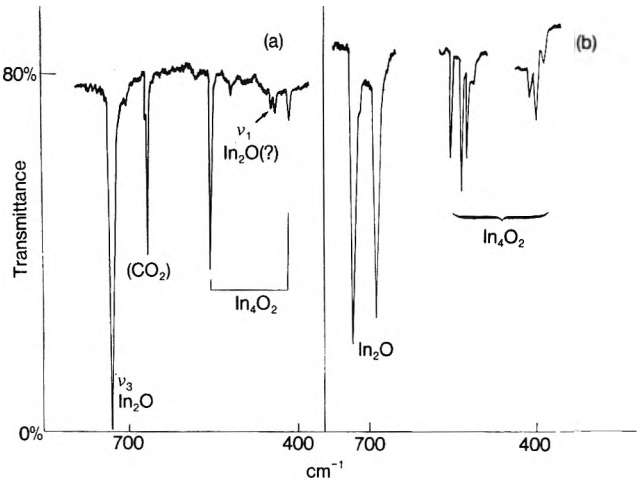

Figure 2. Ir spectra of indium oxides isolated in nitrogen matrices: (a) from heated $In/^{16}O_2$; matrix ratio ~2000:1; (b) after passing $^{16}O_2 + {}^{18}O_2$ gas over heated indium.

close to those reported by Carlson, *et al.*,[10] but as in the case of the gallium oxide experiments, Carlson's diffusion experiments in this system differ from the results obtained here, and this point is discussed below.

A number of very weak features are also present in Figure 2a, notably at 442, 436, 512, 524, 491, and 579 cm^{-1} and the diffusion behavior of these bands was studied in heavy deposits. In particular, it was found that the band at 442 cm^{-1} decreased in intensity at a rate comparable with that observed for the 722.4-cm^{-1} band, and that in contrast the other weak features either disappeared very rapidly or remained unchanged. By analogy with the corresponding gallium oxide system, the 722.4 and 442-cm^{-1} bands are assigned as the ν_3 and ν_1 fundamentals of $In_2{}^{16}O$, and the bands at 550.2 and 412.2 cm^{-1} to a dimer species In_4O_2. This assignment differs[11] from that suggested by Carlson, *et al.*, but is supported by ^{18}O enrichment experiments.

Figure 2b shows a spectrum of matrix isolated indium oxides obtained by passing ^{18}O enriched oxygen gas over heated indium. It is evident that the band at 722.4 cm^{-1} is now accompanied by a single extra feature at 684.3 cm^{-1} and that this vibration therefore involves only one atom of oxygen. In contrast, the 550.3 and 412.2-cm^{-1} bands now appear as components of two triplet patterns indicating that two equivalent oxygen atoms are involved in these vibrations. Deposition at window temperatures above 20°K produces, in addition, weak satellite bands on the low-frequency side of ν_3 at 708 and 697 cm^{-1} which behave in a similar way to the satellites observed in the gallium oxide system. Thus on diffusion, the 697-cm^{-1} component grows rapidly in intensity at the expense of the 708-cm^{-1} band.

The frequencies observed in these indium oxide experiments are listed in Table I, and their assignments may now be discussed.

In_2O. Mass spectrometric studies[1-4] show that the vapor above heated In_2O_3 contains In_2O, In, O_2, and InO and that In_2O is the most predominant species. Diatomic InO is known to absorb at 695.7 cm^{-1} in the gas phase,[16] and the intense band at 722.4 cm^{-1} has been assigned to ν_3 $In_2{}^{16}O$ principally on the basis of diffusion studies and ^{18}O enrichment.

If one assumes that this molecule has C_{2v} symmetry, then following eq 1 and 2, the observed frequencies yield an apex angle of 135° with error limits of +10 and −8° arising directly from the frequency uncertainty of ±0.1 cm^{-1}. The corresponding value of $F_r - F_{rr}$ is 2.66 mdyn/Å. As in the case of Ga_2O, this apex angle represents a lower limit, in view of the neglect of anharmonicity, and the inclusion of a modest anharmonic correction will result in an apex angle much closer to 180°. The identification of ν_1 at 442 cm^{-1} is rather less conclusive as it was not possible to obtain ^{18}O data, but if this assignment is correct, In_2O would appear to be nonlinear in nitrogen matrices. The gas-phase ir spectrum of In_2O[8] shows two very broad bands centered at ~680 and ~360 cm^{-1} which are assigned as ν_3 and ν_1, respectively. This suggests a bent structure in the gas phase, and if one considers that the apparent centers of these broad gas-phase absorptions might be shifted to low frequency as a result of hot bands, the agreement with the matrix frequencies is moderately satisfactory.

In_4O_2. The two bands at 550.2 and 412.2 cm^{-1} were observed to increase in intensity on diffusion, and two triplet patterns are produced on ^{18}O enrichment (Figure 2b). These bands thus probably arise from a molecule containing two equivalent oxygen atoms, and by analogy with the gallium oxide system, are assigned to a dimer species In_4O_2. There is no evidence from mass spectrometry that a species of this molecular weight is present in the vapor above heated indium oxides, but this molecule could readily be formed during deposition *via*

$$2In_2O \longrightarrow In_4O_2$$

and this reaction may also be responsible for the intensity changes observed here during controlled diffusion.

In their parallel series of experiments, Carlson, *et al.*,[10] assign similar bands at 550.5 and 412.6 cm^{-1} in nitrogen as fundamentals of monomeric In_2O rather than as absorptions of a dimer, but this assignment is not supported by our ^{18}O enrichment results.

Other Features. Deposition at window temperatures above 20°K produced satellite bands on the low-frequency side of ν_3 $In_2{}^{16}O$ at 708 and 697 cm^{-1}, and the diffusion behavior of these bands was very similar to that observed for the corresponding Ga_2O satellites. These bands are assigned to In_2O molecules trapped on different matrix sites (Table II).

Finally, a number of very weak features were also observed in heavy deposits, and these are included in Table I. Apart from the observation that they all lie in what appears to be the In–O stretching region, little can be said about their assignment, and they will not be discussed further.

Indium–Gallium Oxides. In the first type of mixed metal experiment, oxygen gas was passed over an alloy of indium and gallium heated to ~1100°K and the products were trapped in nitrogen matrices as described earlier. Figure 3a shows a typical spectrum obtained from an indium-rich alloy (In:Ga = 8:1) in which the vapors have been condensed at 25°K to augment the polymer features. In the region above 700 cm^{-1}, three strong bands are observed at 809.4, 781.9, and 722.4 cm^{-1}, together with a number of weaker satellite features. Apart from the prominent band at 781.9 cm^{-1} and its two satellites at 765 and 757 cm^{-1}, all the other absorptions in this region were previously observed in the pure Ga–O or In–O systems, and have been assigned to Ga_2O and In_2O. The prominent new absorption lies approximately midway between the intense antisymmetric stretching modes in Ga_2O and

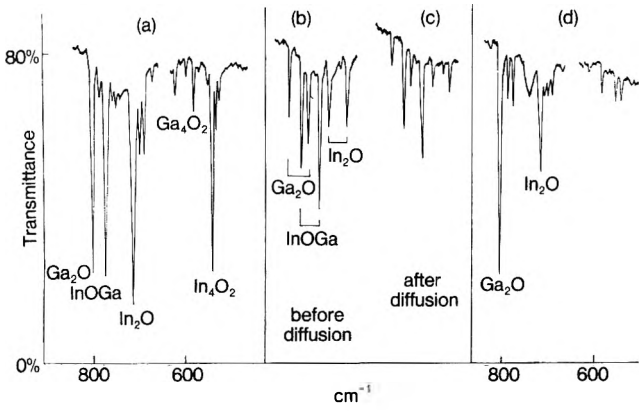

Figure 3. Ir spectra of mixed gallium–indium oxides in nitrogen matrices: (a) after passing $^{16}O_2$ gas over a heated alloy with In:Ga in the proportions 8:1; products condensed at 25°K; (b) after passing $^{16}O_2$ + $^{18}O_2$ gas over the same alloy; products condensed at 16°K; (c) after warming deposit (b) at 32°K; (d) after passing $^{16}O_2$ gas over pure gallium and indium heated in separate tubes; products co-condensed at 25°K.

TABLE II: Ir Frequencies (cm^{-1}) Observed for Mixed Indium–Gallium Oxides Isolated in Nitrogen Matrices

InOGa				
783.0[a]	781.9[b] 765.0[b] 757.0[b]	$In^{16}OGa$ and satellites	781.9[c] 742.3[c]	$In^{16}OGa$ $In^{18}OGa$

$Ga_xIn_{4-x}O_2$ Molecules[b]

Tentative assignments[d]	Alloy composition (In:Ga) 2:1	8:1	25:1	Pure In + pure Ga in separate tubes
	Monomer species observed			
	Ga_2O + InOGa	Ga_2O + InOGa + In_2O	In_2O + InOGa	In_2O + Ga_2O
Ga_4O_2	590.9	590.9	—	590.9
Ga_3InO_2 (I)	554.5	554.5	—	—
Ga_3InO_2 (II)	606.5	606.5	—	—
$Ga_2In_2O_2$ (A)	561.4	561.4	—	561.4
$Ga_2In_2O_2$ (B or	536	536	—	—
$Ga_2In_2O_2$ C)	—	584	—	—
$GaIn_3O_2$ (I)	—	543	543	—
$GaIn_3O_2$ (II)	—	564	564	—
In_4O_2	—	550.2	550.2	550.2

[a] Reference 10. [b] This work, ^{16}O only. [c] This work, ^{16}O + ^{18}O species. [d] Roman numerals indicate the possibility of isomerization in Ga_3InO_2 and $GaIn_3O_2$. The isomers A, B, and C of $Ga_2In_2O_2$ are discussed in the text. Frequency accuracy, ±0.1 cm^{-1} for InOGa, ±0.2 cm^{-1} for Ga_4O_2 and In_4O_2, and ±0.5 cm^{-1} for the remaining bands. The absorptions at 584 and 564 cm^{-1} were always relatively weak, and the band at 561.4 cm^{-1} was only prominent in the double tube experiments.

In_2O, and is assigned to a corresponding vibration in the mixed metal suboxide InOGa. In the frequency region associated with the more intense dimer vibrations (525–625 cm^{-1}), In_4O_2 and Ga_4O_2 are observed, but several additional features are also present at 606.5, 584, 564, 554.5, 543, and 536 cm^{-1}.

The effect of ^{18}O enrichment on this system is shown in Figure 3b. In this particular experiment, interest has been focused on the region above 700 cm^{-1}, and this figure shows a spectrum obtained after passing a mixture of $^{16}O_2$–$^{18}O_2$ (4:5) over the same heated alloy and condensing the products at 16°K. A prominent six-line pattern is produced at 809.4, 781.9, 768.5, 742.3, 722.4, and 684.3 cm^{-1}. A number of very weak features were also present in the lower frequency region. Four of the components of the sextet are immediately identified as the ν_3 fundamentals of $In_2{}^{16}O$, $In_2{}^{18}O$, $Ga_2{}^{16}O$, and $Ga_2{}^{18}O$ (Table I) and the remaining two are assigned to $In^{16}OGa$ and $In^{18}OGa$. This assignment is supported by the intensity changes which are observed on warming this deposit to ~32°K. All the components of the sextet decrease in intensity, and in addition to confirming that the pairs of bands at 722.4 and 684.3 cm^{-1} (In_2O), 809.4 and 768.5 cm^{-1} (Ga_2O), 781.9 and 742.3 cm^{-1} (InOGa), do indeed belong to molecules containing one atom of oxygen, this experiment also indicates that the relative rates of reaction for these monomers are in the order In_2O > Ga_2O > InOGa.

One curious feature of these experiments is that although indium oxide is more volatile than gallium oxide, an 8:1 ratio of In:Ga was required in order to produce the In_2O, Ga_2O, and InOGa peaks in approximately the same relative intensity. Although the relative extinction coefficients of these bands are not known, one might have expected that gallium-rich alloys would be required to produce this type of spectrum. In these alloy experiments, the relative band intensities of Ga_2O, InOGa, and In_2O were found to vary with spray-on time, and initial spectra always showed relatively more Ga_2O and InOGa. As the alloy gradually became depleted in gallium, the In_2O band became relatively more intense, and the spectrum shown, for example, in Figure 3a might therefore be regarded as the superposition of spectra obtained from gallium-rich and indium-rich deposits. Increasing the proportion of indium in the original alloy to ~25:1 produced essentially In_2O and InOGa and very little Ga_2O, while decreasing the indium content had the reverse effect. Corresponding intensity variations were observed in the "dimer" region, and Table II lists the nine distinct bands observed here in pure ^{16}O experiments using different alloy compositions. An attempt is made to assign some of these bands on the basis of variations in relative intensity with alloy composition, and some structural information may also be deduced from the number of different chemical species which appear to be represented.

When $^{16}O_2$ was passed over pure indium and gallium heated *separately* in different sample holders, *no* InOGa was produced, and Figure 3d shows a typical spectrum from this system. In this experiment, deposition has been carried out at 25° in order to enhance dimer band intensities and has resulted in the formation of a small amount of "polymeric" Ga_2O at 749 cm^{-1} (Table I) and the appearance of satellite bands on ν_3 Ga_2O and ν_3 In_2O. The upper dimer region shows bands previously assigned to Ga_4O_2 and In_4O_2 and one additional prominent band at 561.4 cm^{-1}. Since Ga_2O and In_2O are the only monomer species present, this band is assigned to $In_2Ga_2O_2$.

Several experiments were also carried out in which mixtures of In_2O_3 and Ga_2O_3 were heated to 950–1050°K and the vapors condensed in nitrogen matrices. The ir spectra obtained were very similar to those produced in the O_2–alloy type of experiment and the relative proportions of In_2O, InOGa, and Ga_2O in the matrix again depended upon the composition of the oxide mixture. The trapped species behaved in a similar way on diffusion and these experiments will not therefore be described in detail.

TABLE III: Observed and Calculated Molecular Parameters for Ga_2O, InOGa, and In_2O

Molecule		Vibration frequencies, cm^{-1}			Bond lengths, Å		Apex angles[c]
		Observed in N_2 matrix	Calculated I[a]	Calculated II[a]			
$Ga_2{}^{16}O$	ν_3	809.4	809.4	809.4			
	ν_1	472	471.9	472.0			
	ν_2	—	192.6	75.0	1.84 ± 0.01[b]	1.81 ± 0.02[c]	≥142°
$Ga_2{}^{18}O$	ν_3	768.5	768.5	768.5			
$In^{16}OGa$	ν_3	781.9	782.1	782.1			
	ν_1	—	450.0	450.0			
	ν_2	—	164.5	58.7			
$In^{18}OGa$	ν_3	742.3	742.2	742.2			
$In_2{}^{16}O$	ν_3	722.4	722.4	722.4			
	ν_1	442	442.0	442.0			
	ν_2	—	140.2	53.4	2.02 ± 0.01[b]	1.98 ± 0.03[c]	≥135°
$In_2{}^{18}O$	ν_3	684.3	684.3	684.3			

[a] Assuming apex angles of 142, 138, and 135° for Ga_2O, InOGa, and In_2O, respectively, and force constants (mdyn/Å) given by (calculation I and II, respectively): $F(r_1)$, 3.45, 3.86; $F(r_2)$, 2.89, 3.41; $F(r_1r_1)$, 0.39, 0.80; $F(r_2r_2)$, 0.23, 0.74; $F(r_1r_2)$, 0.21, 0.67; $F_\phi/r_1{}^2$, 0.19, 0.023; $F_\phi/r_2{}^2$, 0.18, 0.020; F_ϕ/r_1r_2, 0.18, 0.018; Fr_ϕ/r, 0.0, 0.0. r_1 refers to r_{Ga-O} and r_2 refers to r_{In-O}. [b] From electron diffraction, ref 6. [c] Values derived from this work.

These results may be compared with the related experiments of Carlson, *et al.*, in which samples of Ga_2O_3 mixed with indium metal were vaporized and the products isolated in low-temperature matrices. In addition to showing absorptions assigned to "pure" indium and gallium oxide species, their nitrogen matrix spectra show a prominent band at 783.0 cm^{-1} and a weaker feature at 544.2 cm^{-1}, both of which are assigned to InOGa. Our experiments confirm their assignment of the 783.0-cm^{-1} band, but we believe that their 544.2-cm^{-1} band should be assigned to a mixed metal dimer as it lies in the same region of the spectrum as the Ga_4O_2 and In_4O_2 vibrations described earlier. A band at 543 cm^{-1} was observed in our indium-rich alloy experiments (Table II).

Force Constant Calculations and Molecular Structures

The general valence force field for a C_{2v} triatomic molecule XY_2 contains four independent force constants[15]

$$2V = F_r(\Delta r_a{}^2 + \Delta r_b{}^2) + 2F_{rr}\Delta r_a\Delta r_b + F_\phi\Delta\phi^2 + 2F_{r\phi}\Delta\phi(\Delta r_a + r_b)$$

and for nonlinear XYZ, two further parameters are required to describe the vibrations. There are clearly insufficient data from these experiments to attempt a unique solution for the three species Ga_2O, In_2O, and InOGa, and a number of approximations must therefore be made.

Ga_2O and In_2O. If one assumes that for these C_{2v} molecules, the stretch-bend interaction constant $F_{r\phi}/r$ is zero, it is then possible to solve the secular equations for Ga_2O and In_2O if one knows the three fundamental vibration frequencies for the ^{16}O species, and the apex angle $2\theta = \phi$. In these experiments, the apex angle used was obtained directly from ^{18}O data on ν_3, and two of the fundamentals of both $Ga_2{}^{16}O$ and $In_2{}^{16}O$ have been identified. A range of solutions is therefore possible depending upon the position of the (unobserved) bending mode ν_2. This vibration is presumed to lie below 200 cm^{-1} for both Ga_2O and In_2O, and Table III compares the frequencies observed for Ga_2O and In_2O with those calculated assuming first, that the bending frequencies lie in the range 140-200 cm^{-1}, and secondly, that they lie below 80 cm^{-1}. A comparison may then be made between the two sets of calculated force constants.

As expected, the most significant difference is observed in F_ϕ/r^2, but in contrast, the principal metal-oxygen stretching constants are only slightly affected. This analysis therefore suggests that an acceptable range of values for F_r is F_{Ga-O} = 3.65 ± 0.2 mdyn/Å and F_{In-O} = 3.15 ± 0.25 mdyn/Å, respectively, and that the interaction constants F_{rr} are always positive. These calculations have been made assuming that $F_{r\phi}/r$ = 0.0, but even if one allows this parameter to assume finite values in the range 0-0.1 mdyn/Å, the above conclusions remain valid.

Several empirical relationships exist between principal stretching force constants and internuclear distances, and in particular the Laurie-Herschbach equations[17]

$$r = a - b \log F_r$$

where a and b are tabulated constants, yield values of r_{Ga-O} = 1.81 ± 0.02 and r_{In-O} = 1.98 ± 0.03 Å, respectively, from F_{Ga-O} and F_{In-O}. These bond length estimates compare favorably with the electron diffraction data on Ga_2O and In_2O in the vapor phase and are included in Table III.

InOGa. For a nonlinear XYZ molecule, there is no straightforward method of determining the apex angle, and no attempt is made to solve the secular equations for InOGa directly. Instead, we have assumed that the apex angle in this molecule lies between the values obtained for Ga_2O and In_2O and that the principal force constants F_{Ga-O} and F_{In-O} in InOGa may be directly transferred from Ga_2O and In_2O. With these constraints, and the assumption that stretch-bend interaction constants are zero, it is possible to solve for the interaction constant $F(r_1r_2)$ and the bending constant F_ϕ/r_1r_2 using the observed frequencies of $In^{16}OGa$ and $In^{18}OGa$. If the assumption regarding transferability of F_{Ga-O} and F_{In-O} is valid, the values of $F(r_1r_2)$ and F_ϕ/r_1r_2 obtained should be similar to the corresponding parameters in Ga_2O and In_2O. The results shown in Table III clearly show that this is true for both sets of force constant data.

In practice, it is unlikely that the principal stretching constants are exactly transferable, but the fact that the

vibrations of InOGa can be reproduced using parameters derived essentially from Ga_2O and In_2O indicates that the bonding in all these species is rather similar. These results may also be compared with the corresponding group I oxides Li_2O, Na_2O, K_2O, and Cs_2O in which the metals are also in a formal oxidation state of +I. The ir spectra of all these species have recently been obtained by Andrews, *et al.*,[18] and they conclude that the apex angles in these molecules vary from 180° (Li_2O) to ~140° (Cs_2O), and that the corresponding force constants range from 2.0 to 1.1 mdyn/Å, respectively. The similarity between these two sets of molecules seems rather close, and in contrast to the conclusions reached by Carlson there is no reason to invoke any form of metal-metal bonding in Ga_2O or In_2O to interpret the results described here.

Dimeric Species. The bands below 625 cm^{-1} have been assigned to dimer species on the basis of diffusion experiments and the observation that in the pure Ga–O and In–O systems, ^{18}O enrichment indicates the presence of two equivalent oxygen atoms. Numerous geometries may be considered which fulfil this requirement but with the limited experimental data available, it is not possible to deduce or even confirm any one structure. However, it is known[19] that molecules such as R_3Ge–O–GaR_2 readily dimerize to give structures based on a four-membered Ga_2O_2 ring, and we believe that the structure of Ga_4O_2 is probably

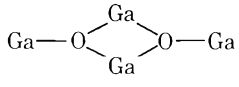

This type of dimer structure is frequently found in the study of triatomic systems[20] and if this is the structure adopted by Ga_4O_2, one might expect a total of nine dimer-type molecules $Ga_xIn_{4-x}O_2$ (x = 0–4) to be produced in experiments where monomeric Ga_2O, In_2O, and InOGa are all present. Our experiments show (Table II) that at least nine bands are observed in the alloy–O_2 systems, and their intensities appear to vary *independently*, which indicates that they arise from different molecular species. Two of these bands, however, were always very weak, and their assignment remains tentative. A number of isomers are possible for these mixed species, and in particular, $Ga_2In_2O_2$ could be

A

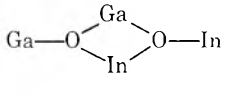

B

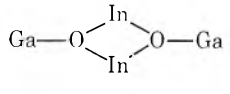

or

C

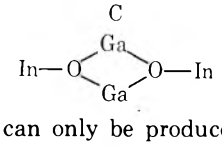

Isomers B and C can only be produced by the dimerization of InOGa, but an alternative route to A is afforded by Ga_2O + In_2O, and this isomer is in fact the *only* mixed dimer which can be formed in the double tube experiment (Figure 3d). The fact that InOGa appears to react rather slowly in controlled diffusion experiments (Figures 3b, c) may possibly explain why some bands are more predominant than others in Table II.

Detailed force constant calculations were not attempted for any of these dimer species, but the frequency shifts observed for Ga_4O_2 and In_4O_2 on ^{18}O substitution are consistent with the assignment of these bands as metal–oxygen vibrations.

Conclusions

These experiments show that for the Ga–In–O systems described here, the simple triatomic molecules Ga_2O, In_2O, and InOGa are the most important oxide species found in low-temperature matrices, but that dimeric species with the general formula $Ga_xIn_{4-x}O_2$ may also be present if isolation is poor or controlled diffusion is allowed to take place.

It is shown that some bands previously assigned as fundamentals of Ga_2O, In_2O, and InOGa must be reassigned to these dimer molecules, and with the aid of ^{18}O enrichment, a revised normal coordinate analysis is presented for Ga_2O, In_2O, and InOGa. The structures of these molecules are discussed in the light of this analysis, and while it is not possible to reach a firm conclusion regarding the value of the apex angle in Ga_2O or In_2O, the assignment of weak bands at 472 and 442 cm^{-1} to the ν_1 modes in these species indicates that the molecules are bent, and estimates of 142 and 135° are suggested as lower limits.

The two oxygen atoms in the dimer species Ga_4O_2 and In_4O_2 are shown to be equivalent, and a structure is proposed for these molecules which is based on a four-membered ring.

Acknowledgments. We gratefully acknowledge the financial support of the Science Research Council and the Central Electricity Generating Board for this work.

References and Notes

(1) R. P. Burns, *J. Chem. Phys.*, **44**, 3307 (1966).
(2) R. P. Burns, G. DeMaria, J. Drowart, and M. G. Inghram, *J. Chem. Phys.*, **38**, 1035 (1963).
(3) S. A. Shchukarev, G. A. Semenov, and I. A. Rat'kowski, *Russ. J. Inorg. Chem.*, **14**, 1 (1969).
(4) S. A. Shchukarev, G. A. Semenov, and I. A. Rat'kowski, *Zh. Prikl. Khim.*, **35**, 1454 (1962).
(5) F. J. Kohl and C. J. Stearns, unpublished observations quoted in ref 10.
(6) N. G. Rambidi and S. M. Tolmachev, *Teplofiz. Vys. Temp.*, **3**, 487 (1965).
(7) N. G. Rambidi and Y. S. Ezhov, *Zh. Strukt. Khim.*, **9**, 363 (1968).
(8) A. A. Mal'tsev, and V. F. Shevel'kov, *Teplofiz. Vys. Temp.*, **2**, 650 (1964).
(9) A. J. Hinchcliffe and J. S. Ogden, *Chem. Commun.*, 1053 (1969).
(10) D. M. Makowiecki, D. A. Lynch, Jr., and K. D. Carlson, *J. Phys. Chem.*, **75**, 1963 (1971).
(11) A. J. Hinchcliffe and J. S. Ogden, *J. Phys. Chem.*, **75**, 3908 (1971).
(12) J. S. Anderson and J. S. Ogden, *J. Chem. Phys.*, **51**, 4189 (1969).
(13) See, for example, "Vapor Pressure of the Chemical Elements," A. N. Nesmayanov and R. Gary, Ed., Elsevier, New York, N. Y., 1963.
(14) M. Allavena, R. Rysnik, D. White, V. Calder, and D. E. Mann, *J. Chem. Phys.*, **50**, 3399 (1969); J. Overend, *Ann. Rev. Phys. Chem.*, **21**, 265 (1970).
(15) See, for example, G. Herzberg, "Molecular Spectra and Molecular Structure," Vol. II, Van Nostrand, New York, N. Y., 1964, pp 229, 148.
(16) G. Herzberg, "Molecular Spectra and Molecular Structure," Vol. I, Van Nostrand, Princeton, N. J., 1959.
(17) D. R. Herschbach and V. W. Laurie, *J. Chem. Phys.*, **35**, 458 (1961).
(18) R. C. Spiker and L. Andrews, *J. Chem. Phys.*, **58**, 713 (1973).
(19) B. Armer and H. Schmidbaur, *Chem. Ber.*, **100**, 1521 (1967).
(20) J. W. Hastie, R. Hauge, and J. L. Margrave In "Spectroscopy in Inorganic Chemistry," Vol. I, C. N. R. Rao and J. R. Ferraro, Ed., Academic Press, New York, N. Y., 1970.

Formation Constants for Aniline–Tetracyanoethylene Charge-Transfer Complexes

P. G. Farrell* and Phi-Nga Ngô

Department of Chemistry, McGill University, Montreal 101, Canada *(Received May 22, 1973)*

Publication costs assisted by the National Research Council of Canada

The formation constants and extinction coefficients for the charge-transfer complexes formed between tetracyanoethylene and various anilines have been determined by the usual graphical methods and by two iterative methods. One of the latter methods, a "hill-climbing" optimization procedure devised by Rosenbrock, has not previously been applied to charge-transfer complexes. The methods are compared in terms of the final results and the Rosenbrock technique is shown to be an alternative to the non-linear least-squares method. The properties of the π complexes are discussed.

Introduction

In studies of charge transfer, or π complexes, one of the major sources of concern has been the discrepancies among published values of the formation constant, K_{CT}, and the molar extinction coefficient, ϵ_{CT}, for a given donor–acceptor system. For the system

$$A + D \overset{K_{CT}}{\rightleftharpoons} AD$$

where A, D, and AD are, respectively, the acceptor, donor, and 1:1 charge-transfer complex, spectroscopic determinations of K_{CT} and ϵ_{CT} are normally carried out with the donor in large excess, $[D]_0 \gg [A]_0$, or with equimolar concentrations. In the presence of a large excess of donor, if only the complex absorbs at the wavelength of measurement and Beer's law is obeyed by the complex, then the original Benesi–Hildebrand equation (eq 1),[1] or any of its alternative forms (*e.g.*, eq 2 and 3),[2,3] may be applied to

$$[A]_0/OD = 1/(K_{CT}\epsilon_{CT}[D]_0) + 1/\epsilon_{CT} \quad (1)$$

$$[D]_0[A]_0/OD = [D]_0/\epsilon_{CT} + 1/(K_{CT}\epsilon_{CT}) \quad (2)^2$$

$$OD/([D]_0[A]_0) = -OD\,K_{CT}/[A]_0 + K_{CT}\epsilon_{CT} \quad (3)^3$$

the experimental data. (OD is the absorbance at the wavelength of interest.) Under equimolar conditions $[D]_0 = n[A]_0$, where $n \simeq 1$, and eq 4 may be derived from a

$$[A]_0/OD = (n + 1)/(n\epsilon_{CT}) + 1/(nK_{CT}\epsilon_{CT}[A]_0) \quad (4)$$

consideration of the donor–acceptor equilibrium shown above.[4] From each of the above equations a linear plot, which allows the evaulation of K_{CT} and ϵ_{CT}, may be obtained. However, results obtained graphically using any of these equations often show an apparent dependence of K_{CT} and ϵ_{CT} on the donor and acceptor concentrations, *although their product remains constant.*[5] In some systems, where $[D]_0 \gg [A]_0$, an apparent dependence of K_{CT} upon the wavelength of measurement has been reported.[6–9]

Numerous tentative explanations for these anomalies have been proposed and these fall into two categories. The first of these suggests that the postulated model, which constitutes the basis of the determination, is inexact, *e.g.*, the nonobeyance of Beer's law by the complex,[7,10] specific solvation,[11,12] etc. The second category critically examines the graphical methods, especially eq 1, to determine the optimum conditions for their use, *e.g.*, equimolar donor and acceptor concentrations,[4] a saturation fraction[13] of the most dilute component (= $[AD]/[A]_0$) between 0.2 and 0.8, etc. In spite of the problems of interpretation of the experimental data, spectroscopic studies of π complexes (including nmr studies) are still very extensively employed because of their technical simplicity. It is therefore somewhat surprising that iterative techniques have not been more widely used for the evaluation of K_{CT} and ϵ_{CT} from such experimental data.[14–17] Rosseinsky and Kellawi[14] applied the non-linear least-squares (NLLS) treatment to published data in a reevaluation of some K_{CT} and ϵ_{CT} values, and in some systems found results that differed considerably from those obtained graphically, but there have been few other applications of this method. With the increasing availability of computing facilities iterative techniques may be more widely utilized and we report here the application of the "hill-climbing" optimization method due to Rosenbrock[18] for the evaluation of K_{CT} and ϵ_{CT} values. We are unable to find any previous application of this method to charge-transfer complexes and the essential details of the method are given in Appendix I.[19] To confirm the applicability of the method, we have calculated K_{CT} and ϵ_{CT} for all the systems studied by Rosseinsky, together with some additional systems which had previously only been analyzed by graphical methods.

The Rosenbrock method has been applied here in a study of the charge-transfer complexes formed by aniline and some of its derivatives with tetracyanoethylene (TCNE). It has been suggested that the irreversible reaction occurring in these systems proceeds *via* the π complex[20] and accurate values of K_{CT} and ϵ_{CT} are therefore necessary for the evaluation of the kinetic and thermodynamic parameters for the systems.

Results

(*i*) *TCNE-Aniline System.* Dichloromethane was used as solvent for all experiments. TCNE and aniline undergo an irreversible reaction in dichloromethane, *via* the π complex, to yield *N*-tricyanovinylaniline. The reaction has been studied kinetically and the decay of the π complex follows first-order kinetics when aniline is in large excess.[20] Thus, extrapolation of the first-order plot to the time of mixing yields the absorbance due to the π complex prior to any reaction. Values of K_{CT}, ϵ_{CT}, and $K_{CT}\epsilon_{CT}$ obtained under the condition $[D]_0 \gg [A]_0$ at four tempera-

TABLE I: Values of K_{CT} and ϵ_{CT} Obtained from both Graphical and Iterative Methods for the Aniline–TCNE Complex in Dichloromethane[a]

Method	$K_{CT}\epsilon_{CT}$	K_{CT}, M^{-1}	ϵ_{CT}, M^{-1} cm^{-1}	Correl. coeff.	$\Sigma(OD_{obsd} - OD_{calcd})^2 \times 10^4$	Temp, °C
Eq 1	5820	2.30 ± 0 13	2530 ± 122	0.9990		25.4
Eq 2	5800	2.25 ± 0.12	2575 ± 168	0.9870		
Eq 3	5805	2.26 ± 0.12	2570 ± 136	0.9774		
Rosenbrock	5770	2.20	2620		3.87	
NLLS	5730	2.20 ± 0.13	2622 ± 11		3.86	
Eq 1	6380	2.50 ± 0.12	2550 ± 103	0.9992		20.7
Eq 2	6320	2.40 ± 0.12	2630 ± 100	0.9885		
Eq 3	6311	2.39 ± 0.12	2640 ± 132	0.9807		
Rosenbrock	6340	2.43	2610		4.79	
NLLS	6320	2.42 ± 0.15	2619 ± 117		4.76	
Eq 1	7080	2.60 ± 0.15	2730 ± 126	0.9990		16.8
Eq 2	7112	2.66 ± 0.15	2678 ± 114	0.9866		
Eq 3	7081	2.61 ± 0.15	2720 ± 156	0.9763		
Rosenbrock	7120	2.67	2670		4.91	
NLLS	7120	2.65 ± 0.16	2684 ± 120		4.92	
Eq 1	7670	3.04 ± 0.19	2525 ± 121	0.9985		15.0
Eq 2	7480	2.74 ± 0.18	2730 ± 129	0.9837		
Eq 3	7497	2.79 ± 0.18	2680 ± 173	0.9714		
Rosenbrock	7420	2.70	2752		5.16	
NLLS	7550	2.52 ± 0.19	2894 ± 158		4.81	

[a] $[A]_0 \ll [D]_0$.

TABLE II: Typical Values of the Equilibrium Constant, K_{CT}, for Aniline–TCNE Charge-Transfer Complex Formation

System (temp, °C)	$K_{CT}\epsilon_{CT}$	ϵ_{CT}	K_{CT},[a] M^{-1}	K_{CT},[b] M^{-1}
Aniline–TCNE (25.4°)				
Set I	5960	453 ± 95	13.16 ± 2.92	2.25
Set II	6130	700 ± 97	8.76 ± 1.30	2.31
[N,N-$^2H_2$]-Aniline–TCNE (25.4°)				
Set I	5940	1100 ± 134	5.40 ± 1.03	2.24
Set II	6080	880 ± 96	6.91 ± 1.67	2.30
Aniline–TCNE (20.7°)	6380	1062 ± 368	6.01 ± 2.01	2.41

[a] Values obtained from eq 4. This equation is derived assuming that $[AD] \ll [A]_0$ and this is not true in practice when $K \simeq 2$. These data thus reveal in part errors arising from the use of eq 4 and errors arising from working at all times at the upper concentration limit of A. When $D_0 \simeq A_0$ then [AD] is very small and the errors in the data are maximized. [b] Derived from values of $K_{CT}\epsilon_{CT}$ given by eq 4, assuming $\epsilon_{CT} = 2650$.

TABLE III: Values of the Equilibrium Constant K_{CT} for the Aniline–TCNE Complex at Various Temperatures[a]

Temp, °C	$[D]_0 = [A]_0$ eq 4	$[D]_0 \gg [A]_0$					
		Eq 1	Eq 2	Eq 3	Rosenbrock	NLLS	Average
25.4	2.30	2.22	2.23	2.23	2.17	2.17	2.22 ± 0.03
20.7	2.41	2.41	2.39	2.40	2.40	2.40	2.40 ± 0.01
16.8		2.68	2.69	2.68	2.70	2.70	2.69 ± 0.01
15.0		2.90	2.83	2.83	2.80	2.85	2.84 ± 0.03

[a] Based on $\epsilon_{CT} = 2650$.

tures, by both graphical and iterative methods, are given in Table I. Assuming that ϵ_{CT} is constant within the experimental temperature range (15.0–25.4°), an average value was calculated from the results. This average value (ϵ_{CT} = 2650 ± 46) was then used to calculate K_{CT} from the products $K_{CT}\epsilon_{CT}$.

Under equimolar conditions the π complex reacts very slowly and the absorbance at zero time may be obtained by linear extrapolation of the absorbance *vs.* time curve. Table II shows typical K_{CT} and ϵ_{CT} values obtained from eq 4, together with K_{CT} values obtained assuming ϵ_{CT} = 2650.

Average values of K_{CT} derived by the different methods at four temperatures are shown in Table III. From the linear variation of ln $K_{CT}\epsilon_{CT}$ *vs.* $1/T$ the enthalpy of complex formation was estimated to be −4.20 ± 0.26 kcal mol^{-1} and hence the entropy to be −12.50 ± 0.90 eu (at 25.4°).

An examination of the [N,N-$^2H_2$]-aniline–TCNE system showed no differences in the derived K_{CT} and ϵ_{CT} values between the deuterated and protiated species, indicating the absence of any isotope effect upon complex formation.

(*ii*) *TCNE-Substituted Aniline Systems.* The long wavelength absorption maxima, K_{CT}, and ϵ_{CT} values for

TABLE IV: Values of K_{CT} and ϵ_{CT} Obtained from Both Graphical and Iterative Methods for the Complexes of TCNE with Some Aniline Derivatives in Dichloromethane at 25.4°[a]

Method	$K_{CT}\epsilon_{CT}$	K_{CT}, M^{-1}	ϵ_{CT}, M^{-1} cm^{-1}	Correl. coeff.	$\Sigma(OD_{obsd} - OD_{calcd})^2 \times 10^4$
		p-Chloroaniline			
Eq 1	1,840	0.41 ± 0.10	4,500 ± 1070	0.9995	
Eq 2	1,850	0.50 ± 0.10	3,740 ± 731	0.8595	
Eq 3	1,848	0.48 ± 0.10	3,850 ± 802	0.8427	
Rosenbrock	7,636	0.76	10,100		2.59
NLLS	6,716	0.0776 ± 0.0026	86,546 ± 1878		21.8
		p-Methylaniline			
Eq 1	13,600	4.74 ± 0.35	2,875 ± 173	0.9992	
Eq 2	13,600	4.70 ± 0.31	2,900 ± 193	0.9862	
Eq 3	13,615	4.83 ± 0.35	2,840 ± 207	0.9767	
Rosenbrock	13,710	4.98	2,753		0.634
NLLS	13,765	5.02 ± 0.39	2,742 ± 158		0.648
		p-Methoxyaniline			
Eq 1	20,200	12.20 ± 3.57	1,660 ± 396	0.9870	
Eq 2	19,000	9.25 ± 0.53	2,060 ± 241	0.9436	
Eq 3	19,100	9.50 ± 1.67	2,010 ± 353	0.8842	
Rosenbrock	18,493	8.52	2,168		1.98
NLLS	18,506	8.54 ± 1.28	2,167 ± 225		1.99

[a] $[A]_0 \ll [D]_0$.

the π complexes formed between *p*-chloroaniline, *p*-toluidine, and *p*-anisidine in dichloromethane were determined at 25.4°, and the results are shown in Table IV.

Discussion

A comparison of the results obtained by the different graphical methods and the two iterative techniques is made initially, followed by detailed discussion of the aniline–TCNE system.

Graphical Methods. With large excess of donor, eq 1–3 have all been used to evaluate K_{CT} and ϵ_{CT}. The results derived from one equation may be used as a check against those computed from the others and each result shows for aniline that all three equations yield very similar values for $K_{CT}\epsilon_{CT}$ within a system, but that the separate values are not in good agreement. This confirms the conclusions of other workers who have discussed at length the insensitivity of the Benesi–Hildebrand equation to both experimental errors[10] and the existence of species other than the 1:1 complex.[6,21] Tables I and IV show that for all systems the Benesi–Hildebrand equation has the highest correlation whereas eq 3 has the lowest. This is also illustrated in Figures 1–3 where plots corresponding to the three equations are shown for the same set of data. These conclusions are also corroborated by the error analysis shown in Appendix II.[19] Hammond[22] showed that the effect of experimental errors increases markedly for small K_{CT} values so that any of the above equations becomes inapplicable, in practice, for weak donor–acceptor interactions.

From a comparison of results obtained by both optical and nmr studies, Foster[4] suggested that the most consistent K_{CT} values for π-complex formation are those derived from optical data when $[D]_0 = [A]_0$. In the present study this consistency has not been observed for the aniline–TCNE system (Table II) in spite of the very good linear data plots obtained experimentally.

Iterative Techniques. The results of Tables I and IV show that the Rosenbrock and NLLS methods yield very close values of $K_{CT}\epsilon_{CT}$ together with the same function minima, with the exception of the *p*-chloroaniline–TCNE systems. Such agreement is gratifying especially as the NLLS is an analytical method whereas the Rosenbrock is a direct search method, entirely heuristic in nature. Although in the present work the two methods have only been applied to optical data obtained under the condition

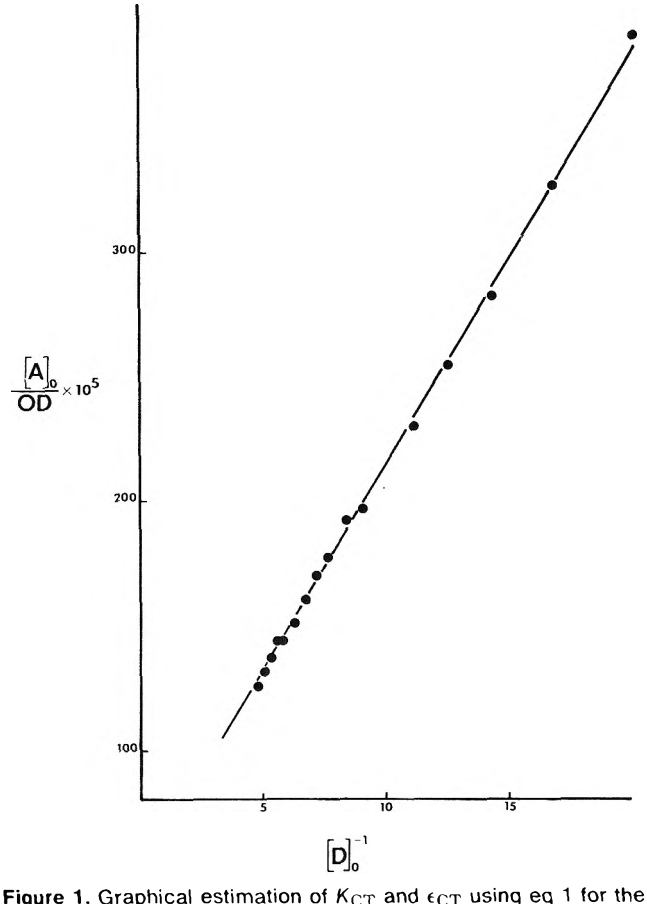

Figure 1. Graphical estimation of K_{CT} and ϵ_{CT} using eq 1 for the aniline–TCNE complex in dichloromethane at 25.4°, the donor being in excess.

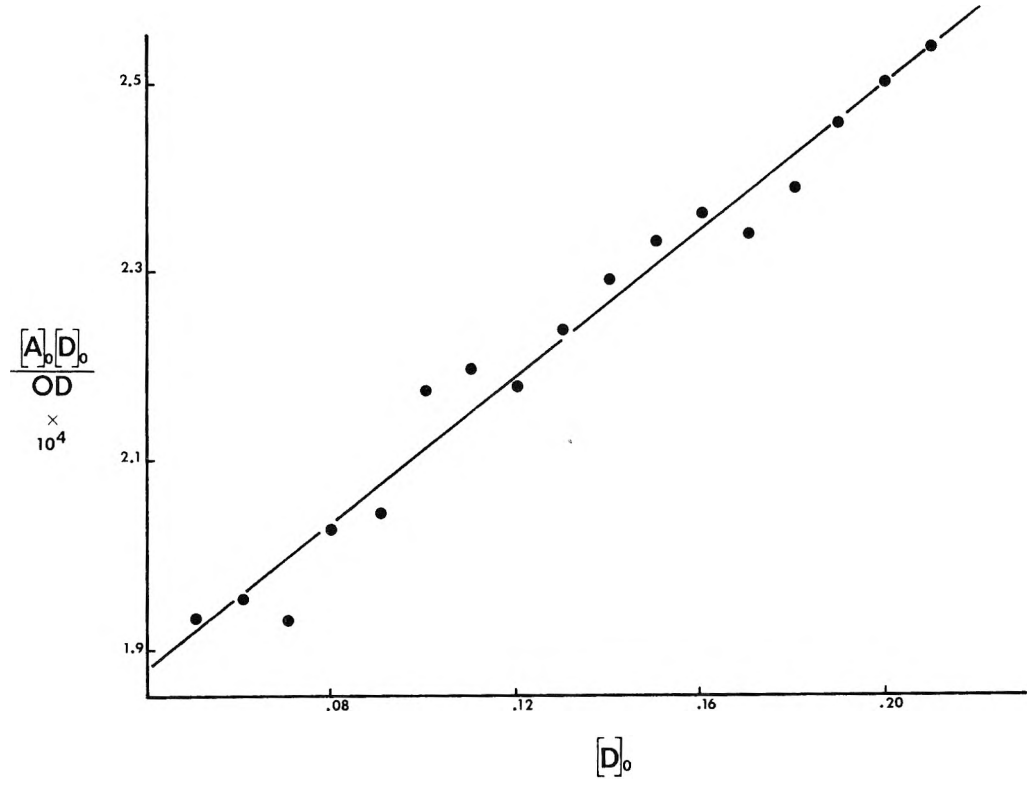

Figure 2. Graphical estimation of K_{CT} and ϵ_{CT} using eq 2 for the aniline–TCNE complex in dichloromethane at 25.4°, the donor being in excess.

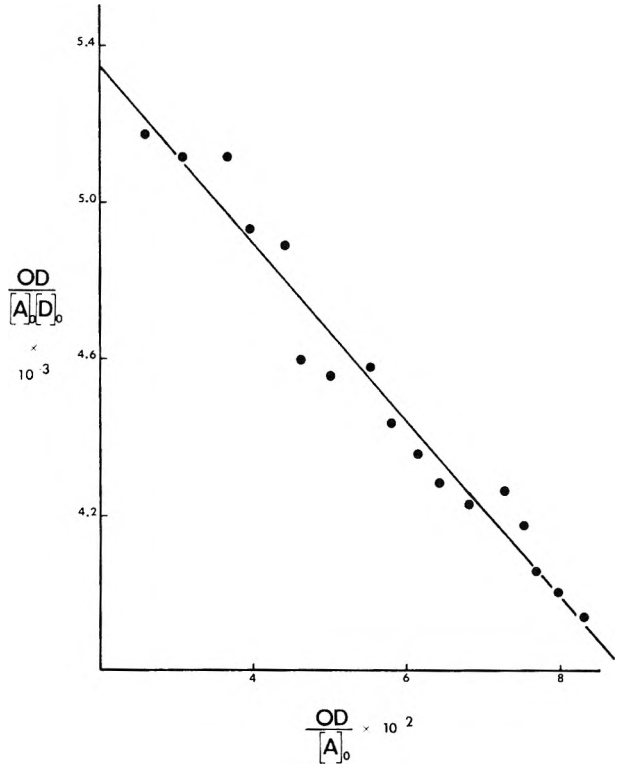

Figure 3. Graphical estimation of K_{CT} and ϵ_{CT} using eq 2 for the aniline–TCNE complex in dichloromethane at 25.4°, the donor being in excess.

$[D]_0 \gg [A]_0$, they may also be applied to data obtained under equimolar concentration conditions.

In order to compare more widely the results obtained by both the Rosenbrock and the NLLS technique a number of data reported in the literature has been reanalyzed. The results are reported in Table VI[19] and a comparison of these techniques is limited to a comparison of the final estimates of K_{CT} and ϵ_{CT}. Neither method requires any assumptions to be made in the appropriate equations although in the derivation of the y function in the Rosenbrock program $[D]_0 - [AD] \simeq [D]_0$ was assumed. As evidenced by the agreement in the results obtained by the two methods, this assumption was valid. No such assumption was made in the NLLS method.

The Rosenbrock method has the general advantage over the NLLS method in that it does not require a computation of first derivatives. For the assumed model of a 1:1 charge-transfer complex this would not be a problem, but may be more difficult or even impossible in other more complex systems. The obvious disadvantage of the Rosenbrock method is that there is no simple way of estimation of the errors in the computed parameters. The only indication of the fit of the experimental data to the model is the resulting value of the function minimum, y. Standard deviations are readily computed in the NLLS method in addition to the function minima and an examination of Table VI shows that, of the 26 systems studied, the two methods gave identical estimates of K_{CT} and ϵ_{CT}, within the limits of error of the NLLS method, for 19 of these. For some of the remaining systems, the NLLS program did not converge while the Rosenbrock method gave results which are in good agreement with those obtained by graphical methods (entries 3, 7, and 15).

A close examination of the data of this table shows that the values obtained by the Rosenbrock technique are always within the errors estimated by the NLLS method and we have therefore assumed that the obtained values are acceptable. In all cases the accuracy of the experimental data provides the limitation upon the accuracy of the obtained results and an indication of this is given by the value of the function minimum y.

TABLE V: Ranges of Saturation Fraction Studied, Wavelengths of Maximum Absorption, Equilibrium Constants, and Molar Extinction Coefficients for the Various Aniline–TCNE Charge-Transfer Complexes in Dichloromethane at 25.4°

Amine	s	$\lambda_{max,CT}$, nm	Av K_{CT}, M^{-1}	Av ϵ_{CT}	pK_a[a]
p-Chloroaniline	0.03–0.08	580	~0.50	~4000	4.07
Aniline	0.10–0.32	600	2.22	2650	4.60
p-Methylaniline	0.11–0.30	652	4.85	2820	5.03
p-Methoxyaniline	0.05–0.42	700	9.58	2010	5.40

[a] Reference 34.

Graphical Methods and Iterative Techniques. The results for the aniline–TCNE system under conditions of excess donor show that the graphical methods and the iterative techniques all yield very similar values of the products, $K_{CT}\epsilon_{CT}$, and also of the separated values. The final values of K_{CT} were computed from the products using the value of ϵ_{CT} = 2650. The consistency between the K_{CT} values obtained by this method is shown in Table III.

From the results of the present study, the best analysis of optical data for 1:1 complex formation seems to be a combination of both graphical and iterative techniques. The graphical presentation assists in the detection of systematic errors, *e.g.*, curvature, and also provides the initial guesses needed for the iterative methods. If the experimental data are reliable these latter methods yield good values of $K_{CT}\epsilon_{CT}$, provided that the postulated model is correct. It still however remains true that the limits of accuracy of all the methods are determined by the experimental conditions. This has been emphasized by other workers, in particular Person[23] who emphasized that the equilibrium concentration of the charge-transfer complex should be of the same order of magnitude as the equilibrium concentration of the more dilute component of the system. This same principle was expressed by Deranleau[13] as a function of the saturation fraction, s, of the most dilute component (= $[AD]/[A]_0$). He suggested that the theoretical minimum errors in K_{CT} and ϵ_{CT} would be obtained for solutions where the saturation fraction lies between 0.2 and 0.8, and that a study of 75% of the saturation curve is required to show the correspondence between the equation of the model and the equation fitting the data.

The ranges of saturation fraction studied for the different TCNE–aniline systems are shown in Table V. Although in no system both the upper and lower limits are within the range suggested by Deranleau, the stronger complexes all have upper limits greater than 0.2. The failure of the methods to provide a reliable value for K_{CT} for the *p*-chloroaniline–TCNE complex is probably due to the fact that the *maximum* value of s for this complex was less than 0.2. A large value of s corresponds to the use of high donor concentrations, and as this is not possible in a number of systems for practical reasons, such as the limited solubility of either donor or acceptor, the fast disappearance of the π complex with high donor concentration due to reaction, etc., greater errors in the determined values K_{CT} and ϵ_{CT} will result. Owing to the insolubility of *p*-chloroaniline in dichloromethane, an upper limit upon the concentration which may be used is established. For this reason the saturation curve could not be studied over the range which Deranleau suggested would show the correspondence between the model and the data equation.

Aniline–TCNE Charge-Transfer Complexes. In Table V some of the properties of the complexes formed between TCNE and the anilines used are shown. The data indicate an increase in $\lambda_{max,CT}$ and in K_{CT} in going from the weaker to the stronger bases. Increasing base strength is accompanied by lowering of the ionization potential of the amine, thus favoring an increased extent of complex formation. The enthalpy and the entropy of charge-transfer complex formation between aniline and TCNE compare well with those values for other similar amines such as *N,N*-dimethylaniline,[24] *N*-methylaniline,[25] and indole.[26] The values of K_{CT} and ϵ_{CT} for the aniline–TCNE and the *p*-chloroaniline–TCNE systems differ from those found by Isaacs,[27] but he did indicate that his values were "not of any great accuracy." The value for ϵ_{CT} for the *p*-methoxyaniline–TCNE complex is less than that for the other complexes shown in Table V, whereas the reverse should be true. Andrews and Keefer[28] observed a similar behavior in iodine–methylbenzene complexes in carbon tetrachloride and such an effect was attributed by Mulliken and Orgel to the occurrence of contact charge-transfer within the system.[29] This would lead to a greater apparent molar extinction coefficient, ϵ_{app}, which is related to the true extinction coefficient ϵ_{CT} by the expression

$$\epsilon_{app} = \epsilon_{CT}\left(1 + \frac{P}{K_{CT}}\right) \tag{5}$$

where $P = \alpha(\epsilon_{contact}/\epsilon_{CT})$, α being the number of possible contact sites for the component in excess around any molecule of the second species; $\epsilon_{contact}$ is the extinction coefficient for the contact charge-transfer process. The above equation implies that ϵ_{app} becomes increasingly greater than ϵ_{CT} as K_{CT} decreases. If this explanation applies to the data in Table V it would imply that the true ϵ_{CT} value for the *p*-methoxyaniline–TCNE complex may be close to 2010, whereas those for the aniline and *p*-methylaniline complexes should be much less than 2650 and 2820, respectively. An alternative possibility is that mixing of the charge-transfer excited state with excited states of either the donor or the acceptor occurs, as was proposed by Murrell.[30] The linearity of the plot of ln K_{CT} *vs.* T^{-1} for the aniline–TCNE system suggests that if either of these possibilities occur they are of relatively minor importance.

Isotope Effects in Charge-Transfer Complexes. An examination of Table II indicates that, within the experimental errors, there is no difference between the equilibrium constants and molar extinction coefficients of charge-transfer complexes of TCNE with aniline and [*N,N*-$^2H_2$]-aniline, and that both complexes have identical absorption maxima in dichloromethane. Substitution of deuterium on the nitrogen atom thus has no observable effect upon the spectroscopically measured properties of the π complex. Previous studies of the effect of isotopic replacement on the properties of charge-transfer complexes have suggested that indeed isotope effects should be observed. Thus the methyl deuteration of both toluene and *m*-xylene decreases the equilibrium constant for their complexes with chloranil by some 7%.[31] This inverse isotope

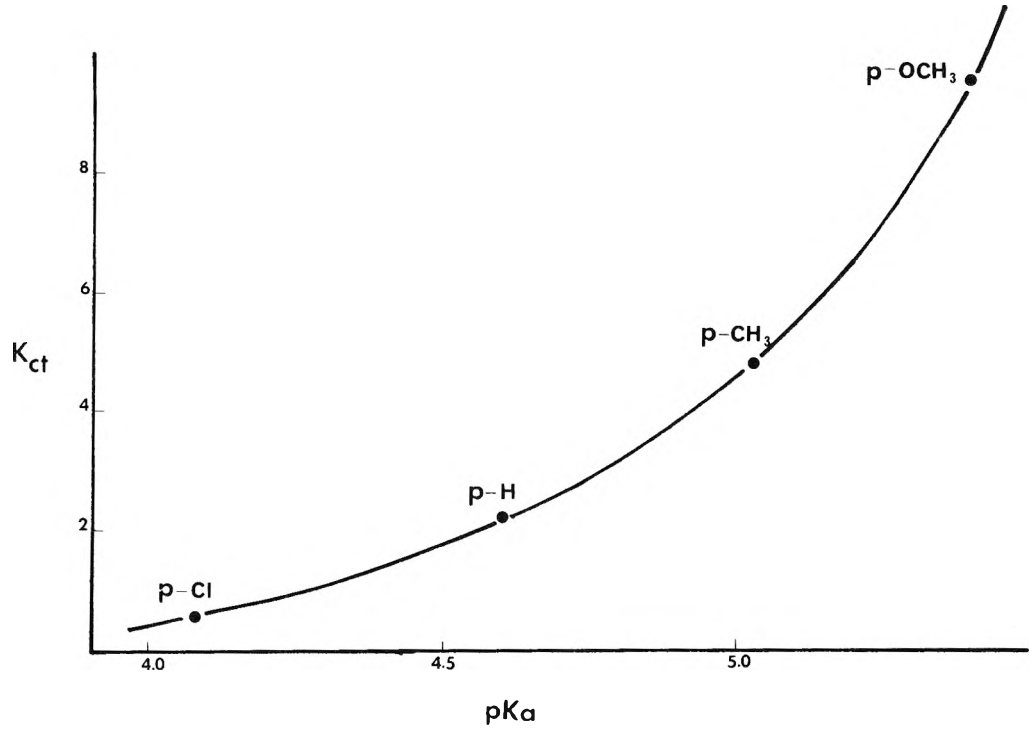

Figure 4. Variation of K_{CT} with pK_a of the donor for some aniline–TCNE complexes.

effect was assigned to a smaller hyperconjugative stabilization by trideuteriomethyl than by methyl, which is sufficient to overcome the inductive effect in the reverse direction. Emslie and Foster[32] reported a value of 0.73 at 22° for the ratio $K_{CT}(D)/K_{CT}(H)$ for complexes of TCNE with benzene and benzene-d_6. This is a significantly greater apparent effect from that observed for the chloranil complexes. It was proposed that deviations from Beer's law were the cause of the apparent isotope effect and the authors quoted as supporting evidence the equal enthalpies of formation and similar excitation energies for both complexes, the virtually identical ionization potentials of benzene and benzene-d_6,[33] and the absence of any isotope effect in the equilibrium constants of the complexes of these donors with 1,3,5-trinitrobenzene obtained by nmr studies.[34]

It is of interest to note that the products $K_{CT}\epsilon_{CT}$ for both the benzene and benzene-d_6–TCNE complexes were identical and that the apparent isotope effect may arise in the separation of the values of K_{CT} and ϵ_{CT}. It would therefore be of interest to treat the data obtained for these complexes by one of the iterative methods discussed above.

Values of $K_{CT}(D)/K_{CT}(H)$ less than unity are surprising in the above systems where hyperconjugation cannot occur and especially as there is ample literature evidence for the greater inductive effect of deuterium as compared to protium.[35] In terms of electronic effects the transition energy for the complex of [N,N-$^2H_2$]-aniline with TCNE should be less and the equilibrium constant greater than those corresponding to protiated aniline. In the present system such differences may well exist but were not detectable because they fall within the limits of experimental error.

Zollinger, *et al.*,[36] measured the pK_a of aniline, 2,3,4,5,6-pentadeuterioaniline, and 2,4,6-trideuterioaniline and found respectively values of 4.714, 4.737, and 4.731 (in water at 20°, ionic strength = 0.10). These values indicate δpK_a differences of +0.023 and +0.017 between aniline and the pentadeuterio and trideuterio derivatives, respectively. N-deuteration should have a greater positive effect upon the pK_a value for aniline than should ring deuteration and we had previously estimated this as $\delta pK_a \simeq 0.1$. At the lower end of the curve of Figure 4 this would give rise to a difference in the K_{CT} values only marginally greater than the experimental error. However, the recently reported study of solvent isotope effects on the pK_a values of anilinium ions in aqueous sulfuric acid shows that $pK_a(D_2O) - pK_a(H_2O) = 0.56$ for aniline and [N,N-$^2H_2$]-aniline.[37] This value gives [N,N-$^2H_2$]-aniline a pK_a greater than that of p-toluidine and Figure 4 implies an isotope effect approaching 3 for $K_{CT}(D)/K_{CT}(H)$. Together with the experimental lack of any isotope effect, Figure 4 implies that the anilines studied here are predominantly π rather than n donors, and pK_a changes caused by N-substitution are not accommodated by this figure.

Effect of Solvent on Aniline–TCNE Complexes. In their early work on TCNE complexes, Merrifield and Phillips[38] suggested a competitive complex formation between TCNE and the solvent dichloromethane. They estimated that the equilibrium constant K_s between TCNE and the solvent would be 0.21 in mole fraction units, with chloroform as the standard solvent. More recently a value of $K_s = 0.29\ M^{-1}$ at 25° using carbon tetrachloride as standard has been obtained by other workers.[39] This latter work shows that competitive complex formation by the solvent has no effect upon the molar extinction coefficient, but that the equilibrium constant obtained by the Benesi–Hildebrand treatment is only an apparent value K_{app}, related to the true value by

$$K_{CT} = K_{app}(1 + [S]_0 K_s) \qquad (6)$$

where $[S]_0$ is the solvent concentration and K_s is the equilibrium constant for the TCNE–solvent complex. In the present study no account has been taken of competitive solvent interaction with TCNE as the basic analysis is not

affected by such competition. Furthermore, the kinetic analysis of this system[19] is not affected by solvent competition for TCNE, if this occurs. The linearity of the plot of $\ln K_{CT}\epsilon_{CT}$ *vs.* T^{-1} suggests that this process is negligible in the aniline–TCNE system.

Experimental Section

Materials. The amines and TCNE were purified commercial products, aniline being stored under nitrogen in a desiccator at 0° after fractional distillation. Dichloromethane (Fisher spectrograde) was dried for 1 day ($CaCl_2$) and distilled (bp 39.8°) immediately before use into polythene bottles.

Spectroscopic Measurements. Stock solutions of the reactants were prepared immediately before use at the appropriate temperature. Aliquots of these solutions were rapidly mixed in stoppered silica absorption cells (40 or 10 mm pathlength) contained in the constant-temperature cell housing of a Beckman DB spectrophotometer, the time at half-addition being taken as $t = 0$. The variation of the absorbance at a constant wavelength was then recorded. The temperature inside the reaction cell was measured by means of a copper–constantan thermocouple (±0.1°). For experiments using large excess of donor ($30 < [D]_0/[A]_0 < 400$), a series of runs at constant $[TCNE]_0$ and varying $[D]_0$ was studied at each temperature, and absorbance values used in eq 1–3 were obtained by extrapolation to zero time. For the determinations of K_{CT} and ϵ_{CT} using equimolar concentrations, a series of runs with constant $[D]_0/[A]_0$ values ($\simeq 1$) were studied. Absorbance values for use in eq 4 were again obtained by extrapolation to zero time.

Acknowledgments. We are grateful to the National Research Council of Canada for financial support, and to McGill University for the award of a McConnell Fellowship (to P. N. N.).

Supplementary Material Available. Appendices I and II and Table VI will appear following these pages in the microfilm edition of this volume of the journal. Photocopies of the supplementary material from this paper only or microfiche (105 × 148 mm, 20× reduction, negatives) containing all of the supplementary material for the papers in this issue may be obtained from the Journals Department, American Chemical Society, 1155 16th St., N.W., Washington, D. C. 20036. Remit check or money order for $3.00 for photocopy or $2.00 for microfiche, referring to code number JPC-73-2545.

References and Notes

(1) H. A. Benesi and J. H. Hildebrand, *J. Amer. Chem. Soc.*, **71**, 2703 (1949).
(2) R. L. Scott, *Recl. Trav. Chim. Pays-Bas*, **75**, 787 (1956).
(3) R. Foster, "Organic Charge-Transfer Complexes," Academic Press, London, 1965, p 131.
(4) R. Foster and I. C. B. Matheson, *Spectrochim. Acta, Part A*, **23**, 2037 (1967).
(5) S. D. Ross and M. M. Labes, *J. Amer. Chem. Soc.*, **79**, 76 (1957).
(6) G. D. Johnson and R. E. Bowen, *J. Amer. Chem. Soc.*, **87**, 1655 (1965).
(7) R. Foster and I. Horman, *J. Chem. Soc. B*, 171 (1966).
(8) H. Kuroda, T. Amano, I. Ikemoto, and H. Akamatu, *J. Amer. Chem. Soc.*, **89**, 6056 (1967).
(9) T. Matsuo and O. Higuchi, *Bull. Chem. Soc. Jap.*, **41**, 518 (1968).
(10) P. H. Emslie, R. Foster, C. A. Fyfe, and I. Horman, *Tetrahedron*, **21**, 2843 (1965).
(11) S. Carter, J. N. Murrell, and E. J. Rosch, *J. Chem. Soc.*, 2048 (1965).
(12) S. Carter, *J. Chem. Soc. A*, 404 (1968).
(13) D. A. Deranleau, *J. Amer. Chem. Soc.*, **91**, 4044 (1969).
(14) D. R. Rosseinsky and H. Kellawi, *J. Chem. Soc. A*, 1207 (1969).
(15) P. A. D. de Maine and R. D. Seawright, "Digital Computer Programs for Physical Chemistry," Vol. I and II, Macmillan, New York, N. Y., 1963.
(16) K. Conrow, G. D. Johnson, and R. E. Bowen, *J. Amer. Chem. Soc.*, **86**, 1025 (1964).
(17) W. E. Wentworth, W. Hirsch, and E. Chen, *J. Phys. Chem.*, **71**, 218 (1967).
(18) H. H. Rosenbrock, *Compt. J.*, (3), 175 (1960); H. H. Rosenbrock and C. Storey, "Computational Techniques for Chemical Engineers," Pergamon Press, London, 1966.
(19) See paragraph at end of paper regarding supplementary material.
(20) P. G. Farrell and P. N. Ngô, *J. Chem. Soc., Perkin Trans. 2*, 974 (1973).
(21) D. W. Tanner and T. C. Bruice, *J. Phys. Chem.*, **70**, 3816 (1966).
(22) P. R. Hammond, *J. Chem. Soc.*, 479 (1964).
(23) W. B. Person, *J. Amer. Chem. Soc.*, **87**, 167 (1965).
(24) Z. Rappoport, *J. Chem. Soc.*, 4498 (1963).
(25) Z. Rappoport and A. Horowitz, *J. Chem. Soc.*, 1348 (1964).
(26) R. Foster and P. Hanson, *Tetrahedron*, **21**, 255 (1965).
(27) N. S. Isaacs, *J. Chem. Soc. B*, 1053 (1966).
(28) R. M. Keefer and L. J. Andrews, *J. Amer. Chem. Soc.*, **74**, 4500 (1952).
(29) L. E. Orgel and R. S. Mulliken, *J. Amer. Chem. Soc.*, **79**, 4839 (1957).
(30) J. N. Murrell, *J. Amer. Chem. Soc.*, **81**, 5037 (1959).
(31) E. A. Halevi and M. Nussim, *J. Chem. Soc.*, 879 (1963).
(32) P. H. Emslie and R. Foster, *Tetrahedron*, **21**, 2851 1965).
(33) P. G. Wilkinson, *J. Chem. Phys.*, **24**, 917 (1956); *Can. J. Phys.*, **34**, 596 (1956).
(34) R. Foster and C. A. Fyfe, *Trans. Faraday Soc.*, **61**, 1626 (1965).
(35) *E.g.*, E. A. Halevi, M. Nussim, and A. Ron, *J. Chem. Soc.*, 866 (1963).
(36) C. Bernasconi, W. Koch, and H. Zollinger, *Helv. Chim. Acta*, **46**, 1184 (1963).
(37) J. L. Jensen and M. P. Gardner, *J. Phys. Chem.*, **77**, 1557 (1973).
(38) R. E. Merrifield and W. D. Phillips, *J. Amer. Chem. Soc.*, **80**, 2778 (1958).
(39) R. X. Ewall and A. J. Sonnessa, *J. Amer. Chem. Soc.*, **92**, 2845 (1970).

A Quantum Mechanical Treatment of Bond and Molecular Polarizabilities of Some Substituted Hydrocarbons with Ring and Chain Structures

Nitish K. Sanyal,* Parvez Ahmad, and L. Dixit

Department of Physics, University of Gorakhpur, Gorakhpur, 273001, India *(Received September 5, 1972; Revised Manuscript Received May 3, 1973)*

The one-dimensional semiempirical δ-function potential model of chemical binding, proposed by Lippincott and Stutman, has been applied to calculate the average molecular polarizabilities of some substituted hydrocarbons with ring and chain structures. The residual atomic polarizability degrees of freedom of these molecules vary from 7 to 58. Results have been discussed in the view of available experimental values reported by LeFevre and others.

Introduction

Lippincott and Stutman[1] proposed the use of a one-dimensional δ-function potential model to calculate the bond and molecular polarizabilities of simple systems. The model has been successfully applied to simple polyatomic molecules by Lippincott, *et al.*,[2] Nagarajan,[3] and Sanyal, *et al.*[4] These studies include such molecular geometries for which the residual atomic polarizability degrees of freedom (n_{df}, defined in ref 1) is relatively small (5–13). Beran and Kevan[5] have used this model to calculate the molecular polarizabilities of fluorocarbons, substituted fluorocarbons, ethers, esters, ketones, and aldehydes. Recently, Puranchandra and Ramamurthy[6] have extended the use of the δ-function model for the calculation of molecular polarizabilities of some substituted benzenes. In the present communication, we have examined the applicability of the δ-function potential model of chemical binding to relatively large organic molecules with ring and chain structures. The results have been compared with known experimental values of average molecular polarizabilities.

Polarizability Calculations

The general expression for molecular polarizability expressed in Cartesian coordinates is given by

$$\alpha = \frac{2}{3}\sum_{i\neq 0}\frac{(\mu_x)_i^2 + (\mu_y)_i^2 + (\mu_z)_i^2}{E_i - E_0} \tag{1}$$

where

$$(\mu_x)_i = \left(\psi_i^*\left|\sum_j ex_j\right|\psi_0\right) \tag{2}$$

e is the electronic charge, ψ_0 is the ground-state δ-function wave function, and E denotes the energy. Equation 2 is difficult to evaluate in general, except in the case of diatomic systems where the accurate wave functions give rise to calculated polarizabilities that show reasonable agreement with the experimental ones.[7,8] To calculate the molecular polarizabilities for the general class of polyatomic molecules, Lippincott and Stutman[1] used the semiempirical δ-function model of chemical binding.[9,10] The δ-function model was obtained by replacing the coulomb potentials in the Schrodinger equation of a molecular system with δ-function potentials. The molecular wave functions are obtained from linear combinations of atomic δ-function wave functions.

On the basis of the variational treatment[11] first introduced by Hylleraas[12] and Hasse,[13] the xx component of the polarizability is expressed in the form

$$\alpha_{xx} = \frac{4nA}{a_0}[\overline{(x_1 - \bar{x})^2} - (n-1)\overline{(x_1 - \bar{x})(x_2 - \bar{x})}]^2 \tag{3}$$

where x is the coordinate of any one of n equivalence class of electrons which falls in the first equivalence class, $\bar{x}$ is the average coordinate of any one of these electrons, A is the δ-function strength determined[9] from the reduced electronegativity of the atom, and a_0 is the radius of the first Bohr orbit. Since the δ-function wave function does not allow any interaction between the coordinates, $(x_1 - \bar{x})(x_2 - \bar{x}) = 0$. The model with the mean δ-function strength predicts $\bar{x} = 0$, so eq 3 becomes

$$\alpha_{xx} = \frac{4nA}{a_0}\overline{[x_1^2]}^2 \tag{4}$$

or equivalently

$$\alpha_{xx} = \frac{4nA}{a_0}\overline{[x_i^2]}^2 \tag{5}$$

Molecular polarizability consists of parallel and perpendicular components of the constituent bond polarizabilities. The bond parallel component is obtained from the contributions by the bonding and nonbonding electrons of the valence shell. The contribution of bonding electrons is calculated by using a linear combination of atomic δ-function wave functions representing the nuclei involved in the bond; *i.e.*, the expectation value of electronic position squared ($\overline{x^2}$) along the bond axis is calculated, and this is used to evaluate the parallel component of bond polarizability $\alpha_{\parallel b}$ from the equation

$$\alpha_{\parallel b} = \frac{4nA_{12}}{a_0}\overline{[x^2]}^2 \tag{6}$$

where

$$\overline{x^2} = \frac{1}{4}R^2 + \frac{1}{2C_{R_{12}}^2};\ A_{12} = (A_1A_2)^{1/2} \tag{7}$$

n is the bond order, R is the internuclear distance at the equilibrium configuration, and

$$C_{R_{12}} = (n_1n_2N_1N_2)^{1/4}(A_1A_2)^{1/2} \tag{8}$$

where n_i and N_i ($i = 1, 2$) represent the principal quantum number and the number of electrons making the con-

tribution to the binding, respectively. For a heteronuclear bond, a polarity correction must be made in the parallel component of the bonding electrons to account for the charge density introduced by the electronegativity difference of the atoms. The degree of polarity ρ defined by Pauling[14] is given as

$$\rho = 1 - e^{-1/4}(X_1 - X_2)^2 \quad (9)$$

The charge density in the bond region then should be related to the per cent covalent character, σ

$$\sigma = e^{-1/4}(X_1 - X_2)^2 \quad (10)$$

where X_1 and X_2 are the electronegativities of the atoms 1 and 2, respectively, on the Pauling[14] scale. The corrected value of parallel component of bond polarizability is given by

$$\alpha_{\|p} = \alpha_{\|b}\sigma \quad (11)$$

The contribution of nonbonded electrons is calculated by evaluating the contribution of electrons in the valence shell of each atom not involved in the bonding. Such calculations are made on the basis of the Lewis-Langmuir[15,16] octet rule modified by Linnett[17] in terms of a double quartet of electrons. This can be expressed as

$$\alpha_{\|n} = \sum_j f_j\alpha_j \quad (12)$$

where f_j is the fraction of the valence electrons in the jth atom not involved in the bonding and α_j is the atomic polarizability of jth atom.

The perpendicular component of the bond polarizability was obtained by an empirical approach made by Lippincott and Stutman,[1] which is expressed as

$$\sum 2\alpha_{\perp j} = \frac{3N - 2n_b}{N}\sum_j \alpha_j \quad (13)$$

where N is the number of atoms and n_b is the number of bonds in the molecule. Taking into account the polarity correction, the sum of the perpendicular components of the bond polarizability is given as

$$\sum 2\alpha_{\perp j} = (3N - 2n_b)\sum_j \frac{X_j^2\alpha_j}{X_j^2} \quad (14)$$

or

$$\sum 2\alpha_{\perp j} = n_{df}\sum_j \frac{X_j^2\alpha_j}{X_j^2} \quad (15)$$

where $n_{df} = (3N - 2n_b)$, the residual atomic polarizability degrees of freedom obtainable from the consideration of symmetry and geometry of the molecular type.

Now the average molecular polarizability with no bond polarity corrections can be written as

$$\alpha_M = \frac{1}{3}\left[\sum_i \alpha_{\|b_i} + \sum_j f_j\alpha_j + \frac{3N - 2n_b}{N}\sum_j \alpha_j\right] \quad (16)$$

and with bond polarity correction

$$\alpha_M = \frac{1}{3}\left[\sum_i \alpha_{\|p_i} + \sum_j f_j\alpha_j + n_{df}\sum_j \frac{X_j^2\alpha_j}{X_j^2}\right] \quad (17)$$

Equation 17 was used in the present calculation of average molecular polarizabilities.

Results and Discussion

Calculated values of molecular polarizabilities (in 10^{-25} cm^3) of formamide, acetamide, and the molecules of ring structure are given in Table I. The bond lengths were taken from the work of Sutton.[18] A bond order of 2.5 was used in nitrogen-oxygen (NO_2) bonds owing to the coordinate characteristic of the bonding. In order to discuss the computed results, it is worthwhile to consider the classes of molecules tackled pertaining to single, double, and triple rings and chain structures individually.

Single-Ring Molecules. In this class, the molecules examined are benzamide, aniline, *p*-toluidine, toluene, *p*-xylene, mesitylene, durene, hexamethylbenzene, pyridine, and halogen, nitro, and cyno derivatives of some of the above molecules. The n_{df} value for these molecules has been taken as 18 except in the case of pyridine, where it is 15. Here a contrived but justified consideration has been made that only nine bonds forming the ring are taken into account in the evaluation of n_{df} of benzene ($n_{df} = 3N - 2n_b = 36 - 18 = 18$) and it is assumed that whatever substitutions are made on the benzene ring, the n_{df} value remains constant.

It is evident from the results that in most of the molecules our calculated values are in reasonable agreement with experimental values.[19-28] The calculated value of polarizability for toluene (123.091, see Appendix) is in agreement with the experimental values reported by Landolt-Bornstein[19] (122.6) and LeFevre[20] (118.33).

Double-Ring Molecules. Molecular polarizabilities of naphthalene and its derivatives have been discussed here. The n_{df} value of this class has been determined on the same considerations as in the case of benzene. In naphthalene, there are 18 atoms and 16 bonds (forming the ring) and hence $n_{df} = 54 - 32 = 22$. The calculated value (163.94) of naphthalene is in good agreement with the experimental value (164.6) of LeFevre.[29] In the case of derivatives, experimental values are not available for the comparison but the calculated values seem to be reasonably accurate.

Triple-Ring Molecules. Anthracene and its derivatives belong to this class where three benzene rings are fused to each other. The n_{df} value of anthracene has been evaluated from the following considerations. (a) One benzene ring has 18 atomic polarizability degrees of freedom. (b) The second ring fused in the benzene ring contributes only four to the n_{df} value of the resulting molecule, as in the case of naphthalene.

The structure of anthracene shows two side rings attached by a third middle ring. The contribution to the n_{df} value by the two side rings will be 36 (by "a") and by the middle ring only 2 (by "b"). Hence the total value of n_{df} for anthracene will be 38. It is evident from Table I that the calculated values of molecular polarizabilities of anthracene and its derivatives are in reasonable agreement with experimental values.[30,31]

Molecular polarizabilities of phenazine and thianthrene have also been calculated. The structures of these molecules are

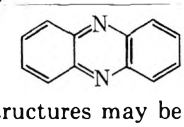
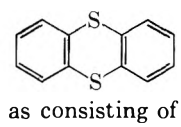

These structures may be treated as consisting of two benzene rings attached by two nitrogen and two sulfur atoms, respectively. Hence the n_{df} value of these molecules will be 36, the contribution of two benzene rings only. In the case of phenazine, the calculated value (234.87) is in excellent agreement with the experimental value (234.3).[28]

Molecules of Chain Structure. Table II represents the molecular polarizabilities (in 10^{-25} cm^3) of some alkyl

TABLE I: Calculated Values of Molecular Polarizabilities of Some Substituted Hydrocarbons (10^{-25} cm^3)

Molecules	$\Sigma \alpha_{\parallel}$	$\alpha_{\parallel n}$	$\Sigma 2\alpha_{\perp}$	α_M	α_M, obsd	Ref
Formamide	47.599	6.918	54.767	36.428	38.8	21
Acetamide	97.807	6.918	63.254	55.993	53.886	21
Benzamide	231.758	6.918	140.818	126.495	127.466	21
Aniline	208.667	2.772	143.397	118.346	115.3	22
p-Fluoroaniline	208.622	7.172	135.296	117.030	115.13	23
p-Chloroaniline	231.359	14.869	157.068	134.432	134.96	23
p-Bromoaniline	241.484	19.602	165.394	142.160	145.466	23
p-Iodoaniline	266.665	28.442	176.344	157.150	...	...
p-Nitroaniline	237.351	13.327	135.629	128.769	139.0	23
Difluoroaniline	208.577	8.400	129.062	115.346	...	...
Dichloroaniline	254.052	23.794	169.288	149.044	151.83	24
Dibromoaniline	274.301	33.260	185.599	164.387	...	...
Diiodoaniline	324.663	50.940	207.795	194.466	...	...
p-Toluidine	245.416	2.972	142.089	130.159	134.666	23
Dimethylaniline	284.314	2.972	141.148	142.812	152.333	24
Toluene	224.249	0.000	145.023	123.091	122.6	19
					118.33	20
p-Fluorotoluene	224.270	4.200	136.862	121.755	117.0	25
p-Chlorotoluene	246.942	11.897	158.333	139.057	137.0	25
p-Bromotoluene	257.067	16.630	166.509	146.735	148.0	25
p-Iodotoluene	276.262	25.470	177.256	159.663	171.0	25
p-Cyanotoluene	261.317	2.970	147.937	137.402	139.0	25
p-Nitrotoluene	260.507	10.355	136.937	135.926	141.0	25
p-Xylene	258.269	0.000	143.478	133.916	137.0	26
Mesitylene	300.838	0.000	142.359	147.732	153.76	27
Nitromesitylene	324.334	10.355	136.596	157.095	...	...
Durene	338.478	0.000	141.512	159.999	174.0	27
Hexamethyl-benzene	409.803	0.000	140.314	184.700	208.1	27
Pyridine	169.444	2.972	121.115	97.843	91.8	28
Naphthalene	307.307	0.000	184.520	163.942	164.6	29
1,5-Dichloro-naphthalene	333.211	23.794	209.332	188.779	...	...
1,5-Dinitro-naphthalene	363.506	20.710	175.162	186.459	...	...
β-Naphthol	337.001	3.946	178.476	173.141	...	...
Anthracene	435.958	0.000	322.486	252.800	253.6	30
9-Chloro-anthracene	470.212	11.897	339.188	273.766	273.466	30
9,10-Dichloro-anthracene	496.775	23.794	354.802	291.790	...	...
9-Bromo-anthracene	495.030	16.630	349.772	287.144	283.2	30
9,10-Dibromo-anthracene	536.179	33.260	375.706	315.048	...	...
9-Nitro-anthracene	485.040	10.355	308.045	267.813	...	...
9,10-Dinitro-anthracene	509.772	20.710	298.030	276.171	...	...
9-Cyano-anthracene	474.245	2.972	325.126	267.447	283.2	31
Anthraquinone	442.458	7.893	312.103	254.152	...	...
Anthraldehyde	487.267	3.946	316.574	269.262	...	...
Phenazine	396.690	5.944	301.992	234.870	234.3	28
Thianthrene	465.768	24.266	343.011	277.682	...	...

bromides, calculated with the aid of the δ-function model, and those reported by LeFevre, *et al.*[32] The n_{df} values of this series have been determined by the same relation ($n_{df} = 3N - 2n_b$), which varies from 7 to 58. Calculated values of substituted *n*-alkanes show a continuous increasing deviation from the LeFevre values. This deviation increases regularly by approximately 2 units for the addition of each CH_2 group. The causes of this discrepancy are not clear. It may be either due to the weakness of this model to take into account the increased interaction with lengthening of the hydrocarbon chain or inaccuracies in experimental values. Further experimental work is needed to settle this point.

Table III shows the bond parallel component of polarizabilities with bond polarity corrections. Results show that this component may be transferred from one molecular system to another having similar chemical bonds. In nitroanthracene, the value of bond parallel component for

TABLE II: Molecular Polarizabilities of Bromine-Substituted *n*-Alkanes (10^{-25} cm^3)

Molecules	$\Sigma\alpha_p$	$\Sigma\alpha_n$	$\Sigma 2\alpha_\perp$	α_M	α_M, obsd[a]
CH_3Br	70.128	16.630	74.719	53.826	55.3
C_2H_5Br	108.349	16.630	95.532	73.503	72.8
C_3H_7Br	145.427	16.630	117.262	93.106	90.7
C_4H_9Br	183.076	16.630	139.338	113.015	108.6
$C_5H_{11}Br$	220.720	16.630	161.582	132.978	126.5
$C_6H_{13}Br$	258.375	16.630	183.919	152.974	144.4
$C_7H_{15}Br$	296.025	16.630	206.314	172.989	162.3
$C_8H_{17}Br$	333.674	16.630	228.747	193.014	180.2
$C_9H_{19}Br$	371.324	16.630	251.206	213.053	198.1
$C_{10}H_{21}Br$	408.973	16.630	273.684	263.096	216.0
$C_{11}H_{23}Br$	446.623	16.630	296.177	253.143	...
$C_{12}H_{25}Br$	484.272	16.630	318.681	273.161	251.8
$C_{16}H_{33}Br$	634.870	16.630	408.766	353.422	323.4
$C_{18}H_{37}Br$	710.169	16.630	453.834	393.544	359.2

[a] Reference 32.

the C–N bond is 19.55 and in cyanoanthracene the value for the C≡N bond is 21.89, which is in accordance with the observation that π and σ electrons do not contribute equally to the bond parallel component of polarizability and that the contribution of electrons in the π orbital is less than those of the electrons in the σ orbital. Individual contribution of the π and σ orbitals to the polarizability can possibly be estimated from the calculations based on molecular orbital theory. Further investigations can only provide this information.

The excellent agreement obtained between the calculated and experimental values indicates the wide applicability of the δ-function model of chemical binding to complicated molecular systems such as ring structures and complex metal carbonyl,[33,34] etc.

Acknowledgment. The authors are thankful to Professor D. Sharma for his continued interest in the project. Financial assistance received by two of us (P. A. and L. D.) from the University Grants Commission and Council of Scientific and Industrial Research, New Delhi, in the form of research fellowships is gratefully acknowledged.

Appendix

Sample calculations of bond and molecular polarizabilities for toluene are given here.

C–H = 1.11 Å, $(C-C)_r$ = 1.39 Å, C–C = 1.52 Å, A_H = 1.00 au, A_C = 0.846 au, $\alpha_H = 5.92 \times 10^{-25}$ cm^3, $\alpha_C = 9.78 \times 10^{-25}$ cm^3, X_H = 2.1, X_C = 2.5, and n_{df} = 18.

For the C–H bond

$$\bar{x}^2 = 0.337257 \times 10^{-16}\ \text{cm}^2$$

$$\alpha_{\parallel b} = \frac{(4)(1)(0.91978)(0.113742)}{0.529} \times 10^{-24}\ \text{cm}^3 = 7.9106 \times 10^{-25}\ \text{cm}^3$$

$$\alpha_{\parallel p} = \alpha_{\parallel b}\sigma = (7.9106)(0.960789)(10^{-25}) = 7.600417 \times 10^{-25}\ \text{cm}^3$$

For 8 C–H bonds

$$\alpha_{\parallel p} = 60.8032 \times 10^{-25}\ \text{cm}^3$$

For the $(C-C)_r$ bond

$$\bar{x}^2 = 0.495218 \times 10^{-16}\ \text{cm}^2$$

$$\alpha_{\parallel b} = \frac{(4)(1)(0.846)(0.245241)}{0.529} \times 10^{-24}\ \text{cm}^3 = 15.6879 \times 10^{-25}\ \text{cm}^3$$

$$\alpha_{\parallel p} = \alpha_{\parallel b}\sigma = (15.6879)(1) = 15.6879 \times 10^{-25}\ \text{cm}^3$$

TABLE III: Bond Parallel Component of Polarizabilities (10^{-25} cm^3)

Molecules	$(C-C)_r$[a]	C—C	C—H	C—N	C≡N	C=O	N—H	N—O
Formamide	...	...	7.208	13.362	...	16.876	5.076	...
Acetamide	...	38.218	7.113	14.036	...	14.625	4.794	...
Benzamide	15.031	20.048	7.601	12.123	...	16.716	4.794	...
Aniline	16.134	...	7.601	15.724	...	...	4.863	...
p-Nitroaniline	15.272	...	7.601	15.307	...	...	4.863	11.662
p-Tcluidine	15.948	20.905	7.601	18.045	...	...	4.863	...
Toluene	15.688	22.254	7.601	...	...	...	...	...
p-Cyanotoluene	15.688	22.254	7.601	...	22.414	...	...	...
p-Nitrotoluene	15.688	22.254	7.601	20.081	...	...	...	9.511
p-Xylene	16.134	20.964	7.113	...	...	...	...	...
Mesitylene	16.134	23.423	7.113	...	...	...	...	...
Nitromesitylene	15.275	21.500	7.113	19.556	...	...	...	9.823
Pyridine	15.866	...	6.902	13.245	...	...	...	...
Naphthalene	15.882	...	6.649	...	...	...	...	...
1,5-Dinitro-naphthalene	16.589	...	6.649	13.636	...	...	...	6.182
Anthracene	16.092	...	6.649	...	...	...	...	...
9-Nitroanthracene	16.603	...	6.649	19.556	...	...	...	9.511
9,10-Dinitro-anthracene	16.006	...	6.649	18.045	...	...	...	10.471
9-Cyanoanthracene	16.304	17.526	6.649	...	21.889	...	...	...
Anthraquinone	16.561	...	6.649	...	...	12.454	...	...
Anthraldehyde	16.808	19.009	6.649	...	...	15.190	...	...
Phenazine	16.128	...	5.226	13.460	...	...	...	...

[a] Represents the carbon–carbon bond of ring structure.

For 9 $(C\text{-}C)_r$ bonds

$$\alpha_{\parallel p} = 141.1911 \times 10^{-25}\ cm^3$$

For the C-C bond

$$\bar{x}^2 = 0.589818 \times 10^{-16}\ cm^2$$

$$\alpha_{\parallel b} = \frac{(4)(1)(0.846)(0.347885)}{0.529} \times 10^{-24}\ cm^3 = 22.2541 \times 10^{-25}\ cm^3$$

$$\alpha_{\perp p} = \alpha_{\perp b}\sigma = (22.2541)(1) = 22.2541 \times 10^{-25}\ cm^3$$

Total bond parallel polarizability of toluene is

$$\Sigma\alpha_{\parallel p} = 224.2485 \times 10^{-25}\ cm^3$$

$$\Sigma\alpha_{\parallel n} = 0$$

(There are no nonbonding electrons in C-H and C-C bonds.)

$$\Sigma_{2\alpha_\perp} = \frac{(18)(636.7326)}{79.03} \times 10^{-25}\ cm^3 = 145.0232 \times 10^{-25}\ cm^3$$

$$\alpha_M = \frac{1}{3}(\Sigma\alpha_{\parallel p} + \Sigma\alpha_{\parallel n} + \Sigma 2\alpha_\perp) = 123.091 \times 10^{-25}\ cm^3$$

References and Notes

(1) E. R. Lippincott and J. M. Stutman, *J. Phys. Chem.*, **68**, 2926 (1964).
(2) E. R. Lippincott, G. Nagarajan, and J. M. Stutman, *J. Phys. Chem.*, **70**, 78 (1966).
(3) G. Nagarajan, *Z. Naturforsch. A*, **21**, 864 (1966).
(4) N. K. Sanyal, L. Dixit, and A. N. Pandey, *Indian J. Pure Appl. Phys.*, **10**, 329 (1972).
(5) J. A. Beran and L. Kevan, *J. Phys. Chem.*, **73**, 3860 (1969).
(6) B. Purnachandra Rao and V. Ramamurthy, *Curr. Sci.*, **41**, 15 (1972).
(7) R. M. Stevens, R. M. Pitzer, and W. N. Lipscomb, *J. Chem. Phys.*, **38**, 550 (1963); R. M. Stevens and W. N. Lipscomb, *ibid.*, **40**, 2238 (1964); **41**, 184, 3710 (1964).
(8) H. J. Kolker and M. Karplus, *J. Chem. Phys.*, **39**, 2011 (1963).
(9) E. R. Lippincott and M. O. Dayhoff, *Spectrochim. Acta*, **16**, 807 (1960).
(10) A. A. Frost, *J. Chem. Phys.*, **22**, 1613 (1954); **23**, 985 (1955); **25**, 1150, 1154 (1956).
(11) J. W. Hirschfelder, C. F. Curtiss, and R. B. Bird, "Molecular Theory of Gasses and Liquids," Wiley, New York, N. Y. 1967, pp 942-946.
(12) E. A. Hylleraas, *Z. Phys.*, **65**, 209 (1930).
(13) H. R. Hasse, *Proc. Cambridge Phil Soc.*, **26**, 542 (1930); **27**, 66 (1931).
(14) L. Pauling, "The Nature of the Chemical Bonc," Cornell University Press, Ithaca, N. Y., 1960.
(15) G. N. Lewis, *J. Amer. Chem. Soc.*, **38**, 762 (1916).
(16) I. Langmuir, *J. Amer. Chem. Soc.*, **38**, 2221 (1916).
(17) J. W. Linnett, *J. Amer. Chem. Soc.*, **83**, 2643 (1961).
(18) L. E. Sutton, *Chem. Soc. Spec. Publ.*, **No. 11** (1958); **No. 18** (1965).
(19) H. H. Landolt and R. Bornstein, "Zahlenwerte and Functionen," 6 Auflage, 3 Teil, Springer-Verlag, Berlin, 1950, pp 509-517.
(20) R. J. W. LeFevre and L. Radom, *J. Chem. Soc. B*, 1295 (1967).
(21) M. J. Aroney, R. J. W. LeFevre, and A. N. Singh, *J. Chem. Soc.*, 3179 (1965).
(22) M. J. Aroney, R. J. W. LeFevre, L. Radom, and G. L. D. Ritchie, *J. Chem. Soc. B*, 507 (1968).
(23) M. J. Aroney, K. E. Calderbank, R. J. W. LeFevre, and R. K. Pierens, *J. Chem. Soc. B*, 561 (1968).
(24) R. J. W. LeFevre, L. Radom, and G. L. D. Ritchie, *J. Chem. Soc. B*, 913 (1969).
(25) M. J. Aroney, K. E. Calderbank, R. J. W. LeFevre, and R. K. Pierens, *J. Chem. Soc. B*, 159 (1969).
(26) K. E. Calderbank, R. J. W. LeFevre, and R. K. Pierens, *J. Chem. Soc. B*, 968 (1969).
(27) M. J. Aroney, H. H. Huang, R. J. W. LeFevre, and G. L. D. Ritchie, *J. Chem. Soc. B*, 416 (1966).
(28) J. Hurley and R. J. W. LeFevre, *J. Chem. Soc. B*, 824 (1967).
(29) C. G. LeFevre and R. J. W. LeFevre, *J. Chem. Soc.*, 1641 (1955).
(30) R. J. W. LeFevre, L. Radom, and G. L. D. Ritchie, *J. Chem. Soc. B*, 775 (1968).
(31) P. H. Gore, J. A. Hoskins, R. J. W. LeFevre, L. Radom, and G. L. D. Ritchie, *J. Chem. Soc. B*, 227 (1969).
(32) C. G. LeFevre, R. J. W. LeFevre, and A. J. Williams, *J. Chem. Soc.*, 4188 (1965).
(33) G. Nagarajan and M. W. Lindauer, *Phys. Rev. A*, **5**, 557 (1972).
(34) N. K. Sanyal, P. Ahmad, and L. Dixit, paper presented at the First International Conference on Quantum Chemistry held at Menton, France, July 1973.

Location of Nickel Ions in Y Zeolites. II. Influence of Various Reagents Adsorption on Nickel Positions

P. Gallezot, Y. Ben Taarit, and B. Imelik*

Institut de Recherches sur la Catalyse CNRS, 69, 100 Villeurbanne, France

(Received March 22, 1973)

Publication costs assisted by the Centre National de la Recherche Scientifique

The crystal structures of NiY zeolite containing various sorbed phases (NH_3, NO, C_5H_5N, $C_{10}H_8$, C_4H_8, C_2H_4, CO) were determined in order to localize the Ni^{2+} ions. Neither $C_{10}H_8$, C_4H_8, and C_2H_4 nor CO changes the distribution of Ni^{2+} ions previously determined for the dehydrated zeolite. NH_3 can readily extract the cations from the S_I sites. On the other hand, NO and C_5H_5N generate only a slow migration process favored by the presence of residual water molecules. The structure of Ni-NO complex is discussed and a mechanism for the cation motion is proposed.

Introduction

In order to understand the behavior and catalytic activity of zeolites better, the positions of the cations in the framework have to be known. However, it is not sufficient to determine these positions after a given pretreatment since the cations may migrate under the influence of adsorbates or reagents, as was shown in a previous investigation for copper-exchanged zeolites.[1] After dehydration, Cu^{2+} ions are mainly found in S_I sites but they migrate very readily toward the supercages if large molecules such as pyridine, naphthalene, or butene are admitted into the solid. In part I of this work,[2] nickel ion positions were determined in Y zeolites as a function of both exchange level

and dehydration temperature. It was shown that nickel ions strongly prefer S_I sites, where they are strongly coordinated and probably difficult to reach by the reagents. As for copper-exchanged zeolites, X-ray analysis was used in order to test the possibilities of nickel ion migration. The influence of small molecules such as NH_3, CO, and NO which can enter the sodalite cages, as well as larger ones like pyridine and various hydrocarbons, was examined.

Experimental Section

The preparation of the dehydrated $Ni_{14}Na_{23}H_5Y$ (sample A of part I) was described in a previous paper.[2] Gases were introduced through a break-seal into the grease-free cell containing the pretreated sample. Special care has been taken to dry the gases before adsorption; ammonia vapor, carbon monoxide, nitric oxide, ethylene, and 1-butene were trapped at liquid nitrogen temperature on activated molecular sieves and warmed up until a 100-Torr pressure was established in the gas line. Pyridine and naphthalene vapors were preadsorbed on activated molecular sieves before introduction in the adsorption cell. The gases were kept in contact with the zeolite for 12 hr or more at room temperature, then excess gas was evacuated for 6 hr at the same temperature and a residual pressure of 10^{-5} Torr was achieved. No attempt has been made to determine the amount of desorbed gas; however, this treatment removes most of the physisorbed molecules but leaves the molecules complexed with the Ni^{2+} ions. The treated samples were transfered into connected glass capillaries and sealed off from the vacuum system for X-ray investigation. The treatment conditions applied to the investigated samples are listed in Table I.

X-Ray powder diffraction patterns were taken with filtered Cu Kα radiation, using a high-resolution Debye–Scherrer camera. Films were measured with a linear comparator and measurements were corrected for radius camera and film shrinkage errors. Cubic unit cell constants were obtained by averaging the values derived from ten well defined diffraction lines in the region 30–40° θ. Acquisition of line intensities and the least-squares refinement program were previously described.[1] Each observation was weighted at unity. The scale factor, the coordinates, and temperature factors of framework atoms have been refined together with the coordinates and occupancy factors of extra-framework atoms. The temperature factors of the latter were kept at the same value for all the structures investigated; however, many trials have proved that when refined these parameters do not diverge to abnormal low or high values, and meanwhile it was ascertained that the occupancy factor for most of the cation sites does not change appreciably.

Results

The crystal structures of A3AM, A3NO1, A3NO2, A6PY, A3PY, and A2PY were determined. No attempt has been made to locate adsorbed molecules and nickel ions in the supercages.

For samples A6PY and A3PY, scattering matter was only found on S_I, $S_{I'}$, and S_{II} sites. The first two sites were assigned to Ni^{2+} ions and the last one to Na^+ ions.

An additional electron density peak at $x = y = z = 0.16$ was found in the sodalite cages of samples A2PY and A3AM. It was attributed to H_2O and NH_3 molecules, respectively.

The assignment of extra-framework species in A3NO1 and A3NO2 was difficult because a difference Fourier map showed double $S_{II'}$ peaks at $x = y = z = 0.14$ and 0.165. Assuming that the double peaks are due to oxygen atoms, the refinement resulted in a significant R index decrease from 0.075 and 0.08 to 0.067 and 0.063 for samples A3NO1 and A3NO2, respectively. Moreover, these two diffracting species are about 1.2 Å apart which fits the nitrogen–oxygen distance occurring in NO reasonably well and we therefore suggest that these atoms belong to nitric oxide molecules.

Crystallographic parameters and listings of structure factors will be given in the microfilm edition of the journal.[3] Cubic unit cell constants, final R indexes, and populations of extra-framework sites are given in Table II. Table III shows the interatomic distances.

The crystal structures of A6AM, A6NO, A6CO, A2CO, A6ET, A2ET, A6BU, A2BU, A6NA, and A2NA were not determined. The population of the hexagonal prisms (hp) was estimated from the chart given in part I[2] which relates the population N of hp to the cubic unit-cell constant a. The use of this chart for samples contacted with NH_3 (A6AM) and NO (A6NO) is quite valid since the values of N *vs.* a for A3AM, A3NO1, and A3NO2 are well on the A line of the chart. (The test is also quite satisfactory for A6PY, A3PY, and A2PY.)

Discussion

Frequent unreferenced mentions of the results reported in part I of this work[2] will be made in the present discussion.

Ammonia Adsorption (Sample A3AM). Adsorption of ammonia on a sample pretreated at 300° induced a nearly total removal of the nickel ions occupying the hp (site S_I). Most of the unlocated Ni^{2+} are probably complexed with

TABLE I: Treatment Conditions of the Samples

Samples	Dehydration temp,[a] °C	Nature of adsorbed gas	Time of contact,[b] hr	Samples	Dehydration temp °C	Nature of adsorbed gas	Time of contact, hr
A6AM	600	NH_3	24	A3PY[c]	300	Pyridine	72
A3AM[c]	300	NH_3	24	A2PY[c]	200	Pyridine	72
A6NO	600	NO	12	A6ET	600	Ethylene	15
A3NO1[c]	300	NO	12	A2ET	200	Ethylene	15
A3NO2[c]	300	NO	96	A6BU	600	1-Butene	15
A6CO	600	CO	15	A2BU	200	1-Butene	15
A2CO	200	CO	15	A6NA	600	Naphthalene	15
A6PY[c]	600	Pyridine	72	A2NA	200	Naphthalene	15

[a] Before gas adsorption. [b] At room temperature. [c] Structures entirely determined.

TABLE II: Tabulated Data for the Number of Species per Unit Cell, Assignment of Species Type and Its $x = y = z$ Coordinates

Sample	Final R indexes[a]	Unit cell constant, Å (±0.01)	S_I	$S_{I'}$	$S_{I'}$	$S_{II'}$	$S_{II'}$	S_{II}
A3AM	0.067	24.66	2.9(2) Ni	4.0(2) Ni			11(1) NH_3	19(1) Na
	0.094		0.0	0.060(1)			0.168(1)	0.2340(5)
A3NO1	0.067	24.575	6.6(2) Ni	3.8(2) Ni	1.9(2) Ni	5.5(1) N or O	3.5(1) N or O	21(1) Na
	0.092		0.0	0.056(1)	0.078(3)	0.141(3)	0.167(5)	0.2368(4)
A3NO2	0.063	24.62	3.3(2) Ni	5.2(2) Ni	2.5(2) Ni	6(1) N or O	8(1) N or O	24(1) Na
	0.082		0.0	0.054(1)	0.080(2)	0.135(3)	0.165(3)	0.2343(3)
A6PY	0.068	24.475	11.1(2) Ni	1.5(2) Ni				22(1) Na
	0.097		0.0	0.059(2)				0.2360(4)
A3PY	0.077	24.525	9.0(2) Ni	2.5(2) Ni				17(1) Na
	0.113		0.0	0.058(2)				0.2358(6)
A2PY	0.103	24.655	1.7(2) Ni	4.8(2) Ni			20(2) H_2O	18(2) Na
	0.132		0.0	0.072(3)			0.163(3)	0.2377(8)

[a] The first index correspond to $R = \Sigma||F_o| - k|F_c||/\Sigma|F_o|$ and the second index to $R = \Sigma|I_o - kI_c|/\Sigma I_o$. Estimated standard errors (in parentheses) may in some case be greatly underestimated especially for atoms with low occupancy factors.

TABLE III: Interatomic Distances (Å)[a]

	A3AM	A3NO1	A3NO2	A6PY	A3PY	A2PY
T-O(1)	1.657(5)	1.655(5)	1.649(5)	1.659(5)	1.639(6)	1.654(7)
T-O(2)	1.602(4)	1.621(4)	1.623(4)	1.621(4)	1.613(6)	1.624(7)
T-O(3)	1.671(5)	1.668(5)	1.669(5)	1.706(7)	1.689(7)	1.682(9)
T-O(4)	1.626(5)	1.584(4)	1.620(4)	1.597(4)	1.621(5)	1.619(7)
M	1.639	1.632	1.640	1.645	1.640	1.644
O(1)-O(2)	2.672(8)	2.673(9)	2.701(7)	2.678(9)	2.697(10)	2.701(12)
O(1)-O(3)	2.698(10)	2.645(10)	2.691(9)	2.693(2)	2.683(12)	2.751(16)
O(1)-O(4)	2.677(5)	2.706(4)	2.675(4)	2.684(5)	2.674(5)	2.668(6)
O(2)-O(3)	2.654(7)	2.681(8)	2.639(6)	2.646(8)	2.651(9)	2.635(11)
O(2)-O(4)	2.637(8)	2.613(7)	2.627(7)	2.653(8)	2.651(9)	2.631(11)
O(3)-O(4)	2.720(12)	2.668(11)	2.735(10)	2.760(12)	2.714(14)	2.731(17)
M	2.676	2.664	2.678	2.685	2.678	2.686
Ni(I)-O(2)	3.51(1)	3.56(1)	3.53(1)	3.51(1)	3.53(1)	3.53(1)
Ni(I)-O(3)	2.58(1)	2.50(1)	2.55(1)	2.32(1)	2.44(1)	2.61(2)
Ni(I')-O(3)	2.30(2)	2.20(2)	2.15(1)	2.21(5)	2.21(3)	2.51(3)
Ni(I')-X(II')	2.76(4)	2.88(8)	2.93(3)			2.29(4)
Ni(I')-X(II')*		2.77(5)	2.90(4)			
Ni(I')*-O(3)		2.70(8)	2.73(4)			
Ni(I')*-X(II')		2.2(1)	2.1(1)			
Ni(I')*-X(II')*		1.9(1)	1.8(1)			
X(II')-X(II')*		1.1(2)	1.3(1)			
Na(II)-O(2)	2.37(1)	2.34(1)	2.33(1)	2.36(1)	2.34(1)	2.39(2)
Na(II)-O(4)	2.92(1)	2.98(1)	2.94(1)	3.03(1)	3.02(1)	2.95(2)

[a] (I')* means $S_{I'}$ with $x = y = z \simeq 0.08$. X(II') means O or N atom at $x = y = z \simeq 0.165$. X(II')* means O or N atom at $x = y = z \simeq 0.14$.

ammonia in the supercages. However, four Ni^{2+} remained in the sodalite cages and occupy $S_{I'}$ sites. They are bonded to three O(3) framework oxygens in addition to three NH_3 molecules localized on $S_{II'}$ sites, since there are actually three times more NH_3 (II') than Ni(I') within the standard deviations (Table II).

As soon as ammonia was adsorbed, the pink color of the zeolite turned to green. Similar color changes (corresponding to the new nickel coordination) were also observed when samples pretreated at 600° were contacted with ammonia. Simultaneously, a sharp increase of unit cell constants occurred, which corresponds to a decrease of the hp population according to the chart given in part I of this work. Hence Ni^{2+} ions could be withdrawn from S_I sites whatever the pretreatment temperature. Ammonia molecules which can always enter the sodalite cavities may subsequently attract Ni^{2+} ions out of the hp; this is probably due to the small size, high polarity, and strong ligand field of NH_3 molecules.

Nitric Oxide Adsorption (Samples A6NO, A3NO1, and A3NO2). Adsorption of NO on a sample preliminarily heated at 600° did not affect its unit cell constant (24.47 Å); therefore it may be assumed that its hp population was unchanged. On the contrary, when a sample preheated at 300° was kept in contact with NO, its unit cell constant increased continuously. Structure results actually show that an important decrease of hp population occured under these conditions. Thus, about $^1/_3$ (sample A3NO1) and $^2/_3$ (sample A3NO2) of Ni^{2+} ions, respectively, were withdrawn from hp after 12 and 96 hr of contact with ni-

tric oxide. The displaced cations mainly occupy $S_{I'}$ (0.05) and $S_{I'}$ (0.08) sites in the sodalite cages. $S_{I'}$ (0.05) cations are bonded to three O(3) framework oxygens but rather far away from S_{II} (0.14) and $S_{II'}$ (0.165) sites assumed to be occupied by NO molecules. The coordination scheme of $S_{I'}$ (0.08) nickel ions is quite different; in addition to long range interaction with three O(3) framework oxygens 2.7 Å apart, they are coordinated by three nitrogen and three oxygen atoms belonging to three NO molecules (there were actually three times more $S_{II'}$ (0.14) and $S_{II'}$ (0.165) species than $S_{I'}$ (0.08) nickel ions within the standard errors).

The $S_{I'}$ (0.08) Ni^{2+} ions are equidistant from the two $S_{II'}$ sites; therefore the Ni–NO bonds are not linear but have a T-like configuration. Strong interactions are likely to occur because of the short (2.0 Å) distances involved in these bonds. This suggests that an NO molecule is bonded to a Ni^{2+} ion through a π-electron transfer from the NO molecular orbital to the nickel 3d orbital. The behavior of these NO ligands is not surprising because nitric oxide is known as a strong electron donor and the T bonding scheme in which the two atoms of the NO molecule are nearly equidistant from the cation has already been encountered.[4] Esr and ir spectroscopy measurements performed in this laboratory[5] and elsewhere[6] are quite consistent with the above results. An esr signal attributed to a Ni^{+} ion appeared when NO was adsorbed on NiNaY zeolite while ir spectra gave clear indication of nitrosyl ion formation. These observations show that a $Ni^{+}NO^{+}$ complex is formed *via* a π-electron transfer. Moreover, the esr signal intensity increased as a function of the NO time of contact with the zeolite. This means that a larger number of Ni^{2+} ions are increasingly available to react with NO in the sodalite cages and thus corroborates the time dependence of Ni^{2+} withdrawal from hp reported above.

However, subsequent interactions between sorbed NO and the zeolite framework may lead to a framework oxygen capture. This is suggested by the broadening and rapid fall of diffraction line intensities toward large Bragg angles, observed on the diffraction patterns of A3NO1 and A3NO2, indicating the probable occurence of point defects in the zeolite lattice. Similar conclusions were reached by Lunsford, *et al.*,[7] in an infrared study of NO disproportionation on CuY zeolite.

Pyridine Adsorption (Samples A6PY, A3PY, and A2PY). The S_I sites nickel population of A6PY is almost unchanged compared with that of a 600° treated sample (A_{600} of part I). On the other hand, 1 and 1.6 Ni^{2+} were withdrawn from hp after pyridine adsorption on samples preheated at 300 and 200°, respectively. While A_{600} is fully dehydrated, A_{300} and A_{200} still contain 1.3 and 2.9 hydrated $S_{I'}$ (0.08) Ni^{2+} ions. One may conclude that pyridine adsorption does not affect the hp population of fully dehydrated samples whereas small Ni^{2+} displacements may occur when water traces remain in the sodalite cages.

Adsorption of Carbon Monoxide, Naphthalene, Ethylene, and Butene. Whatever the pretreatment temperature, CO or $C_{10}H_8$ adsorption on the zeolite does not affect its unit cell constant (24.47 and 24.615 Å for samples pretreated at 600 and 200°, respectively) and it may be assumed that the hp population is unchanged.

On the other hand, admission of C_2H_4 or C_4H_8 onto samples pretreated at 600 and 200° produced a decrease of a from 24.47 to 24.44 Å and from 24.615 to 24.60 Å, respectively. According to the chart this should mean an increase of S_I sites population. However, it is noteworthy that: (i) the set of diffraction lines intensity was unchanged; (ii) these variations of a were almost quantitatively reversible upon simple evacuation at room temperature; and (iii) ethylene or butene adsorption on NaY zeolite induces a similar decrease of a and we may conclude that the phenomenon is not specific to nickel ions. Additional data and extensive discussion about the influence of hydrocarbon physisorption on NaY zeolite will be given elsewhere.[8]

Recently, Egerton and Stone[9] have shown that the amount of CO adsorbed on Ni^{2+} ions in NiY zeolites sharply increases only when the exchange level rise above 45%. These observations corroborate the previous results,[2,10] indicating that the filling of hp is limited to about 12 Ni^{2+}/unit cell, but the present results also show that these cations remain in their hidden sites on CO adsorption.

In conclusion, CO, $C_{10}H_8$, C_2H_4, and C_4H_8 are unable to withdraw significant amounts of Ni^{2+} ions from the hp regardless of the zeolite pretreatment temperature.

Mechanism of Ni^{2+} Ion Migration Out of the hp. From the experiments presented in this paper, we may first conclude that the degree of dehydration of NiY zeolite is an important factor for the migration of Ni^{2+} ions. Thus, for the fully dehydrated sieve (A_{600}) the migration of nickel ions out of the hp can occur only under particular conditions. It seems that only small, strong polar molecules are able to react and withdraw the cations from S_I sites, since all absorbates tested, with the exception of ammonia, have no effect on the hp population. On the other hand, when some water molecules are still present (probably 1–2 H_2O per unit cell is sufficient) a decrease of S_I population is observed after adsorption of NO and pyridine, whereas CO, C_2H_4, C_4H_8, and $C_{10}H_8$ are completely ineffective even in these conditions. Hence, the steric hindrance is not the predominant factor, since C_5H_5N is unlikely to enter the sodalite cavities, whereas CO, for example, is small enough to penetrate the sodalite cages. Although the data now available are not sufficient to postulate a precise mechanism of the Ni^{2+} ion migration, the following suggestions may be made: (i) the adsorbate should be able to displace water molecules still attached to Ni^{2+} ions; and (ii) water molecules act as a cation carrier.

We consider two steps. First, the adsorbate attracts an $S_{I'}$ nickel ion; H_2O attached to the cation is displaced by the new ligand and a complex ion is formed. In a second step, the liberated water molecules move back close to hp and extract an Ni^{2+} from the S_I site, which in turn may migrate and react with other adsorbate molecules. This process is slow for large size molecules (pyridine) remaining in the supercages but may be enhanced for small molecules like NO, able to enter the sodalite cages. In this latter case the migration path is shorter, since nickel ions may be complexed already in the sodalite cages. On the other hand, CO, C_2H_4, C_4H_8, and $C_{10}H_8$ are too weak ligands to exchange with the water coordinated to nickel ions. Thus these molecules would react with the dehydrated nickel ions occupying the sodalite cages (for only CO) or supercages but the hydrated Ni^{2+} and the numerous cations occupying the hp should be out of range.

Conclusion

This study has shown some interesting aspects of the coordination chemistry of nickel ions in the Y zeolite host

lattice. Thus, the particular stereochemistry of the complex formed by Ni^{2+} ions and NO molecules is of interest.

Furthermore, it has indicated that the accessibility of the Ni^{2+} ions to the reagents depends upon the initial cation location, the residual water content of the zeolite, and the reagent's ability to displace the H_2O ligands from the cations. Thus, nickel ions which occupy the supercages are always available provided that they are not coordinated by a too strong ligand which would prevent direct contact with the reagent.

Nickel ions occupying the sodalite cages may be directly reached by small molecules which can enter the sodalite cages, but these cations will have to migrate toward the supercages in order to react with larger molecules.

In contrast, nickel ions occupying the hp cannot be reached by any molecule but may be withdrawn by H_2O or NH_3 molecules. An ion-transfer process may even occur and continue with the help of these molecules acting as carriers provided that these ligands are easily displaced by the reagent molecules.

The behavior of Cu^{2+} ions is very different since they migrate readily from their initial $S_{I'}$ sites and then become accessible to the reagents occupying the supercages.[1] Considering the catalytic properties for the copper and nickel zeolites, we may assume that the activity of CuY will increase with the copper content whereas NiY will not be active until the hexagonal prisms are filled up (around 12 Ni^{2+}/unit cell).

Acknowledgments. The authors express their gratitude to Mr. A. Theolier for helpful technical assistance and Mr. H. Urbain for performing the chemical analysis.

Supplementary Material Available. Listings of structure factors, atomic coordinates, temperature factors, and occupancy factors will appear following these pages in the microfilm edition of this volume of the journal. Photocopies of the supplementary material from this paper only or microfiche (105 × 148 mm, 20× reduction, negatives) containing all of the supplementary material for the papers in this issue may be obtained from the Journals Department, American Chemical Society, 1155 16th St., N.W., Washington, D. C. 20036. Remit check or money order for $3.00 for photocopy or $2.00 for microfiche, referring to code number JPC-73-2556.

References and Notes

(1) P. Gallezot, Y. Ben Taarit, and B. Imelik, *J. Catal.*, **26**, 295 (1972).
(2) P. Gallezot and B. Imelik, *J. Phys. Chem.*, **77**, 652 (1973).
(3) See paragraph at end of paper regarding supplementary material.
(4) P. R. H. Alderman and P. G. Owston, *Nature (London)*, **178**, 1071 (1956).
(5) C. Naccache and Y. Ben Taarit, *J. Chem. Soc., Faraday Trans. 1*, **69**, 1475 (1973).
(6) P. H. Kasai and R. J. Bishop, *J. Amer. Chem. Soc.*, **94**, 5560 (1972).
(7) C. C. Chao and J. H. Lunsford, *J. Amer. Chem. Soc.*, **93**, 71 (1971).
(8) P. Gallezot and B. Imelik, *J. Phys. Chem.*, **77**, 2364 (1973).
(9) T. A. Egerton and F. S. Stone, *J. Chem. Soc., Faraday Trans. 1*, **69**, 22 (1973).
(10) E. Dempsey and D. H. Olson, *J. Phys. Chem.*, **74**, 305 (1970).

A Semiempirical Study of Hydrogen Bonding in the Diaquohydrogen Ion, $H_5O_2^+$

George R. Anderson* and George J. Jiang

Department of Chemistry, Bowdoin College, Brunswick, Maine 04011 *(Received April 9, 1973)*

Publication costs assisted by the National Science Foundation

The diaquohydrogen ion, $[H_2OHOH_2]^+$, is a hydrogen (H)-bonded species of considerable stability and is one for which both experimental and theoretical data are available. In this study, H-bonding properties of $H_5O_2^+$ are computed by means of a semiempirical model for linear H bonds reported earlier and the results are compared and discussed. Agreement is found to be favorable particularly with respect to vibration (infrared) frequencies. Furthermore, the model potential energy function contains semiempirical parameters which are not found to change appreciably from one system (reported earlier, HF_2^-) to another ($H_5O_2^+$). These results suggest that perhaps the model for H bonding is sufficiently general to be applied to other H-bonded species for which fewer experimental data are available.

Introduction

The study of the diaquohydrogen ion, $H_5O_2^+$, is part of a more extended study of hydrogen (H) bonding in a series of compounds for which experimental data and theoretical model calculations are reported. The bifluoride ion, HF_2^-, study was reported earlier.[1] Spectroscopic and crystallographic data together with *ab initio* MO results of HF_2^- were fit to a semiempirical model of the H bond. Numerical parameters originating in the model calculation were evaluated, and ground-state and excited vibrational-state properties of HF_2^- ion were computed and discussed.

In the present $H_5O_2^+$ ion study, we follow a similar approach beginning with a least-squares fit to reported *ab initio* MO data using appropriate empirical constants and the same three model parameters (m, b, and g) as before. These results are further analyzed by comparison of computed and observed infrared frequencies. The final con-

clusions suggest the possibility that the proposed H-bond model may be applicable to other H bonded systems perhaps without significant changes in the three model parameters; they are about the same for HF_2^- and $H_5O_2^+$. Further studies, therefore, are underway to test and extend the model calculations to a variety of weaker H-bonded systems which include some of possible biological significance. By this approach, we hope eventually to shed new light on possible mechanistic implications of the H bond in areas of chemical dynamics and proton conductivity in biological membranes.[2]

The $H_5O_2^+$ ion is observed and studied in the gas phase (naturally occurring in the lower ionosphere, 80–90 km altitude) and in crystalline solids where it exists as one of a series of stable polyhydrated mineral acids. The structure of $H_5O_2^+$ is similar to that of hydrazine where the N–N bond is replaced by the O···H···O bond. In our calculations, we assume that the four H atoms at the ends of the molecule are uncoupled from the motion of the central H atom and that the net effect of the terminal H atoms is a slight increase in the effective mass of the two oxygen atoms, 16 to 18 amu. Also, we will concern ourselves solely with the linear motions of the H bond, the two coordinates that measure the relative displacement of the O···H···O atoms as given previously.[1] Bending and torsional modes of the H bond are assumed to be of lesser importance to the energetics of H bonding. The justification for these approximations will be discussed below.

The heat of formation of $H_5O_2^+$ from H_2O and H_3O^+ was measured in the gas phase by mass spectrometry and reported by Kebarle, Searles, *et al.*[3] They found $\Delta H(H_5O_2^+) = -150.6$ kJ/mol (−36 kcal/mol). This is about ⅕ the energy released when water is protonated, $\Delta H(H_3O^+) = -690.4$ kJ/mol (−165 kcal/mol), and it is about ⅗ the energy of the strongest H bond known $\Delta H(HF_2^-) = -242.7$ kJ/mole[4] (−58 kcal/mol).

Ab initio MO calculations on $H_5O_2^+$ are reported by Kollman and Allen,[5] Kraemers and Diercksen,[6] and by Janoschek, *et al.*[7] Kollman and Allen's calculations agree quite well with mass spectrometry data of Kebarle, *et al.* They calculate an H bond energy of −154.4 kJ/mol (−36.9 kcal/mol), a value we have used in our calculations. The shape of the potential surface near the bottom of the potential "well" probably is a shallow single minimum surface although Janoschek, *et al.*,[7] report calculations which leave some doubt as to whether their results predict a symmetric double-minimum potential surface or one having a single minimum. The two calculated equilibrium O···O bond distances are R_e(KA) = 2.38 Å[5] and R_e(KD) = 2.39 Å,[6] where the H atom is on center corresponding to the single potential energy minimum. The calculations of Janoschek, *et al.*, only covered the range R = 2.50–2.80 Å, which did not include an energy minimum in R.

Crystal structure studies of $H_5O_2^+$ involving X-ray and neutron diffraction techniques were reviewed by Pimentel and McClellan.[8] The evidence clearly shows the H-bond distance in this species to be "short," R_0 = 2.51–2.424 Å, depending upon crystalline environment. The infrared and Raman spectra of diaquohydrogen ion perchlorate, $H_5O_2^+ClO_4^-$, have also been reported.[9-12] They show that the H absorption, ν_H, is broad and shifted to 1700–1900 cm^{-1}.[10,11] The same absorption mode upon deuterium substitution, ν_D, is near 1250 or 1400 cm^{-1};[9,11] the assignment is not clear. The O···O vibration (ν_4) which is Raman active occurs at 412 cm^{-1}.[11]

Results and Discussion

Fit of the Potential Function. The potential function of the model H bond was given in an earlier paper[1] for the symmetric H bond

$$V/D = 1 - f(s) - f(t) + gf(s)f(t) + F(R)$$

where the coordinates s and t measure the linear displacement of the H atom from the two respective oxygen atoms such that the total O···O distance $R = s + t$; the displacement of the H-atom off center is given by $r = (s - t)/2$. The functions $f(s)$ and $f(t)$ are symmetric upon exchange of coordinates and are of the form

$$f(s) = \exp\{-n(s - s_{e\infty})^2/2s\}$$

where $n = k_e s_{e\infty}/D$. The R-dependent term looks like

$$F(R) = C_1 \exp\{-bR\} - C_2(R_e/R)^m$$

The empirical constants and best-fit parameters are listed in Table I.[13-16] Note that the first three constants listed (D, k_e, and $s_e/s_{e\infty}$) are related entirely to the H_3O^+ species; the next two (V_e and R_e) are empirical constants relating to the H-bonded species, $H_5O_2^+$; and the last three (m, b, and g) are constants used in the least-squares fit to *ab initio* data. The ranges over which the parameters were individually varied are as follows: m varied from 1 to 9 with m = 6 being the only value at which any least-squares fit could be achieved; g varied from 0.10 to 1.0; and b varied from 1.0 to 10.0. The three sets of *ab initio* data were first treated separately.

Janoschek, *et al.*,[7] reported the largest number of theoretical data points (28 points). Yet we were unable to make a least-squares fit due to insufficient data near the equilibrium position. Furthermore, when using their coordinates of potential energy minima at R_e = 2.48, r_e = ±0.16 Å (estimated from Figure 12 of ref 7), we could not "force" the model to duplicate the double minima potential surface except for large values of the g parameter ($g \simeq$ 0.8–0.99). This suggested to us that a double minima potential surface for the $H_5O_2^+$ data was out of range of our model-fitting procedure. Following a suggestion from one of the referees, however, R_e was chosen at 2.39 Å, and a least-squares fit was obtained at g = 0.665, b = 2.60.

TABLE I: The Spectroscopic and Structural Constants, and Parameters

			Ref
Empirical Constants			
Dissociation energy of H_3O^+, D	64,013	cm^{-1}	3,13
Harmonic force constant of H_3O^+, k_e	6.134	$mD/Å$	14,15
O–H bond length of H_3O^+, $S_{e\infty}$	1.02	Å	16
Hydrogen bonding energy, V_e	12,908	cm^{-1}	3
Potential energy minimum, R_e	2.39	Å (r_e = 0)	3,5
Least-square fit parameters m = 6 (for all determinations)			

b	g	*Ab initio* data	Ir frequency agreement
2.568	0.665	KA (ref 5)	Good
2.680	0.675	KD (ref 6)	Good
2.60	0.670	Average	Best
3.80	0.910	KA	Poor
3.50	0.930	KD	Poor
3.20 (fixed)	0.680	KD, g fit only	Good
2.60	0.665	J *et al.* (ref 7)	Good

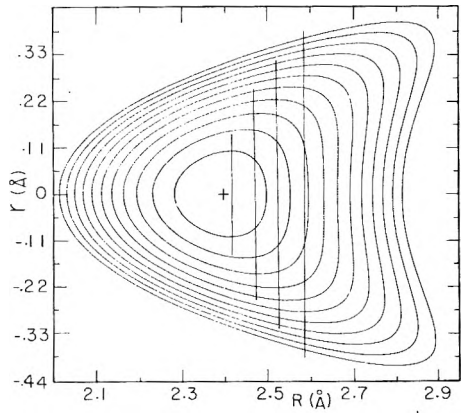

Figure 1. Potential energy contour plot of $H_5O_2^+$ at 500-cm^{-1} intervals using "best" fit parameters given in Table I. The center contour is at $V = -12{,}500$ cm^{-1}, the outer at $V = -7500$ cm^{-1}. The cross (+) marks the potential minimum at $R_e = 2.390$ Å. The solid straight lines depict the positions of the H atom between the classical turning points at the minimum R values in the four lowest-lying H vibrational states, E_0^+ to E_1^-.

This showed good agreement with the fits to the other two sets of data (see following).

The Kollman and Allen[5] data set (11 points) produced two least-squares fits as did the Kraemers and Diercksen[6] data set (8 points); see Table I. Noting agreement between two of the independent determinations, we constructed a potential surface using the average values of the parameters, $m = 6$, $b = 2.60$, and $g = 0.67$, and this potential surface is shown in Figure 1. Contour plots of the three potential surfaces in fact were identical within 2-3% so that we felt we had reached a reasonable level of refinement for combining all three independent data sets.

The potential surface in Figure 1 has contour lines drawn at 500-cm^{-1} intervals starting at $-12{,}500$ cm^{-1}, ending at -7500 cm^{-1}. The single minimum of energy of $-12{,}908$ cm^{-1}, -154.4 kJ/mol (-36.9 kcal/mol), is at $R_e = 2.39$ Å. Sections through the potential energy surface at constant R show a progression of curves going from single minimum (small R) to double minima potential curves (larger R). The boundary between these two domains is at $R = 2.63$ Å where the potential curve indeed is a flat bottomed well (see Figure 2).[17]

Returning to the second least-squares fit of Kollman and Allen's *ab initio* data set where $m = 6$, $b = 3.80$, and $g = 0.91$, we find a corresponding potential surface (Figure 3)[17] that is clearly distinctive from the "hybrid" potential surface shown in Figure 1. The potential well is much "flatter" near the bottom of the well and the central barrier (to proton motion) rises to higher prominence for similar R values. For instance at $R = 2.49$ Å, a small barrier (less than 150 cm^{-1}) sets in, and when $R = 2.79$ Å the barrier grows to $\sim$1200 cm^{-1}. By visual comparison with a similar diagram of Kollman and Allen (Figure 4 of ref 3), the potential surface looks very similar to the curves presented by these authors.

The second least-squares fit of Kraemers and Diercksen's data set (for $b = 3.50$ and $g = 0.93$) is also very similar. We therefore were confronted with essentially two potential surfaces for the $H_5O_2^+$ ion, each fit to an *ab initio* data base. This duality problem was resolved on the basis of infrared absorption and Raman spectroscopic data.

Calculated Vibrational Energies and Spectra of $H_5O_2^+$. The vibrational eigenfunctions and eigenvalues of the H (and deuterium, D) atoms were calculated using the approximation of "clamped" heavy nuclei following the procedure of Anderson and Lippincott.[18] Four lower vibrational states were calculated for a range of O···O separations from 2.2 to 5.0 Å (Figure 4).[17] For the "hybrid" potential surface where $m = 6$, $b = 2.60$, and $g = 0.67$ we obtained the following results.

TABLE II: Calculated Results and Experimental Values[a]

	This work	Experimental
Ground state minimum for H	$R_0 = 2.415 \pm 0.001$ Å	$\sim$2.40–2.50[b]
Ground state minimum for D	$R_0 = 2.407 \pm 0.001$ Å	Unobserved
Isotope shift	$\Delta R_0 = -0.008$ Å	Unobserved
H asymmetric stretch	$\nu_H = 1783$ cm^{-1} (Ir)	$\sim$1700–1900[c]
ν_H' overtone	$\nu_H' = 3850$ (R)	Unobserved
ν_H'' overtone	$\nu_H = 6060$ (Ir)	Unobserved
D asymmetric stretch	$\nu_D = 1242$ (Ir)	1250 or 1400[c]
Symmetric stretch	$\nu_{O\cdots O} = 480 \pm 120$ (R)	412[c]
Isolated ion H_3O^+	$\nu_H(H_3O^+) = 3210$ (R, Ir)	3200[d]

[a] The calculations are based upon the "best" potential surface with parameters given in Table I. Infrared (Ir) and Raman (R) active modes are predicted by symmetry selection rules. [b] References 7, 8, 16. [c] Reference 11. [d] References 14, 15.

At large O···O separations, the first two vibrational states (E_0 and E_1, see ref 1 for notation) are doubly degenerate since the proton may be localized near one oxygen (water molecule) or the other. The separation between the states $E_1 - E_0 = 3210$ cm^{-1} at $R = \infty$ was fixed (by k_e) to correspond to an infrared absorption of H_3O^+ observed at $\sim$3200 cm^{-1}. By the harmonic oscillator approximation, $\nu = (2\pi c)^{-1}(k_e/m_p)^{1/2}$, a frequency $\nu_{HO} = 3316$ cm^{-1} is calculated. The 3.6% shift in calculated frequency shows that the model potential function includes a typical anharmonic deviation characteristic of many molecular species but not directly observed in H_3O^+.

At shorter O···O separations, the first two vibrational states (see Figure 4)[17] split when H atom tunnelling becomes important: near $R \simeq 3.1$ Å for the upper (E_1) state and $R \simeq 2.9$ Å for the ground (E_0) state. The degeneracy is lifted and the four states are now designated by the symmetry (+ and −) of their respective eigenfunctions, E_0^+, E_0^-, E_1^+, E_1^-. The bottom "dip" of each curve corresponds to the O···O separation for which the energy is minimal in the $E_0^+ \cdots E_1^-$ states, 2.415, 2.470, 2.52, and 2.58 Å, respectively. The ground-state minima for the H and D calculations are given in Table II. The difference of these two R values is the isotope shift and is found to be negative in this instance. For weak H bonds, the isotope shift is experimentally and theoretically found to be positive.[18] For $H_5O_2^+$ no experimental determination has been reported.

The infrared spectral absorption of $H_5O_2^+$ is calculated on the assumption of "vertical" transitions between the E_0^+ to E_0^- states at the position of minimum of energy, $R_0 = 2.415$ Å. The observed H and D asymmetric stretch data are listed in Table II and the calculation is based (again) upon the "hybrid" potential surface. One may notice that the agreement is excellent and that our deuterium calculation (at 1242 cm^{-1}) is very close to the 1250-cm^{-1} observed absorption. Thus, the model clearly favors the assignment of ν_D to the 1250-cm^{-1} band over the 1400 cm^{-1} band which the authors also suggested as a possibility.

The other potential surfaces mentioned above (b = 3.5, g = 0.93) predict infrared transitions in considerable disagreement with the observed values listed in Table II. The $H_5O_2^+$ asymmetric stretch frequencies were calculated to be ν_H = 1070 cm^{-1} and ν_D = 680 cm^{-1}, a discrepancy of 30–35% with observed frequencies. Therefore, this potential surface may be assumed to be significantly less descriptive of the "true" $H_5O_2^+$ potential surface for the $H_5O_2^+$ ClO_4^- crystalline solid.

An interesting comparison of theoretical data was made based upon the previous study of the HF_2^- ion.[1] We transferred two of the best-fit parameters (m = 6, b = 3.20) from the HF_2^- *ab initio* data fit and held these fixed while varying g to make a least-squares fit using the Kraemers and Diercksen data set on $H_5O_2^+$. This gave a fit for $g(H_5O_2^+)$ = 0.68 compared with the bifluoride ion results $g(HF_2^-)$ = 0.65. The infrared frequencies calculated from this surface were ν_H = 1810 cm^{-1} and ν_D = 1246 cm^{-1}. Compared with results in Table II, the agreement again is good. We therefore may state one important result of this investigation by recognizing the very close similarity of parameters (m, b, and g) found in the analysis of two entirely different chemical systems, $H_5O_2^+$ and HF_2^-. The value of m = 6 seems to be fixed while the remaining two are only roughly set over the range $b \simeq 2.6$–3.2 and $g \simeq 0.64$–0.68. Calculations on the family of bihalide salts beyond HF_2^- are currently being carried out on the basis of the possibility of transferable (constant) parameters when *ab initio* MO data are unavailable.

Vibrational overtone transitions of ν_H are also predicted by the model calculations as given in Table II, but none as yet have been reported in the infrared or by the Raman technique. Supposing that excitation from the ground state is somehow induced to any of vibrational states (shown in Figure 4),[17] subsequent vibrational relaxation to the ground state may likely cause observable changes in O···O separation according to model predictions. The changes of course are expected to be short lived ($\tau \simeq 10^{-7}$ sec) with an *expansion* of the H bond distance fixed by the minimum of energy of the state to which the system has been excited. This type of vibrational Franck–Condon effect has been discussed previously[1,18] and may be one source of the line width of the ν_H transition.

One of the characteristic features of the strong hydrogen bond is the high anharmonicity of the H stretching vibration (see Table II). This can be seen from the calculated fundamental, $E_0^- - E_0^+ = \nu_H$ (1783 cm^{-1}) and its first symmetry-allowed overtone, $E_1^- - E_0^+$ (6060 cm^{-1}), a frequency ratio of 3.40 which is similar as the case in bifloride ion.[1] We would expect also that the ratio of ν_H/ν_D in $H_5O_2^+$ will deviate significantly from the harmonic value (1.38). Our calculated ratio, 1.436, is higher than the harmonic value and is close to the bifloride ion value of ν_H/ν_D = 1.506 (calcd) and = 1.42 (obsd).

The symmetric H_2O - - - - - OH_2 stretching frequency is calculated from force constant evaluated from the curvature of the ground state energy (see Fig 4)[17] using the harmonic oscillator approximation. The calculated O–O stretching frequency, $\nu_{O\text{-}O}$ = 480 ± 120 cm^{-1}, is averaged over of six calculations with the 25% standard deviation error due to the limitations of the numerical procedure and computer round-off errors. The general agreement with experimental value (412 cm^{-1}) is good.

The limitations of this linear model of H bonding should not be overlooked, however. The first-order approximations involving the separation of motion of large numbers of particles (electrons and nuclei) have been discussed earlier[1,18] and are certainly apparent. Particularly in $H_5O_2^+$, Chemouni, *et al.*,[12] have noted the strong coupling between the end OH bending vibration (1680 cm^{-1}) and the asymmetric H vibration of the bridge (1780 cm^{-1}). Thus, our comparisons of calculated and observed frequencies to 3–4 significant figures is perhaps not too meaningful. Still, we feel we have obtained considerable insight into the dynamics of the H bonding by the semiquantitative correlation of (vibrational) states and by roughly accounting for a number of observable effects.

Acknowledgment. We are pleased to acknowledge the National Science Foundation (Grant No. GP-31 725) for financial support of this study. We also wish to thank Dr. E. G. Weidemann for his helpful (written) comments on the least-squares fit of the SCF data.

Supplementary Material Available. Figures 2, 3, and 4 will appear following these pages in the microfilm edition of this volume of the journal. Photocopies of the supplementary material from this paper only or microfiche (105 × 148 mm, 20× reduction, negatives) containing all of the supplementary material for the papers in this issue may be obtained from the Journals Department, American Chemical Society, 1155 16th St., N.W., Washington, D. C., 20036. Remit check or money order for $3.00 for photocopy or $2.00 for microfiche, referring to code number JPC-73-2560.

References and Notes

(1) G. J. Jiang and G. R. Anderson, *J. Phys. Chem.*, **77**, 1764 (1973).
(2) G. Zundel and E. G. Weidemann, *Eur. Biophys. Congr. Proc., 1st*, **43** (1971).
(3) P. Kebarle, S. K. Searles, A. Zolla, J. Scarborough, and M. Arshadi, *J. Amer. Chem. Soc.*, **89**, 6393 (1967).
(4) T. C. Waddington, *Trans. Faraday Soc.*, **54**, 25 (1958).
(5) P. A. Kollman and L. C. Allen, *J. Amer. Chem. Soc.*, **92**, 6101 (1970).
(6) W. Kraemers and G. Diercksen, *Chem. Phys. Lett.*, **5**, 463 (1970).
(7) R. Janoschek, E. G. Weidemann, H. Pfeiffer, and G. Zundel, *J. Amer. Chem. Soc.*, **94**, 2387 (1972).
(8) G. C. Pimentel and A. L. McClellan, *Ann. Rev. Phys. Chem.*, **22**, 358 (1971).
(9) R. Blinc, D. Hadzi, and A. Novak, *Z. Elektrochem.*, **64**, 567 (1960).
(10) R. D. Gillard and G. Wilkinson, *J. Chem. Soc.*, 1640 (1964).
(11) A. C. Pivia and P. A. Giguere, *J. Chem. Phys.*, **52**, 355 (1970).
(12) E. Chemouni, M. Fournier, J. Ragiere, and J. Potier, *J. Chim. Phys.*, **67**, 517 (1970).
(13) M. A. Haney and J. L. Franklin, *J. Chem. Phys.*, **50**, 2028 (1967).
(14) R. D. Gillard and G. Wilkinson, *J. Chem. Soc.*, 1640 (1964).
(15) J. T. Mullplaupt and D. F. Hornig, *J. Chem. Phys.*, **24**, 769 (1956).
(16) W. C. Hamilton and J. A. Ibers, "Hydrogen Bonding in Solids," W. A. Benjamin, New York, N. Y., 1968, p 116.
(17) See paragraph at end of paper regarding supplementary material.
(18) G. R. Anderson and E. R. Lippincott, *J. Chem. Phys.*, **55**, 4077 (1971).

The Complex Solubility of Silver Bromide in Ethanol–Water, Methanol–Water, Acetone–Water, and Dioxane–Water Mixtures

Keith P. Anderson, Eliot A. Butler, and Earl M. Woolley*

Department of Chemistry, Brigham Young University, Provo, Utah 84602 *(Received January 29, 1973)*

Publication costs assisted by the Department of Chemistry, Brigham Young University

Results of a study of the solubility of silver bromide at 25° as a function of bromide ion concentration in water, in 10, 20, 30, 40, and 50% by weight methanol–water, ethanol–water, acetone–water, and dioxane–water mixtures, and in a 60% by weight dioxane–water mixture are presented. These results were obtained with previously established radiotracer techniques that are modified to include specific ion electrode measurements. All observed solubilities are interpreted in terms of the presence of silver ions, undissociated silver bromide molecules, dibromoargentate ions, and tribromoargentate ions. Values of the thermodynamic equilibrium constants relating the activities of these species to the bromide ion activity are obtained by a least-squares treatment of the solubility data for each solvent mixture. The observed changes in these equilibrium constants are discussed in terms of electrostatics theory, solvation theory, and other specific solvent effects.

Introduction

The work reported in this paper is a continuation[1,2] of our study of the solubilities of slightly soluble silver salts as functions of anion concentration in aqueous–nonaqueous mixtures. The solubility of silver bromide and the various equilibria involved have been investigated in 0, 10, 20, 30, 40, and 50% by weight ethanol–water, methanol–water, acetone–water, and dioxane–water mixtures and in a 60% dioxane–water mixture at bromide ion concentrations between 10^{-9} and 10^{-1} *M*. A radiotracer technique described previously[2] was used to determine total silver concentrations. Silver ion activities were measured with an Orion Model 94-16 silver–sulfide specific ion electrode. Our purpose was to determine quantitatively the effects of the composition of the solvent on the concentrations and equilibrium constants of the silver-containing species in solution and to interpret these effects.

Experimental Section

All chemicals used were reagent grade. Solutions were prepared from doubly distilled water which had a specific conductance $<1.3 \times 10^{-6}$ ohm^{-1} cm^{-1} at 25°. Gas chromatographic analysis of the four organic solvents used in solution preparations indicated the absence of water (<0.1%) and volatile organic impurities.

The method of solution preparation, equilibration, and analysis has been described.[2] Solubility determinations (25), each at a different bromide ion concentration, were made in each aqueous–organic mixture. The solubility product constant, K_s, associated silver bromide formation constant, K_1, and the stepwise bromoargentate ion formation constants, K_2 and K_3, were calculated using the modified least-squares method of data treatment previously outlined[2,3] with the inclusion of an iterative procedure to avoid unequal weighting of data. The notation for the various equilibria is the generally accepted notation for consecutive or stepwise constants. The mass balance equation (eq 1a, 1b, and 1c) for these systems includes previously defined activity coefficients.[1] As can be seen in eq 1b and 1c, γ_0*, the activity coefficient of the uncharged species in any solvent mixture, is constrained to be unity. This constraint forces the effect of the solvent to appear as variations in B values. Values for the densities and dielectric constants of the solutions were obtained by interpolation of data as reported previously.[1,2] The potential difference between an Orion Model 94-16 silver–sulfide electrode (which senses free silver ion in solution and free sulfide ion when silver ion is absent) and a double-junction calomel reference electrode was measured in each equilibrated solution. An Orion Model 801 digital pH meter was used to measure the potential differences. The silver–sulfide electrode was calibrated to read silver ion concentrations by measurements in standard $AgNO_3$ solutions of the same organic solvent content as the equilibrated sample solutions. Corrections for ionic strength effects were made.

$$[Ag_{total}] = [Ag^+] + [AgBr] + [AgBr_2^-] + [AgBr_3^{2-}] \quad (1a)$$

$$[Ag_{total}] = \frac{K_s}{[Br](\gamma_1^*)^2} + \frac{K_1K_s}{\gamma_0^*} + K_1K_2K_s[Br^-] + K_1K_2K_3K_s[Br^-]^2/(\gamma_1^*)^2 \quad (1b)$$

$$[Ag_{total}] = \frac{A}{[Br^-](\gamma_1^*)^2} + B + C[Br^-] + D[Br^-]^2/(\gamma_1^*)^2 \quad (1c)$$

The bromide ion concentrations were calculated from total bromide mass-balance equations. A value for the solubility product constant for AgBr was calculated from the electrode-determined silver ion activity and the bromide ion activity in each of the equilibrated solutions. Values of K_s determined in this manner agree with each other with an average deviation of only a few hundreths of a log unit so long as the mass-balance determination of free-bromide ion can be made reliably. At low free-bromide ion concentrations the concentrations of other bromide-containing species are no longer negligible in the determination of free-bromide ion. Free-bromide ion concentrations were calculated in this low-concentration region using values of the mean solubility product constant and silver ion activities calculated from selective-ion electrode readings. Free-

bromide ion concentrations and total silver concentrations[4] were used to determine equilibrium constants by a least-squares fit of the data to eq 1c as discussed previously.[1,2] In the calculations it has been assumed that $\gamma_2^* = (\gamma_1^*)^4$.

Results and Discussion

The log values for K_s, K_1, K_2, and K_3 listed in Table I were calculated from the least-squares solubility curves. The B term of Table I is K_1K_s/γ_0^* and is equal to the molar concentration of the undissociated AgBr species in each solution. The values of $-\log B$ are plotted *vs.* the reciprocal of the dielectric constant of the solvent mixtures in Figures 1 and 2. The deviation of B from its value in pure water appears to be too large to be attributed to experimental error. Examination of Figure 1 indicates that deviations are possibly caused by solvent–solvent interactions.[5] If it is supposed that the product K_1K_s is constant in all solvent mixtures, then variations in B ($B = K_1K_s/\gamma_0^*$) can be interpreted in terms of differences between γ_0^* and γ_0, where γ_0 is the activity coefficient of the uncharged species in water solvent. An assumed constancy of K_1K_s implies the choice of a solvent-independent standard state for the undissociated AgBr molecules so that variations in the value of K_1 with solvent composition reflect changes in the sum of the standard chemical potentials of Ag^+ and Br^-, while variations in the value of K_2 with solvent composition reflect changes in the difference between the standard chemical potentials of Br^- and $AgBr_2^-$. The effect of holding K_1K_s constant is to subtract out the nonlinear effects that are apparently associated with the uncharged species.[5] Thus plots of log K_2 *vs.* solvent composition show greatly improved linearity when K_1K_s is taken to be constant. (See Figures 1–3.) The values of log K_1 and log K_2 given in Table I are those calculated using the assumption that K_1K_s is always equal to its value in pure water. Values of log K_3 listed in Table I are independent of this assumption.

The values we report in Table I for pure water are in good agreement with values from the literature. Typical values of log K_s are -12.27,[6] -12.3,[7] and -12.54[8] compared to our value of -12.46. Our values of 6.09 for log K_1 and -6.37 for log B indicate that there is somewhat more undissociated AgBr in solution than others have often suggested. Previous workers have reported values of log K_1 of 4.23,[6] 4.15,[9] and 5.08.[10] On the other hand, the values we give in Table I for log K_2 and log K_3 indicate that we found somewhat smaller amounts of $AgBr_2^-$ and $AgBr_3^{2-}$ in solution than had been reported previously. Among values reported in the literature are the following; log K_2: 3.0,[6] 2.5,[7] 2.0,[8] 3.0,[9] and 3.4;[11] log K_3: 1.4,[6] 1.2,[7] and 0.9.[8]

There is much less in the literature on values of the various equilibrium constants in mixed solvents. Kratohvil and Težak[8] report values of K_s (estimated), K_2, and K_3 in 30% and 50% ethanol–water, 62% methanol–water, and in 48.5% acetone–water that are consistent with our results. More recently it has been reported[12] that log K_s becomes more negative by about 1.0 by changing from water to a 40% acetone–water solvent, which is also in agreement with our results.

Log K_1 ($-\log K_s$) *vs.* $1/D$ data fit straight lines constrained to pass through the water point fairly well. However, there appears to be no way to rationalize the inclusion of the water points for a straight line fit for log K_2 and log K_3 data.

TABLE I: Equilibrium Constants in the Solvent Mixtures[a]

Wt % nonaqueous component	Dielectric constant	$-\log K_s$	$\log K_2$	$\log K_3$	$-\log B$	% SD[b]
		A. Ethanol–Water Mixtures				
0.00	78.54	12.46	0.45	2.10	6.37	10.6
9.67	72.99	12.52	1.74	0.70	8.14	16.3
19.86	67.08	12.80	1.87	0.69	6.88	25.2
34.47	58.37	13.00	2.43	−0.14	6.84	31.9
42.15	53.66	13.12	2.62	−0.55	6.83	34.7
54.23	46.66	13.71	2.74	0.34	6.06	28.4
		B. Methanol–Water Mixtures				
9.47	74.36	12.69	1.11	0.60	6.95	13.2
19.84	69.28	12.84	1.88	0.95	6.66	27.6
34.48	62.19	12.99	1.76	1.00	6.71	19.1
42.10	58.61	13.22	2.25	−0.08	7.76	37.8
54.20	52.88	13.50	2.12	0.84	6.31	25.4
		C. Acetone–Water Mixtures				
9.64	73.28	12.52	1.79	0.64	>8.5	22.4
19.80	67.73	12.99	2.03	0.75	8.47	7.2
34.43	59.17	13.23	2.73	0.40	7.31	21.0
42.08	54.41	13.47	3.12	0.06	7.65	12.0
54.15	46.87	13.49	3.72	−0.52	6.92	17.7
		D. Dioxane–Water Mixtures				
8.24	71.28	12.42	0.47	2.47	6.36	32.3
20.47	60.37	12.70	2.26	0.36	6.56	26.5
28.49	53.24	12.48	2.50	−0.04	6.12	15.3
40.75	42.33	12.84	3.02	−0.48	5.71	18.1
48.75	35.25	12.98	3.28	−0.56	6.18	19.9
60.73	25.24	13.25	3.89	<−0.6	6.52	17.5

[a] The assignment of meaningful values of uncertainties to be associated with our reported values of equilibrium constants is a difficult problem. The values we report here are given to what we consider to be a "reasonable" number of significant figures. [b] Relative (percentage) standard deviation of the experimental solubility data from the least-squares calculated solubility curve of eq 1.

The slopes for the log K_1 ($-\log K_s$) *vs.* $1/D$ curves (Table II) appear to be inversely proportional to the molar volume of the organic component and directly proportional to its dipole moment as observed for AgCl solutions.[1] Methanol–water (slope = 175, molar volume = 40.5, dipole moment = 1.70) is used as the reference solvent to calculate values of the slopes for the other solvents in eq 2, 3, and 4.

$$175 \times \frac{40.5}{58.5} \times \frac{1.69}{1.70} = 120 \quad \text{(ethanol)} \tag{2}$$

$$175 \times \frac{40.5}{73.5} \times \frac{2.89}{1.70} = 164 \quad \text{(acetone)} \tag{3}$$

$$175 \times \frac{40.5}{85.2} \times \frac{(0.655)_{\text{calcd}}}{1.70} = (32)_{\text{measd}} \quad \text{(dioxane)} \tag{4}$$

The results for ethanol–, methanol–, and acetone–water mixtures are in good agreement with those reported for AgCl solutions. The slopes differ for the two solutes, possibly indicating a difference in the radii of the chloride and bromide ions. Apparently the bromide ion, being somewhat larger than the chloride ion, is affected by both of the oxygens in dioxane rather than just one as was suggested by the experimental results for AgCl.[1]

If the point for water as solvent is omitted, the plots of log K_2 and log K_3 *vs.* $100/D$ are approximately linear. The

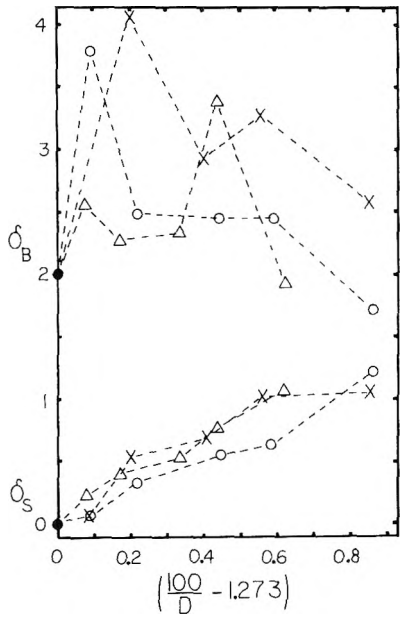

Figure 1. Plots of δ_B = log B (water) − log B (solvent) + 2.00 and δ_S = log K_S (water) − log K_S (solvent) according to the Born electrostatic model:[1] ●, solvent = water; O solvent = ethanol–water mixtures; △, solvent = methanol–water mixtures; X, solvent = acetone–water mixtures.

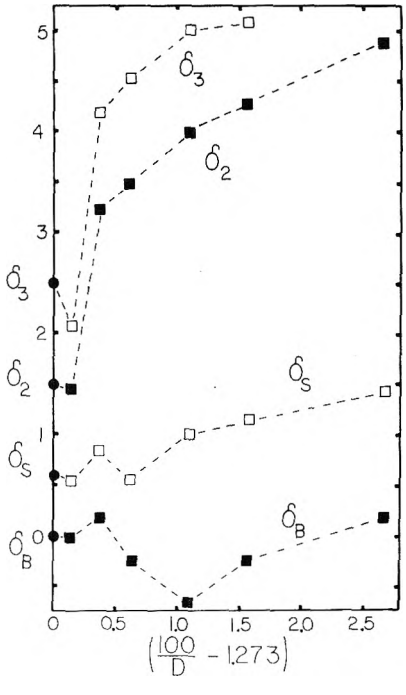

Figure 2. Plots of δ_B = log B (water) − log B (solvent); δ_S = log K_S (water) − log K_S (solvent) + 0.60, δ_3 = log K_3 (water) − log K_3 (solvent) + 2.50, and δ_2 = log K_2 (solvent) − log K_2 (water) + 1.50 according to the Born electrostatic model:[1] ●, solvent = water; □ and ■, solvent = dioxane–water mixtures.

TABLE II: Slopes of Plots of log K vs. $1/D$ (Figures 1–3)

	MeOH	EtOH	Acetone	Dioxane
−Log K_S and log K_1	175	120	191[a]	32
Log K_2[b]	252[a]	188[a]	283	89[c]
−Log K_3[b]	169[a]	272[a]	189	77[c]

[a] The 50% point is omitted. [b] The 0% point is omitted. [c] The 10% and 60% points are omitted.

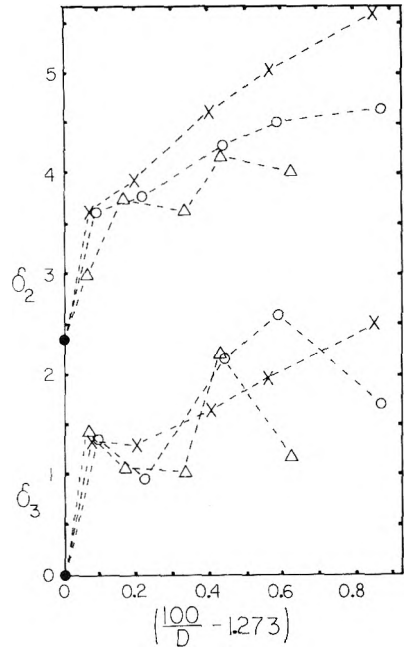

Figure 3. Plots of δ_2 = log K_2 (solvent) − log K_2 (water) + 2.40 and δ_3 = log K_3 (water) − log K_3 (solvent) according to the Born electrostatic model:[1] ●, solvent = water; O, solvent = ethanol–water mixtures; △, solvent = methanol–water mixtures; X, solvent = acetone–water mixtures.

fact that points for water do not lie on these lines suggests that the addition of the nonaqueous component possibly causes a drastic change in some property of the species in solution such as solvation, effective ionic radii, or effective dielectric constant of the solvent near the solute species.

One can use the treatment of Marshall[13] to try to estimate values of the hydration numbers of the several species present as was done previously with AgCl data.[1] However, this approach leads to negative values for hydration numbers for some of the species. It should also be noted that the validity of this approach has been challenged by Matheson.[14]

Acknowledgment. We are grateful to the Brigham Young University Research Division and to the NDEA Title IV Fellowship program for support of part of this work.

Supplementary Material Available. Solubility data consisting of [Br⁻], [Ag(total)], and ionic strengths of equilibrated solutions will appear following these pages in the microfilm edition of this volume of the journal. Photocopies of the supplementary material from this paper only or microfiche (105 × 148 mm, 20× reduction, negatives) containing all of the supplementary material for the papers in this issue may be obtained from the Journals Department, American Chemical Society, 1155 16th St., N.W., Washington, D. C. 20036. Remit check or money order for $3.00 for photocopy or $2.00 for microfiche, referring to code number JPC-73-2564.

References and Notes

(1) K. P. Anderson, E. A. Butler, and E. M. Woolley, *J. Phys. Chem.*, **75**, 93 (1971).
(2) K. P. Anderson, E. A. Butler, D. R. Anderson, and E. M. Woolley, *J. Phys. Chem.*, **71**, 3566 (1967).
(3) (a) K. P. Anderson and R. L. Snow, *J. Chem. Educ.*, **44**, 756

(1967); (b) T. P. Kohman, *ibid.*, **47**, 657 (1970).
(4) See paragraph at end of paper regarding supplementary material.
(5) K. P. Anderson, E. A. Butler, and E. M. Woolley, *J. Phys. Chem.*, **71**, 4584 (1967).
(6) D. D. Wagman, W. H. Evans, V. B. Parker, I. Halow, S. M. Bailey, and R. H. Schumm, *Nat. Bur. Stand. Tech. Note.* **No. 270-3** (1968); **No. 270-4** (1969).
(7) L. G. Sillén and A. E. Martell, "Stability Constants of Metal-Ion Complexes," The Chemical Society, London, 1964.
(8) J. Kratohvil and B. Težak, *Ark. Kemi*, **26**, 243 (1954).
(9) K. B. Katsimirskii and V. P. Vasil'ev, "Instability Constants of Complex Compounds," Russian Translation, Consultants Bureau, New York, N. Y., 1960.
(10) J. Kratohvil, B. Težak, and V. B. Vouk, *Ark. Kemi*, **26**, 191 (1954).
(11) R. Alexander, E. C. F. Ko, Y. C. Mac, and A. J. Parker, *J. Amer. Chem. Soc.*, **89**, 3703 (1967), in conjunction with data from ref 6.
(12) C. Barraqué, J. Vedel, and B. Trémillon, *Bull. Soc. Chim. Fr.*, 3421 (1968).
(13) W. L. Marshall, *J. Phys. Chem.*, **74**, 346 (1970).
(14) R. A. Matheson, *J. Phys. Chem.*, **73**, 3635 (1969).

Diffusion Coefficients of Tetrabutylammonium Halides in Water at 25°[1,2]

Hyoungman Kim,* Arnold Revzin,[3] and Louis J. Gosting[4]

Institute for Enzyme Research and Department of Chemistry, University of Wisconsin, Madison, Wisconsin 53706
(Received October 27, 1972; Revised manuscript received June 18, 1973)

Publication costs assisted by the National Institute of Arthritis and Metabolic Diseases

Diffusion coefficients measured with a new optical diffusiometer are reported for tetrabutylammonium halides (Bu_4NX) in water at 25°. The concentration range studied extended up to 0.6 *M* for Bu_4NCl, 0.8 *M* for Bu_4NBr, and 0.06 *M* for the less soluble Bu_4NI. The diffusion coefficients for a given concentration decreased with increasing anion size while the mobility terms, which were obtained by dividing the diffusion coefficients by a thermodynamic term, showed the reverse order. Refractive index derivatives were also determined as well as density data from which partial molal volumes were computed.

Introduction

In recent years, there has been much interest in the physical chemical properties of tetraalkylammonium halides in aqueous solution. A large number of experimental results on both the equilibrium and the transport behavior of these materials has been published. These results have shown that the larger tetraalkylammonium ions significantly increase the degree of structure among neighboring water molecules. There are also cation–cation as well as cation–anion interactions in solutions of tetrabutyl- and tetraamylammonium salts, although the detailed mode of interaction is not known.

The present study provides another of the fundamental transport properties, the isothermal diffusion coefficients of tetrabutylammonium chloride, bromide and iodide. It is hoped that these diffusion coefficients can be combined with activity data and with other transport properties such as the conductance and transport numbers, to compute the ionic transport coefficients, l_{ij}, which have been described by Miller.[5] The ionic transport coefficients may give better insight into the nature of ionic interactions than either conductivity or diffusion data alone.[6,7]

As a by-product of the diffusion experiments, we have also obtained refractive index derivative and density data; from the latter we have computed the partial molal volumes of the tetrabutylammonium halides.

Experimental Section

Materials. Tetrabutylammonium chloride, bromide, and iodide were obtained from Eastman Organic Chemicals. Both tetrabutylammonium bromide, Bu_4NBr, and tetrabutylammonium iodide, Bu_4NI, were recrystallized three or more times from once-distilled acetone. Tetrabutylammonium chloride, Bu_4NCl, was first dissolved in once-distilled acetone and then was precipitated by adding purified ether. Recrystallization was performed three times. All salts were dried in the vacuum oven for at least 1 week and then were stored in a vacuum desiccator over P_2O_5. For the highly hygroscopic Bu_4NCl, the transfer into a weighing bottle was made in a polyethylene glove bag (Instruments for Research and Industry, Cheltenham, Pa.) filled with dry nitrogen gas. The molecular weights used are 277.925 for Bu_4NCl, 322.376 for Bu_4NBr, and 369.376 for Bu_4NI.

All solutions were prepared with distilled water which had been further purified with a Barnstead water purifier and then saturated with air. The density values used to calculate the air-buoyancy corrections in preparing the solutions were 1.1 for Bu_4NCl and Bu_4NBr, 1.5 for Bu_4NI, and 8.4 for the metal weights.

Diffusion Experiments. All diffusion measurements were performed on a new optical diffusiometer, using procedures similar to those used with previous instruments.[8] A detailed description of the new device will be given elsewhere;[9] here we shall describe only its main features.

The heart of the instrument is a rigid steel beam, 884 cm in length, to the top of which are bolted accurately aligned stainless steel dove-tailed ways. All optical components (light source, lens, water bath windows, diffusion cell, cylinder lens, and camera) are firmly supported on the ways. Owing to its heavy weight, the water bath is not supported by the beam but instead is bolted to the floor

and ceiling of the laboratory. Watertight seals between the windows and the bath itself are formed with flexible rubber bellows which allow minor movements of the water bath relative to the ways without inducing strains.

Illumination was provided with a GE H-100A4 mercury vapor lamp fitted with a Kodak Wratten 77A filter, which emits light at a wavelength of 5460.7 Å (in air). The source slit can be made precisely horizontal or vertical as required. Our experiments were performed using a single main collimating lens of focal length about 145 cm; the optical lever arm, b, was about 309 cm. The cylinder lens is mounted in a special housing which permits it to be swung out of the light path (for Gouy experiments) or into an accurately reproducible position in the light path (for Rayleigh measurements).

Diffusion cells used were the glass and fused quartz Tiselius type and had cell dimensions, *a*, along the optical axis of about 2.5 cm. The initial boundary between the upper and lower solutions was formed by siphoning through a single stainless steel capillary or a single platinum capillary. For both δ-corrections and the fractional part of the total number of fringes, photographs were taken on Kodak Metallographic glass plates. During free diffusion, 6 to 12 photographs of Gouy fringes were taken on Kodak Spectroscopic IIIG glass plates. One or two Rayleigh photographs were also taken. An unusual property of Bu_4NCl is that the density of its aqueous solution is less than that of pure water and decreases with increasing concentration. Therefore, the upper solution must be more concentrated than the lower solution, and the Gouy fringes lie *above* the undeviated slit image in contrast to the usual case.

The measurements of the photographic plates were made with a photoelectric null indicator[10,11] mounted on a Gaertner Model M2001RS-B Toolmakers' microscope. This microscope is provided with two encoders and each axis position is displayed on a Tyco Digi-Point Readout to the nearest 0.0001 cm. The Digi-Point readout is connected to an IBM No. 29 keypunch through an interface (Instrumentation Systems Center, University of Wisconsin) and the displayed numbers on the Digi-Point Readout were directly punched onto data cards. The calculations were made with a Univac 1108 digital computer at the University of Wisconsin Computation Center.

The temperature of the water bath was measured during diffusion with a mercury-in-glass thermometer which had been calibrated against a platinum resistance thermometer. The temperature of the water bath during diffusion runs was within ±0.005° of 25° and never fluctuated by more than 0.003° during a run.

The density of each solution was measured in triplicate with single-neck pycnometers of volume about 30 ml in a water bath maintained at 25°.

Results and Discussion

Tables I, II, and III present the diffusion coefficients and other data from experiments on Bu_4NCl, Bu_4NBr, and Bu_4NI, respectively. In these tables $\bar{c}$ and $\bar{C}$ are the mean solute concentrations (the average for the upper and lower starting solutions) expressed in g/100 ml and mol/l., respectively, Δc is the initial concentration difference between the upper and lower solutions, J is the total number of fringes, $(\Delta n/\Delta c)$ is the refractive index derivative, and $(D)_v$ is the mutual diffusion coefficient for the volume-fixed frame of reference. Also given in Tables I and II are values for the mobility term, $\mathfrak{M}$, which is expressed by the following equation.[12]

$$\mathfrak{M} = \frac{(D)_0}{1 + C\ \mathrm{d}\ \ln\ y/\mathrm{d}C} = \frac{(D)_v}{1 + m\ \mathrm{d}\ \ln\ \gamma/\mathrm{d}m} \quad (1)$$

In eq 1, $(D)_0$ is solvent-fixed mutual diffusion coefficient, m is the molality, and y and γ are the activity coefficients on the molar and molal scales, respectively. Values of $[1 + m\ \mathrm{d}\ \ln\ \gamma/\mathrm{d}m]$, evaluated using the molal activity coefficients given by Lindenbaum and Boyd[13] are also given in Tables I and II. Activity data for Bu_4NI are not available.

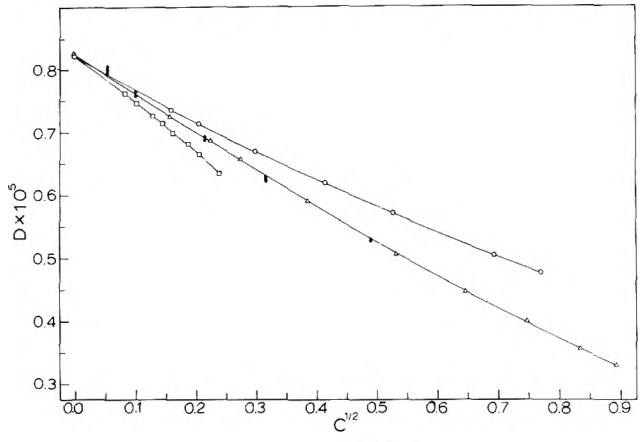

Figure 1. $D \times 10^5$ plotted against $\sqrt{C}$ for tetrabutylammonium halides in water at 25°: ○, Bu_4NCl; △, Bu_4NBr; □, Bu_4NI; ●, Bu_4NBr by Pepela, Steel and Dunlop.[15]

Figure 1 shows the variation of $(D)_v$ with $\sqrt{\bar{C}}$ for the three systems studied. The low solubility of Bu_4NI restricts the concentration range over which we could study this salt. The limiting diffusion coefficients at infinite dilution were calculated using the Nernst equation and they are found to be 0.8205×10^{-5}, 0.8244×10^{-5}, and 0.8217×10^{-5} for Bu_4NCl, Bu_4NBr, and Bu_4NI, respectively. The limiting equivalent conductivities were taken to be[14] 19.31 for Bu_4N^+, 76.39 for Cl^-, 78.22 for Br^-, and 76.98 for I^-. The limiting diffusion coefficients for the three salts studied here are equal within about 0.5% because the limiting equivalent conductivities of the anions are very nearly the same.

The filled circles in Figure 1 are the diffusion coefficients of Bu_4NBr obtained by Pepela, Steel, and Dunlop[15] using shearing interference optics.[16] It can be seen that results from the shearing diffusiometer and the Gouy method agree within the precision of the former.

The concentration dependence of the density, d, at 25°, is given by the expressions

$$d = 0.99707 - 5.30 \times 10^{-4}c + 4.25 \times 10^{-5}c^{3/2} \quad (\text{for } Bu_4NCl)$$

$$d = 0.99707 + 6.44 \times 10^{-4}c + 4.34 \times 10^{-5}c^{3/2} \quad (\text{for } Bu_4NBr)$$

and

$$d = 0.99707 + 1.56 \times 10^{-3}c \quad (\text{for } Bu_4NI)$$

where d is expressed in g/ml and c is in g/100 ml. In these expressions, 0.99707 is the rounded value of the density of pure water at 25° while the coefficients of c and $c^{3/2}$ were determined by the method of least squares. The average deviation of the measured densities from these functions is less than 0.02%.

Figure 2 presents the apparent molal volumes, ϕ_v, and the partial molal volumes, $\bar{V}$, for Bu_4NCl and Bu_4NBr,

TABLE I: Experimental Results for Bu_4NCl in Water at 25°

$\bar{c}$, g/100 ml	$\bar{C}$, mol/l.	m	$-\Delta c$, g/100 ml	J	$(\Delta n/\Delta c) \times 10^3$, (g/100 ml)$^{-1}$	$(D)_v \times 10^5$, cm^2/sec	$1 + m\, d\ln\gamma/dm$	$\mathfrak{M} \times 10^5$, cm^2/sec
0.7200	0.02590	0.02618	0.7731	59.18	1.6670	0.7353	0.943	0.780
1.1758	0.04231	0.04297	1.2251	93.98	1.6706	0.7142	0.927	0.770
2.4780	0.08916	0.09182	0.6560	50.72	1.6838	0.6701	0.906	0.740
4.8122	0.17315	0.18291	0.7727	60.43	1.7031	0.6195	0.896	0.691
7.7213	0.27782	0.30316	1.3875	109.99	1.7263	0.5725	0.887	0.645
13.3779	0.48135	0.56094	0.5879	47.51	1.7599	0.5064	0.944	0.536
16.4915	0.59338	0.71818	3.5835	293.14	1.7815	0.4787	0.979	0.489

TABLE II: Experimental Results for Bu_4NBr in Water at 25°

$\bar{c}$, g/100 ml	$\bar{C}$, mol/l.	m	Δc, g/100 ml	J	$(\Delta n/\Delta c) \times 10^3$, (g/100 ml)$^{-1}$	$(D)_v \times 10^5$, cm^2/sec	$1 + m\, d\ln\gamma/dm$	$\mathfrak{M} \times 10^5$, cm^2/sec
0.8131	0.02522	0.02549	0.8192	58.36	1.5600	0.7258[a]	0.895	(0.812)[b]
0.8131	0.02522	0.02549	1.6262	115.88	1.5604	0.7225[a]	0.895	
1.6309	0.05059	0.05152	0.7979	57.34	1.5650	0.6860	0.845	0.812
2.4035	0.07455	0.07649	0.6780	48.62	1.5703	0.6566	0.831	0.790
4.8214	0.14956	0.15703	0.6045	43.86	1.5888	0.5888	0.790	0.745
9.1336	0.28332	0.31039	1.2655	93.33	1.6149	0.5060	0.711	0.712
13.5280	0.41963	0.48087	1.2656	94.52	1.6354	0.4468	0.687	0.650
18.0646	0.56035	0.67400	1.2575	94.86	1.6518	0.3981	0.690	0.577
22.5134	0.69835	0.88286	0.7164	54.25	1.6582	0.3548	0.682	0.520
25.7892	0.79996	1.05083	0.7023	53.46	1.6667	0.3277	0.664	0.494

[a] The two experiments at $\bar{c} = 0.8131$ showed behavior which indicated a concentration dependence of $(D)_v$ and/or dn/dc across the diffusion boundary. Thus the values given in the "D" column are not differential diffusion coefficients but are reduced height-area ratios, $\mathfrak{D}_A$, [L. J. Gosting and H. Fujita, *J. Amer. Chem. Soc.*, **79**, 1359 (1957)]. A plot of $\mathfrak{D}_A$ *vs.* $(\Delta c)^2$ was extrapolated to $\Delta c = 0$ to yield the differential diffusion coefficient of 0.7269 $\times 10^{-5}$ cm^2/sec at this concentration [P. J. Dunlop and L. J. Gosting, *J. Amer. Chem. Soc.*, **77**, 5238 (1955)]. [b] Using the differential diffusion coefficient above.

TABLE III: Experimental Results for Bu_4NI in Water at 25°

$\bar{c}$, g/100 ml	$\bar{C}$, mol/l.	Δc, g/100 ml	J	$(\Delta n/\Delta c) \times 10^3$, (g/100 ml)$^{-1}$	$(D)_v \times 10^5$, cm^2/sec
0.2576	0.00698	0.4064	29.20	1.5647	0.7613
0.4062	0.01100	0.6092	43.77	1.5647	0.7443
0.6342	0.01717	0.6788	48.30	1.5656	0.7250
0.7981	0.02160	0.9949	71.58	1.5668	0.7132
0.9932	0.02689	0.9256	66.30	1.5670	0.6980
1.2394	0.03555	1.4799	106.59	1.5686	0.6820
1.5862	0.04294	0.7522	54.21	1.5695	0.6633
2.1349	0.05780	0.7172	51.76	1.5717	0.5348

calculated from the density values using the equations

$$\phi_v = \frac{1}{m}\left(\frac{1000 + mM}{d} - \frac{1000}{d_0}\right)$$

and

$$\bar{V} = \phi_v + \left[\frac{1000 - C\phi_v}{2000 + C\sqrt{C}\dfrac{d\phi_v}{d\sqrt{C}}}\right]\sqrt{C}\,\frac{d\phi_v}{d\sqrt{C}}$$

where M is the molecular weight of the solute and d_0 is the density of pure water. The values of $d\phi_v/d\sqrt{C}$ were obtained from the slopes of ϕ_v *vs.* $\sqrt{C}$ curves. The apparent and partial molal volumes of Bu_4NI did not change within the small concentration range studied and the average value obtained is 312.5 ml/mol. Our ϕ_v and $\bar{V}$ values check very closely with corresponding results of Wen and Saito[17] for Bu_4NBr.

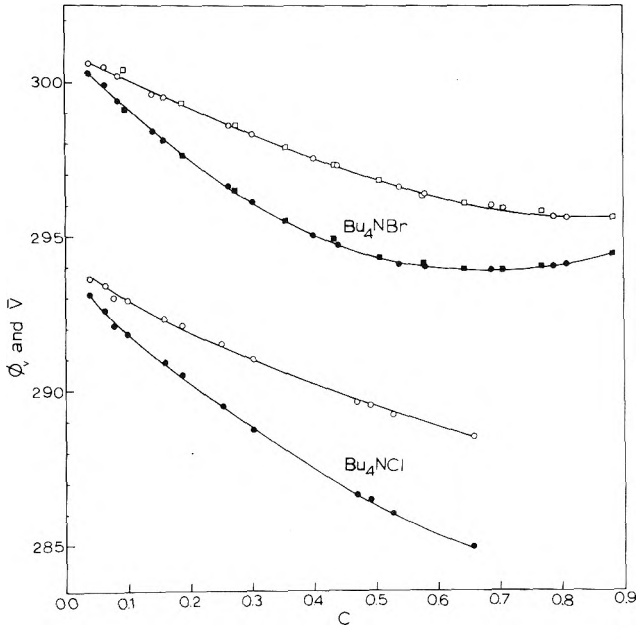

Figure 2. Apparent and partial molal volumes (ml/mol) of Bu_4NCl and Bu_4NBr plotted against C: O, ϕ_v; ●, $\bar{V}$; □ and ■, Wen and Saito.[16]

It is of interest to compare the concentration dependence of the diffusion coefficients of these tetrabutylammonium halides with that of more familiar 1-1 electrolytes such as the chlorides, bromides, and iodides of potassium and sodium. For the latter electrolytes the diffusion coefficients initially decrease, bottom out, and then

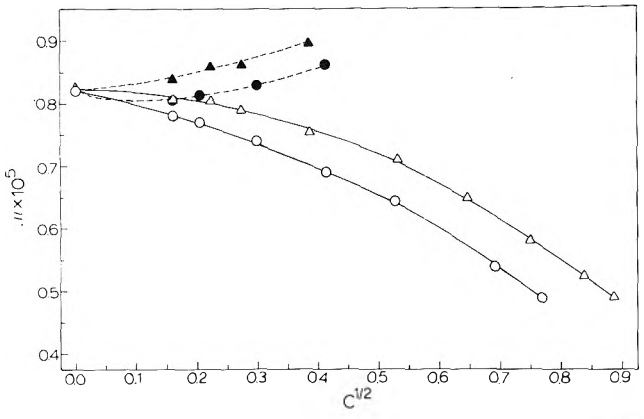

Figure 3. $\mathfrak{M} \times 10^5$ and $\mathfrak{M}(\eta/\eta_0) \times 10^5$ plotted against $\sqrt{C}$: O, $\mathfrak{M}$ for Bu_4NCl; Δ, $\mathfrak{M}$ for Bu_4NBr; ●, $\mathfrak{M}(\eta/\eta_0)$ for Bu_4NCl; ▲, $\mathfrak{M}(\eta/\eta_0)$ for Bu_4NBr.

increase with increasing concentration.[18-21] The magnitude of the initial decrease in $(D)_v$ is largest for the chlorides and smallest for the iodides, and at higher concentrations $(D)_v$ values for iodides are always larger than those for bromides which, in turn, are larger than those for chlorides. Identical trends are observed for the concentration dependencies of activity coefficients. It is striking that the ordering of diffusion coefficients and of activity coefficients for tetrabutylammonium halides is opposite to that of the "simple" electrolytes as described above.

The fact that the limiting equivalent conductivities of Cl^-, Br^-, and I^- have nearly identical values is attributed to ionic hydration, with the extent of hydration increasing in the order $I^- < Br^- < Cl^-$, thus making the sizes of the hydrated anions about the same.[22] This hydration effect alone, however, should give an order of activity coefficients opposite to the experimentally found order for both potassium and sodium halides.[23,24] To explain this observation, Diamond[22] proposed a type of ion pairing "through the agency of the water molecules," with the extent of ion-pair formation in the order of NaCl > NaBr > NaI (*or* KCl > KBr > KI).

The ordering of the dependence of Λ on C for tetrabutylammonium halides which has an order opposite to that for the alkali halides has been also explained in terms of ion-pair formation; it was proposed that the extent of ion-pairing, unlike to alkali halides, increases with the anion size.[13] The conductance data of tetrabutylammonium halides at low concentrations have been discussed in the same terms.[14]

The interpretation of diffusion data, especially at higher concentrations, is more complicated because $(D)_v$ contains both mobility and thermodynamic terms. The mobility term obtained using eq 1 depends on a large number of factors, such as long range Coulombic effects, electrophoretic effects, ion-solvent interactions, viscosity, and ion-pairing. It is of interest, however, to note that the $\mathfrak{M}$ values for both Bu_4NCl and Bu_4NBr decrease with increasing concentration while those of other 1-1 electrolyte systems[25,26] where ion pairing is relatively well established increase with concentration. The increase in the value of $\mathfrak{M}$ was attributed to the fact that when two ions form an ion pair they offer less resistance to motion.[25,27]

If tetrabutylammonium halides also form ion pairs as suggested by other studies,[13,14] it is clear that some other effect is overcoming the effect by the ion pairing. The most obvious effect is the viscosity and this can be clearly seen in Figure 3 where the values of $\mathfrak{M}$ and $\mathfrak{M}(\eta/\eta_0)$ are plotted against $C^{1/2}$. The values of relative viscosity were calculated using the viscosity coefficients of Desnoyers and Perron.[28] They obtained the coefficients from their viscosity data of concentrations of up to 0.3 M and therefore the $\mathfrak{M}(\eta/\eta_0)$ values in Figure 3 are also given up to that concentration. The values of $\mathfrak{M}(\eta/\eta_0)$ for both Bu_4NCl and Bu_4NBr increase with concentration and, unlike the values of $(D)_v$, both $\mathfrak{M}$ and $\mathfrak{M}(\eta/\eta_0)$ values of Bu_4NBr for a given value of C are larger than the corresponding values of Bu_4NCl. These observations are in agreement with the suggestion that tetrabutylammonium halides form ion pairs and that the extent of ion pairing increases with the anion size. However, those observations should not be construed as unambiguous support for the above suggestion because it is not known whether other factors such as the electrophoretic effect, ion-solvent interactions, and cation-cation interactions[29-32] affect the mobilities of these electrolytes significantly. As mentioned earlier, a better picture of these aqueous solutions may emerge when the ionic transport coefficients are obtained. It is hoped that other data necessary for the calculation of the ionic transport coefficients will soon be forthcoming.

References and Notes

(1) This investigation was supported in part by Public Health Service Research Grant AM-05177 from the National Institute of Arthritis and Metabolic Diseases.
(2) Portions of this work were submitted by A. R. to the Graduate School of the University of Wisconsin in partial fulfillment of the requirements for the Ph.D. degree.
(3) Recipient of Wisconsin Alumni Research Foundation Fellowship (1964-1965) and National Institutes of Health Predoctoral Fellowship (1965-1969).
(4) Deceased, May 31, 1971. Recipient of PHS Research Career Award, AM-K6-16,715.
(5) D. G. Miller, *J. Phys. Chem.*, **70**, 2639 (1966).
(6) M. J. Pikal, *J. Phys. Chem.*, **75**, 663 (1971).
(7) D. G. Miller and M. J. Pikal, *J. Solution Chem.*, **1**, 111 (1972).
(8) G. Reinfelds and L. J. Gosting, *J. Phys. Chem.*, **68**, 2464 (1964).
(9) L. J. Gosting, H. Kim, M. A. Loewenstein, G. Reinfelds, and A. Revzin, *Rev. Sci. Instrum.*, in press.
(10) R. P. Wendt, Ph.D. thesis, University of Wisconsin, 1961.
(11) J. G. Albright, Ph.D. thesis, University of Wisconsin, 1963.
(12) Equations 33 and 35 of ref 5.
(13) S. Lindenbaum and G. E. Boyd, *J. Phys. Chem.*, **68**, 911 (1964).
(14) D. F. Evans and R. L. Kay, *J. Phys. Chem.*, 70, 366 (1966).
(15) C. N. Pepela, B. J. Steel, and P. J. Dunlop, *J. Amer. Chem. Soc.*, **92**, 6743 (1970).
(16) O. Bryngdahl, *Acta Chem. Scand.*, **11**, 1017 (1957).
(17) W.-Y. Wen and S. Saito, *J. Phys. Chem.*, **68**, 2639 (1964).
(18) R. H. Stokes, *J. Amer. Chem. Soc.*, **72**, 2243 (1950).
(19) P. J. Dunlop and R. H. Stokes, *J. Amer. Chem. Soc.*, **73**, 5456 (1951).
(20) L. J. Gosting, *J. Amer. Chem. Soc.*, **72**, 4418 (1950).
(21) V. Vitagliano and P. A. Lyons, *J. Amer. Chem. Soc.*, **78**, 1549 (1956).
(22) R. M. Diamond, *J. Amer. Chem. Soc.*, **80**, 4808 (1958).
(23) R. A. Robinson and R. H. Stokes, "Electrolyte Solutions," 2nd ed, revised, Butterworths, London, 1965.
(24) Appendix 8.10 of ref 23.
(25) B. F. Wishaw and R. H. Stokes, *J. Amer. Chem. Soc.*, **76**, 2065 (1954).
(26) J. G. Albright and D. G. Miller, *J. Phys. Chem.*, **76**, 1853 (1972).
(27) See also page 300 of ref 23.
(28) J. E. Desnoyers and G. Perron, *J. Solution Chem.*, **1**, 199 (1972).
(29) W.-Y. Wen and K. Nara, *J. Phys. Chem.*, **71**, 3907 (1967).
(30) R. H. Wood, *et al.*, *J. Phys. Chem.*, **71**, 2149 (1967).
(31) A. LoSurdo and H. E. Wirth, *J. Phys. Chem.*, **76**, 1333 (1972).
(32) P. S. Ramanathan, C. V. Krishnan, and H. C. Friedmann, *J. Solution Chem.*, **1**, 237 (1972).

Surface Studies of the Adsorption of Sulfur-Containing Gases at 423°K on Porous Adsorbents. I. The Adsorption of Hydrogen Sulfide, Methanethiol, Ethanethiol, and Dimethyl Sulfide on Silica Gels

R. W. Glass*[1] and R. A. Ross

Department of Chemistry, Lakehead University, Thunder Bay, Ontario, Canada *(Received February 26, 1973)*

Calorimetric heats of adsorption have been determined at coverages up to one-tenth of a monolayer for hydrogen sulfide, methanethiol, ethanethiol, and dimethyl sulfide, adsorbed at 423°K on silica gels of varying surface hydroxyl group concentrations. Adsorption isotherms have been determined and entropies of adsorption calculated to provide additional data on the nature of the adsorbed species. The high values of the initial heats of adsorption of up to 30 kcal mol^{-1} are associated with surface heterogeneity. Subsequently, at coverages greater than 0.020 μmol m^{-2} a similar type of adsorbed species is probably formed by all gases through interactions involving the formation of hydrogen bonds between surface hydroxyl hydrogen atoms and the sulfur atoms of the adsorbate. The differences in heats, entropies, and adsorption capacities for these gases are believed to be related to the magnitude of the inductive effect on the sulfur atom. A decrease in the heat of adsorption and adsorption capacity and an increase in the entropy of the adsorbed species occurred with all gases as the surface hydroxyl group concentration of the silica gels was decreased.

Introduction

This investigation contributes to a series of studies on the adsorption of sulfur-containing gases on various solids. The studies are largely motivated by the possibility of using adsorption or adsorption with catalysis as effective processes for the removal of deleterious sulfur compounds from industrial stack gases.

Although many studies[2-5] have been reported of the adsorption of specific sulfur-containing gases on solid adsorbents, few have been detailed and very few have included essential thermodynamic measurements. Those studies that have included thermodynamic data were carried out at temperatures near the boiling point of the adsorbate.[6-8] Thus while the data were of considerable theoretical importance, their practical value was limited since much higher temperatures are normally encountered when solid adsorbents or catalysts are used to remove sulfur-containing gases from industrial effluents.

Earlier, results were described[8] for the adsorption of hydrogen sulfide, methanethiol, ethanethiol, and dimethyl sulfide on silica gels at their respective boiling points. Adsorption–desorption isotherms and isosteric heats of adsorption for surface coverages above one-tenth of a monolayer were determined. These data showed that hydrogen bonding was involved at low surface coverages and that the heats decreased with increasing surface coverage to values approaching the heat of liquefaction of the respective gases at monolayer completion.

In the present work calorimetric heats of adsorption, adsorption isotherms, and entropies of adsorption have been determined for hydrogen sulfide, methanethiol, ethanethiol, and dimethyl sulfide adsorbed at 423°K at coverages up to one-tenth of a monolayer on silica gels of different surface hydroxyl group concentrations.

Experimental Section

Materials. Davison 923 grade silica gel (surface area, 630 m^2 g^{-1}; particle size, 75–150 μm) was used as the adsorbent. The surface hydroxyl group concentration was varied by heat treatment of the adsorbent for 20 hr at 240, 550, and 700° in a static air atmosphere. Surface hydroxyl group concentrations, surface areas, "lump" densities by displacement of mercury, and pore size distributions for these heat-treated gels have been given earlier[9] and the key data are summarized in Table I.

After heat-treatment the adsorbent was cooled over phosphoric anhydride, transferred to the appropriate apparatus, and then outgassed at 150° overnight at $<10^{-4}$ Torr.

CP grade hydrogen sulfide (99.7 mol %, Matheson) was drawn, after line flushing, from the cylinder to a trap attached to the apparatus. It was then outgassed at 10^{-4} Torr and vacuum distilled over trays of phosphoric anhydride. Middle fractions only were used and mass spectrometric analysis showed these to be >99.9% pure.

Methanethiol (Matheson) had a stated purity of 99.6 mol %. It was drawn, after line flushing, from the cylinder to a trap attached to the adsorption apparatus. The procedure followed in the purification of hydrogen sulfide was again repeated. Mass spectrometric analysis of the purified gas showed it to be >99.9% H_2S.

Ethanethiol, Eastman Kodak Ltd., was shown by mass spectrometric analysis to be at least 99.9% pure. The liquid was obtained in a sealed glass bottle and was transferred by pipet in a nitrogen atmosphere to a removable reservoir. The reservoir was quickly attached to the apparatus and the liquid was thoroughly outgassed and then frozen using a liquid nitrogen trap. The gas was then vacuum distilled over trays of phosphoric anhydride, the first and last fractions being discarded, and was stored at liquid nitrogen temperature. The sample was always outgassed prior to use.

Dimethyl sulfide, Eastman Kodak Ltd., was obtained in a sealed glass bottle. The specification was Standard Grade laboratory reagent, 0.84 g ml^{-1} at 20°, and on mass spectrometric analysis it was shown to be 99.9% pure. The transferral and purification procedures followed for ethanethiol were repeated here.

Apparatus and Procedure. Heats of adsorption and adsorption isotherms were determined in an apparatus similar to that described earlier.[10] Entropies of adsorption were calculated from the classical thermodynamic equations[11] taking the standard state of each gas at 1 atm and ignoring deviations from the ideal gas law. Thus

$$\bar{S}_s = S_g - R \ln p - (q_{st}/T) \quad (1)$$

where $\bar{S}_s$ is the differential molar entropy of the adsorbed species at temperature T and equilibrium pressure p; S_g is the entropy of the gas and q_{st} is the isosteric heat of adsorption.

Since differential heats of adsorption were measured experimentally, eq 1 may be rewritten

$$\bar{S}_s = S_g - R \ln p - (q_d + RT)/T \quad (2)$$

since the differential heat of adsorption, $q_d \simeq q_{st} - RT$.

Thus if values of S_g are obtained from the literature and the differential heat of adsorption and the equilibrium pressure are known at a variety of surface coverages, the differential molar entropy of adsorption at these coverages can be calculated.

The experimental entropy values were compared with theoretical values calculated for mobile and immobile layers. In the model of immobile adsorption the atoms are firmly bound to adsorption sites and there are no translational motions perpendicular or parallel to the surface. The only entropy of the adsorbed layer present is that of the differential molar configurational entropy[12] which is given by

$$\bar{S}_{sc} = -R \ln [\theta/(1 - \theta)] \quad (3)$$

where θ is the degree of surface coverage.

The other extreme model of adsorption is that of an ideal two-dimensional adsorbed surface gas in which the degrees of rotation are retained and there is also the possibility of the adsorbed species moving perpendicular to the surface.[13] In this case the differential molar entropy of the species is given by

$$\bar{S}_s = \bar{S}_{2t} + \bar{S}_{rot} + \bar{S}_{vib} \quad (4)$$

where $\bar{S}_{2t}$ is the two-dimensional translational entropy of an adsorbed species and $\bar{S}_{rot}$ and $\bar{S}_{vib}$ are the corresponding rotational and vibrational entropies.

$\bar{S}_{2t}$ for an ideal surface gas may be evaluated[12] using the equation

$$\bar{S}_{2t} = R \ln MTA + 63.8 \quad (5)$$

where M is the molecular weight of the gas and A is the area occupied per molecule which is a function of the number of molecules adsorbed. $\bar{S}_{rot}$ and $\bar{S}_{vib}$ may be obtained from the literature or they can be calculated from the usual statistical thermodynamic equations.[14]

Results

Hydrogen Sulfide. Heats of adsorption were determined at 423°K for surface coverages between 0.005 and 0.150 μmol m^{-2} and are shown in Figure 1. At 423°K, 7.5 μmol m^{-2} is approximately equivalent to monolayer coverage.[8]

All adsorbents exhibited relatively high heats at the lowest coverage. At 0.005 μmol m^{-2} the 240° gel gave a heat of adsorption of 30.0 kcal mol^{-1}. The heats then fell rapidly with increasing surface coverage. The heat curves for the 550 and 700° gels were similar but exhibited a more rapid fall in heat for the same increase in surface coverage, and the "limiting" heats were reduced to 7.3 kcal mol^{-1} for the 550° gel and to 5.8 kcal mol^{-1} for the 700° gel.

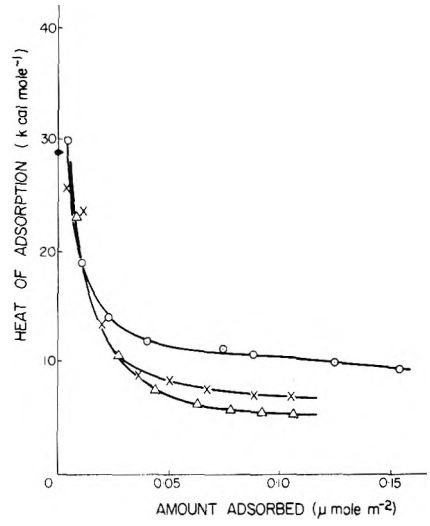

Figure 1. Variation of heat of adsorption of hydrogen sulfide with amount adsorbed at 423°K on heat-treated silica gels. Heat treatment at 240° (O), 550° (×), and 700° (Δ).

TABLE I: Surface Areas, "Lump" Densities, and Surface Hydroxyl Group Concentrations for Heat-Treated Silica Gels

Temp of heat treatment, °C	Surface area, $m^2\ g^{-1}$	"Lump" density, $g\ cm^{-3}$	Surface OH group concn, μmol of OH m^{-2}
240	630	1.182	7.2
550	580	1.275	2.4
700	490	1.391	1.3

The adsorption isotherms at 423°K for the 240, 550, and 700° gels exhibit the same general features as those obtained for sulfur dioxide on the same materials (Figure 2). The curves were linear and had slopes that decreased with increasing temperature of heat treatment of the sample. However, for a given heat-treatment temperature and a given adsorbate pressure, the amount of gas adsorbed was generally only half of that for sulfur dioxide. Equilibrium times were of the order of 30 min for all points on the isotherm and did not vary significantly with the sample used. Reversibility tests[7] showed that the adsorption was reversible for each adsorbent.

Infrared analysis of the gas desorbed from each sample at 423°K showed that no component other than hydrogen sulfide was present. In addition, no trace of free sulfur was detected on chemical analysis of the solid residues.

The variation of the experimental differential molar entropy as a function of surface coverage for adsorptions at 423°K on silica gels is shown in Figure 3. The curves for the 550 and 700° gels were very similar rising rapidly from low entropy values of about 5 cal deg^{-1} mol^{-1} at 0.010 μmol m^{-2} to relatively constant values of 36.5 and 39.8 cal deg^{-1} mol^{-1}, respectively, at 0.100 μmol m^{-2}. At this coverage the curves for the 550 and 700° gels were 1.0 and 4.5 cal deg^{-1} mol^{-1}, respectively, higher than that calculated for mobile adsorption. In contrast the curve for the 240° gel was 5.0 cal deg^{-1} mol^{-1} below the theoretical curve at 0.130 μmol m^{-1} having risen from a value of about 25.0 cal deg^{-1} mol^{-1} at 0.010 μmol m^{-1}.

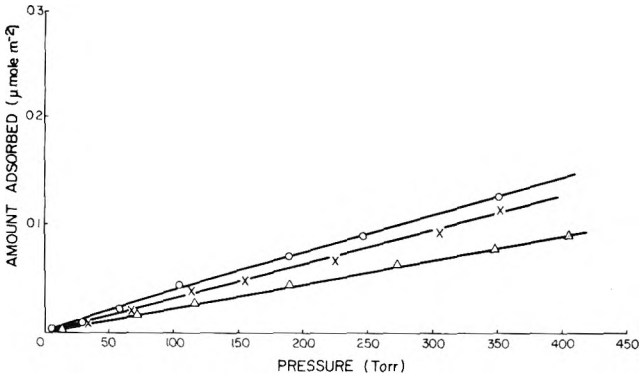

Figure 2. Adsorption isotherms for hydrogen sulfide at 423°K on heat-treated silica gels. Heat treatment at 240° (O), 550° (×), and 700° (△).

Methanethiol. There was a tendency for the value of the heats of adsorption[15] on all the adsorbents to level out above a coverage of 0.200 μmol m^{-2} following the relatively rapid falls between 0.010 and 0.050 μmol m^{-2}. The 700° gel exhibited the most rapid fall from 28.0 kcal mol^{-1} at 0.010 μmol m^{-2} to 15.0 kcal mol^{-1} at 0.050 μmol m^{-2} and began to level out toward the lowest heat value determined, about 6.5 kcal mol^{-1}, at 0.400 μmol m^{-2}.

Adsorption isotherms for methanethiol[15] were determined at 423°K on the three gel samples and the familiar trend of decreasing amounts adsorbed, at a given pressure, with increase in the temperature of heat treatment of the gel was shown by this gas. The isotherms of the 240 and 550° gels were slightly concave to the pressure axis while that of the 700° gel was essentially a straight line. No significant differences in the equilibrium times were observed for the samples. Normally equilibrium was reached in approximately 20 min for adsorbate pressures up to 100 Torr and beyond this increased to 50 min for pressures up to 400 Torr. The adsorption was reversible for each adsorbent.

Infrared analysis of the desorbed products from each of the samples indicated that only methanethiol was present. No elemental sulfur was detected in the solid residues.

The experimental differential molar entropies of adsorption at 423°K[15] showed that for the 550 and 700° gels a rapid increase in entropy from about 9.0 cal deg^{-1} mol^{-1} at 0.010 μmol m^{-2} to 30.0 cal deg^{-1} mol^{-1} at 0.025 μmol m^{-2}. At higher coverages the entropy of adsorption on the 700° gel began to level out to 51.5 cal deg^{-1} mol^{-1} at 0.400 μmol m^{-2}, 3 cal deg^{-1} mol^{-1} above the theoretical entropy for a mobile adsorbed gas. A rapid increase in entropy was not observed at low surface coverages for the 240° gel, and at coverages above 0.050 μmol m^{-2} the entropy for the 240° gel was 5 cal deg^{-1} mol^{-1} less than for the 550° gel.

Ethanethiol. The heat curves were very similar in shape to those for the adsorption of methanethiol on these materials.[15] The heats for the 240° gel fell rapidly between 0.010 and 0.050 μmol m^{-2} from 27.3 to 20.1 kcal mol^{-1}, respectively, before beginning to level out to around 12.3 kcal mol^{-1} at 0.400 μmol m^{-2}. The 550° gel gave a fairly similar heat curve to that of the 240° gel while the most rapid heat fall occurred with the 700° gel up to about 0.100 μmol m^{-2}.

Adsorption isotherms[15] for ethanethiol at 423°K were determined up to a pressure of only 150 Torr in order to avoid any problems associated with condensation of the

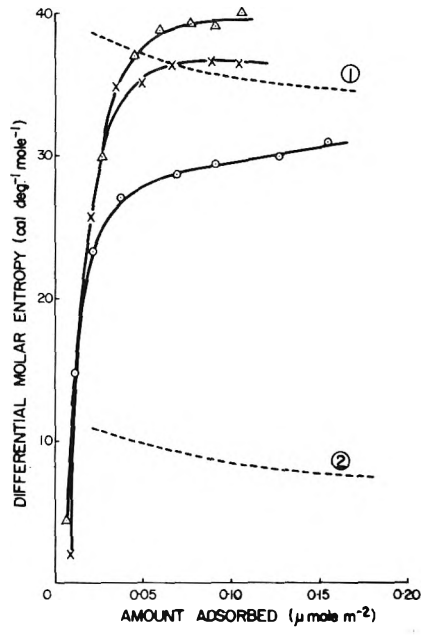

Figure 3. Experimental differential molar entropy of hydrogen sulfide adsorbed at 423°K on silica gels. Heat treatment at 240° (O), 550° (×), and 700° (△). Curve 1, mobile adsorption; curve 2, immobile adsorption.

vapor in the apparatus since at room temperature (23°) the vapor pressure of ethanethiol is 506 Torr.[16] However, even within this limited pressure range the familiar trend of decreasing adsorption with increasing temperature of gel heat treatment was observed. Equilibrium times were of the same order throughout any given isotherm but decreased with increasing temperature of sample heat treatment. Thus equilibrium was reached in approximately 60, 45, and 35 min for gels heat-treated at 240, 550, and 700°, respectively. Again the adsorption was reversible for each adsorbent.

Infrared analysis of the gas desorbed from each sample at 423°K showed that ethanethiol was the only component present. Sulfur was not detected on chemical analysis of the solid residues.

The entropy curves for the 240 and 550° gels[15] were very similar having entropies which increased rapidly from 29.0 to 50.0 cal deg^{-1} mol^{-1} between 0.010 and 0.200 μmol m^{-2}, respectively. The entropy curve for the 700° gel also increased rapidly between 0.100 and 0.200 μmol m^{-2} but the curve generally lay at 7 cal deg^{-1} mol^{-1} above the other two curves and leveled out at 57.2 cal deg^{-1} mol^{-1}, approximately 3 cal deg^{-1} mol^{-1} below the theoretical curve for mobile adsorption.

Dimethyl Sulfide. The magnitude of the heats of adsorption at a given coverage fell with increase in the sample heat-treatment temperature.[15] Thus at a coverage of 0.010 μmol m^{-2} the heats were 29.1, 21.0, and 18.8 kcal mol^{-1} for the 240, 550, and 700° gels, respectively. The heats decreased with increasing coverage for all the samples up to a coverage of 0.200 μmol m^{-2} to 17.5, 14.7, and 12.3 kcal mol^{-1} for the 240, 550, and 700° gels, respectively.

Isotherms for the adsorption of dimethyl sulfide[15] at 423°K were determined up to a pressure of 150 Torr for the reasons given above. The isotherms were concave to the pressure axis and the amount of gas adsorbed at a given pressure decreased with increase in the temperature of gel heat treatment in the same manner as that for the

TABLE II: Summary of Adsorption Data for Hydrogen Sulfide, Methanethiol, Ethanethiol, and Dimethyl Sulfide Adsorbed at 423°K on Heat-Treated Silica Gels

Temp of heat treatment, °C	Adsorbate	Adsorption capacity at 150 Torr, μmol m^{-2}	"Limiting" heat of adsorption, kcal mol^{-1}	$\Delta\bar{S}(=\bar{S}_{2l} - \bar{S}_s)$ at 0.400 μmol m^{-2}, cal deg^{-1} mol^{-1}
240	H_2S	0.05	9.8	5.8
	CH_3SH	0.29	11.5	11.5
	C_2H_5SH	0.50	12.3	8.6
	$(CH_3)_2S$	0.57	17.5	28.0
550	H_2S	0.04	7.3	−2.5
	CH_3SH	0.23	10.5	5.5
	C_2H_5SH	0.40	11.7	8.5
	$(CH_3)_2S$	0.48	14.7	15.5
700	H_2S	0.03	5.8	−4.5
	CH_3SH	0.15	6.5	−3.0
	C_2H_5SH	0.32	9.7	2.9
	$(CH_3)_2S$	0.40	12.3	9.0

other sulfur-containing gases. The equilibration times for all samples were of the same order of magnitude at all points on the isotherms (~45 min) and did not differ significantly with gel heat-treatment temperature. Again the adsorption was reversible for each adsorbent.

Infrared analysis of the gas desorbed from each sample at 423°K showed that no component other than dimethyl sulfide was present in the sample, and no sulfur was detected in the solid residues.

The entropy curves obtained for adsorption on the 550 and 700° gels[15] were similar in shape; however, the values for the 550° gel were approximately 7.0 cal deg^{-1} mol^{-1} lower than those of the 700° gel. Much lower entropy values were obtained for adsorption on the 240° gel than for the other two and the values increased over a wider surface coverage range from 4.2 to 30.0 cal deg^{-1} mol^{-1} at 0.030 and 0.450 μmol m^{-2}, respectively, compared with 42.0 to 48.5 cal deg^{-1} mol^{-1} at 0.030 and 0.110 μmol m^{-2}, respectively, for the 700° gel.

Table II summarizes the principal data for the adsorption of hydrogen sulfide, methanethiol, ethanethiol, and dimethyl sulfide on heat-treated silica gels.

Discussion

The adsorption data obtained for each gas on the three adsorbents follow similar trends, and similar interactions between adsorbate and adsorbent are believed to have taken place.

Other studies of the adsorption of gases on silica surfaces[17,18] have shown that surface hydroxyl groups play a very important part in the nature of the adsorbed species. It has been shown[17,18] that a fully hydroxylated silica surface has approximately 4.6 OH groups/100 Å^2 of surface. Since the 240° gel had 4.3 OH groups/100 Å^2 (≡ 7.2 μmol of OH m^{-2}) it can be assumed that many adjacent hydroxyl groups are present on this surface. Infrared studies by Kiselev[19] have indicated that for adsorbates containing oxygen, two adjacent hydroxyl groups are the most important adsorption sites when there are more than 3.0 OH groups/100 Å^2, while "free" surface hydroxyl groups become the more important adsorption site when there are less than 3.0 OH groups/100 Å^2. Thus "free" surface hydroxyl groups can be expected to be the most important groups for the 550 and 700° gels.

The magnitudes of the "limiting" heats of adsorption are too high to be caused by purely physical interactions and the similar trends of the heats, adsorption capacities, and entropies with variation of the surface hydroxyl group content suggests that there is a specific interaction between the surface hydroxyl groups and the adsorbate molecules, probably of a hydrogen bond nature.

The formation of a hydrogen bond involves a form of charge-transfer process in which charge is displaced from the proton acceptor to the proton donor,[20] and for the adsorption of these gases on a largely dehydroxylated (700°) silica gel surface this may be represented by

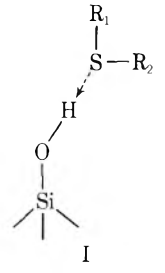

I

where R_1 = H, CH_3, C_2H_5 and R_2 = H, CH_3.

The strength of the hydrogen-sulfur hydrogen bond would be expected to be increased by the presence of adjacent hydroxyl groups which enhance the inductive effect on the atom H_A shown below. Thus

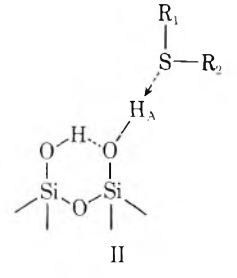

II

These two types of proposed adsorbed species would be expected to exhibit the following properties. For species II the strength of the S–H hydrogen bond should be greater than that for species I; the entropy of I is expected to be greater than that for II, but the proportion of the entropy increase caused by either rotational or translational restrictions cannot be distinguished; a reduction in the number of surface hydroxyl groups would be expected to decrease the adsorption capacity, and no decomposition of the adsorbate should take place.

These proposed adsorbed species are supported by the heat, isotherm, and entropy data. All of these gases exhibit heats and adsorption capacities which at a given coverage decrease with increase in temperature of heat treatment, and entropies which increase with increase in heat-treatment temperature (see Table II). Further support for this concept of weak hydrogen bonds is obtained from the ready desorption of the gas from all of the adsorbents, the absence of sulfur in the residues, and the absence of any gases other than the adsorbate in the gas desorbed from the adsorbents.

Consider the adsorption of hydrogen sulfide in more detail. In general, it is typical of the other adsorbates, and similar arguments can be made for them.

The high heats of adsorption observed for hydrogen sulfide at 423°K on silica gels heat treated at 240, 550, and 700° at coverages less than 0.030 μmol m^{-2}, approximately one three-hundredth of a monolayer,[8] are believed to be due to interactions with a very small number of energeti-

cally heterogeneous sites since subsequently the heats fall so rapidly. For example, with the 240° gel the heats fall from 30.0 to 10.8 kcal mol^{-1} for the small increase in surface coverage from 0.005 to 0.040 μmol m^{-2}. This is a much more rapid fall than that observed for the same coverage range with sulfur dioxide when the heats of adsorption were 22.0 and 16.3 kcal mol^{-1} and 0.010 and 0.040 μmol m^{-2}, respectively. It is difficult to define the nature of these heterogeneous sites without further detailed experiments; however, it is possible that contributions to the high initial heats could arise from interactions of the adsorbate with impurities in the adsorbent[21] (TiO_2 = 55 ppm; ZnO_2, 30 ppm) or possibly by adsorption within the micropores of the adsorbent.[22]

The values of the "limiting" heats of adsorption increase with increasing surface hydroxyl group concentration from 5.5 kcal mol^{-1} for a surface possessing 1.3 μmol of OH (as H_2O) m^{-2} to 9.8 kcal mol^{-1} for one with 7.2 μmol of OH m^{-2}. In addition, the adsorption capacity increases in the order 0.058, 0.073, and 0.098 μmol m^{-2} for surface hydroxyl group concentrations of 1.3, 2.4, and 7.2 μmol of OH m^{-2}, respectively. These data are in agreement with the species proposed above.

The values of the experimental differential molar entropies[15] are also in accord with this view. For each adsorbent, the extremely rapid increase in the entropy of the adsorbed species from about 5.0 cal deg^{-1} mol^{-1} at 0.010 μmol m^{-2} to 37.0 cal deg^{-1} mol^{-1} at 0.100 μmol m^{-2}, follows the expected pattern for a surface possessing a small number of very heterogeneous sites.[23] The mobility of the adsorbed hydrogen sulfide varies from an essentially immobile state to one that has been described as "supermobile,"[24] that is when the experimental entropy is greater than that for a theoretical model of a perfect two-dimensional adsorbed gas. This phenomenon has been observed in several cases of physically adsorbed gases[13,25] and interpreted to indicate that the vibration replacing the translational motion perpendicular to the surface is not negligible, as assumed in the calculation, and is beginning to make a significant contribution to the entropy.[25] A similar argument may be proposed to explain the present results.

The "limiting" entropy of the hydrogen sulfide adsorbed on the 240° gel is, however, at least 10 cal deg mol^{-1} lower than that of the gas adsorbed on the other heat-treated gels and hence the gas adsorbed is not "supermobile" or even fully mobile. This is consistent with the value for the heat of adsorption at 0.100 μmol m^{-2} of 9.8 kcal mol^{-1} for the 240° gel and in accord with the conclusion that the hydrogen sulfide molecule is held by two or more bonds. For adsorptions on surfaces containing largely isolated hydroxyl groups, *i.e.*, the 550 and 700° gels, the entropy is much greater. Thus as the gel heat-treatment temperature is increased, more isolated hydroxyl groups are present on the surface, and hence the mobility of the adsorbed species at a given coverage should increase with increasing gel heat-treatment temperature. This is observed in practice.

The Effect of Increase in Methylation of the Adsorbate. Distinct differences are apparent in the values of the "limiting" heats of adsorption for a given silica gel surface. Thus, for the series hydrogen sulfide, methanethiol, ethanethiol, and dimethyl sulfide, the heat values are 5.5, 7.0, 10.0, and 12.2 kcal mol^{-1}, respectively, for the 700° gel, which perhaps reflects the different electronic structures of the molecules which, in turn, influence the likelihood of the formation of hydrogen bonds.

If the heat data are compared for ethanethiol and dimethyl sulfide, it can be seen that the heats of adsorption for dimethyl sulfide lie 3 to 5 kcal mol^{-1} above those for ethanethiol for a given surface coverage. Similar displacements of the heat values occur irrespective of the surface hydroxyl group concentration. These results suggest that steric hindrance is not a predominant factor in influencing the values of the heats since the larger ethanethiol molecule[7] has a lower heat of adsorption than dimethyl sulfide at any given hydroxyl group concentration on the silica gel surface.

Considering the disposition and nature of the orbitals in the molecules of methanethiol, ethanethiol, and dimethyl sulfide, it can be observed that as the inclusion of the 3s function in the bonding orbitals increases then there is less 3s character associated with the nonbonding orbitals of sulfur and so these must have greater 3p character than in hydrogen sulfide. Further, for the formation of a third bond to sulfur, the optimum outward extension of a third pair of electrons would occur when they occupy an sp^3 orbital[26] and this situation is approached when the bond angle increases with increasing methylation of the sulfur atom (*cf.* bond angles of 93.3, 100.3, 103.0, and 105.0° for hydrogen sulfide, methanethiol, ethanethiol, and dimethyl sulfide, respectively). Thus the base strength of the molecules in the series will progressively increase along with the ability to form bonds with an electron acceptor.[27]

The trend shown by the heats of adsorption to increase with increasing methylation of the adsorbate is consistent with these phenomena since the base strengths of the adsorbates increase in the order $(CH_3)_2S > C_2H_5SH > CH_3SH > H_2S$.[26]

Supplementary Material Available. Graphs of the heats of adsorption, adsorption isotherms, and differential molar entropies of adsorption as functions of surface coverage have been plotted for each of these gases adsorbed on the heat-treated silica gels and will appear following these pages in the microfilm edition of this volume of the journal. Photocopies of the supplementary material from this paper only or microfiche (105 × 148 mm, 20× reduction, negatives) containing all of the supplementary material for the papers in this issue may be obtained from the Journals Department, American Chemical Society, 1155 16th St., N.W., Washington, D. C. 20036. Remit check or money order for $3.00 for photocopy or $2.00 for microfiche, referring to code number JPC-73-2571.

References and Notes

(1) Present address, Ontario Research Foundation, Sheridan Park, Clarkson, Ontario, Canada.
(2) (a) E. B. Miller, *Chem. Met. Eng.*, **23**, 1155, 1219, 1251 (1920); (b) G. E. Mapstone, *Aust. Chem. Inst. J. Proc.*, **14**, 61 (1946).
(3) W. Stober, *Kolloid-Z. Z. Polym.*, **145**, 17 (1956).
(4) F. C. Boston, *Hydrocarbon Process.*, **43** (8), 141 (1964).
(5) "Applicability of Metal Oxides to the Development of New Processes for Removing Sulfur Dioxide from Flue Gases," Vol. II (8), Contract PH 86-68-68, Tracor (1969).
(6) R. A. Beebe and H. Dell, *J. Chem. Phys.*, **39**, 746 (1955).
(7) W. J. Jones and R. A. Ross, *J. Chem. Soc. A*, 1021 (1967).
(8) W. J. Jones and R. A. Ross, *J. Chem. Soc. A*, 1787 (1968).
(9) R. W. Glass and R. A. Ross, *Can. J. Chem.*, **50**, 1241 (1972).
(10) R. W. Glass and R. A. Ross, *Can. J. Chem.*, **49**, 2832 (1971).
(11) D. H. Everett, *Trans. Faraday Soc.*, **46**, 453, 942, 957 (1950).
(12) A. Clark, "The Theory of Adsorption and Catalysis," E. M. Loebl, Ed., Academic Press, London, 1970.
(13) J. J. F. Sholten and S. Kruyer, "Physical and Chemical Aspects of Adsorbents and Catalysts," B. G. Linsen, Ed., Academic Press, London, 1970, p 148.

(14) C. Kemball, *Advan. Catal.*, 2, 237 (1950).
(15) See paragraph at end of paper regarding supplementary material.
(16) "Handbook of Chemistry and Physics," Chemical Rubber Publishing Co., Cleveland, Ohio, 1970, p F 156.
(17) A. V. Kiselev and V. I. Lygin, *Kolloid. Zh.*, **21**, 581 (1959).
(18) J. Uytterhoeven, M. Sleex, and J. J. Fripiat, *Bull. Soc. Chim. Fr.*, **6**, 1800 (1965).
(19) A. V. Kiselev, "Structure and Properties of Porous Materials," D. H. Everett and F. S. Stone, Ed., Butterworths, London, 1958, p 210.
(20) M. L. Hair, Ed., "Infrared Spectroscopy of Surface Chemistry," Edward Arnold, Ltd., London, 1967.
(21) S. G. Ash, A. V. Kiselev, and B. V. Kuznetsov, *Trans. Faraday Soc.*, **67**, 3118 (1971).
(22) E. Robinson and R. A. Ross, *J. Chem. Soc. A*, 84 (1970).
(23) J. M. Thomas and W. J. Thomas, "Introduction to the Principles of Heterogeneous Catalysis," Academic Press, London, 1967.
(24) C. Kemball and E. K. Rideal, *Proc. Roy. Soc., Ser. A*, **187**, 53 (1946).
(25) A. Clark and V. C. F. Holm, *J. Catal.*, **2**, 21 (1963).
(26) A. B. Burg, "Organic Sulphur Compounds," N. Kharasch, Ed., Pergamon Press, London, 1961, p 30.
(27) M. L. Hair, "Infrared Spectroscopy in Surface Chemistry," Edward Arnold, Ltd., London, 1967.

Surface Studies of the Adsorption of Sulfur-Containing Gases at 423°K on Porous Adsorbents. II. The Adsorption of Hydrogen Sulfide, Methanethiol, Ethanethiol, and Dimethyl Sulfide on γ-Alumina

R. W. Glass*[1] and R. A. Ross

Department of Chemistry, Lakehead University, Thunder Bay, Ontario, Canada *(Received February 26, 1973)*

Calorimetric heats of adsorption have been determined for hydrogen sulfide, methanethiol, ethanethiol, and dimethyl sulfide adsorbed at 423°K on γ-alumina at coverages up to $\theta = 0.5$. Adsorption isotherms have been measured and the entropies of the adsorbed species have been calculated. Heats of adsorption and adsorption capacities at a given coverage increased with increasing methylation of the adsorbate. A similar type of adsorbed species involving hydrogen-bond type interactions between the sulfur atoms of the adsorbate and hydroxyl hydrogen atoms on the alumina surface is proposed to account for all the results. Differences in heats, entropies, and adsorption capacities among the systems are explained by the increasing inductive effect on the sulfur atoms with increasing methylation of the adsorbate which results in the formation of stronger hydrogen bonds with the adsorbent.

Introduction

Many different types of adsorbents and catalysts are used in industry to remove obnoxious sulfur-containing gases from gas streams. λ-Alumina either by itself[2a] or doped with NaOH[2b] or other compounds is one of the most commonly used materials and yet few data have been reported in the literature on the thermodynamic properties of such systems or on the nature of the adsorbed surface complexes formed.

Studies of the adsorption of sulfur dioxide at relatively elevated temperatures on γ-alumina have been reported.[3] A recent paper[4] on the adsorption of hydrogen sulfide, methanethiol, ethanethiol, and dimethyl sulfide at 423°K on heat-treated silica gels has shown that for any given adsorbate the strongest bonds were formed with the adsorbent possessing the highest surface hydroxyl group concentration and that for any given adsorbent the strength of the adsorbate–adsorbent interaction increased with increased electron-donating power of the adsorbate.

In the present work calorimetric heats of adsorption, adsorption isotherms, and entropies of adsorption have been determined for hydrogen sulfide, methanethiol, ethanethiol, and dimethyl sulfide at 423°K on λ-alumina heat-treated to 700°.

Experimental Section

Materials. γ-Alumina was prepared by heating boehmite in air at 700° for 20 hr. The boehmite was prepared by a method described earlier.[3] The surface area, "water content," "lump" density by displacement of mercury, and pore size distribution data, determined by the nitrogen adsorption method, of the γ-alumina have been reported[3] along with similar data for other samples heat-treated at other temperatures. In brief, the γ-alumina had a surface area of 160 $m^2 g^{-1}$, a "water content" of 18.6 $\mu mol\ m^{-2}$, a "lump" density of 0.6864 $g\ cm^{-3}$, and a mean pore diameter of 35 Å.

After heat treatment, the adsorbent was cooled over phosphoric anhydride, transferred to the appropriate apparatus, and then outgassed at 150° overnight at $<10^{-4}$ Torr. Hydrogen sulfide, methanethiol, ethanethiol, and dimethyl sulfide were each purified to >99.9% in the manner described earlier.[4]

Apparatus and Procedure. Heats of adsorption and adsorption isotherms were determined in apparatus similar

to that described earlier,[5] and entropies of adsorption calculated from the heat data as before.[4]

Results

The heat curves for hydrogen sulfide, methanethiol, ethanethiol, and dimethyl sulfide adsorbed at 423°K on γ-alumina are shown in Figure 1. The curves for methanethiol, ethanethiol, and dimethyl sulfide, although similar, were separated from each other by approximately 3.0 kcal mol^{-1} above a surface coverage of 0.700 μmol m^{-2}. For these adsorbates the heats of adsorption tended to level out at a coverage of about 0.700 μmol m^{-2} after falling relatively rapidly from 0.400 μmol m^{-2}.

The results for hydrogen sulfide adsorption were limited because of the small adsorption capacity of γ-alumina for this gas (Table I). However, the results that were obtained showed a relatively rapid fall in the heats of adsorption from 31.5 kcal mol^{-1} at 0.050 μmol m^{-2} to 16.3 kcal mol^{-1} at 0.340 μmol m^{-2}, and at coverages above this latter value the heats tended to level out to 16.0 kcal mol^{-1}. For methanethiol, ethanethiol, and dimethyl sulfide the relatively constant heat values at a coverage of 1.40 μmol m^{-2} were 16.5, 18.4, and 20.7 kcal mol^{-1}, respectively.

The adsorption isotherms for hydrogen sulfide, methanethiol, ethanethiol, and dimethyl sulfide at 423°K on λ-alumina are shown in Figure 2. All of the isotherms were concave to the pressure axis while the amount of hydrogen sulfide adsorbed was very much smaller than that for the other gases. At a pressure of 150 Torr the amount of gas adsorbed was 0.370, 1.20, 1.51, and 1.72 μmol m^{-2} for hydrogen sulfide, methanethiol, ethanethiol, and dimethyl sulfide, respectively.

Reversibility tests[6] showed that approximately 100 μg of hydrogen sulfide could not be desorbed from the sample, whereas the adsorption was reversible with the other three gases.

In all cases infrared analysis of the gases desorbed from the γ-alumina samples on completion of the isotherm showed the absence of foreign components. Analyses of the solid residues showed the presence of sulfur on γ-alumina exposed to hydrogen sulfide at 423°K. Sulfur was not detected on the other residues.

Experimental differential molar entropies of hydrogen sulfide, methanethiol, ethanethiol, and dimethyl sulfide adsorbed at 423°K on γ-alumina are shown as a function of surface coverage in Figure 3.

TABLE I: Comparison of the Adsorption Characteristics of Hydrogen Sulfide, Methanethiol, Ethanethiol, and Dimethyl Sulfide Adsorbed at 423°K on γ-Alumina Heat-Treated at 700°

Adsorbate	"Limiting" heat at 1.40 μmol m^{-2}, kcal mol^{-1}	Amount adsorbed at 150 Torr, μmol m^{-2}	ΔS ($= \bar{S}_{2t} - \bar{S}_s$) at 0.120 μmol m^{-2}, cal deg^{-1} mol^{-1}
Hydrogen sulfide	16.0[a]	0.37	10.0[a]
Methanethiol	16.5	1.20	17.3
Ethanethiol	18.4	1.51	25.7
Dimethyl sulfide	20.7	1.72	29.5

[a] "Limiting" heats and $\Delta\bar{S}$ values for hydrogen sulfide are quoted for a surface coverage of 0.410 μmol m^{-2}.

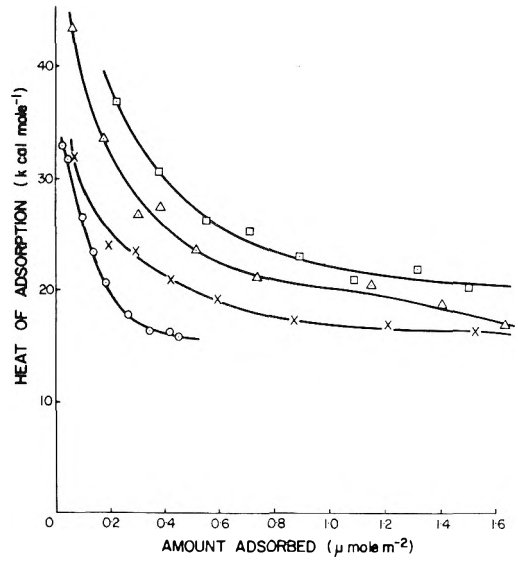

Figure 1. Variation of the heats of adsorption with surface coverage for hydrogen sulfide (⊙), methanethiol (×), ethanethiol (△), and dimethyl sulfide (⊡) adsorbed at 423°K on γ-alumina heat-treated at 700°.

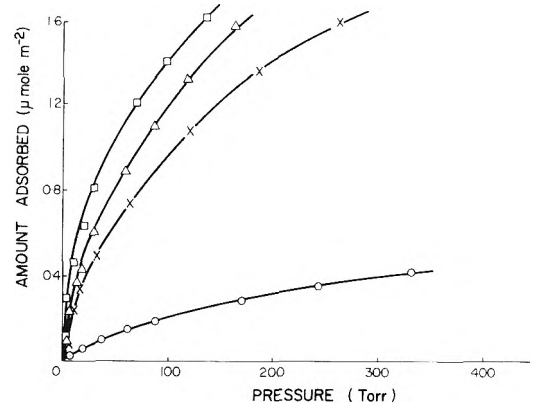

Figure 2. Adsorption isotherms for hydrogen sulfide (⊙), methanethiol (×), ethanethiol (△), and dimethyl sulfide (⊡) adsorbed at 423°K on γ-alumina heat-treated at 700°.

The entropy curves for methanethiol, ethanethiol, and dimethyl sulfide adsorptions were very similar in shape. They exhibited negative entropy values at their lowest coverages followed by a rapid increase in positive entropy values between 0.100 and 0.120 μmol m^{-2}. At this latter coverage the entropy values had leveled off to 29.2, 32.3, and 26.0 cal deg^{-1} mol^{-1} for methanethiol, ethanethiol, and dimethyl sulfide, respectively. The entropy curve of hydrogen sulfide was very similar to that of methanethiol up to the maximum surface coverage measured. Table I summarizes the principal adsorption characteristics for all of the gases.

Discussion

Recently[4] it was demonstrated that a correlation appeared to exist between the heats of adsorption of all of these gases on silica gel and the degree of methylation of the adsorbate. A similar correlation can be made for γ-alumina. The heats of adsorption and adsorption capacities increase, and the entropies of adsorption decrease with increasing methylation of the adsorbate.

The "water content" of the γ-alumina is apparently equivalent to two monomolecular layers of water. How-

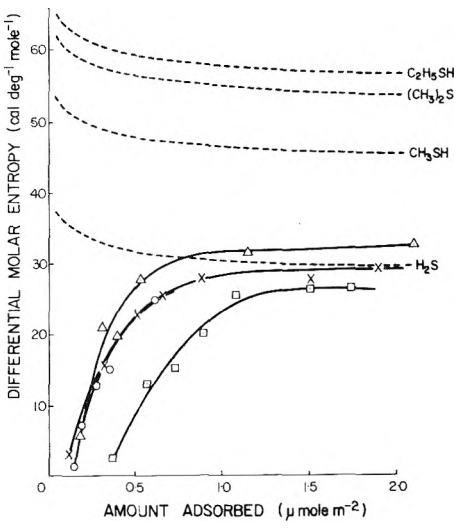

Figure 3. Experimental differential molar entropies of adsorption for hydrogen sulfide (⊙), methanethiol (×), ethanethiol (△), and dimethyl sulfide (⊡) adsorbed at 423°K on γ-alumina heat-treated at 700°; -----, "mobile" adsorption entropy values.

ever, it has been shown[7] that water molecules that are not desorbed as such during heat-drying up to 300° react to form surface hydroxyl groups. Thus, it can be assumed that after heat treatment for 20 hr at 700° a large proportion of this water is present in the bulk of the adsorbent, while not excluding the possibility that a large number of hydroxyl groups exist on the surface. Thus the surface of the 700° γ-alumina may be considered to be similar with regard to hydroxyl group distribution to that for silica gel, and similar properties may be expected.

It is pertinent to note that infrared studies of the adsorption of hydrogen sulfide on alumina[8] suggest that fairly strong interactions occur involving the formation of hydrogen bonds. A comparison was made of the shifts of the SH stretching frequency to a lower value, and of the HSH bending frequency to a higher value, with the shifts obtained for adsorbed water and it was concluded that a likely representation of adsorbed hydrogen sulfide was

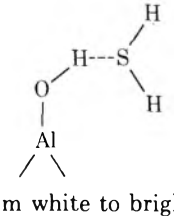

A color change from white to bright violet was noted on adsorption of hydrogen sulfide on the γ-alumina at room temperature, and it was postulated that this may have been due to dissociation of the hydrogen sulfide molecule or possibly to the formation of some higher polymeric form of sulfur. More recently, further infrared work[9] has suggested that decomposition of hydrogen sulfide has taken place on γ-alumina. This was confirmed in the present work where the residue was pale yellow and chemical tests showed the presence of ~100 μg of sulfur in an unknown state. It should be noted that this amount represents an extremely small fraction of available adsorbent surface and the effect on heat and entropy results can be assumed to be insignificant.

The heats of adsorption of hydrogen sulfide at 423°K fell from 32.5 kcal mol^{-1} at a coverage of 0.020 μmol m^{-2} to an almost constant value of 16.3 kcal mol^{-1} at 0.420 μmol m^{-2}. These results compare reasonably well with isosteric heats determined for hydrogen sulfide on γ-alumina[10] at 573 and 737°K when the values were 25 and 38 kcal mol^{-1}, respectively, at surface coverages of 0.170 and 0.114 μmol m^{-2}. Entropy values calculated subsequently from these latter heats indicated that the mobility of the hydrogen sulfide molecule was highly restricted,[10] possibly by reaction as a base at Lewis acid sites on the oxide surface.

While alternative mechanisms have been proposed[11,12] to account for infrared investigations on the adsorption of methyl and ethyl alcohols on alumina surfaces at 543°K it is generally agreed[11,12] that surface alkoxyl species are formed.

Thus, all of these studies indicate that strong interactions may he expected for the adsorption of hydrogen sulfide, methanethiol, ethanethiol, and dimethyl sulfide on a γ-alumina heat treated at 700° on which Lewis acid sites are probably present.[13]

In the present work, no color changes were observed with the residues obtained after the adsorption of methanethiol, ethanethiol, and dimethyl sulfide and no sulfur was detected in the residues. For these gases adsorption on two different types of sites is proposed: (a) adsorption on a relatively high energy Lewis acid site, probably more significant at low surface coverages, and (b) adsorption involving hydrogen bonds between the sulfur and hydroxyl hydrogen atoms, which may predominate at higher surface coverages.

The argument used to account for the results for the adsorption of these gases on silica gels can also be applied plausibly to explain the adsorptions at higher surface coverages on γ-alumina. Thus the influence of the methyl groups on the inductive effect and hence the strength of the hydrogen bond formed between the sulfur atom and the hydroxyl hydrogen atom should be reflected in the values of the entropy differences ($\Delta\bar{S}$) and the heats of adsorption. This is consistent with the results since the ΔH and $\Delta\bar{S}$ values are, respectively, 16.0 kcal mol^{-1} and 10.0 cal deg^{-1} mol^{-1} for hydrogen sulfide; 16.5 kcal mol^{-1} and 17.3 cal deg^{-1} mol^{-1} for methanethiol; 18.4 kcal mol^{-1} and 25.7 cal deg^{-1} mol^{-1} for ethanethiol; and 20.7 kcal mol^{-1} and 29.5 cal deg^{-1} mol^{-1} for dimethyl sulfide. Hence at a given coverage for a given gas, the heats are higher for adsorption on γ-alumina than on silica gel. This feature may be explained by the greater acidity of the hydroxyl hydrogens on alumina[14] which would give rise to stronger hydrogen bonds on association with electron donor molecules.

References and Notes

(1) Present address, Ontario Research Foundation, Sheridan Park, Clarkson, Ontario, Canada.
(2) (a) See, for example, W. Strauss, "Air Pollution Control, Part I," W. Strauss, Ed., Wiley-Interscience, New York, N. Y., 1971; (b) J. I. Paige, J. W. Town, J. H. Russell, and H. J. Kelly, *U. S. Govt. Res. Develop. Rep.*, **70**(21), 55 (1970).
(3) R. W. Glass and R. A. Ross, *Can. J. Chem.*, **50**, 2451 (1972).
(4) R. W. Glass and R. A. Ross, *J. Phys. Chem.*, **77**, 2571 (1973), Part I of this series.
(5) R. W. Glass and R. A. Ross, *Can. J. Chem.*, **49**, 2832 (1971).
(6) W. J. Jones and R. A. Ross, *J. Chem. Soc. A*, 1021 (1967).
(7) J. B. Peri and R. B. Hannan, *J. Phys. Chem.*, **64**, 1526 (1960).
(8) A. V. Deo, I. G. Dalla Lana, and H. W. Habgood, *J. Catal.*, **21**, 270 (1971).
(9) T. L. Slager and C. H. Amberg, *Can. J. Chem.*, **50**(21), 3416 (1971).
(10) A. J. de Rosset, C. G. Finstrom, and C. J. Adams, *J. Catal.*, **1**, 235 (1962).
(11) R. G. Greenler, *J. Chem. Phys.*, **37**, 2094 (1962).
(12) A. V. Kiselev and V. I. Lygin, "Infrared Spectra of Adsorbed Species," L. H. Little, Ed., Academic Press, New York, N. Y., 1966.
(13) J. B. Peri, *J. Phys. Chem.*, **69**, 220 (1965).
(14) M. L. Hair, Ed., "Infrared Spectroscopy in Surface Chemistry," Edward Arnold Ltd., London, 1967.

Correlation of Homogeneous Self-Exchange and Electrochemical Rate Data. Further Evidence for Anomalously Low Reorganizational Barriers in Electron Transfer Reactions of Cobalt Complexes[1a]

John F. Endicott, Ronald R. Schroeder,* Dale H. Chidester, and Donald R. Ferrier[1b]

Department of Chemistry, Wayne State University, Detroit, Michigan 48202 *(Received October 12, 1971; Revised Manuscript Received August 8, 1973)*

Publication costs assisted by the Public Health Service

The staircase voltammetric technique has been applied to the determination of the standard heterogeneous rate constants (k_s) for one electron reductions of several coordination complexes. Some of these determinations together with literature data suggest a correlation between k_s and the homogeneous self-exchange rate constants (k_{exch}) similar in form to that suggested by Marcus: $\log k_{exch} \simeq (2.0 \pm 0.5) \log k_s + (4.0 \pm 1)$. Contrasting behavior is exhibited by cobalt(III) complexes for which little variation in k_s is found for complexes whose self-exchange rates vary by more than a factor 10^{12}. Similar behavior has previously been reported for outer-sphere homogeneous reduction of cobalt(III) complexes. It must be concluded that the reorganizational barriers which are so important in cobalt(III)-(II) self-exchange reactions are not as significant in cross reactions of cobalt complexes.

Owing to their apparent simplicity, electron transfer reactions of coordination complexes have been the subject of many experimental and theoretical studies.[2] Although most of the systematic investigations have dealt with homogeneous reactions, the theoretical treatment of Marcus[2a,b,3] suggests a relationship (1) between the homogeneous self-exchange rate constant (*e.g.*, for the $Ru(NH_3)_6^{3+,2+}$ exchange reaction), k_{exch}, the standard (reference to E^0 for the exchange related couple) heterogeneous rate constant, k_s, and the homogeneous and heterogeneous diffusion rates (Z and Z_{el}, respectively). Although Marcus' arguments have been in the literature for several years, there does not appear to have been any previous attempt to systematically examine the validity of (1) or to examine the possibility that there may be a general empirical correlation between k_{exch} and k_s.

$$(k_{exch}/Z)^{1/2} = k_s/Z_{el} \quad (1)$$

The studies reported in the present manuscript were undertaken to complement studies of the outer-sphere electron transfer reactions of cobalt complexes in homogeneous aqueous solutions.[2,4-8] The Marcus-type free energy correlations (2) have not been precisely applicable to homogeneous electron transfer reactions of cobalt complexes.[2a-d,4-8] Several studies[5,8] have demonstrated that the major discrepancy between (2) and observed behavior arises because reorganizational barrier in cross reactions is much smaller than would be inferred from the usual[2a,b] relation, $\lambda_{12} = \frac{1}{2}(\lambda_{11} + \lambda_{22}) = \frac{1}{2}(\lambda_{Co} + \lambda_{22})$. Rate parameters from heterogeneous reactions provide a more direct means of examining this anomalous behavior of cobalt complexes.

$$\Delta G_{12} = \frac{\lambda_{12}}{4} + \frac{\Delta G_{12}}{2} + \frac{(\Delta G_{12})^2}{4\lambda} \quad (2)$$

The present study examines the relationship between k_{exch} and k_s, and is a result of our interests in the energetics of homogeneous, outer-sphere electron transfer reactions[4,7,8] and in the development of convenient and accurate methods for determining standard heterogeneous rate constants.[9-11]

It is to be noted that the widely cited[2-4,6,12] success in correlating heterogeneous rates of reduction of $Co^{III}(NH_3)_5X$ complexes with outer sphere homogeneous reduction rate constants is probably due to the fact that Vlcek[12] referred all his heterogeneous rate constants to a common reference potential (since standard potentials, E^0, are unknown for these complexes) and variations in the cross reaction rates whether homogeneous or heterogeneous depend strongly on ΔG_{12}.

Experimental Section

Three different instrument systems were used to obtain the staircase voltammetry data.[9,11,13] Each system was composed of an electrolysis cell, a potentiostat, a central timing unit, a staircase waveform generator, a current sampler, and a data recording device.

The same cell potentiostat and waveform sources were used with each of the three instrument systems. The cell was of the conventional three electrode type composed of a working electrode (either a hanging mercury drop, a platinum wire, or a slowly dropping mercury electrode), a platinum wire counter electrode, and a saturated calomel reference electrode connected to the cell by a salt bridge and capillary probe. The cell was a 50-mm diameter weighing bottle with a snug-fitting Teflon cap which held the electrodes and the nitrogen gas inlet tube. The potentiostat was an operational amplifier based adder-controller of conventional design and included a voltage follower input to which the reference electrode was connected, a dc voltage source for setting the initial potential, and a precision resistor for current monitoring.

The staircase generator was a binary up-down counter, triggered by the central timing unit. The counter output was connected to a digital to analog converter to produce the staircase waveform. The staircase waveform consisted of 128 steps of 5, 10, or 20 mV amplitude.

The first instrument system[9,11] used for preliminary and qualitative work included a square wave signal generator as the central timer. The differentiated square wave triggered the waveform counter and a delay timer; the delay timer in turn triggered the current sampling by modulating the electron beam of an oscilloscope. The delay timer turned "on" the beam during each step only at the preselected current sampling time. The voltammogram was recorded using an oscilloscope camera with a Polaroid back using 3000 speed film.

The second instrument system[11,13] utilized a transient recorder (Biomation 610, Biomation Inc., Palo Alto, Calif.) as the central timer and as a digital recorder. A delay timer connecting the transient recorder and the waveform counter provided the delay needed for selectable current sampling times. The voltammogram was stored in the transient recorder memory as 128 six-bit binary words. A teletype inferfaced to the transient recorder provided a punched paper tape recording of the voltammogram. This tape recording was processed through the university's IBM 360/67 time-shared system to produce decimal output. Programs stored in the time-shared system were used for signal averaging, peak finding, automatic baseline correction, unit conversion, and plotting.

The third system[13] used a minicomputer (JRA-5 spectrum computer, JOEL, Inc., Tokyo, Japan) as the central timer and data gathering device. This system provided up to five current samples per step at five preselected times and was used with the slow dropping mercury electrode. The computer averaged the data from five experiments (one experiment per DME drop) and provide a punched paper tape output identical in form with the previously described system except in providing eight-bit binary numbers.

Solutions were prepared from reagent grade chemicals using distilled solvents. The cobalt macrocyclic complexes were kindly donated by Dr. D. P. Rillema.[14] Other cobalt complexes were prepared by standard literature procedures.[15,16] The $[Ru(NH_3)_6](ClO_4)_3$ used was obtained as the chloride salt from Mathey-Bishop, Malvern, Pa., and recrystallized from perchloric acid. All solutions used in the staircase studies were shown by polarography to contain no significant impurities.

The solutions for voltammetric studies were made up just before use to be approximately millimolar or less in the complex and either 0.05 or 0.1 M in $NaClO_4$ or $HClO_4$.

For each complex, voltammograms were run on solutions containing 0.05 and 0.1 M perchlorate. Voltammograms were recorded using several step times and at least five step to sampling time ratios.[9-11,13] The data were used to determine experimental i_q values. These were compared with i_q values calculated from the theory presented by Ferrier and Schroeder.[10] The theoretical k_s values giving i_q corresponding most closely to the experimental values were chosen. These results are listed in Table I. The measured k_s values were corrected for double layer effects using the data of Wroblowa, Kovac, and Bockris for $NaClO_4$.[17] For this purpose graphs of the outer Helmholtz plane potential, ϕ, *vs.* applied potential (referenced to sce) were constructed for several perchlorate concentrations[18] (see Figure 1). For each set of voltammograms, run in either 0.05 or 0.1 M perchlorate, a ϕ value corresponding to the peak potential was selected and a corrected k_s value was calculated. Corrections were made according to eq 3

$$\log k_{s_{corr}} = \log k_s + \frac{(z - \alpha n_a)\phi}{0.059} \qquad (3)$$

where z is the formal charge on the reacting species, α is the transfer coefficient, and n_a is the number of electrons involved in the rate determining portion of the electron transfer reaction.[18,19]

Our measurements showed that αn_a was close to 0.5 for the various reactions studied here and this value was used for all corrections.[20] Corrected k_s values and the measured values for each complex in each supporting electrolyte are listed in Table I.

Significance of the k_s Values. The measured k_s values and the corresponding corrected k_s values listed in Table I warrant some further discussion in regard to reliability and consistency of the results. From the k_s values listed all of the complexes studied would be polarographically reversible, a conclusion consistent with previous observations in this[9,11] and other laboratories.[21,22] In fact the results given here serve merely to support with quantitative data a trend previously noted for numerous cobalt complexes. The effects of chemical reactions and adsorption on the measured k_s values are considered minimal. For the species studied here, cyclic voltammograms taken at moderate scan rates have shown both cathodic and anodic waves indicating that chemical decomposition of the electron transfer products is slow on the relevant experimental time scale.[23]

Adsorption peaks or other anomalous peaks where observed were sufficiently removed from the normal voltammetric wave to allow its complete characterization *via* normal means. The trend in peak current with variations in sampling time was entirely consistent with the behavior predicted by the staircase theory.[9,10]

For $Ru(NH_3)_6^{3+}$ the k_s value reported is the upper limit measurable by the staircase technique with the apparatus currently available. For cases where a measured k_s value was obtained, we feel the values in Table I and II are accurate to within ±30%.

The double layer corrections merit additional comment. Our anticipation of somewhat dissimilar results at the two perchlorate concentrations[24] was not entirely satisfied as similar results were generally obtained. Corrections for double layer effects should have reduced any dissimilarities but instead increased them. Thus, the uncorrected results for any one complex seem more consistent than do the corrected values. It should be noted, however, that the

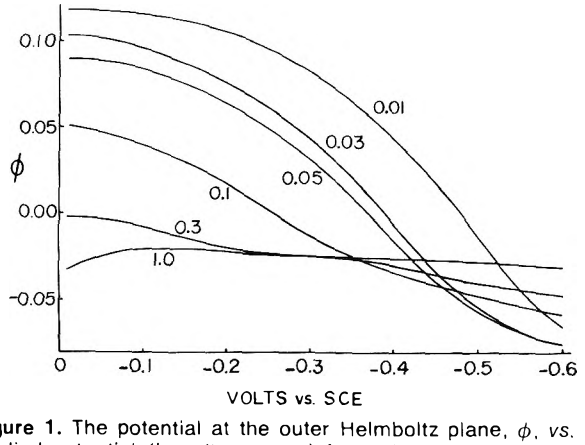

Figure 1. The potential at the outer Helmboltz plane, ϕ, *vs.* the applied potential (in volts *vs.* sce) for various concentrations of $NaClO_4$. Based on the data presented in ref 17.

TABLE I: Measured and Corrected k_s Values for Several Metal Complexes

Complex[a]	Electrolyte[b]	E_p[c]	i_q	i_q(theor)	k_s'[d]	k_s[e]	ϕ[f]	k_{scorr}[e,g]
$Co([14]dieneN_4)(NH_3)_2^{3+}$	0.050 *M* $HClO_4$	−0.08	1.22	1.22	1.0	2.45×10^{-2}	0.085	>1
			1.30	1.30				
			1.42	1.37				
	0.10 *M* $HClO_4$	−0.06	1.24	1.23	0.9	2.2×10^{-2}	0.044	>1
			1.33	1.32				
			1.41	1.40				
$Co([14]tetraeneN_4)(NH_3)_2^{3+}$	0.050 *M* $HClO_4$	−0.56	1.17	1.18	0.55	1.35×10^{-2}	−0.067	2×10^{-5}
			1.24	1.24				
			1.29	1.29				
			1.37	1.33				
	0.01 *M* $HClO_4$	−0.54	1.21	1.21	0.75	1.84×10^{-2}	−0.063	4×10^{-5}
			1.28	1.29				
			1.35	1.35				
			1.53	1.42				
$Co(en)_3^{3+}$	0.050 *M* NaClO	−0.47	1.27	1.26	1.2	2.94×10^{-2}	−0.043	4×10^{-4}
			1.36	1.36				
			1.37	1.47				
	0.10 *M* $NaClO_4$	−0.47	1.28	1.30	2.5	6.5×10^{-2}	−0.043	9×10^{-4}
			1.46	1.47				
			1.66	1.65				
$Ru(NH_3)_5^{3+}$	0.10 *M* $NaClO_4$	−0.21	1.30	1.33	Rev	>1	+0.013	≫1
			1.51	1.54				
			1.81	1.85				
			1.94	2.45				

[a] For complex abbreviations see ref 25. [b] All in H_2O, at 25 ± 0.1°. [c] Volts *vs.* sce. [d] From ref 9, $k_s' = k_s\sqrt{\tau}\gamma^{an_a}/\sqrt{D}$. [e] Cm/sec. [f] From Figure 1, values in volts. [g] Using eq 3.

TABLE II: Standard Heterogeneous Rate Constants for Reduction of Several Coordination Complexes

Complex[a]	Solvent[b]	E_p, V[c]	k_s,[d] cm sec^{-1}	k_{exch}, M^{-1} sec^{-1} [d]
		A. Cobalt(III) Complexes		
$Co([14]aneN_4)(CN)_2^+$	AN	−1.1	0.01–0.02	
$Co([14]dieneN_4)(CN)_2^+$	AN	−1.1	0.01–0.02	
$Co([14]dieneN_4)(NH_3)_2^{3+}$	H_2O	−0.06	0.023	10^{-9} [e]
$Co([14]dieneN_4)Cl_2^+$	AN	+0.05	0.005	
$Co([14]dieneN_4)Br_2^+$	AN	+0.16	0.005	
$Co([14]tetraeneN_4)(NH_3)_2^{3+}$	H_2O	−0.56	0.015	10[f]
$Co(en)_3^{3+}$	H_2O	−0.47	0.040	5×10^{-5}
$Co(EDTA)^-$	H_2O	−0.04	0.01–0.02	10^{-6}
$Co(NH_3)_6^{3+}$			$0.5–1.3 \times 10^{-3}$ [g]	3×10^{-12} [h]
		B. Other Metallo Complexes		
$Fe(CN)_6^{3-,4-}$			10^{-1} [i]	5×10^2
$Ru(NH_3)_6^{3+,2+}$	H_2O	−0.21	>1	10^3 [j]
$Fe^{3+,2+}$			5×10^{-3} [i]	4
$V^{3+,2+}$			3×10^{-3} [i]	$1.0 \times 10^{-2}(10^{-3})$ [k]
$Eu^{3+,2+}$			2×10^{-4} [i]	1×10^{-4}
$Cr^{3+,2+}$			10^{-5} [i]	$2 \times 10^{-5}(3 \times 10^{-7})$ [k]

[a] For ligand abbreviations see ref 25. [b] AN = acetonitrile. [c] Peak potential *vs.* sce. [d] Values taken from ref 2c or 24 except as indicated. [e] Based on the self-exchange rate observed for *trans*-$Co([14]dieneN_4)(OH_2)_2^{3+,2+}$ (ref 4d). [f] Based on the self-exchange rate observed for $Co([14]tetraeneN_4(OH_2)_2^{3+,2+}$ (ref 4d). From the rate constant for the $Ru(NH_3)_6^{2+}$ reduction of *trans*-$Co([14]tetraeneN_4(NH_3)_2^{3+}$,[4c] we estimate that $k_{exch} = 10^{0.4\pm0.8}$ M^{-1} sec^{-1}. [g] Reference 25. [h] Reference 24. [i] Reference 19. [j] T. J. Meyer and H. Taube, *Inorg. Chem.*, **7**, 2369 (1968); G. Navon and D. Meyerstein, *J. Phys. Chem.*, **74**, 4067 (1970). [k] Values in parentheses estimated from cross reactions with $Ru(NH_3)_6^{3+}$ using the Marcus relation, $k_{12} = (k_{11}k_{22}k_{12}f_{12})^{1/2}$. See ref 4.

correction applied (eq 3) is in fact an overcorrection for double layer effects, and that the actual k_s for each complex lies between the corrected and uncorrected values. It is our opinion, though not supported by existing theories, that the uncorrected values more closely approximate the true k_s value than do the corrected ones. Furthermore, considering the similarities in the complexes one would expect them to exhibit some similarities in behavior and here again the uncorrected k_s values appear to be more reasonable than the corrected ones.

Results and Discussion

Values of the standard heterogeneous rate constant, k_s, for reduction of several cobalt complexes are listed in Table II.[25] To facilitate comparisons we have also included, where possible, estimates of the homogeneous self-ex-

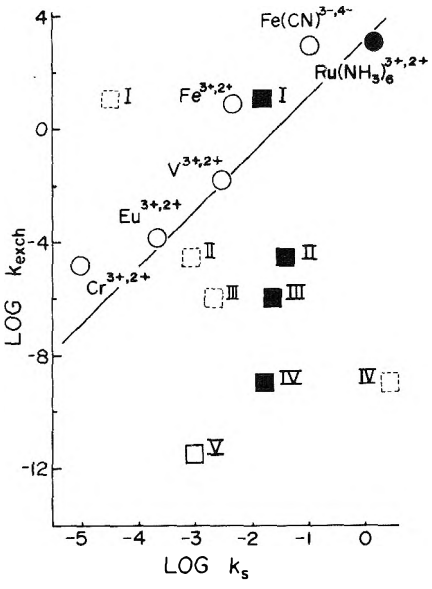

Figure 2. Correlation of homogeneous self-exchange rate constants with heterogeneous rate constants: circles are data from part B of Table II; squares are entries for cobalt couples (part A, Table II). Complexes included are Co([14]tetraeneN$_4$)(NH$_3$)$_2^{3+,2+}$ (I), Co(en)$_3^{3+,2+}$ (II), Co(EDTA)$^{-,2-}$ (III), Co([14]dieneN$_4$)(NH$_3$)$_2^{3+,2+}$ (IV), and Co(NH$_3$)$_6^{3+,2+}$ (V). The line is drawn to fit eq 1 assuming $Z = 10^{11}\ M^{-1}\ \text{sec}^{-1}$ and $Z_{eI} = 10^4$ *cm* sec^{-1}. Solid circles of squares represent values measured in this work, corrected values are indicated by dashed line squares.

change rates for the appropriate cobalt(III)-(II) couples and some similar data previously reported for Co(NH$_3$)$_6^{3+}$ and other complexes.[26-29]

It is a most remarkable observation that the measured values of k_s vary by no more than a factor of 10^2 for a series of cobalt complexes whose homogeneous self-exchange rates vary by a factor of more than 10^{12}. In a way this result might have been anticipated since it is known that many cobalt(III) complexes are polarographically reversible[21,22] whereas the corresponding homogeneous self-exchange rates are well known to be very slow; *e.g.*, both qualitative observations apply to the Co(en)$_3^{3+,2+}$ and Co(EDTA)$^{-,2-}$ couples. However, the magnitude of the discrepancy has certainly not been commonly recognized. Since there has been so much speculation about the kinetic significance of metal ligand interactions in electron transfer cross reactions, whether the interactions be due to bond strengths,[8,30] crystal field strengths,[31] or metal ligand stretching in the activated complex,[8,32] it is very important to note that k_s is relatively independent of the ligands (axial or other) coordinated to cobalt(III). It seems to be a characteristic of both the heterogeneous and homogeneous reactions that the rates of electron transfer reactions of cobalt complexes are very often faster than predicted by the Marcus cross relation (1 or 2).

Despite the anomalous behavior noted for cobalt complexes, such limited information as is available suggests that k_s and k_{exch} are reasonably well correlated by (1) for complexes of many other metals (Figure 2); for example, the empirical relation 4 is in reasonable agreement with (1) and is a reasonable representation of data for complexes not containing cobalt. In fact if one takes cognizance of the relatively poor quality of the values of k_{exch} and k_s currently available the agreement between (4) and (1) is far better than might have been expected. Such problems as reactant adsorption in the heterogeneous reactions and specific ion effects in the homogeneous reactions may require that empirical relations of type (4) are intrinsically imprecise.

$$\log k_{exch} = (2.0 \pm 0.5) \log k_s + (4 \pm 1) \quad (4)$$

The very large difference in the magnitude of the variations observed in k_s and k_{exch} for cobalt complexes suggest some differences in the fundamental physical parameters determining the rates of the two kinds of one electron reductions, heterogeneous and self-exchange. On the other hand, the outer sphere (*e.g.*, with Ru(NH$_3$)$_6^{2+}$ or V^{2+}) reduction rates of these same cobalt complexes in homogeneous solution exhibit a similar independence of the cobalt self-exchange rates.[8] It seems necessary to conclude that the rate constants for cobalt(III)-(II) self-exchange reactions are limited by some factor (or factors) which is less significant in heterogeneous or homogeneous cross reactions of cobalt complexes. At the present time it does not appear that there are significant "spin restrictions" on the cobalt(III)-(II) self-exchange rates.[8,33-37] Much of the variation in these self-exchange rates has been rationalized in terms of ligand reorganizational barriers a view that has received much experimental support and has been widely accepted.[2-8,28,29,35,38] In the sense that (1), a prediction based on such a theory, is consistent with the experimental correlation (4) of k_{exch} and k_s, the present study further corroborates this model. However, we do not find a basis within the context of this model for rationalizing the order observed for self-exchange rates (or standard heterogeneous reduction rates) even of all the complexes not containing cobalt; *i.e.*, the decrease of k_{exch} in the order Fe(CN)$_6^{3-,4-}$ $\sim$ Ru(NH$_3$)$_6^{3+,2+}$ > Fe$^{3+,2+}$ > V$^{3+,2+}$ > Eu$^{3+,2+}$ > Cr$^{3+,2+}$ is extremely difficult to understand only on the basis of the variation in ligand reorganizational barriers.

Despite such reservations the most notable exceptions to reactivity correlations based on (1) or (4) involve reactions of cobalt complexes and these seem most deviant with regard to the reorganizational contributions inferred from cobalt(III)-(II) self-exchange data. It is possible to postulate that self-exchange and cross reaction rate data are intrinsically unrelatable, but this would again be true only in the case of cobalt and would attribute a very unsatisfying complexity and capriciousness to an intrinsically simple class of reactions.

The cobalt(III)-(II) self-exchange reactions do have the relatively unique feature that both the donor and acceptor orbitals are antibonding $^*e_g$. Although it is commonly believed[2] that the reactant orbital overlap integrals, $\int \phi_D \phi_A \, d\tau$, make a negligible contribution to the reaction energetics, it is also evident that in order for the transmission coefficient $\kappa \simeq 1$, $\int \phi_D \phi_A \, d\tau$ must be greater than some minimum value, γ. Since the $^*e_g$ orbitals are buried within the ligation of the complex ion while the t_{2g} orbitals are not, the condition $\int \phi_D \phi_A \, d\tau \geq \gamma$ in effect requires shorter distances of closest approach and different activated complex geometries when the donor and acceptor orbitals are both $^*e_g$ in character than when both are t_{2g} in character or when only the acceptor orbital is $^*e_g$ in character. Thus it seems plausible that variations in cobalt(III)-(II) self-exchange rates arise in part from the work required to achieve the $\int \phi_D \phi_A \, d\tau \geq \gamma$ condition as the ligands are changed.

Acknowledgment. The authors are grateful to Dr. D. P. Rillema for samples of cyclic complexes and for assistance in preparing some of the nonaqueous solutions. One of the authors (J. F. E.) is indebted to Professor J. K. Beattie for some stimulating discussions and for a preliminary report of some of his work.

References and Notes

(1) (a) Partial support of this research by the Public Health Service (Grant No. AM 14391) is gratefully acknowledged. (b) N.D.E.A. Fellow 1967-1969.
(2) For recent reviews see (a) R. A. Marcus, *Ann. Rev. Phys. Chem.*, **15**, 155 (1969); (b) W. L. Reynolds and R. W. Lumry, "Mechanisms of Electron Transfer," Ronald Press, New York, N. Y., 1966; (c) A. G. Sykes, *Advan. Inorg. Chem. Radiochem.*, **10**, 153 (1967); (d) H. Taube, "Electron Transfer Reactions of Complex Ions in Solution." Academic Press, New York, N. Y., 1970; (e) J. E. Earley, *Progr. Inorg. Chem.*, **13**, 243 (1970); (f) R. G. Linck, *MTP Int. Rev. Sci., Inorg. Chem., Ser. 1*, **9**, 303 (1971); (g) N. Sutin, *Chem. Britain*, **8**, 148 (1972).
(3) R. A. Marcus, *J. Phys. Chem.*, **67**, 853 (1963).
(4) J. F. Endicott and H. Taube, *J. Amer. Chem. Soc.*, **86**, 168 (1964).
(5) R. J. Campion, N. Purdie, and N. Sutin, *Inorg. Chem.*, **3**, 1091 (1964).
(6) J. P. Candlin, J. Halpern, and D. D. Trim, *J. Amer. Chem. Soc.*, **86**, 109 (1964).
(7) R. C. Patel and J. F. Endicott, *J. Amer. Chem. Soc.*, **90**, 6364 (1968).
(8) (a) D. P. Rillema, J. F. Endicott, and R. C. Patel, *J. Amer. Chem. Soc.*, **94**, 394 (1972); (b) D. P. Rillema and J. F. Endicott, *Inorg. Chem.*, **11**, 2361 (1972); (c) *J. Amer. Chem. Soc.*, **94**, 8711 (1972).
(9) D. R. Ferrier, Ph.D. Thesis, Wayne State University, 1971.
(10) D. R. Ferrier and R. R. Schroeder, *J. Electroanal. Chem.*, **45**, 343 (1973).
(11) D. R. Ferrier, D. H. Chidester, and R. R. Schroeder, *J. Electroanal. Chem.*, **45**, 361 (1973).
(12) (a) A. A. Vlcek, "Advances in the Chemistry of Coordination Compounds," Macmillan, New York, N. Y., 1961, p 289; (b) *Progr. Inorg. Chem.*, **5**, 211 (1963).
(13) D. H. Childester, Ph.D. Thesis, Wayne State University, 1973.
(14) D. P. Rillema, J. F. Endicott, and E. Papaconstantinou, *Inorg. Chem.*, **10**, 1739 (1963).
(15) R. Angilici, "Synthesis and Technique of Inorganic Chemistry," W. B. Saunders, Philadelphia, Pa., 1969, p 71.
(16) F. P. Dwyer, E. Gwarfas, and D. Meller, *J. Phys. Chem.*, **59**, 296 (1955).
(17) H. Wroblowa, Z. Kovac, and J. O'M. Bockris, *Trans. Faraday Soc.*, **61**, 1523 (1965).
(18) P. Delahay, "Double Layer and Electrode Kinetics," Interscience, New York, N. Y., 1965.
(19) Although eq 3 is the standard correction used to correct measured rate constants for double layer effects, its application to the data presented here is subject to question. For lack of a more appropriate correction it has been used. The sources of our concern are the nonequilibrium double layer involved in the staircase experiment due to the large overall potential changes and the subsequent concentration changes and reactant mass transfer. We anticipate from these considerations that eq 3 overcorrects the measured values. This overcorrection is probably amplified by the use of the formal charges of the reactants without considering ion pairing, activity effects, or the effects of the reactant on the double layer structure. Thus, the measured and corrected rate constants can be considered only to define the range within which the true value falls. This rather large uncertainty in the true rate constant values does not however detract from the conclusions given or from the questions raised in this work.
(20) (Actually αn_a values ranging between 0.4 and 0.6 were estimated from our data; no attempt was made to determine a more accurate αn_a value. Even a large uncertainty in αn_a has little effect on the corrected k_s values especially considering the large uncertainty in z).
(21) Polarographic reversibility is usually observed, in the presence of excess ligand, for those complexes where cobalt(II) complex formation constants are fairly large. For example, see H. A. Laitinen and M. W. Greib, *J. Amer. Chem. Soc.*, 77, 5201 (1955).
(22) See also comments on this point in ref 8 and 14.
(23) R. S. Nicholson and I. Shain, *Anal. Chem.*, **34**, 706 (1964).
(24) If double layer effects are to be significant, then the rather large differences in ϕ for the same complex at the two different perchlorate concentration should have caused major differences in the measured k_s values.
(25) Ligand abbreviations used in this paper are [14]aneN$_4$ = 5,7,7,12,14,14-hexamethyl-1,4,7,11-tetraazacyclotetradecane; [14]dieneN$_4$ = 5,7,7,12,14,14-hexamethyl-1,4,8,11-tetraazacyclotetradeca-4,11-diene; [14]tetraeneN$_4$ = 2,3,9,10-tetramethyl-1,4,8,11-tetraazacyclotetradeca-1,3,8,10-tetraene; en = ethylenediamine; EDTA = ethylenediaminetetraacetate.
(26) N. Tanaka and R. Tamamushi, *Electrochim. Acta*, **9**, 963 (1964).
(27) A value of $k_s = 0.5$–3×10^{-3} cm sec^{-1} for Co(NH$_3$)$_6^{3+}$ has been obtained. H. Bartelt and S. Landazury, *J. Electroanal. Chem.*, **22**, 195 (1969). A value of 1.3×10^{-3} cm/sec is also obtained from Vlcek's data using an E^0 of -0.211 *vs.* sce and diffusion coefficient of 7×10^{-6} cm^2/sec.
(28) N. Sutin, *Ann. Rev. Nucl. Sci.*, **12**, 285 (1962).
(29) An upper limit of 3.3×10^{-12} M^{-1} sec^{-1} for the Co(NH$_3$)$_6^{3+,2+}$ self-exchange rate has been estimated in ref 4 from data of D. R. Stranks, *Discuss. Faraday Soc.*, **29**, 73 (1960); N. S. Biradar and D. R. Stranks, *Trans. Faraday Soc.*, **58**, 2921 (1963).
(30) See discussion in ref 2c-f and C. Bifano and R. G. Linck, *J. Amer. Chem. Soc.*, **89**, 2945 (1967).
(31) P. Benson and A. Haim, *J. Amer. Chem. Soc.*, **87**, 3826 (1965).
(32) H. Diebler, P. H. Dodel, and H. Taube, *Inorg. Chem.*, **5**, 1688 (1966).
(33) J. K. Beattie, private communication, 1971.
(34) R. Farina and R. G. Wilkins, *Inorg. Chem.*, **7**, 514 (1968).
(35) For example, the Co([14]dieneN$_4$)(OH$_2$)$_2^{3+,2+}$ self-exchange rate is slow (10^{-7} M^{-1} sec^{-1} at 70°) despite the fact that Co([14]dieneN$_4$)(OH$_2$)$_2^{2+}$ is predominantly low spin.[36] Recent structural studies have shown that the Co^{II}–OH$_2$ bond lengths are 0.5 Å longer than the Co^{III}–OH$_2$ bond lengths; M. D. Glick, J. Kuszaj, and J. F. Endicott, *J. Amer. Chem. Soc.*, **95**, 5097 (1973).
(36) (a) D. D. Rillema, J. F. Endicott, and N. A. D. Kane-Maguire, *J. Chem. Soc., Chem. Commun.*, 495 (1972); (b) manuscript in preparation.
(37) (a) J. T. Yardley and J. K. Beattie, *J. Amer. Chem. Soc.*, **94**, 8925 (1972); (b) J. K. Beattie, N. Sutin, D. H. Turner, and G. W. Flynn, *ibid.*, **95**, 2052 (1973).
(38) For a contrary point of view see H. L. Stynes and J. A. Ibers, *Inorg. Chem.*, **10**, 2304 (1971).

Excited-State Chemistry of Indigoid Dyes. III. The Interaction of Indigo and Thioindigo with Tin(IV) Tetraphenyltetrahydroporphyrin Triplets: the Photosensitized Isomerization of Thioindigo[1]

George M. Wyman,* Bizhan M. Zarnegar, and David G. Whitten

Department of Chemistry, University of North Carolina-Chapel Hill, Chapel Hill, North Carolina *(Received February 26, 1973)*

Publication costs assisted by the U.S. Army Research Office

The photosensitized cis–trans isomerization of thioindigo, using tin(IV) tetraphenyltetrahydroporphyrin (E_T = 36.5 kcal) as sensitizer resulted in a photostationary-state concentration of 78% trans isomer. The interaction of the dye (cis or trans) with the sensitizer triplet was found to take place at a slightly lower rate than diffusion-controlled, with the cis isomer reacting a little faster than the trans. The sensitizer triplet was also quenched by indigo and by 6,6′-dimethoxyindigo at somewhat slower rates, but without any detectable trans to cis isomerization.

Introduction

It has been known for some time that the direct irradiation of solutions of indigoid dyes (with the exception of indigo and its ring-substituted derivatives) in inert solvents results in cis–trans isomerization.[2] More recently a number of studies have attempted to put this information on a more quantitative basis by developing precise analytical methods for the pairs of isomers[3] and by determining the quantum efficiencies of the various competing photochemical and photophysical processes.[4] Nonetheless far less is known about the photochemistry of these molecules than of other related conjugated unsaturated compounds. Thus, during the past decade the photosensitized cis–trans isomerization of a number of stilbenes and other conjugated olefins has been investigated in depth:[5] these studies have not only extended our knowledge of the particular systems studied, but have also improved our understanding of the mechanism of photochemical reactions in general.

The present work on the attempted photosensitized isomerization of thioindigo (I) (as the prototype of isomerizable indigoid dyes)[4,6] and of indigo (II) and 6,6′-dimethoxyindigo (III) (two indigo dyes that cannot be isomerized by direct irradiation) was undertaken with this dual purpose in mind. *vic*-Tin(IV) tetraphenyltetrahydroporphyrin was selected as the sensitizer (E_T = 36.5 kcal), because its long-wavelength absorption band (at 611 nm) does not overlap with the first absorption bands of I and III (543 and 563 nm, respectively) and only relatively little with that of II (599 nm).

Experimental Section

(A) Materials. Thioindigo was a research sample from the Dupont Co., further purified by recrystallization from chloroform. Indigo and 6,6′-dimethoxyindigo were kindly provided by Professor W. Luettke, University of Goettingen. *vic*-Tin(IV) tetrahydrotetraphenylporphyrin was prepared according to the method of Whitten, Yan, and Carroll.[7] Spectroscopic grade benzene and Merck "Uvasol" toluene were used as solvents.

(B) Preparation of Solutions. Solutions of thioindigo in benzene (or toluene) contained in a 50-ml Erlenmeyer flask were irradiated with filtered light from a 300-W projector lamp for 15 min in order to enrich them with respect to one or the other isomer prior to mixing with an equal volume of sensitizer solution. Irradiation with Corning Filter No. 3-67 gave a cis-rich solution (*ca.* 65% cis), while irradiation with Corning Filter No. 5-60 gave a trans-rich solution (95% trans). Sensitizer concentration was adjusted to yield an optical density of 0.95 at 611 nm in a 1-cm cell in the final mixture. Since indigo and 6,6′-dimethoxyindigo exist only as the trans isomers, preirradiation of these solutions was omitted.

In the experiment involving the determination of the quenching rates of the sensitizer triplet by cis and trans I a cis-rich solution was first prepared as above, degassed and flashed. After flashing *in vacuo*, the solution was exposed to blue light for 15 min (Corning Filter No. 5-60) to convert some of the cis isomer to trans and flashed again. The cis-rich solution was found to contain 56% trans isomer just prior to flashing, while the trans-rich solution contained 78%, as determined spectroscopically.

(C) Photostationary State Measurements. Undegassed solutions (contained in a standard 1-cm absorption cell) were irradiated with filtered light from a 300-W projector lamp for 7 min. (This time period was found to be sufficient to reach the photostationary state.) A Corning No. 2-61 or a Jena RG-610 filter was used to cut out all light with λ <595 nm and the light was passed through a rectangular water bath (i.d. 7 cm) to eliminate heat effects.

(D) Flash Photolysis. Flash photolysis was carried out in an apparatus described earlier[8] with a decay time of 10 μsec. The light output from the flash was filtered by means of the Jena RG-610 filters. The solutions contained in a cyclindrical quartz cell (length, 10 cm; i.d., 1.5 cm) were degassed prior to flashing. The T–T absorption of the sensitizer was monitored at a suitable wavelength in the 435–460-nm region and lifetimes calculated from the observed decay curves. For the measurements on I, in view of its photosensitivity, the monitoring beam was passed through a monochromator before entering the sample cell.

(E) Absorption Spectra. Absorption spectra were measured on a Cary Model 17 recording spectrophotometer using matched quartz absorption cells.

Results

(A) Photostationary-State Measurements. The absorption spectrum characteristic of the photostationary state

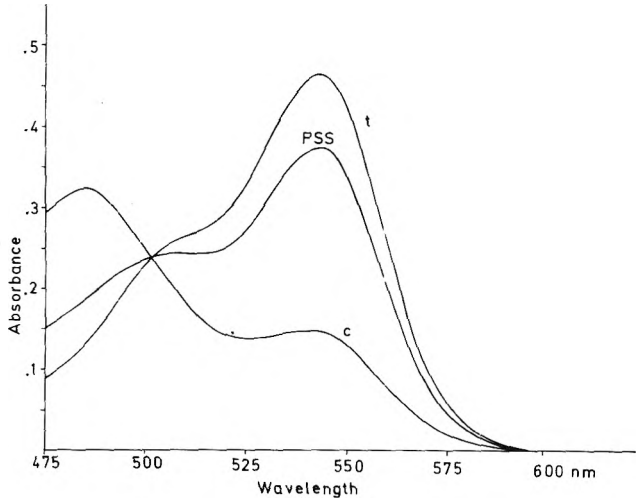

Figure 1. Absorption spectra of thioindigo in benzene with tin(IV) tetraphenyltetrahydroporphyrin sensitizer. PSS curve represents the photostationary state that is reached either from a trans-rich (t) or a cis-rich (c) starting solution. rradiation: 7 min, $\lambda > 595$ nm; reference: sensitizer at the same concentration.

TABLE I: Triplet Lifetimes and Quenching Rate Constants in Toluene

Sensitizer	Quencher	Concn, *M*	τ_{obsd}, μsec	k_q ($\times 10^9$)
Sn^{IV}-THPP	"cis-rich" I	8.05×10^{-6} [a]	49	2.6[b]
Sn^{IV}-THPP	"trans-rich" I	8.05×10^{-6} [a]	51	2.0[c]
Sn^{IV}-THPP	II	1.6×10^{-5}	45	1.2
Sn^{IV}-THPP	III	2.4×10^{-5}	45	0.8
Sn^{IV}-THPP	None	0	446	

[a] Total concentration of I. [b] Calculated for cis-I. [c] Calculated for trans-I.

composition of I in benzene, starting with either a cis-rich or a trans-rich solution is shown in Figure 1 Substantially the same result was obtained when toluene was used as the solvent. The photostationary-state concentrations were found to be independent of sensitizer concentration over a range involving a tenfold variation of the latter. Under similar conditions dyes II and III exhibited no isomerization, but a slow degradation of both dye and sensitizer could be observed upon prolonged irradiation.

(B) Flash Photolysis. The specific rates of the interactions (k_q) with the sensitizer triplet were estimated by determining the dependence of the triplet lifetimes (τ) on the concentration of the dye (quencher).[9] The results are tabulated in Table I. The hope to be able to determine the values for cis-I and trans-I accurately was only partially fulfilled. Although precautions had been taken to protect the cis-rich solution from light during the degassing process, considerable isomerization appears to have occurred during the manipulations that were necessary prior to flashing. As a consequence, since the concentrations of the two isomers were not greatly different in the "cis-rich" and the "trans-rich" solutions and since, as expected, the respective k_q values appear to be quite similar, the measured lifetimes were found to be almost identical. For this reason, not too much credence should be attached to the second digits of the k_q values for cis-I and trans-I in Table I, although there is little doubt that the specific rate constant of the former is slightly greater than that of the latter.

(C) Determination of E_T. The energy level of the sensitizer triplet was determined by observing the weak $S_0 \rightarrow T_1$ transition at 777 nm in methyl iodide solution (E_T = 36.5 kcal). This absorption also appears (at 774 nm and at a reduced intensity) in toluene solutions of the porphyrin indicating the presence of a "built-in" heavy atom effect due to the tin atom in this molecule. Unfortunately, neither thioindigo nor the far more soluble 5,5′-di-*tert*-butylthioindigo was found to exhibit $S_0 \rightarrow T_1$ absorption in the 650–1000-nm region.

Discussion of Results

The observed photosensitized cis-trans isomerization of I is consistent with the behavior of other conjugated unsaturated compounds.[5,10] Under the conditions of the present work direct excitation of the dye could not occur, since the sensitizer was the only species present that could absorb the exciting radiation. The alternative process of energy transfer by a singlet mechanism was also eliminated for every practical purpose, because the singlet energy levels of trans-I and cis-I are considerably higher (by 6.0 and 12.4 kcal, respectively) than that of the sensitizer. Although the E_T values for the two dye isomers are not known, the high, almost diffusion-controlled rates found for this process (*cf.* Table I) attest to the efficient transfer of energy from the sensitizer triplet to both isomers. As a consequence, the S–T splittings in trans-I and, especially in cis-I, must be quite large in order to lower their E_T values below that of the sensitizer (E_T = 36.5 kcal), since it is well known that only exothermic T–T energy transfer processes take place at such high rates.[11]

The results indicate that the photochemical cis-trans isomerization of thioindigo can take place *via* two separate routes: (1) direct isomerization by a singlet mechanism and (2) sensitized isomerization through a triplet intermediate. This is evident from the dramatically different decay ratios found for the two types of processes. In the direct isomerization this ratio was estimated to be 1.22;[4] from the present results, if the photostationary composition of 22/78 (*cf.* Figure 1) is combined with the ratio of the quenching constants from Table I according to eq 1[10]

$$\text{decay ratio} = \frac{k_{T \rightarrow cis}}{k_{T \rightarrow trans}} = \frac{(cis)_{PSS}}{(trans)_{PSS}} \frac{k_q^{cis}}{k_q^{trans}} \qquad (1)$$

(where $k_{T\ cis}$ and $k_{T\ trans}$ represent the respective rate constants for the decay of the twisted intermediate to cis and trans products) a decay ratio of 0.37 is obtained for the photosensitized reaction.[12,13] Thus it appears that the intermediate in the direct reaction yields slightly more cis isomer than trans, while the intermediate in the sensitized reaction decays to the trans isomer about three times as fast as to the cis. (This is in sharp contrast with what has been observed for the stilbenes, where substantially the same decay ratios have been observed in the direct and the sensitized isomerizations;[10] as a consequence there are still some unresolved questions concerning the mechanisms of these reactions.[5]) The inferred large S–T splittings in thioindigo are also consistent with a duality of mechanisms for the isomerization, since this would be expected to make intersystem crossing slow and therefore probably inefficient and less able to compete with the other deactivating processes of the S_1 state. It should be mentioned in this connection that the thioindigo triplet has recently been detected optically by flash or laser-flash excitation.[14]

The unique photostability of indigo and its ring-substituted derivatives (in contrast with thioindigo) has recently been attributed to the possibility of an intramolecular proton-transfer in the S_1 state that is so fast that it takes precedence over the other deactivating processes (fluorescence, twisting, and radiationless decay) normally associated with molecules of this type.[15] Inasmuch as the acidity (*viz.* basicity) characteristics of functional groups in the triplet state frequently more closely resemble the ground state than the S_1 state,[16] it was hoped that trans → cis isomerization could be brought about by photosensitization, bypassing the S_1 state. In addition to indigo, its 6,6′-dimethoxy derivative was selected for this purpose, because (1) its long-wavelength absorption band was sufficiently blue-shifted from that of the parent compound to allow the carrying out of a "clean" photosensitization experiment and (2) by analogy with the corresponding thioindigo compounds the quantum yield of the trans → cis conversion might be expected to be enhanced over that of the parent compound.[17] On the other hand, indigo offered the advantage that, even in the event of a relatively small S–T splitting, the energy transfer from the sensitizer could still be exothermic.

It is apparent from the data in Table I that the two indigos (II and III) differ little from thioindigo with respect to their behavior toward quenching the sensitizer triplets: the rates of this process, though somewhat slower, are still of the order of 10^9 M^{-1} sec^{-1}. It is possible that the slightly lower values indicate that the triplet energies of the two indigo dyes are closer to that of the sensitizer than are those of cis and trans I; this would correspond to considerably less splitting in the former than in the latter compounds. Although the two indigos appear to be efficient quenchers of the sensitizer triplets, it is remarkable that, in contrast with thioindigo, no isomerization can be detected. While quenching without energy transfer remains a distinct possibility, it is perhaps more reasonable to assume that indigo triplets are formed and that these do not undergo isomerization. It is not clear whether this should be attributed to a proton-transfer similar to that proposed for the S_1 state;[15] this would be consistent with the findings of Godfrey, Porter, and Suppan on *p*-hydroxybenzophenone where it was concluded on the basis of chemical evidence that for the CT triplet state of that molecule pK^* is substantially the same ($= -4$) as for its S_1 state.[16] Another possibility is that the triplet potential surface of the indigos is altered to favor the trans form due to hydrogen bonding; such a transoid hydrogen-bonded species would be required to be short-lived and decay only to the trans ground state. In any event indigo derivatives continue to be unique among conjugated unsaturated compounds possessing a central double bond in that they appear to resist both direct and sensitized trans to cis isomerization.

Acknowledgments. The authors are greatly indebted to the Max Planck Institute for Biophysical Chemistry, Göttingen, where most of this work was carried out, for the hospitality extended to two of them (G. M. W. and D. G. W.). It is also a pleasure to thank Professors E. Fischer, A. Weller, and Dr. K.-H. Grellmann for several helpful discussions. Financial support of this research by the Max Planck Society and the U. S. Army Research Office is gratefully acknowledged.

References and Notes

(1) This research was carried out in the Spectroscopy Department of the Max Planck Institute for Biophysical Chemistry, Gottingen, West Germany.
(2) G. M. Wyman and W. R. Brode, *J. Amer. Chem. Soc.*, **73**, 1487 (1951); J. Weinstein and G. M. Wyman, *ibid.*, **78**, 4007 (1956); G. M. Wyman and A. F. Zenhausern, *J. Org. Chem.*, **30**, 2348 (1965).
(3) J. Blanc and D. L. Ross, *J. Phys. Chem.*, **72**, 2817 (1968).
(4) G. M. Wyman and B. M. Zarnegar, *J. Phys. Chem.*, **77**, 831 (1973).
(5) *Cf.* D. L. Ross and J. Blanc in "Techniques of Chemistry," Vol. 3, A. Weissberger, Ed., Wiley-Interscience, New York, N. Y., 1971, pp 479–486, and references quoted therein.
(6) G. M. Wyman, *Chem. Commun.*, 1332 (1971).
(7) D. G. Whitten, J. C. Yau, and F. A. Carroll, *J. Amer. Chem. Soc.*, **93**, 2291 (1971).
(8) K. H. Grellmann, E. Heilbronner, P. Seiler, and A. Weller, *J. Amer. Chem. Soc.*, **90**, 4238 (1968).
(9) C. A. Parker, "Photoluminescence of Solutions," Elsevier, Amsterdam, 1968, p 93.
(10) G. S. Hammond, *et al.*, *J. Amer. Chem. Soc.*, **86**, 3197 (1964).
(11) A. A. Lamola in "Technique of Organic Chemistry," Vol. 14, A. Weissberger, Ed., Interscience, New York, 1969, pp 44–50.
(12) That this is a true decay ratio is indicated by its independence of the sensitizer concentration. Such a result would not be expected, if the triplet decay were to be complicated by selective quenching, *e.g.*, of a transoid triplet[13] by the sensitizer. This suggests that thioindigo triplets decay very rapidly in solution and that E_T for both cis- and trans-I lie below that of the sensitizer.
(13) J. Saltiel, *J. Amer. Chem. Soc.*, **90**, 6394 (1968); 89, 1036 (1967).
(14) *Note Added in Proof.* (a) Using a pulsed nitrogen laser (τ = 2–3 nsec) a short-lived intermediate has been detected in solution. (A. Schomburg, private communication). (b) Thioindigo and 5,5′-di-*tert*-butylthioindigo have recently been found to yield triplets by flash excitation in EPA glass at −196°. (D. Schulte-Frohlinde and H. Herrmann, private communication).
(15) G. M. Wyman and B. M. Zarnegar, *J. Phys. Chem.*, **77**, 1204 (1973).
(16) T. S. Godfrey, G. Porter, and P. Suppan, *Discuss. Faraday Soc.*, **39**, 194 (1965).
(17) D. L. Ross, *Appl. Opt.*, **10**, 571 (1971).

There's nothing theoretical about the value of I&EC Process Design and Development

The original papers contained in this quarterly present theoretical anc experimental results relating to the development of processes and process equipment—and the value of our publication is a known quantity to our constant readers. Subjects covered include:

- Empirical or Semi-theoretical correlations of data
- Experimental determinations of design parameters
- Methods of integrating systems analysis and process control into process design and development
- Scale-up procedures
- Many other experimental process development techniques.

Put us to the test. Complete and return the order form below today.

. . . another ACS service

I&EC Process Design and Development
American Chemical Society
1155 Sixteenth Street, N.W.
Washington, D.C. 20036

Yes, I would like to receive I&EC PROCESS DESIGN AND DEVELOPMENT at the one-year rate checked below:

	U.S.	*Canada*	*Latin America*	*Other Nations*
ACS Member Personal-Use One-Year Rate	☐ $ 7.00	☐ $10.00	☐ $10.00	☐ $10.50
Nonmember	☐ $21.00	☐ $24.00	☐ $24.00	☐ $24.50

Bill me ☐ Bill company ☐ Payment enclosed ☐

Name

Street Home ☐ Business ☐

City State *Zip*

O-73

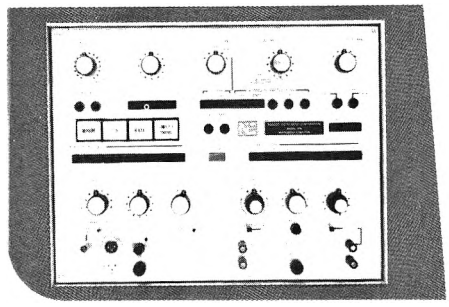

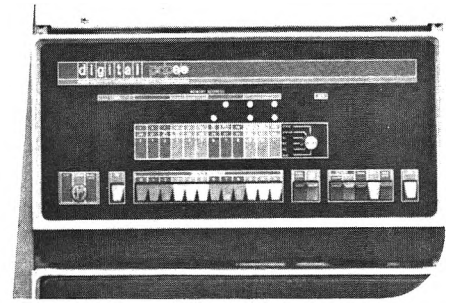

Do you need a signal averager...or a general purpose computer?

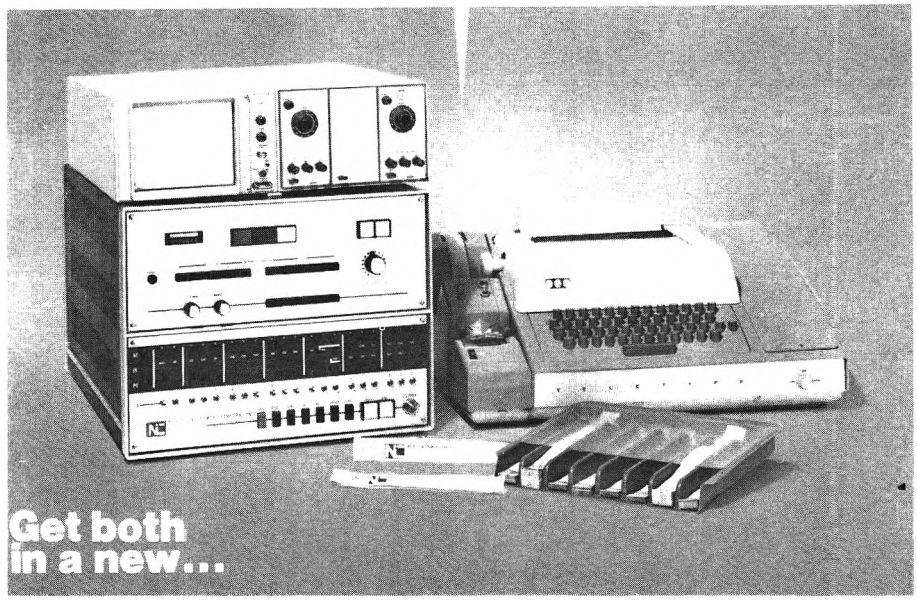

NICOLET NIC-80 DATA SYSTEMS

The new NIC-80 Series data acquisition and processing system combines the benefits of a hard-wired signal averager with the advantages of a general purpose computer. The result is an easy-tc-use data system that permits the scientist to concentrate on his research rather than on electronic data processing.

The NIC-80 Series offers digitizing speeds of up to 10 microseconcs with 12-bit resolution, high resolution timing of up to 1 microsecond, high timing accuracy (100 nanoseconds), 20-bit word length to eliminate double precision programming, easy interface with a wide range of experiments through specialized hardware and software, extensive processing capability through available software, flexible control of experimental variables through keyboard entries, continuous display even at high data rates, a broad selection of peripheral equipmert, and the most thorough applications assistance offered anywhere. For ultra-high-speed applications, digitizing speeds of up to 10 nanoseconds can be achieved with an optional transient recorder.

The NIC-80 Series is presently offered in three different configurations which differ only slightly in hardware design but have a unique software package for each system. For example, the NMR-80 System contains complete programs for Ft nmr work. The MED-80 System is oriented to biomedical applications where the statistical analysis of bioelectric potentials is the task. A third system, called the LAB-80 System is a general purpose laboratory data system designed for use with various spectrometers or other laboratory instruments.

Included in all of the above systems is the hardware for on-line CRT display of incoming data or processed data as well as software for the control of x-y or y-t recorders.

Options and accessories include a high-speed paper tape reader, a disk memory unit, a silent keyboard/printer, x-y or y-t recorders, a transient recorder, paper tape punch, and magnetic tape interface.

LAB-80 capabilities include: averaging and processing of fast scan infra-red spectrophotometer data for sensitivity improvement, background compensation, and color correction; ultra-high-speed data acquisition (10 nanoseconds sampling interval, via Biomation transient recorder), averaging, and processing of data from laser-excited fluorescence decay studies; averaging and processing of electron paramagnetic resonance spectrometer data; and high-speed acquisition (via transient recorder), averaging and processing of pulsed nmr data.

Call or write to discuss your averaging and processing requirements.

NICOLET INSTRUMENT CORPORATION

5225 Verona Road, Madison, Wisconsin 53711
Phone 608/271-3333 TWX: 910-286-2713